

**Department of Chemical Engineering**

**Engineering Carbon Nanocomposites for Energy Storage and  
Conversion**

**Hao Tian**

**This thesis is presented for the Degree of  
Doctor of Philosophy  
of  
Curtin University**

**September 2017**

# Declaration

To the best of my knowledge and belief this thesis contains no material previously published by any other person except where due acknowledgment has been made.

This thesis contains no material which has been accepted for the award of any other degree or diploma in any university.

Signature: ..... ..

Date: .....05/09/2017.....

To my beloved wife and mom

# Abstract

Carbon nanocomposites have been successfully applied in the field of energy storage and conversion such as supercapacitors and lithium ion batteries. Controlled morphologies such as hollow, core-shell and yolk-shell structures have been fabricated to enhance the electrochemical performance of carbon nanocomposites. Recently, a growing social and scientific attention has been paid on carbon nanomaterials with excellent electrical conductivity and high specific surface area. However, it is still very challenging to synthesize carbon nanoparticles with desired morphologies, compositions and porosities. Therefore, this thesis aims to develop facile and effective methods to prepare carbon nanocomposites in well-designed morphologies and controlled compositions, porosities and functionalities in the area of energy storage and conversion.

In the first part of my thesis, we demonstrate a facile synthesis of polymer-silica nanospheres by using an extended Stöber method via triconstituent co-assembly of 3-aminophenol, formaldehyde, and bis[3-(triethoxysilyl)propyl] tetrasulfide followed by copolymerization. N,S-doped carbon-silica nanospheres with either smooth or rough surface can be obtained by direct carbonization of the polymer-silica nanospheres. The carbon-silica spheres present multifunctional properties and exhibit excellent performance as adsorbents for CO<sub>2</sub> capture (67 cm<sup>3</sup>/g at 0 ± 1 °C and 1.0 bar) and as supercapacitor electrodes with high specific capacitance (221 F/g).

The second aspect in this thesis is to investigate a facile synthesis strategy of unique core-shell, yolk-shell and hollow Fe<sub>3</sub>O<sub>4</sub>@carbon microboxes through a one-step Stöber coating method followed by carbonization process. Different calcination temperatures were investigated to manipulate the various structures, and the impact of layer thickness on the battery performance is also assessed. Our results show that the core-shell structured Fe<sub>3</sub>O<sub>4</sub>@carbon microboxes with a nitrogen-doped carbon layer shell having thickness of 15 nm exhibits an excellent performance for lithium-ion batteries with a

high reversible capacity of 857 mAh g<sup>-1</sup> that can be retained after 100 cycles at a current density of 0.1 A g<sup>-1</sup>.

Thirdly, the rational design synthesis of novel yolk-shell structured metal particles loaded ZnO core and microporous carbon shell has been developed. Uniform zeolitic imidazolate framework-8(ZIF-8)@polymer core-shell structures are first synthesized by using ZIF-8 and subsequent hydrothermal treatment resulted in the formation of yolk-shell structure. The following carbonization process resulted in the generation of yolk-shell structured ZnO@carbon. Hydrothermal temperatures were varied to assist to understand the formation of yolk-shell structure and ZnO nanoribbon while the impact of layer thickness is also assessed. Nanoribbon evolution is observed to occur via the formation of the intermediate needle-like nanoparticles. During the carbonization process, it is found that the metal nucleation rate follows the sequence Pd>Au>Pt and the conversion rate of ZnO nanoribbon shows the opposite trend. Examination of Au, Pd and Pt-encapsulated ZnO@carbon for the selective hydrogenation of phenylacetylene to phenylethylene gave >99% selectivity. The outstanding performance of Pd-encapsulated ZnO@carbon nanoparticles gave higher turn over number than Au, Pt-encapsulated ZnO@carbon nanoparticles, Pd/ZnO and Pd/C with the similar Pd loading. Furthermore, all three yolk-shell structured catalysts show superior catalytic stability, and no deactivation occurs after 25 h reaction. This strategy is very promising for the design of multifunctional nanoreactors or nanocontainers for various applications.

Lastly, we presented a synthetic approach of a novel series of nitrogen doped cobalt/carbon nanocomposites and their evaluation of electrochemical properties. Novel yolk-shell structured Co nanoparticles@polymer materials are fabricated from the facile coating polymer strategy on the surface of ZIF-67. After calcination in nitrogen atmosphere, the cobalt/N/C nanocomposites in which cobalt metal nanoparticles are embedded in the highly porous and graphitic carbon matrix are successfully achieved. The cobalt nanoparticles containing cobalt metal crystallites with an oxidized shell and/or smaller (or amorphous) cobalt-oxide deposits appear on the surface of graphitic

carbons. The prepared Co-N-C nanoparticles showed favorable electrocatalytic activity of oxygen evolution reactions, which is attributed to its high graphitic degree, large surface area and the large amount existence of Co-N active sites.

These finding in this thesis provided a series of well-controlled and designed carbonaceous nanomaterials with core-shell, hollow and yolk-shell structures. In addition, these materials have a great potential in the aspect of energy storage and conversion, thus paving a new way at molecular level for multi-purpose applications.

# Acknowledgements

I owe my gratitude to all the people who have made this thesis possible.

I express my warm thanks to my principle supervisor, Dr Jian Liu, for his careful guidance, infectious enthusiasm and encouragement during my study. His great support and inspiration through my PhD research in Curtin University have made the completion of this project possible. I owe my sincere gratitude to my co-supervisor Prof. Shaomin Liu, for his extensive guidance and valuable knowledge. His strong support helped me overcome many problems in both scientific research and daily life. I would like to extend my gratitude to my thesis committee chairperson, Prof. Shaobin Wang, for his assistance and advice throughout this research.

I gratefully acknowledge the Curtin Strategic International Research Scholarship (CSIRS), 2016 Mobility Scholarship from Curtin University, 2016 Chinese Government Award for Outstanding Self-Financed Students Abroad to support my PhD study.

My sincere gratitude goes to Prof. Martin Saunders and Dr Aaron Dodd in the University of Western Australia for the training and valuable knowledge in transmission electron microscopy (TEM) measurements and analyses, Miss Kelly Merigot from John de Laeter Centre in Curtin University for the training and analysis of scanning electron microscopy (SEM), Dr Kane O'Donnell and Dr Jean-Pierre Veder from the Department of Imaging and Applied Physics at Curtin University for the help with the XPS measurements and Dr Sui Boon Liaw and Mr Andrew Chan for the assistance in ICP analysis from Department of Chemical Engineering at Curtin University.

I am thankful to Prof. Degang Li from Shandong University of Technology for his invaluable skills and experiences in the research area of electrochemistry. Special thanks go to Mr Xin Guo, Dr Hao Liu and Prof. Guoxiu Wang from University of Technology

## ACKNOWLEDGEMENTS

---

Sydney for their great support of electrochemical tests of lithium ion batteries. I am grateful to Mr Songcan Wang and Prof. Lianzhou Wang from University of Queensland for their investigation of photocatalytic properties. I also thank Dr Yihan Zhu and Prof. Han Yu from King Abdullah University of Science and Technology for providing excellent theoretical calculations of 3D tomography. I also would like to express my appreciation to Mr Miao Guo and Prof. Qihua Yang from Dalian Institute of Chemical Physics, Chinese Academy of Sciences for catalytic tests. I am also thankful to Prof. Zhiqun Lin from Georgia Institute of Technology, USA for his great support and assistance during my visits in USA.

I would like to offer my special thanks to all Chemical Engineering Department lab technical staffs, Mr. Yu Long, Mr. Xiao Hua, Mr. Andrew Chan, Ms Ann Carroll, Mr. Guanliang Zhou, Ms Roshanak Doroushi, Mr. Jason Wright, Mr. Araya Abera and Ms Anja Werner for their technical support in the lab. From our research group in the Department of Chemical Engineering, I would like to acknowledge all the past and present members including Ms Meiwen Wang, Dr Kun Zhang, Mr Chi Zhang, Mr Zhangfeng Shen and Mr Xiaochen Guo.

I am very grateful to Prof. Zifeng Yan and Prof. Xinmei Liu from China University of Petroleum for their long-time encourage and suggestions in my research career. Most importantly, I would like to thank the loving support from my family especially my wife Mengzhuo Gong and my mother for their love, understanding and encouragement.

# List of Publication

## Published and Accepted papers:

1. **Hao Tian**, Martin Saunders, Aaron Dodd, Kane O'Donnell, Mietek Jaroniec, Shaomin Liu, Jian Liu, *J. Mater. Chem. A*, **2016**, 4, 3721. Triconstituent co-assembly synthesis of N,S-doped carbon-silica nanospheres with smooth and rough surfaces. **(Back Cover)**
2. **Hao Tian**, Jian Liu, Kane O'Donnell, Tingting Liu, Xinmei Liu, Zifeng Yan, Shaomin Liu, Mietek Jaroniec. *J. Colloid Interface Sci.*, **2016**, 476, 55-61. Revisiting the stöber method: design of nitrogen-doped porous carbon spheres from molecular precursors of different chemical structures. **(Front Cover)**
3. **Hao Tian**, Songcan Wang, Chi Zhang, Jean-Pierre Veder, Jian Pan, Mietek Jaroniec, Lianzhou Wang, and Jian Liu, *J. Mater. Chem. A*, **2017**, 5, 11615–11622. **(Back Cover)** Design and synthesis of porous ZnTiO<sub>3</sub>/TiO<sub>2</sub> nanocages with heterojunctions for enhanced photocatalytic H<sub>2</sub> production.
4. **Hao Tian**, Chi Zhang, Hao Liu, Jean-Pierre Veder, Guoxiu Wang, Ming Hu, Mietek Jaroniec and Jian Liu, *Mater. Chem. Front.*, **2017**, 1, 823-830. **(Front Cover)** Fabrication of core-shell, yolk-shell and hollow Fe<sub>3</sub>O<sub>4</sub>@carbon microboxes for high-performance lithium-ion batteries.
5. Chi Zhang, **Hao Tian**, Dong Yang, Jaka Sunarso, Jian Liu, Shaomin Liu, *ChemSusChem*, **2016**, 9, 502. Enhanced CO<sub>2</sub> resistance for robust oxygen separation through tantalum-doped perovskite membranes.
6. Zhangfeng Shen, Guiqiang Wang, **Hao Tian**, Jaka Sunarso, Lihong Liu, Jian Liu, Shaomin Liu, *Electrochim. Acta.*, **2016**, 216, 429-437. Bi-layer photoanode films of hierarchical carbon-doped brookite-rutile TiO<sub>2</sub> composite and anatase TiO<sub>2</sub> beads for efficient dye-sensitized solar cells
7. Juming Liu, Lu Han, Huiyan Ma, **Hao Tian**, Jucai Yang, Qiancheng Zhang, Benjamin J Seligmann, Shaobin Wang, Jian Liu, *Science Bull*, **2016**, 61, 1543-

1550. Template-free synthesis of carbon doped TiO<sub>2</sub> mesoporous microplates for enhanced visible light photodegradation.
8. Jun Yong Chan, Kun Zhang, Chi Zhang, **Hao Tian**, Shaomin Liu. *Ceram. Int.*, **2015**, 10, 14935. Novel tungsten stabilizing SrCo<sub>1-x</sub>W<sub>x</sub>O<sub>3-δ</sub> membranes for oxygen production.
9. Tingting Liu, **Hao Tian**, Jian Liu, Lihong Liu, Shaomin Liu, *J. Nanosci. Nanotechnol.*, **2016**, 16, 9173-9179. Inorganic-salts assisted self-assembly of pluronic F127-organosilica into ordered mesostructures.

### Manuscripts submitted or in preparation

1. **Hao Tian**, Xin Guo, Miao Guo, Hao Liu, Qihua Yang, Mietek Jaroniec, and Jian Liu, to be submitted, ZnO@carbon and Co/CoO@carbon hollow capsules derived from a metal–organic framework for hydrogenation of nitrobenzene and lithium ion batteries.
2. **Hao Tian**, Xin Guo, Hao Liu, Mietek Jaroniec, and Jian Liu, to be submitted, Zn<sub>x</sub>Co<sub>2-x</sub>O<sub>4</sub>@TiO<sub>2</sub> hollow octahedrons derived from a metal–organic framework for lithium ion batteries.
3. **Hao Tian**, Yihan Zhu, Chi Zhang, Shaomin Liu, Yu Han, Mietek Jaroniec and Jian Liu, to be submitted, Yolk-shell structured nanoreactors with metal particles loaded ZnO core and microporous carbon shell.
4. **Hao Tian**, Chi Zhang, Zhangfeng Shen, Shaomin Liu, Mietek Jaroniec, and Jian Liu, to be submitted, Metal–organic-framework-derived formation of Co-N-doped carbon materials for efficient oxygen reduction reaction.

### Conference Paper

1. **Hao Tian**, Shaomin Liu and Jian Liu. Triconstituent co-assembly synthesis of N, S-doped carbon–silica nanospheres with smooth and rough surfaces. The 2nd International Symposium on Renewable Energy Technologies. Sydney, Australia. (Poster)

## LIST OF PUBLICATIONS

---

2. **Hao Tian**, Tianyu Yang, Shaomin Liu and Jian Liu. Engineering Carbon Nanocomposites for Energy Storage and Conversion. Carbon 2017, Melbourne, Australia. (Oral)
3. **Hao Tian**, Shaomin Liu and Jian Liu. 2016 Materials Research Society Fall Meeting. Boston, USA. (Poster).

### Book Chapter

1. **Hao Tian**, Shaomin Liu, Sanping Jiang and Jian Liu. Chapter 1: Functional mesoporous carbons from template methods for energy storage and conversion, Mesoporous materials for advanced energy storage and conversion technologies, CRC Press (Taylor & Francis Group)

# Table of Contents

Declaration .....	I
Dedication .....	II
Abstract .....	III
Acknowledgements .....	VI
List of Publication .....	VIII
Table of Contents .....	XI
List of Figures .....	XV
List of Tables.....	XXI
Chapter 1. Introduction .....	22
1.1 Background .....	22
1.2 Scope and Objectives .....	23
1.3 Thesis Outline .....	24
1.4 References .....	24
Chapter 2. Literature Review .....	26
2. 1 Introduction.....	26
2.2 Synthesis Methods of Carbon Nanocomposites.....	26
2.2.1 The hard template method .....	29
2.2.2 The soft template method .....	29
2.2.3 The hard-soft template method.....	30
2.3. Modification of Carbon Nanocomposites .....	34
2.3.1 Composition.....	34
2.3.2 Porous structure .....	37
2.3.3 Heteroatom-doped effect .....	44
	XI

## TABLE OF CONTENTS

2.3.4 Surface modification.....	51
2.3.5 Graphitization degree .....	55
2.3.6 Morphology effect .....	57
2.4. Applications for carbon materials .....	62
2.4.1 Metal-free electrocatalyst for oxygen reduction reaction.....	62
2.4.2 Batteries (Na-ion sulphur batteries, Na-ion battery, Li-air battery) .....	64
2.4.3 Supercapacitors.....	69
2.5. Summary and future development .....	71
2.6 References .....	72
Chapter 3. Triconstituent Co-assembly Synthesis of N, S-Doped Carbon-Silica Nanospheres with Smooth and Rough Surfaces .....	
89	
3.1 Introduction .....	89
3.2 Experimental Section .....	91
3.2.1 Materials .....	91
3.2.2 Synthesis of N, S-dual functionalized polymer-silica spheres .....	91
3.2.3 Synthesis of N, S-dual functionalized carbon-silica spheres.....	91
3.2.4 Synthesis of silica nanoparticles.....	92
3.2.5 Characterisation .....	92
3.2.6 CO <sub>2</sub> adsorption .....	92
3.2.7 Electrochemical measurement.....	93
3.3 Results and discussion .....	93
3.4 Conclusions .....	107
3.5 References .....	108
Chapter 4. Fabrication of core-shell, yolk-shell and hollow Fe <sub>3</sub> O <sub>4</sub> @carbon microboxes for high-performance lithium-ion batteries .....	
112	
4.1 Introduction .....	112

## TABLE OF CONTENTS

4.2 Experimental Section .....	114
4.2.1 Materials .....	114
4.2.2 Synthesis of Fe <sub>2</sub> O <sub>3</sub> nanocubes .....	115
4.2.3 Synthesis of Fe <sub>2</sub> O <sub>3</sub> @polymer core@shell structures (FP) .....	115
4.2.4 Synthesis of Fe <sub>3</sub> O <sub>4</sub> @carbon core@shell structures (FC) .....	116
4.2.5 Cell assembly and electrochemical testing .....	116
4.2.6 Materials characterization.....	116
4.3 Results and discussion .....	118
4.4 Conclusions .....	132
4.5 References .....	133
Chapter 5. Yolk-shell structured nanoreactors with ZnO core and microporous carbon shell .....	137
5.1. Introduction.....	137
5.2 Experimental section.....	138
5.2.1 Materials .....	138
5.2.2 Synthesis of ZIF-8 .....	138
5.2.3 Synthesis of ZnO@polymer (ZP).....	139
5.2.4 Synthesis of ZnO@carbon (ZC).....	139
5.2.5 Synthesis of metal-loaded ZIF-8 (Au-ZIF-8, Pt-ZIF-8, and Pd-ZIF-8)	
139	
5.2.6 Synthesis of metal-loaded ZnO@polymer (Au-ZnO@polymer, Pt-ZnO@polymer, and Pd-ZnO@polymer).....	140
5.2.7 Synthesis of metal-encapsulated ZnO@carbon (Au, Pt and Pd-encapsulated ZnO@carbon) .....	140
5.2.8 Synthesis of ZIF-8 (without polymer coating) .....	141
5.2.9 Materials Characterization.....	141

## TABLE OF CONTENTS

---

5.3 Results and discussion .....	142
5.4. Conclusion .....	162
5.5 References .....	163
Chapter 6. Metal–organic-framework-derived formation of Co-N-doped carbon materials for efficient oxygen reduction reaction .....	166
6.1. Introduction .....	166
6.2. Experimental section .....	167
6.2.1. Materials .....	167
6.2.2. Synthesis of ZIF-67 .....	167
6.2.3. Synthesis of Co nanoparticles@polymer (CP) .....	168
6.2.4. Synthesis of Co-N-C nanoparticles .....	168
6.2.5. Synthesis of ZIF-67@polymer before hydrothermal reaction.....	168
6.2.6 Oxygen reduction reaction (ORR) performance test .....	169
6.2.7 Materials Characterization .....	169
6.3. Results and discussion .....	170
6.4. Conclusion .....	181
6.5 References .....	182
Chapter 7 Conclusions and recommendations .....	185
7.1 Conclusions .....	185
7.2 Recommendations .....	187
7.3 References .....	189
Appendix I.....	190

# List of Figures

Figure 2.1. Comparison between hard template method and soft template method (a: illustration of hard template;<sup>16</sup> b: TEM images of prepared porous carbon based on hard template method;<sup>17</sup> c: illustration of soft template;<sup>18</sup> d: TEM images of prepared porous carbon based on soft template method;<sup>18</sup> e: illustration of dual template;<sup>19</sup> f: TEM images of prepared porous carbon based on hard-soft template method<sup>19</sup>)..... 28

Figure 2.2. IUPAC classification of porous carbon structure: micropore (SEM image of zeolite Y (a) and A8 carbon (b)),<sup>97</sup> mesopore (TEM image (c) and illustration model (d) of ordered meso-nanoporous carbon),<sup>21</sup> macropore (SEM image (e) and TEM image (f) ordered macro-nanoporous carbon)<sup>32</sup> and hierarchical pore (SEM image (g) and pore size distribution (h) of hierarchical porous carbon.<sup>33</sup> ..... 39

Figure 2.3. Methods of the incorporation of heteroatoms and the example of the correspondent heteroatom doped porous carbon materials for oxygen reduction reaction (ORR) activity. (a) Linear sweep voltammetric curves at different rotation rates for boron-doped ordered mesoporous carbon materials.<sup>118</sup> (b) Linear sweep voltammetric curves for various nitrogen-doped carbon spheres at 1600 rpm.<sup>51</sup> (c) ORR polarization curves for different fluorine-doped mesoporous carbon and Pt/C.<sup>119</sup> (d) Linear sweep voltammetric curves for phosphorus-doped and un-doped ordered mesoporous carbons at different rotation speeds.<sup>120</sup> (e) Rotating disk electrode (RDE) voltammetric curves for various sulfur-doped ordered mesoporous carbons.<sup>121</sup> ..... 45

Figure 2.4. Summary of dual doped porous carbon materials. (a) Adsorption–desorption isotherms and voltage/time plots of the boron and nitrogen co-doped porous carbons.<sup>151</sup> (b) SEM image and linear sweep voltammograms of nitrogen and phosphorous doped porous carbons.<sup>152</sup> (c) TEM image and linear sweep voltammograms of nitrogen and sulphur doped porous carbons.<sup>153</sup> (d) TEM image and specific capacitance cyclic voltammetry (CV) curves of nitrogen and sulphur doped porous carbons.<sup>127</sup> ..... 50

Figure 2.5. Surface modification of porous carbon materials (a): illustration of particle modified carbons; (b) TEM image of Pt/carbon spheres;<sup>55</sup> (c) linear-sweep voltammograms of Pt/carbon spheres for the oxygen reduction reaction (ORR) in an O<sub>2</sub>-

saturated and O<sub>2</sub>-free (under N atmosphere) 0.5m H<sub>2</sub>SO<sub>4</sub> solution at room temperature at a scan rate of 10 mVs<sup>-1</sup>; <sup>55</sup>(d) illustration of surface group modified carbons; (e) (f) TEM image and cyclic voltammogram of mesoporous carbon CMK-3 after oxidation in HNO<sub>3</sub>.<sup>154</sup> ..... 52

Figure 2.6. Tuned carbon nanostructures: (a) spheres, <sup>55</sup> (b) hollow spheres, <sup>202</sup> (c) york-shell nanoparticles, <sup>203</sup> (d) fibres, <sup>204</sup> (e) rods <sup>34</sup> (f) sheets <sup>205</sup> (g) monoliths<sup>206</sup> ..... 58

Figure 2.7. (a) TEM image with the inset of model illustration of cobalt–nitrogen-doped porous carbon material and illustration of oxygen reduction reaction (b) ORR polarization plots of various cobalt–nitrogen-doped porous carbon.<sup>222</sup> ..... 63

Figure 2.8. (a) Schematic cell configurations for the one type of Li-air battery. <sup>246</sup>(b) TEM image mesoporus carbons (MC) and (c) the discharge curve of MC (solid) and Super P carbon black (dash) at 0.5 mA/cm<sup>2</sup>, 0.2 mA/cm<sup>2</sup>, 0.1 mA/cm<sup>2</sup>. <sup>244</sup> ..... 67

Figure 2.9. (a) Representation of an electrochemical double layer capacitor (in its charged state).<sup>256</sup> (b) SEM image and (c) cyclic voltammogram of carbon spheres. <sup>128</sup> ..... 69

Figure 3.1. (a) SEM image, (b) TEM image, (c) STEM and EDS mapping of carbon-silica spheres with N,S-species (N,S-CSS) obtained without hydrothermal treatment. .... 94

Figure 3.2. (a) (b) (c)TEM images, (d) N<sub>2</sub> adsorption-desorption isotherms curve and the inset pore size distribution curve, (e) STEM and EDS mapping of N,S-dually functionalized carbon-silica obtained before hydrothermal treatment with the following calcination at 900 °C (N,S-CSS-900). .... 95

Figure 3.3. (a) SEM image, (b) TEM image, (c) N<sub>2</sub> adsorption-desorption isotherms and the inset pore size distribution curve, (d) high resolution XPS spectrum of N 1s and (e) STEM and EDS mapping of N,S-dually functionalized carbon-silica obtained after hydrothermal treatment (N,S-CSR-1) of N,S-CSR spheres. .... 96

Figure 3.4. XPS survey spectra, high resolution C1s spectra (insert figure) and high resolution S2p spectra (insert figure). .... 97

Figure 3.5. (a) STEM and EDS mapping of N, S-dual functionalized polymer-silica spheres without hydrothermal treatment (N,S-PSS). (b) STEM and EDS mapping of

## LIST OF FIGURES

N,S-dual functionalized polymer-silica spheres after hydrothermal treatment (N,S-PSR). .....	98
Figure 3.6. SEM and TEM images of N,S-CSR-2 (a) (b); N,S-CSR-3(c)(d); N,S-CSR-4(e)(f); N,S-CSR-5(g)(h).....	99
Figure 3.7. (A) N <sub>2</sub> adsorption-desorption isotherms and (B) nonlocal density functional theory (NLDFT) pore size distributions of (a) N,S-CSR-4; (b) N,S-CSR-2; (c) N,SCSS; (d) N,S-CSR-3; (e) N,S-CSR-5.....	100
Figure 3.8. TG profiles of N, S-CSR-1, N,S-CSR-2, N,S-CSR-3, N,S-CSR-4 and N,S-CSR-5.....	100
Figure 3.9. The relationship between particle size of N,S-dual functionalized carbon-silica and molar ratio of TESPTS/AP. ....	102
Figure 3.10. TEM images of air-annealing effect of N,S-CSS-silica (a); N,S-CSR-1-silica (b); N,S-CSR-2-silica (c); N,S-CSR-3-silica (d); N,S-CSR-4-silica (e); N,S-CSR-5-silica(f).....	103
Figure 3.11. The relationship between particle size of hollow silica and molar ratio of TESPTS/AP. ....	104
Figure 3.12. CO <sub>2</sub> adsorption isotherms (T = 0 ± 1 °C) measured for N,S- functionalized carbon-silica spheres N,S-CSR-1, N,S-CSR-3, N,S-CSR-5.....	105
Figure 3.13. CV profiles of N,S-CSS (a) and N,S-CSR-1 (b) measured in basic conditions. ....	106
Figure 4.1. SEM images (a)(b) and TEM images (c)(d) of Fe <sub>2</sub> O <sub>3</sub> cubes, SEM images (e)(f) and TEM images (g)(h) of FP-23. ....	118
Figure 4.2. SEM images (a)(b) and TEM images (c)(d) of FC-23-500; SEM images (e)(f) and TEM images (g)(h), HAADF image, STEM and EDS elemental mapping (i) of FC-23-700; TEM images (j), HAADF image, STEM and EDS mapping (k) of FC-23-900. ....	120
Figure 4.3. TEM images of FP-43 (a)(b), FC-43-500 (c)(d), FC-43-700 (e)(f) and FC-43-900 (g)(h). ....	121
Figure 4.4. TEM images of FP-233 (a), FC-223-500 (b), FC-43-700 (c) and FC-43-900 (d). ....	122
Figure 4.5. TEM images of FP-10 (a)(b), FC-10-500 (c)(d) and FC-10-700 (e)(f)...	123

## LIST OF FIGURES

Figure 4.6. XRD patterns of FC-23-500 (a), FC-23-700 (b), FC-23-900(c), FC-43-500 (d), FC-43-700 (e) and FC-43-900 (f).....	124
Figure 4.7. N <sub>2</sub> adsorption-desorption isotherms and of (a) FC-23-900; (b) FC-23-700; (c) FC-23-500; (d) FC-43-700. ....	124
Figure 4.8. Survey XPS spectra (a)(d)(g)(j), high resolution N 1s XPS spectra (b)(e)(h)(k), high resolution Fe 2p XPS spectra (c)(f)(i)(l) of FC-23-500, FC-23-700, FC-23-900 and FC-43-700, respectively.....	126
Figure 4.9. (a) Discharge capacity versus cycle number plots of FC-23-500, FC-23-700, FC-23-900 and FC-43-700 measured at a current density of 0.1 Ag <sup>-1</sup> , (b) the rate capability of FC-23-500, FC-23-900 and FC-43-700 at different current densities between 0.1 and 5 Ag <sup>-1</sup> .....	128
Figure 4.10. Coulombic efficiency curves of FC-23-500, FC-23-700, FC-23-900 and FC-43-700. ....	130
Figure 4.11. (a) Cyclic voltammograms of FC-23-500 at a scan rate of 0.1 mVs <sup>-1</sup> between 0.01 and 3.0 V, (b) Nyquist plots of the electrodes composed of FC-23-500, FC-23-700, FC-23-900 and FC-43-700. ....	130
Figure 4.12. Cyclic voltammograms of FC-23-700 (a), FC-23-900 (b) and FC-43-700 (c) at a scan rate of 0.1 mVs <sup>-1</sup> between 0.01 and 3.0 V. ....	131
Figure 5.1. XRD patterns of ZIF-8. ....	143
Figure 5.2. TEM images of ZIF-8(a), ZIF-8@polymer before hydrothermal treatment (b). (c)TEM, (d) STEM and EDS mapping of ZP-100. ....	144
Figure 5.3. TEM images of ZIF-8 (without polymer coating). ....	145
Figure 5.4. TEM images of ZP with the sample holder tilted to -30°, 0°, +30° by rotation around the axis of the holder. ....	145
Figure 5.5. TEM images of ZP-3h(a), ZP-6h (b), ZP-12h (c) and XRD patterns of ZP-3h, ZP-6h, ZP-12h and ZP-24h. ....	146
Figure 5.6. (a) The relationship between the hydrothermal temperature and the layer thickness (inset: TEM images of ZP-60 (1), ZP-100 (2), ZP-120 (3), ZP-140 (4)) (b) their corresponding XRD patterns. HRTEM image of ZP-60(c), ZP-100(d) and ZP-140(e) (inset: their corresponding SAED patterns).....	147
Figure 5.7. TEM images of ZP-60 (a), ZP-100 (b), ZP-120 (c), ZP-140 (d). ....	148

## LIST OF FIGURES

Figure 5.8. (a) The relationship between the polymer amount and the layer thickness (inset: TEM images of ZP-1, ZP-100, ZP-2) (b) their corresponding XRD patterns. 150	
Figure 5.9. TEM (a)(b), STEM and EDS mapping(c), XRD pattern (d) and N <sub>2</sub> adsorption–desorption isotherm (e) of ZC, (f)(g)(h) 3D representation of the ZC reconstruction. .... 153	
Figure 5.10. XPS survey spectrum (a) and high resolution N1s spectrum (b) of ZC. 154	
Figure 5.11. TEM images of ZC with the sample holder tilted to -30°, 0°, +30° by rotation around the axis of the holder. .... 154	
Figure 5.12. TEM images of Au-ZIF-8 (a)(d), Pt-ZIF-8 (b)(e), Pd-ZIF-8 (c). HAADF image (f) of Pd-ZIF-8. .... 155	
Figure 5.13. TEM images (a),(e),(i); HAADF images (b)(c), (f)(g), (j)(k) and element mapping images (d),(h),(l) of Au-ZnO@polymer, Pt-ZnO@polymer, and Pd-ZnO@polymer. .... 156	
Figure 5.14. TEM images (a) (b), HAADF images(c), element mapping images (d) of Au-encapsulated ZnO@carbon; TEM images (e), HAADF images (f) (g), element mapping images (h) of Pt-encapsulated ZnO@carbon; TEM images (i), HAADF images (g)(k), element mapping images (l) of Pd-encapsulated ZnO@carbon. .... 157	
Figure 5.15. XRD patterns (a) (b) (c) and N <sub>2</sub> adsorption–desorption isotherm and the corresponding pore size distribution curve (inset) (d) (e) (f) of Au-encapsulated ZnO@carbon, Pt-encapsulated ZnO@carbon and Pd-encapsulated ZnO@carbon... 158	
Figure 5.16. (a) TONs and selectivity to phenylacetylene hydrogenation (b) recycling tests catalysed by metal-encapsulated ZnO@carbon nanoparticles. (Standard conditions: 30 °C; 60 min; 20 mg of catalyst; 1 bar H <sub>2</sub> ; 2.9 mmol of substrate; 25 mL ethanol as solvent. TON = mol phenylacetylene consumed divided by total mol metal. .... 161	
Figure 6.1. XRD pattern of ZIF-67. .... 171	
Figure 6.2. TEM images of ZIF-67 (a), ZIF-67@polymer after hydrothermal treatment (b) (c), STEM and EDS mapping (d). .... 171	
Figure 6.3. TEM images of ZIF-67@polymer before hydrothermal reaction. .... 172	
Figure 6.4. TEM image (a), HRTEM image (b) and HAADF image and mapping images (c) of Co-N-C-700. .... 173	
Figure 6.5. XRD patterns of the prepared catalysts. .... 173	

## LIST OF FIGURES

Figure 6.6. (A) N <sub>2</sub> adsorption isotherms and (B) pore size distributions of (a) Co-N-C-700 (b) Co-N-C-800 and (c) Co-N-C-900. ....	174
Figure 6.7. Full-scan XPS spectra(a), high resolution spectra Co 2p (b), C 1s (c), N 1s (d) of Co-N-C-700.....	176
Figure 6.8. Electrochemical characterizations of Co-N-C catalysts for ORR. (a) CV curves in N <sub>2</sub> -saturated and O <sub>2</sub> -saturated 0.1 M KOH solution. (b) RDE polarization curves in O <sub>2</sub> -saturated 0.1 M KOH solution with a sweep rate of 10 mV s <sup>-1</sup> . (c) K–L plots. (d) LSV curves for Co-N-C-700, Co-N-C-800, Co-N-C-900, and Pt/C nanoparticles. ....	177
Figure 6.9. Tafel plots derived from LSV curves at 1600 rpms for the above catalysts. ....	178
Figure 6.10. Full-scan XPS spectra (a), high resolution spectra Co 2p (b), C 1s (c), N 1s (d) of Co-N-C-800.....	179
Figure 6.11. Full-scan XPS spectra (a), high resolution spectra Co 2p (b), C 1s (c), N 1s (d) of Co-N-C-900.....	179
Figure 6.12. (a) The contents of cobalt and nitrogen (b) The contents of quaternary nitrogen, pyrrolic nitrogen, pyridinic nitrogen, and nitrogen-oxide in above catalysts. ....	181
Figure 6.13. CV curves of Co-N-C-800 (a) and Co-N-C-900 (b) in N <sub>2</sub> -saturated and O <sub>2</sub> -saturated 0.1 M KOH solution. (b) RDE polarization curves of Co-N-C-800 (c) and Co-N-C-900 (d) in O <sub>2</sub> -saturated 0.1 M KOH solution with a sweep rate of 10 mV s <sup>-1</sup> . K–L plots of Co-N-C-800 (e) and Co-N-C-900 (f). ....	182

# List of Tables

Table 2.1. Advantages and disadvantages between hard template method and soft template method.....	28
Table 2.2. Synthesis of nano-porous carbon materials through hard template method	31
Table 2.3. Synthesis of nano-porous carbon materials through soft template method	32
Table 2.4. Synthesis of nano-porous carbon materials through dual template method	33
Table 2.5 Synthesis of core-shell and yolk-shell structured carbon composites derived from MOFs.....	38
Table 3.1. Physical properties of N, S-dual functionalized carbon-silica spheres. ....	101
Table 3.2. Particle size and shell thickness of silica samples. ....	104
Table 3.3. Capacitances of N, S-CSS and N, S-CSR-1 measured in the basic conditions (6mol/L KOH).....	107
Table 4.1. Physical properties of FC.....	125
Table 4.2. The chemical composition of FC-23-500, FC-23-700, FC-23-900 and FC-43-700 obtained by XPS analysis.....	128
Table 4.3. The atomic percentage of pyridinic N, pyrrolic N, quaternary N and oxidized N of FC-23-500, FC-23-700, FC-23-900 and FC-43-700 obtained on the basis of high resolution N 1s XPS spectra.....	128
Table 5.1. Physical properties of FC.....	162
Table 6.1. Physical properties of Co-N-C-700, Co-N-C-800 and Co-N-C-900. ....	176
Table 6.2. The chemical compositions of Co-N-C-700, Co-N-C-800 and Co-N-C-900 obtained by XPS characterization. ....	180
Table 6.3. The atomic percentage of Pyridinic N, Pyrrolic N, Graphitic N and Oxided N of Co-N-C-700, Co-N-C-800 and Co-N-C-900 obtained by their corresponding high resolution N 1s XPS spectrum. ....	181

---

# Chapter 1. Introduction

## 1.1 Background

Since the industrial revolution, energy consumption has been increasing exponentially in the whole world. Energy, which plays a vital role in advancement of the world's economy, continues to be dominantly derived from fossil fuels (natural gas, oil, and coal).<sup>1</sup> However, considering the future global energy requirement and environmental problems sourced from the depletion of natural resources, global warming and pollution from burning fossil fuels, the dependence on fossil fuels has caused urgent energy crisis. Therefore, alternative technologies for using clean and sustainable energy in the field of energy storage and conversion such as fuel cells, supercapacitors and batteries have been developed impressively.

Energy storage and conversion have been recognized as one of most significant energy challenges and received worldwide concern and increasing research interest. Supercapacitors and lithium-ion battery have become dominate power supplies with high energy, power densities and long cycling life. Electrochemical capacitors can accumulate electrical energy due to formation of electrical double layer between electrodes and electrolytes. Rechargeable lithium ion batteries are designed for the storage and conversion of electrochemical energy because lithium is the lightest metal in the periodical table and thus can provide high energy density per electron. Numerous attentions have also been focused on fuel cells which directly convert chemical energy into electricity without conventional combustion process due to the high energy conversion efficiency, Among various types of fuel cells, direct methanol fuel cells and proton exchange membrane fuel cells have drawn much attention because of low operation temperature, abundant fuel supplies, small dimensions and reduced pollution during reaction.<sup>2</sup> This kind of fuel cells consists of oxygen reduction reaction (ORR) at

cathode and hydrogen or methanol oxidation at anode. The rate determining step is the process of the reduction of oxygen and the electrochemical reactions are usually accelerated with the assistance from electrocatalysts.<sup>3</sup> Electrocatalysts are designed to facilitate electron transfer pathways to optimize the produced electricity.<sup>4</sup> However, high cost of commercial electrocatalysts such as platinum particles loaded activated carbons or carbon blacks and the low durability are still two major problems towards large scale productions. In addition, commercial materials usually suffered from some deactivation problems such as the susceptibility to carbon monoxide and methanol poisoning.<sup>4</sup>

To address these problems and acquire superior electrochemical behaviour, high power density and excellent charge-discharge rates, it is important to design and fabricate carbon nanocomposites as electrode materials that provide high surface area and short diffusion paths for ionic transport and electronic conduction. Therefore, it is highly desirable to investigate facile and effective approaches to control the morphologies, structures, porosities, and functionalities of these carbon nanocomposites in the area of energy storage and conversion.

## **1.2 Scope and Objectives**

The overall aim of the thesis is to establish the basic knowledge of preparation of carbon nanocomposites with well-designed and controlled morphologies, porosity and structures and understand the relationship between the physical properties of carbon nanocomposites and chemical performance in energy storage and conversion. Therefore, the detailed objectives of this study are as follows:

1. To development of novel carbon nanocomposites with core-shell, hollow and yolk-shell structures based on the extension stöber method.
2. To establish the necessary understanding of the formation mechanism of these novel carbon nanocomposites through changing synthetic parameters.

3. To examine the chemical properties such as supercapacitor and lithium ion batteries and understand the relationship between their physical and chemical behaviour.
4. To provide better understanding on the design and fabrication of carbon composites with well-controlled morphology for further enhancing their chemical performances.

### **1.3 Thesis Outline**

According to the specific objectives as listed above, this thesis consists of seven chapters. Each chapter in this thesis is outlined below:

- Chapter 1 introduces the background of thesis and objectives of the current research
- Chapter 2 presents the literature reviews on recent development of carbon nanocomposites including wet-chemical synthetic routines, pore size control, doped effect, morphology tuning, surface modification, graphitization degree
- Chapter 3 studies the triconstituent co-assembly synthesis of N,S-doped carbon–silica nanospheres with smooth and rough surfaces and their CO<sub>2</sub> adsorption properties and supercapacitor performance have also been investigated.
- Chapter 4 shows the fabrication of core-shell, yolk-shell and hollow, Fe<sub>3</sub>O<sub>4</sub>@carbon microboxes for high-performance lithium-ion batteries.
- Chapter 5 introduces the preparation of yolk-shell structured nanoreactors with metal particles loaded ZnO core and microporous carbon shell.
- Chapter 6 demonstrates metal–organic-framework-derived formation of Co-N-doped carbon materials for efficient oxygen reduction reaction.
- Chapter 7 concludes the current study and presents the recommendations for future work on carbon nanocomposites with some potential applications.

### **1.4 References**

1. R. D. Cortright, R. R. Davda, and J. A. Dumesic, *Nature*, 2002. **418**. 964-967.

2. R. F. Service, *Science*, 2002. **296**. 1222-1224.
3. Y. Y. Shao, J. H. Sui, G. P. Yin, and Y. Z. Gao, *Appl Catal B-Environ*, 2008. **79**. 89-99.
4. L. P. Zhang and Z. H. Xia, *J Phys Chem C*, 2011. **115**. 11170-11176.

*Every reasonable effort has been made to acknowledge the owners of copyright material. I would be pleased to hear from any copyright owner who has been omitted or incorrectly acknowledged.*

---

# Chapter 2. Literature Review

## 2.1 Introduction

Porous carbon nanocomposites have been used in the area of energy storage and conversion such as batteries and supercapacitors, which have received worldwide concern and increasing research interests.<sup>5</sup> These are attributed to the advantageous properties of porous carbon nanocomposites such as porous structures, low cost, excellent biocompatibility, high resistance to acid and basic environment, large surface area, good mechanical stability, high conductivity.<sup>6</sup>

There are several review papers on the nanoporous carbon for energy storage and conversion.<sup>7-14</sup> Carbon dots, fullerene, amorphous carbons, active carbons and carbon nanotubes are not included in this literature review. The aim of this chapter is to provide basic knowledge of synthesis methods, fabrication and application of carbon nanocomposites. In the first part of this chapter, three main common strategies including hard template method, soft template method and hard-soft template method will be described to prepare porous carbon materials in energy-related fields. Following this, six factors including composition, porosity adjustment, morphology control, doping effect, graphitization and surface modification will be introduced to fabricate the carbon nanocomposites. Finally, the last section describes the major applications of carbon nanocomposites in energy storage and conversion such as supercapacitors, batteries and fuel cells.

## 2.2 Synthesis Methods of Carbon Nanocomposites

Porous carbon nanocomposites with uniform pore sizes are very promising in the field of adsorption, super-capacitors, catalysts and biomedical applications. Most porous carbon materials were usually synthesized through carbonization of raw materials such as coal and wood.<sup>15</sup> Rigid structural inorganic materials such as silica, zeolite and

metal-organic framework have been used as hard template to prepare porous carbons. The hard template method includes several steps (as shown in **Figure 2.1a**<sup>16</sup>): 1) synthesis of hard template materials such as SBA 15, 2) preparation of carbon and hard template composite material, 3) subsequent carbonization of the formed material in an inert atmosphere, 4) the removal of hard template. A representative SEM image (**Figure 2.1b**) showed three dimensionally ordered macroporous carbons (about 200 nm) with mesoporous walls.<sup>17</sup> In addition, preparation of porous carbons through carbonization of block polymers as soft template and resols has also been developed. Relative fewer steps were needed for the soft template method (as shown in **Figure 2.1c**): 1) preparation of the mixture of phenolic resin and block polymer, 2) the removal of block polymer (soft template), 3) carbonization of the formed mesoporous polymer in an inert condition. An example of well-ordered hexagonal carbons was shown in TEM image (**Figure 2.1d**).<sup>18</sup> Advantages and disadvantages between hard template method and soft template method are also summarized in **Table 2.1**. Recently, a combination technique between hard template method and soft template method was developed as well. Hard-soft template method usually involved several steps such as self-assembly of hard and soft template, incorporation with carbon precursors, carbonization of carbon/template complex and then removal of the template matrix (as shown in **Figure 2.1e**). The carbon materials derived from this method presented ordered macroporous/mesoporous structure (in **Figure 2.1f**).<sup>19</sup> In this section, three main different synthetic template methods including hard template method, soft template method and hard-soft template method will be discussed and summarized.

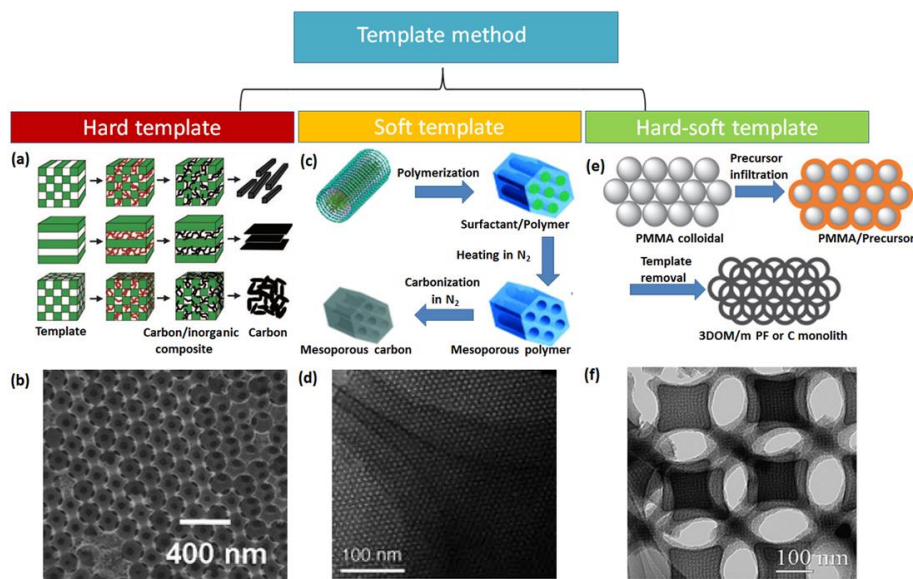


**Figure 2.1.** Comparison between hard template method and soft template method (a: illustration of hard template;<sup>16</sup> b: TEM images of prepared porous carbon based on hard template method;<sup>17</sup> c: illustration of soft template;<sup>18</sup> d: TEM images of prepared porous carbon based on soft template method;<sup>18</sup> e: illustration of dual template;<sup>19</sup> f: TEM images of prepared porous carbon based on hard-soft template method<sup>19</sup>)

**Table 2.1.** Advantages and disadvantages between hard template method and soft template method

	Advantages	Disadvantages
Hard template	<ul style="list-style-type: none"> <li>• Homogeneous and well-defined structure</li> <li>• Easy to control structure</li> </ul>	<ul style="list-style-type: none"> <li>• Multi-step</li> <li>• Template etching</li> <li>• Pore limitation</li> <li>• Mechanically unstable</li> </ul>
Soft template	<ul style="list-style-type: none"> <li>• Tailored architectures</li> <li>• Tuneable surface properties</li> <li>• Mechanically stable</li> <li>• Low cost</li> <li>• Convenient</li> <li>• Large-scale production</li> </ul>	<ul style="list-style-type: none"> <li>• pH-dependent</li> <li>• temperature-control</li> <li>• Surfactant-directed</li> </ul>

### 2.2.1 The hard template method

Meso-porous carbons with controlled porous structure have been synthesized with the help from hard template such as meso-porous silica materials. This kind of materials have attracted intense interests due to the advantageous functionalities such as high specific surface area, uniform pore diameters, large adsorption capacities and high thermal and mechanical stabilities.<sup>20</sup> Therefore, great attention has been paid on advancement of catalysts, hydrogen storage, gas separation, super-capacitors and fuel cell electrodes through utilization of well-regular mesoporous carbons.<sup>21</sup> Various structures and pore diameters have also been designed based on silica template (Table 2.2). Additionally, tailoring pore diameters become quite important to meet the application requirement. But this method is quite complicated, high- priced and difficult for large-scale production.<sup>22</sup> In addition, by using silica template, morphologies and nanostructures of carbon materials are usually restricted. Due to aggregation and cross-linking tendency of silica templates and carbon precursors, it is difficult to obtain small mesoporous carbon nanoparticles through the hard template method.<sup>23</sup> In this section, meso-porous carbon materials synthesized through the hard template method are summarized below.

### 2.2.2 The soft template method

In addition to hard template method, mesoporous carbon materials with various structures could be synthesized through an organic-organic assembly method so called soft template method by using amphiphilic triblock copolymers as templates and phenolic resols as carbon precursors.<sup>18, 24, 25</sup> The preparation of mesoporous materials includes two ways: 1) evaporation induced self-assembly (EISA) method, 2) solvent thermal method.<sup>26, 27</sup> (Table 2.3) The EISA method is used to synthesize mesoporous carbon films and monolithic and solvent thermal method usually produces carbon powders with various particle sizes. There are four important conditions for synthesizing mesoporous carbon materials through soft template method. Firstly, the soft template precursors should own the ability to assemble themselves into nanostructures. Secondly, carbon-generating and pore-forming precursors are necessary. Then, the pore-forming

precursor should tolerate the temperature of the carbon formation, but also should be easily decomposed during carbonization period. Lastly, the carbon-generating precursors should form a highly cross-linked polymeric material and have thermosetting capability to reach the decomposition temperature that the pore-forming precursors need.

28

### 2.2.3 The hard-soft template method

In order to reduce mass transportation derived from long diffusion path lengths, carbon materials with a well-ordered and hierarchically structure containing macropores and mesopores were designed through hard-soft template method (**Table 2.4**).<sup>19</sup> By using colloidal crystal template, macro-pores with a three-dimensionally ordered structure can be produced.<sup>29,30</sup> At the same time, mesoporous structures could be achieved with the assistance of soft template such as Pluronic F127 and P123. Wang et al. reported that this method involved several steps: 1) incorporation polymer spheres with mono-dispersed silica particles, 2) calcination of silica/polymer complex to generate three-dimensionally interconnected and well-ordered macroporous structure with aggregated silica nanoparticles, 3) mixing porous-silica framework with carbon precursors, 4) carbonization of carbon/silica precursor and the subsequent etching of silica particles. They also found the electrochemical activity was enhanced in methanol fuel cell when using hierarchical porous carbons as catalyst support due to the addition of mesoporous structure into the three-dimensionally ordered macroporous structure.<sup>19</sup> In addition, Zhao et al. also used silica colloidal crystals and triblock copolymers PEO-PPO-PEO as dual templates to synthesize hierarchically ordered macro-/mesoporous carbon products.<sup>31</sup> In this section, meso-porous carbon materials synthesized through dual template method are summarized below.

## CHAPTER 2

**Table 2.2.** Synthesis of nano-porous carbon materials through hard template method

Template	Carbon precursor	Porous structure	Pore size (nm)	Pore volume (m <sup>3</sup> /g)	Surface area (m <sup>2</sup> /g)	Application	Reference
Colloidal silica	Monodisperse polystyrene	Three dimensionally ordered macroporous (3DOM) carbons with mesoporous walls	6-90	2.1-2.9	490-1450	Electric double-layer capacitors	<sup>17</sup>
SBA-15	Sucrose	Hexagonally meso-porous	2.2-3.3				<sup>20</sup>
Monodisperse silica particles	Phenol and formaldehyde	Macroporous	62	1.68	750		<sup>32</sup>
Silica synthesized from monodisperse polystyrene (PS) spheres as a template	Furfuryl alcohol	Hierarchical meso-macroporous	17-23,150-170,430-450	1.93	962	Electrocatalytic oxygen reduction	<sup>33</sup>
SBA-15	Sucrose	Meso-porous	4.9-8.8	1.4-1.9	1378-1583		<sup>34</sup>
Colloidal silica crystal	Phenol and formaldehyde	macroporous	200		706	Methanol fuel cell	<sup>35</sup>
SBA-15 and boric acid as pore expanding agent	Sucrose	Meso-porous	3.8-10.5	0.36-0.56	850-1340		<sup>36</sup>
SiO <sub>2</sub> particles (16.8 nm-39 nm)	Sucrose	Meso-porous	12.4-34.5	2.4-3.7	1130-1221		<sup>37</sup>
Meso-macroporous Silica monolith	Furfuryl alcohol	Meso-porous	4.3	1.27	1115		<sup>38</sup>
Micro-meso-macroporous zirconia	Sucrose	Meso-macroporous	10-17, and 25-50	0.44	950		<sup>39</sup>
Macroporous/mesoporous silica	Phenolic resin	Hierarchical macroporous	2.8, 286	0.93	1261		<sup>40</sup>
MgO	Poly(vinyl alcohol) (PVA), hydroxyl propyl cellulose (HPC) and poly(ethylene terephthalate) (PET)	Hierarchical meso-macroporous	2-25		300-1800	Electric double layer capacitor	<sup>41</sup>
Ni(OH) <sub>2</sub>	Phenolic resin	3D hierarchical porous texture with macroporous cores, mesoporous walls, and micropores	1-2, 5-50 and 60-100	0.69	970	Electrochemical performance	<sup>42</sup>
Silica microspheres	Sucrose and cyanamide	Macroporous	150		97	Electrochemical oxygen reduction	<sup>43</sup>

## CHAPTER 2

**Table 2.3.** Synthesis of nano-porous carbon materials through soft template method

Template	Carbon precursor	Porous structure	Pore size (nm)	Pore volume (m <sup>3</sup> /g)	Surface area (m <sup>2</sup> /g)	Application	Reference
Pluronic F127	Phenol/formaldehyde	Meso-porous	6.8	0.51	590		18
Pluronic F127	Phloroglucinol/formaldehyde	Meso-porous	5.4-9.5		378-569		24
Pluronic F127	Phenol/formaldehyde	Meso-porous	2.8	0.38	750		25
Pluronic F127	Resorcinol/formaldehyde	Meso-porous	5.0	0.46	675		26
Pluronic F127/ P123	Phenolic resols	Meso-porous	3.0	0.36	620		27
Polystyrene-block-poly(4-vinylpyridine)	Resorcinol monomers/formaldehyde vapor	Meso-porous	33.7±2.5				44
Pluronic F127	Resorcinol/formaldehyde	Meso-porous	5.9-7.4	0.74-0.81	624-1354		45
Pluronic P123	Phenol/formaldehyde	Meso-porous					46
Poly(ethylene oxide)-block-poly(methyl methacrylate)-block-polystyrene	Resol	Meso-porous	18-24	0/28-0.86	500-1400		47
Poly(ethylene oxide)-block-poly(styrene)	Resol	Meso-porous	32-54	0.7	1000	Magnetization	48
Poly(ethylene oxide)-block-polystyrene and homopolystyrene as a pore expander	Resol	Meso-porous	26-90	0.45-1.1	350-1210		49
Pluronic F127	Phenolic resol	Meso-porous	2.6-3.0	1.1-1.5	940-1130	cell permeability and drug adsorption capacity	50
F123, CTAB	3-aminophenol, formaldehyde	A mesoporous interior with a microporous shell		0.19-0.23	343-394	Electrochemical oxygen reduction	51
FC4 and Pluronic F127	Resorcinol and formaldehyde	Meso-porous	3.5	0.34,0.45	640,857		52

## CHAPTER 2

**Table 2.4.** Synthesis of nano-porous carbon materials through dual template method

Template	Carbon precursor	Porous structure	Pore size (nm)	Pore volume (m <sup>3</sup> /g)	Surface area (m <sup>2</sup> /g)	Application	Reference
Poly(methyl methacrylate) (PMMA) colloidal crystals, Pluronic F127	Phenol-formaldehyde	Hierarchically ordered macro-/mesoporous	3,340	0.35	~500	depth-sensing indentation	<sup>19</sup>
Monodispersed silica colloidal crystals, amphiphilic triblock copolymer PEO-PPO-PEO	Resol	Hierarchically ordered macro-/mesoporous	11, 230-430	1.25	760		<sup>31</sup>
SiO <sub>2</sub> opal, amphiphilic triblock copolymer PEO-PPO-PEO	Phenolic resin	Hierarchically ordered macro-/mesoporous	15-25, 300-400	0.92-4.80	650-1660		<sup>53</sup>

### 2.3. Modification of Carbon Nanocomposites

Different strategies have been proposed for modification of porous carbon composites to achieve optimized performances in the field of energy storage and conversion. This part aims to systematically summarize works for enhancing the properties of carbon composites. Six different aspects including composition, porous structure, doping effect, graphitization degree, morphology control and surface modification are deeply discussed for the design and fabrication of porous carbon composites.

#### 2.3.1 Composition

With regard to the compositions, carbon composites can be used in different research area such as catalysts, supercapacitor, lithium ion batteries and bio-imaging. Carbon composites can be divided into two groups: inorganic carbon composites and metal/metal oxide carbon composites. The composition of the carbon composites could be easily altered by changing the inorganic or metal precursors that embedded in the self-assembly process. The thickness of the carbon shells could be easily tuned by modifying the thickness of the coordination polymer shell.

##### 2.3.1.1 Inorganic carbon composites (silica carbon composites)

Lots of interests have been paid on silica colloids, silica/polymer and silica/carbon with fantastic architectures. One of the representative methodology is the state-of-art stöber method which introduced the synthesis of colloidal silica spheres via the hydrolysis and condensation of silicon precursors such as tetraethyl orthosilicate (TEOS) with ammonia as a catalyst in aqueous alcoholic solution.<sup>54</sup> This routine has also been extended to the construction of monodisperse polymer spheres of resorcinol-formaldehyde (RF) because of the similar reaction mechanism between the silane condensation and RF polymerization.<sup>55, 56</sup>

Recently, this one-step stöber synthesis (sol-gel process) is also utilized prepare highly monodispersed and core-shell structured silica@ resorcinol-formaldehyde sphere and

silica@ carbon spheres.<sup>57-67</sup> For example, Qiao et al. reported the preparation of yolk-shell structured, hollow and mesoporous carbon sphere with controlled particle size by simply using phenolic resols, silica oligomers and hexadecyl trimethylammoniumchloride as raw materials.<sup>59</sup> Core-shell structured silica@carbon nanoparticle can be prepared through coating phenol resin polymer on the surface of silica and the following carbonization process.<sup>67</sup> Recently, an extended Stöber method was used to synthesis polymer-silica nanospheres through triconstituent co-assembly of 3-aminophenol, formaldehyde, and bis[3-(triethoxysilyl)propyl] tetrasulfide. N, S-doped carbon-silica nanospheres with either smooth or rough surface can be obtained by direct carbonization of the polymer-silica nanospheres and high specific capacitance (221 F/g) can be achieved when evaluated as supercapacitor electrodes.<sup>66</sup>

### 2.3.1.2 Metal/metal oxide carbon composites

#### 2.3.1.2.1 Iron carbon composite

Fe<sub>3</sub>O<sub>4</sub>-based nanomaterials with special morphologies and structures have been used as anode materials with superior performance because of their high theoretical capacity, low cost, low toxicity and natural abundance of iron. Designing special core-shell and yolk-shell nanostructure is an efficient strategy to improve the cycling performance of lithium ion battery.<sup>68, 69</sup> Adequate interior can be provided to accommodate large volume change of the Fe<sub>3</sub>O<sub>4</sub> active materials and particle aggregation can also be hindered with the help from the protective shell. Since the extended stöber synthesis of polymer sphere have been developed, this versatile approach for carbon coating have been established to enrich the library of carbon nanocomposites.<sup>70-72</sup> Core-shell and yolk-shell structured Fe<sub>3</sub>O<sub>4</sub>@carbon nanoparticles have been successfully prepared through the following carbonization process of Fe<sub>2</sub>O<sub>3</sub>@polymer.<sup>73-81</sup> For example, Guo et al. described the synthesis of Fe<sub>3</sub>O<sub>4</sub>@Fe<sub>3</sub>C@C yolk-shell nanospindles through coating a layer of resin polymer on the surface of  $\alpha$ -Fe<sub>2</sub>O<sub>3</sub> nanospindles and the following carbonization procedure.<sup>73</sup> The formation mechanism of yolk-shell structure

was also deeply discussed through adjusting carbonization temperature and carbon precursor, indicating that resin polymer coating was important for this well-defined structure and generation of a large pore size and volume. Sufficient internal void space and the  $\text{Fe}_3\text{C}$  shell on  $\text{Fe}_3\text{O}_4$  nanoparticles provided a larger volume expansion and smaller dissolution of the core  $\text{Fe}_3\text{O}_4$  nanoparticles, resulting a higher specific capacity and cycling ability than  $\text{Fe}_3\text{O}_4$ @carbon and  $\text{Fe}_3\text{O}_4$  pure nanoparticles. Paik et al. reported the successful preparation of  $\text{Fe}_3\text{O}_4$ @carbon yolk-shell structure through polymer coating of  $\text{Fe}_2\text{O}_3$  core materials and partially etching the core.<sup>74</sup> The void space between  $\text{Fe}_3\text{O}_4$  cores and carbon shells is also optimized through adjusting the etching time to achieve the highest reversible capacity among the samples.

#### 2.3.1.2.2 Structured carbon composites derived from MOFs

Metal organic frameworks (MOFs) are highly porous materials with high surface areas, large pore volumes and well-defined pore size distributions.<sup>82</sup> MOFs have been considered as sacrificial templates to synthesize varieties of carbon composites. Carbon nanocomposites from MOFs are usually prepared through direct carbonization of MOFs in an inner atmosphere. Xu et al. reported the first example of MOF-derived carbon nanocomposites through carbonization of MOF-5 with impregnation of furfuryl alcohol in the pores.<sup>83</sup> Doping hetero-atoms can also be introduced into the carbon frameworks.<sup>84</sup> Recently, MOFs-based carbon nanocomposites with particular morphology porous structures, good electrical conductivity, and surface functionalities have aroused increasing attention due to their wide applications in catalyst, energy storage and conversion.<sup>85</sup> **Table 2.5** below illustrates the recent development of hollow and core-shell structured carbon nanocomposites derived from metal organic frameworks in lithium ion batteries. For example, Telfer et al. reported the synthesis of nitrogen-doped porous carbon capsules with bimetallic (PtCo) nanoparticles via coating metal-tannic acid coordination polymer or a resorcinol-formaldehyde polymer on the surface of ZIF-8 nanoparticles.<sup>86</sup> The formation of PtCo alloy rather than PtCo segregated nanoparticles is derived from the spatial proximity between the shell and Pt

nanoparticles. The high chemo-selective hydrogenation of nitroarenes to anilines by using these catalysts is ascribed to the small size of PtCo nanoparticles and their especially preferential adsorption with the carbon support. Yamauchi et al. investigated the preparation of nitrogen-doped carbon@graphitic carbon (NC@GC) through the thermal conversion of ZIF-8@ZIF-67 nanoparticles.<sup>87</sup> NC@GC showed better electrochemical specific capacitance (270 F/g) than NC and GC because of combination effect of high surface area, hierarchically micro/mesoporous structures, optimized nitrogen-doping content and graphitic carbon shell thickness.

### 2.3.2 Porous structure

Great efforts have been put on controlling pore size, pore length, pore orientation and pore morphology to enhance catalytic performance of carbon materials. While macropores can provide easy access to the active sites or larger molecules and fast mass transfer, size and shape-selectivity for guest molecules, large surface area and large pore volume can be offered by micropore materials.<sup>88</sup> Therefore, porous structure of carbon material can influence the energy of electro-catalytic reactions and electrochemical corrosion.

There are three types of porous carbon materials according to pore sizes based on the International Union of Pure and Applied Chemistry (IUPAC) regulations: micro-porous < 2 nm, 2 nm < meso-porous < 50 nm and macro-porous > 50 nm (as shown in **Figure 2.2**). Pore size of the nano-porous carbon materials has been tailored from micro-pore to macro-pore. Micro-porous carbons could afford high surface area to enhance reaction rate, but Macro-porous carbon materials could facilitate mass transfer and diffusion of reactants and products in the reaction. Hierarchical structural carbon materials with combined properties will provide the opportunity for the large-scale production of carbon catalyst. Recent developments of the synthesis porous carbon materials with uniform pore sizes were summarized and this part was classified into three sections with regard to pore sizes: micro-porous, meso-porous and macro-porous

## CHAPTER 2

**Table 2.5** Synthesis of core-shell and yolk-shell structured carbon composites derived from MOFs

Materials type	Template	Calcination condition	Particle size (nm)	Shell thickness (nm)	Surface area (m <sup>2</sup> /g)	Pore size (nm)	Pore volume (m <sup>3</sup> /g)	References
Bimetallic nanoparticles supported on porous carbon capsules	ZIF-8 and ZIF-67		100		930		1.28	<sup>86</sup>
Nitrogen-doped carbon@graphitic carbon	Core-shell ZIF-8@ZIF-67	800 °C for 3h	5000		1276		1.78	<sup>87</sup>
ZnO/Ni <sub>3</sub> ZnCo <sub>0.7</sub> /C hybrids yolk-shell microspheres	Zn-Ni-BTC 1,3,5-benzenetricarboxylic acid	450 °C for 2h	1200		112	2-10		<sup>89</sup>
Co-Zn-S@N-S-C-CNT rhombic dodecahedron	Co/Zn-ZIF-67	600 °C for 2h	650	180	19.7	3.8		<sup>90</sup>
Porous ZnO/ZnFe <sub>2</sub> O <sub>4</sub> /C octahedra	MOF-5	500 °C	200	20	140	7.0		<sup>91</sup>
Hierarchical ball-in-ball ZnO/ZnFe <sub>2</sub> O <sub>4</sub> @carbon nanospheres	Zn/Fe-MOF	500 °C	500	50	126			<sup>92</sup>
Core/Shell Structured ZnO/ZnCo <sub>2</sub> O <sub>4</sub> /C hybrids	Zn/Co MOF	400 °C for 1h	800	50	27.9	14	0.146	<sup>93</sup>
Co nanoparticle-embedded carbon@Co <sub>9</sub> S <sub>8</sub> double-shelled nanocages	ZIF-67	600 °C for 2h	1100		106.2			<sup>94</sup>
Carbon-coated hollow mesoporous FeP microcubes	Prussian blue	350 °C for 2h	1000	200	61.3	13.3		<sup>95</sup>
CuO@C multi-yolk-shell octahedra	Cu <sub>3</sub> (BTC) <sub>2</sub> MOF	700 °C for 4h	1500		86	7.0	0.14	<sup>96</sup>

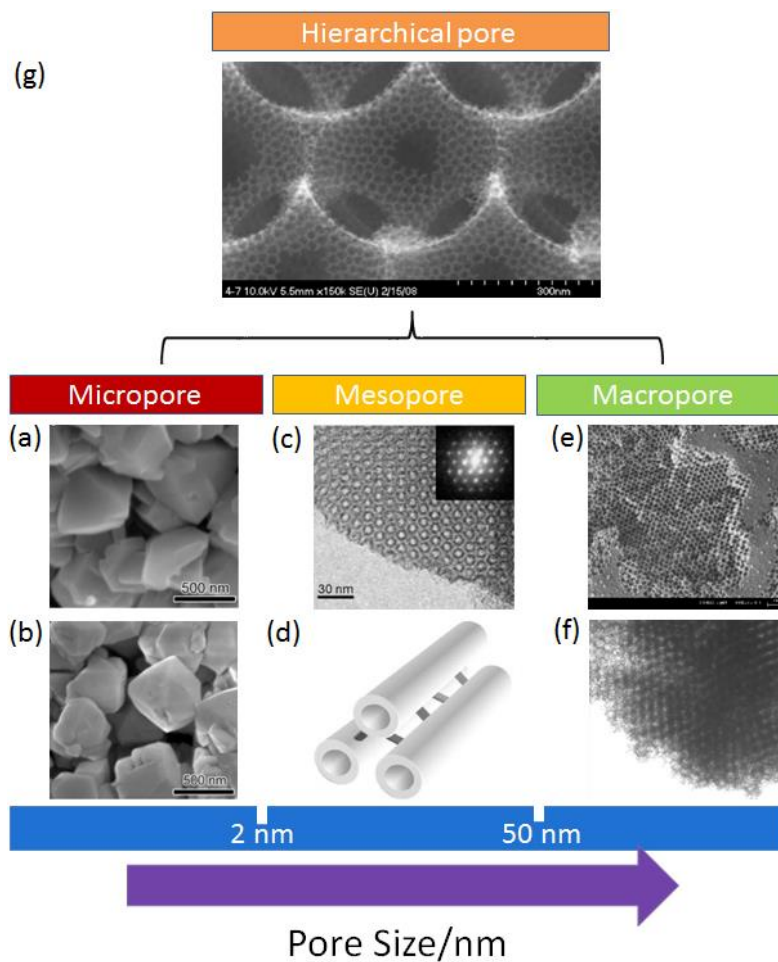


**Figure 2.2.** IUPAC classification of porous carbon structure: micropore (SEM image of zeolite Y (a) and A8 carbon (b)),<sup>97</sup> mesopore (TEM image (c) and illustration model (d) of ordered meso-nanoporous carbon),<sup>21</sup> macropore (SEM image (e) and TEM image (f) ordered macro-nanoporous carbon)<sup>32</sup> and hierarchical pore (SEM image (g) and pore size distribution (h) of hierarchical porous carbon).<sup>33</sup>

### 2.3.2.1 Micro-porous Carbon Materials

Micro-porous carbon materials have been applied in many fields such as gas separation, electrochemical capacitor and shape-selective catalysts. Rigid inorganic templates are usually necessary for synthesizing micro-porous carbon materials with uniform pores

and regular pore arrays. Zeolites with ordered and uniform pores are commonly considered as the inorganic template and utilized in molecular sieves and catalysts.<sup>98</sup>

Kyotani et al. prepared porous carbon materials by using Y zeolite as a template and reported the template synthesis method. Poly(acrylonitrile) and poly(furfuryl alcohol) were used as the carbon precursor and were incorporated into the pores and channels of Y zeolite. Then after carbonization of the complex, the resultants were treated with acid to remove zeolite template to produce micro-porous carbon materials. Due to its high thermal stability, the chemical vapour deposition (CVD) was also investigated as a method to introduce the carbon precursor (propylene gas) into the channels of zeolite, resulting in higher surface areas (over 2000 m<sup>2</sup>/g) and larger pore volume than those of polymer carbons. Transmission electron microscope (TEM) and scanning electron microscope (SEM) results showed the similar morphology of carbon/zeolite and original zeolite template, indicating carbonization occurred in the channel of zeolite. But irregular carbon framework was formed because the carbon layers were stacked together after acid washing with zeolite.<sup>99</sup>

In addition, they also achieved a nitrogen-containing micro-porous carbon with well-ordered structure by using zeolite as an inorganic template. Two-step carbon filling process was operated through impregnation of furfuryl alcohol and the following chemical vapour deposition (CVD) of acetonitrile. The CVD process was necessary for the carbon-loading process in unoccupied channels after poly(furfuryl alcohol) carbonization. SEM image of A8 carbon in **Figure 2.2b** showed smoother surface than zeolite Y in **Figure 2.2a**, indicating the carbons were formed during the zeolite channels in acetonitrile CVD process and that the deposition on the external surface was not significant. The nitrogen-doped well-ordered micro-porous carbon material showed a stronger affinity to water molecular than a non-doped porous carbon material with similar pore structure, indicating nitrogen doping is responsible for the increase of hydrophobicity on the carbon surface.<sup>97</sup>

Recently, an amine functionalized Al-MOF (metal-organic framework) was used to synthesize nitrogen-containing micro-porous carbon material with approximately 1nm narrow pore size and large micro-porous surface area and volume through direct carbonization method by Zhu and his co-workers.. The doped nitrogen atoms in micro-porous carbon material derived from carbonation of amino groups from MOF. They reported that compared with commercial Pt/C (20wt%), the synthesized materials showed higher surface area and specific nitrogen state, which induced the enhancement in the oxygen reduction performance.<sup>100</sup> Han and his colleagues reported the one-step solvothermal carbonization of cyclodextrins to synthesize microporous carbon materials. Moderate sorption capabilities for hydrogen (about 1.07 wt%, 77 K and 1.0 bar) and carbon dioxide (approximately 12.7 wt%, 273 K and 1.0 bar) could be achieved by using these microporous carbon materials.<sup>101</sup>

### 2.3.2.2 Meso-porous Carbon Materials

Many areas including dye adsorbents, catalysts support and electrodes have been involved in the use of meso-porous carbon materials.<sup>22, 102-105</sup> Meso-porous silica materials were synthesized through sol-gel method by using silica precursors with the help of a surfactant self-assembly by Mobil Corporation researchers in 1992.<sup>22</sup> Changing the ratio of the surfactant to the silica precursor and the chain length of the surfactant could control the pore dimension and pore structure of meso-porous silica materials. These materials with uniform pore size, interconnected pore structure and high surface area have been considered as the inorganic templates for the preparation of meso-porous carbon materials. Ryoo group reported that alumina silica material MCM 48 as template could be filled with carbon precursor such as sucrose and also could be polymerized with phenol resin. The following acid dissolution could lead to the removal of the template from the formed complex to produce meso-porous carbon material.<sup>106</sup> They also developed a general method synthesis for highly ordered mesoporous carbons with tuneable diameters by using ordered silica SBA 15 as templates. TEM image (**Figure 2.2c**) and illustration model (**Figure 2.2d**) of ordered meso-nanoporous carbon were also shown. Pt loaded ordered mesoporous carbon material showed superior

electrocatalytic activity for oxygen reduction reaction than that loaded on carbon black due to the enhanced uniformity and the decreased size of Pt cluster.<sup>21</sup>

The applicability of meso-porous carbon materials could be extended to biomolecular related area such as biosensing and separation because carbon could be used as an excellent support for nanoparticles.<sup>34</sup> For example, proteins could be adsorbed in the pores of meso-porous carbons and widening pore size could increase the protein capacitance.<sup>107</sup> Separation capability of biomoleculars could be improved by using well-ordered mesoporous carbons with high surface area.<sup>108</sup> To generate large pores (over 10 nm) in meso-porous material to reach biology-related goal and develop other applications such as electrodes of supercapacitors and pollutant adsorption, ultra-large mesoporous carbon material (about 27 nm) was synthesized by Hyeon group via using meso-cellular aluminosilicate foams as template and phenol resin as carbon source.<sup>109</sup>

In order to enhance electrical conductivity, meso-porous carbon materials with a large surface area and excellent graphitic crystallinity are needed. Fuertes and colleagues prepared meso-porous carbons with graphitic and large porous structures through using polypyrrole-incorporated meso-porous silica materials in the presence of FeCl<sub>3</sub>. Iron salts not only played an important role in polymerization as an oxidant but also promoted the formation of a graphitic structure in carbonization stage. Graphitic carbon materials as electrode in electrical double-layer capacitors (EDLCs) presented better charge-discharge capabilities than non-graphitic materials, because graphitic meso-porous carbon material provided large porosity and highly conductive framework to facilitate electron transfer.<sup>110</sup>

Because meso-porous silica materials are usually high-cost and large-scale unfeasible hard template, a facile, low cost and industrialized method has attracted a lot of attention from researchers. This method is sourced from the self-assembly of inorganic precursors and surfactants in a dilute surfactant water solution.<sup>111-114</sup> The formation of a periodically ordered organic-organic nanocomposite derived from thermosetting polymerized carbon material such as resol and the utilization of a thermally decomposable surfactant like Pluronic 123. For example, a well-ordered meso-porous carbon material with Ia3d symmetry was synthesized through direct assembly of resol

and Pluronic 123 by Zhao et al. The formation of in resol-block-copolymer mesophase in the dilute basic solution was caused by cooperative assembly. After carbonization, the remained meso-porous carbon materials had uniform pore size (about 3 nm) and large surface area (nearly 1150 m<sup>2</sup>/g).<sup>115</sup>

Additionally, hierarchically ordered meso-porous carbon materials had attracted lots of interests and they could be synthesized by using hierarchically ordered meso-porous silica materials. Yoon et al. prepared carbon materials with hollow core and meso-porous shell structure by using solid core with meso-porous shell silica as hard template and resol or poly(divinylbenzene) as carbon source. They also found that appropriate SCMS silica sphere templates could be used to control the diameter of the hollow core and the mesoporous shell thickness.<sup>116</sup>

### **2.3.2.3 Macro-porous Carbon Materials**

Macro-porous carbon materials with different structures could be achieved by using spherical silica particles as template. Yu et al. prepared well-ordered porous carbon materials with different morphologies through utilizing a colloidal crystal template and changing the acid sites for polymerization process of resol as a carbon precursor. Sulphuric acid was needed for silica particles to generate acid sites for polymerization, but strong acid sites existed on the surface of Al-impregnated silica particles. Therefore, the ordered nano-porous carbon formed through filling the whole void around the silica spheres, but Al-impregnated silica particles were considered as the template for polymerization of phenol and formaldehyde, leading to the formation of macro-porous carbons.<sup>35</sup> They also synthesized porous carbon-loaded Pt-Ru materials for methanol oxidation and found the prepared carbon materials showed enhanced activity than commercial E-TEK and Vulcan XC-72 supported Pt-Ru catalysts. This was derived from the high surface area of porous carbons to facilitate metal dispersion and the formation of 3D interconnected uniform macro-pores to improve product diffusion compared with commercial materials. Uniform macro-porous carbons with a pore diameter of 62 nm and BET surface area of 750 m<sup>2</sup>/g were synthesized through using colloidal crystal template and resol as carbon precursor. SEM image and TEM image of

macro-porous carbons were shown in **Figure 2.2e** and **2.2f**, respectively. This material also presented type IV adsorption behaviour due to the well-regular macro-pores.<sup>32</sup>

In addition, anodic aluminium oxide (AAO) films could also be considered as the template to synthesize macro-porous carbon materials. Kyotani and coworkers synthesized carbon nanotubes by depositing propylene in the channels of AAO films and subsequently followed by thermal decomposition of propylene and acid etching. Adjusting current density and oxidation time could control the diameter and the length of the channels in AAO films. Additionally, the wall thickness could also be controlled by altering the carbon deposition period.<sup>117</sup> Hierarchically ordered macroporous carbon materials could also be achieved through hard template method with furfural alcohol as carbon sources. The macropores in the carbon materials, as shown in the SEM (**Figure 2.2g**), were approximately 440 nm with connecting pores (about 160 nm) and mesopores in the wall (almost 20 nm).

### 2.3.3 Heteroatom-doped effect

In order to design cheap and stable nanoporous carbon materials with novel electrochemical and physical properties, heteroatom-doped porous carbons including monodoped atoms such as boron (B), fluorine (F), sulphur (S), nitrogen (N) and phosphorus (P) and dual doped atoms such as boron with nitrogen and nitrogen with sulphur have been reported. In this section, the synthesis methods of doped porous carbons and their catalytic performances will be summarized and discussed below.

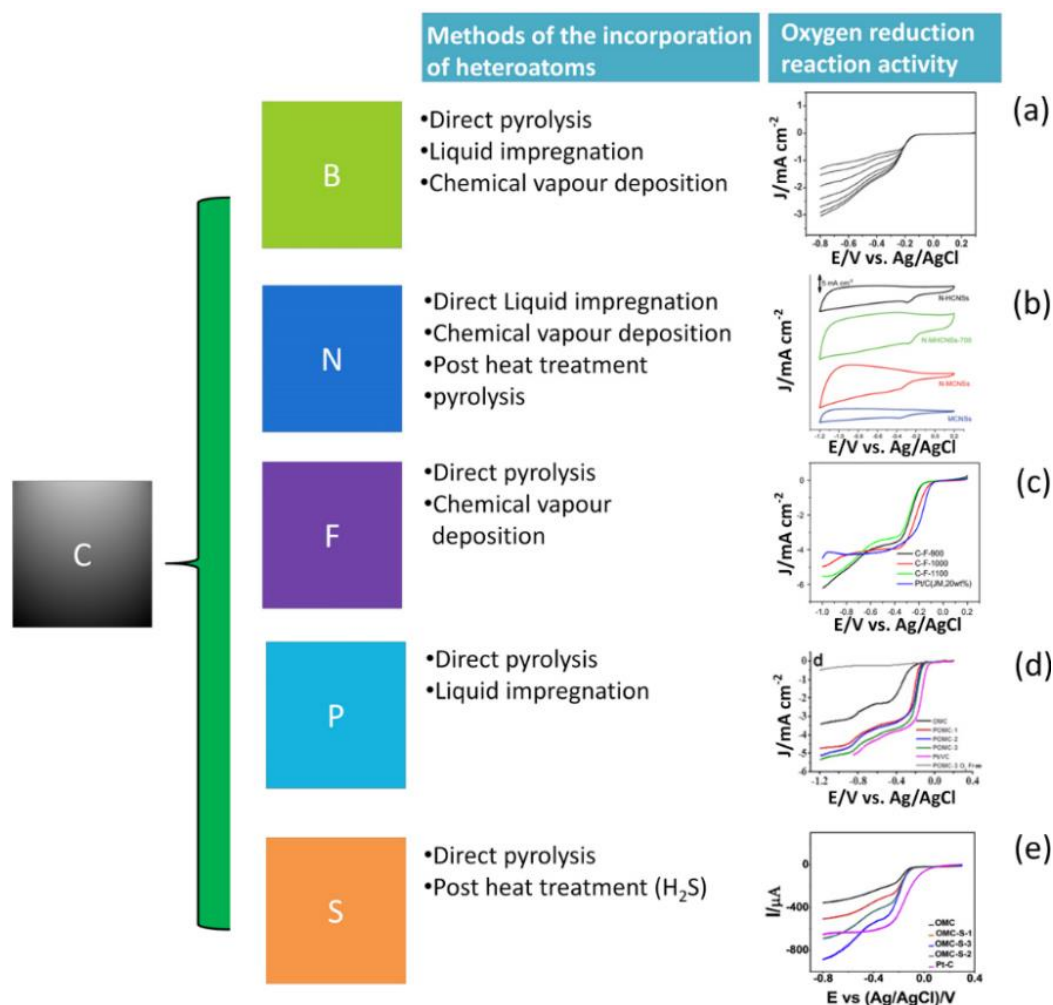


**Figure 2.3.** Methods of the incorporation of heteroatoms and the example of the correspondent heteroatom doped porous carbon materials for oxygen reduction reaction (ORR) activity. (a) Linear sweep voltammetric curves at different rotation rates for boron-doped ordered mesoporous carbon materials.<sup>118</sup> (b) Linear sweep voltammetric curves for various nitrogen-doped carbon spheres at 1600 rpm.<sup>51</sup> (c) ORR polarization curves for different fluorine-doped mesoporous carbon and Pt/C.<sup>119</sup> (d) Linear sweep voltammetric curves for phosphorus-doped and un-doped ordered mesoporous carbons at different rotation speeds.<sup>120</sup> (e) Rotating disk electrode (RDE) voltammetric curves for various sulfur-doped ordered mesoporous carbons.<sup>121</sup>

### 2.3.3.1 Boron-doped

Boron is a unique element that has been reported as replacement in carbon framework to reinforce electrochemical performance.<sup>122</sup> Because the trigonal sites in carbon framework can be substituted by heteroatom boron atoms which could be considered as electron acceptor due to three outer electrons, the electronic band structure of the carbon framework could be modified.<sup>123</sup> This kind of low-level boron doped material also facilitates oxygen chemisorption on carbon surface and assists redox reactions.<sup>124, 125</sup> Therefore, boron doping can be used to modify electrochemical behaviour and metal-free B-doped ordered mesoporous carbons have also been designed in the density of states field of oxygen reduction reaction.<sup>118, 126-128</sup> B-doped ordered mesoporous carbons could be achieved by impregnation of sucrose, 4-hydroxyphenylboronic acid and SBA-15 silica template and the followed carbonization and etching process. As shown in **Figure 2.3a**, catalytic current for this material increased with rotation rate. Both the boron content and surface area affected the catalytic activity for oxygen reduction reaction in alkaline medium. This B-doped mesoporous carbon material also showed higher catalytic selectivity against CO poisoning, superior methanol tolerance and longer stability than commercial Pt/C.<sup>118</sup> He et al. reported the synthesis of ordered boron-doped carbon films with resol as carbon precursor and boric acid as boron precursor via soft template (tri-block polymer F123) method. Graphitization degree of the boron-containing carbon material was increased through the doped method. The prepared boron-doped carbons also presented more corrosion-resistant, hydrophobic and electrically conductive than unmodified carbons.<sup>129</sup>

### 2.3.3.2 Nitrogen-doped

N-doped carbon materials have also attracted lots of attention in recent years. Because nitrogen atoms have higher electronegativity and smaller atomic diameter than carbon atoms, large quantities of defects could be derived from nitrogen doping to provide active sites and further enhance the interaction between nitrogen-doped carbons with reactants. Three different ways are usually used to prepare metal-free N-doped carbon catalysts. The first method is direct pyrolysis of nitrogen-containing precursors such as melamine foam, carbon nitride and polymer framework. For example, Yang et al synthesized N-doped mesoporous carbon spheres with tuneable particle size from 40

to 750 nm through carbonization of nitrogen-containing phenol resin precursors in inert atmosphere. As shown in **Figure 2.3b**, compared with undoped mesoporous carbons, higher specific capacitance was shown for N-doped mesoporous carbons because of the activation of Faradic process in carbons. N-doped mesoporous hollow carbon spheres presented the highest capacitance among these doped carbons due to mesoporous structure, highest surface area and pore volume.<sup>51</sup> The second approach is in situ incorporation of doped nitrogen atom into carbon framework via liquid impregnation or chemical vapour deposition (CVD).<sup>130-134</sup> Xia et al. reported the synthesis of N-doped mesoporous carbons via carbonization of SBA-15 in acetonitrile-saturated nitrogen atmosphere with ordered mesoporous structure, graphitic pore walls and hollow sphere morphology.<sup>130</sup> They also developed this chemical vapour deposition method to synthesize N-doped mesoporous carbon by using various porous silica such as SBA-12, SBA-15, MCM-48, MCM-41 and hexagonal mesoporous silica. Ordered mesoporous carbon materials could not be achieved by using MCM-41 and hexagonal mesoporous silica as templates because of the lack of pore connectivity in their pore channel system. The third way is post heat treatment of carbon materials in ammonia or polyaniline at high temperature.<sup>135-137</sup> Rafael et al. synthesized mesoporous nitrogen-doped carbons through in situ polymerization of polyaniline in the pore channel of SBA-15, followed by calcination of polyaniline and SBA-15 composite materials and etching process. Excellent electrocatalytic activity toward oxygen reduction reaction was also presented by using this obtained N-doped mesoporous carbons.<sup>136</sup>

### 2.3.3.3 Fluorine-doped

Structural and chemical properties of mesoporous carbon materials can be modified through fluorination. The commonly-used method is chemical vapour deposition such as fluorine gas.<sup>138, 139</sup> For example, Dai et al. synthesized fluorinated carbon with an ordered mesoporous structure through reaction between carbon material and fluorine gas.<sup>138</sup> But the problem of nonuniform modification and pore blockage may bring troubles for post-synthesis because of the inert carbon surface. Mesoporous structure may be destroyed under rigorous conditions.<sup>140</sup> Therefore, highly ordered fluorinated

mesoporous carbons were synthesized by the one-pot soft template approach using phenol-formaldehyde/p-fluorophenol as carbon precursors. This material sustained well-ordered porous structure with large pore size (4.4 nm), large pore volume (0.7 cm<sup>3</sup>/g) and high surface area (998 m<sup>2</sup>/g) and C-F covalent bonds were maintained at 900°C. A higher electron transfer rate was also observed by using the synthesized fluorinated mesoporous carbon materials than pure unmodified carbons.<sup>140</sup> Electrocatalytic activity toward oxygen reduction reaction was also evaluated by using F-doped mesoporous carbon materials through hard template method. This material showed comparable activity to Pt/C (as shown in **Figure 2.3c**) due to high surface area, large active sites and partly graphitization degree.<sup>119</sup> In addition, mesoporous carbons with higher F/C ratio (0.81) were prepared through soft template and subsequent fluorination method. The diameter of the prepared carbon material can reach 11 nm and the specific area can also approach 850 m<sup>2</sup>/g after fluorination. Moreover, compared with commercial carbon fluorides with comparable fluorine content, the synthesized carbons showed better performance in Li/CF<sub>x</sub> batteries such as higher discharge potentials, energy and power densities and faster reaction kinetics when applied in high current densities.<sup>141</sup>

#### 2.3.3.4 Phosphorus-doped

Phosphorous atoms own similar chemical properties with nitrogen atoms due to the same number of valence electrons, but larger atomic radius and higher electron-donating capability of phosphorous atoms could induce enhanced catalytic activity and durability.<sup>120</sup> Recently, the phosphorus-doped porous carbon materials were reported to exhibit superior electrochemical performances than non-modified materials as supercapacitor electrodes.<sup>120, 126, 142</sup> For instance, Yu et al. reported the synthesis phosphorus-incorporated ordered mesoporous carbons through co-pyrolyzing a phosphorus precursor and a carbon precursor with SBA 15 as a hard template. This metal-free catalyst showed superior electro-catalytic activities long term stability and resistance to alcohol crossover effects for oxygen reduction reaction (ORR) in alkaline conditions compared with Pt/C (as shown in **Figure 2.3d**). This was attributed to the defects in

carbon framework, leading to enhanced electron delocalization and formed active sites. Through shortening the length of doped carbons, the increased ORR activity was observed due to larger surface area and reduced resistance of shorter channels.<sup>120</sup>

### 2.3.3.5 Sulphur-doped

Sulphur atoms have similar electronegativity with carbon atoms and could also be incorporated into carbon matrix through in situ doping such as direct carbonization of sulphur-containing species (benzyl disulfide<sup>121</sup>, 2-thiophenemethanol<sup>143-146</sup>, p-toluenesulfonic acid<sup>147</sup>, 4,4'-thiodiphenol<sup>148</sup>) and post treatment such as calcination in H<sub>2</sub>S<sup>149</sup> or SO<sub>2</sub><sup>150</sup> at a high temperature. S-doped mesoporous carbon was prepared by infiltration and polymerization of 2-thiophenemethanol in SBA-15 template and the following carbonization and HF etching process. Compared with commercial available sulfur-impregnated activated carbon, this material presented higher mercury saturation binding capacity and faster sorption kinetic of mercury adsorption in aqueous solution. This was probably derived from high sulphur concentration, easy accessibility and lack of blockage in this carbon material. Additionally, Guo et al. reported the synthesis of sulphur-doped ordered mesoporous carbon materials by using SBA-15 as a hard template, sucrose as a carbon source, benzyl disulfide as a sulphur source. The RDE voltammograms (**Figure 2.3e**) clearly showed that all of the S-doped ordered mesoporous carbons have higher currents than undoped materials, indicating that the enhanced electrocatalytic performance was attributed to the formation of covalent bond between carbon and sulphur.<sup>121</sup>

## 2.3.3.6 Dual doped

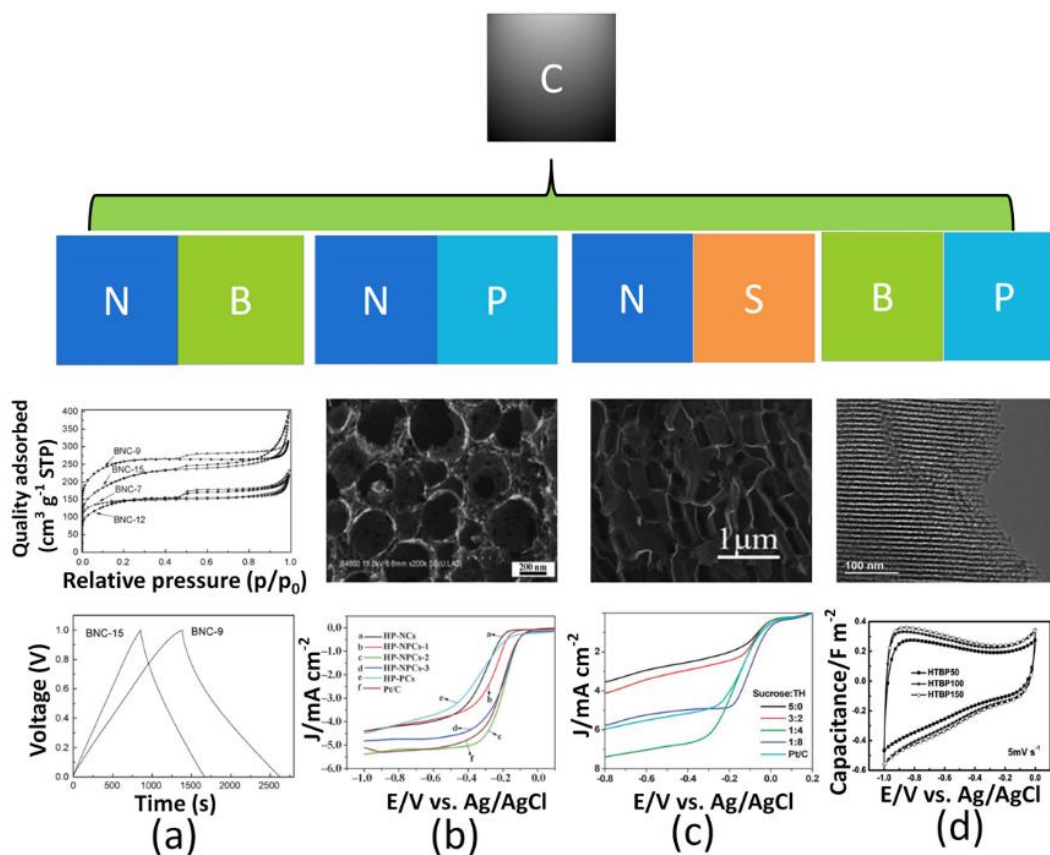


**Figure 2.4.** Summary of dual doped porous carbon materials. (a) Adsorption–desorption isotherms and voltage/time plots of the boron and nitrogen co-doped porous carbons.<sup>151</sup> (b) SEM image and linear sweep voltammograms of nitrogen and phosphorous doped porous carbons.<sup>152</sup> (c) TEM image and linear sweep voltammograms of nitrogen and sulphur doped porous carbons.<sup>153</sup> (d) TEM image and specific capacitance cyclic voltammetry (CV) curves of nitrogen and sulphur doped porous carbons.<sup>127</sup>

Dual doped or multi-doped carbon materials have also been developed and the synergistic effect of co-doped heteroatoms (as shown in **Figure 2.4**) has led to enhanced catalytic activity.<sup>126, 127, 151-153</sup> N and P dual-doped hierarchical porous carbon materials were first synthesized by using poly(vinyl alcohol)/polystyrene hydrogel as template, cyanamide as nitrogen source and phosphoric acid as phosphor source. This material

with hierarchical interconnected macroporous structure (**Figure 2.4b**) exhibited excellent electrocatalytic activity towards oxygen reduction reaction in acid, basic and neutral media. **Figure 2.4b** showed that better performance of methanol tolerance and higher stability were also exhibited compared with Pt/C. Dual doping provided large asymmetrical spin and charge density and the macroporous/mesoporous structure also facilitated the electron and reactant transport and large surface area.<sup>152</sup> Huang et al. reported the synthesis of sulphur and nitrogen co-doped carbon foam with hierarchical pore structure (**Figure 2.4c**) with sucrose as carbon source, thiourea as nitrogen and sulphur source through hard template (SBA) method. They found the mass ratio between sucrose and thiourea was not only responsible for the morphologies and structures of the final carbon materials, but also played a key role in the difference of electrochemical performance. Compared with commercial Pt/C, the carbon foam (sucrose: thiourea=1:4) exhibited higher electrochemical activity and better methanol tolerance, as shown in **Figure 2.4c**. This was resulted from the synergistic effect via co-doping, high graphitic degree caused by high temperature, premium reactant transport from hierarchical porous structure, excellent electron transfer by three dimensional carbon frameworks and the bonding configuration.<sup>153</sup> Boron and phosphor dual doped ordered mesoporous carbon with high homogenous distribution of heteroatoms were achieved through a facile hydrothermal self-assembly method and the following carbonization process. The size of the pores in dual doped carbons, measured by the TEM image (**Figure 2.4d**), was about 12 nm. When applied as supercapacitor electrodes, the supercapacitance increased with the hydrothermal temperature (**Figure 2.4d**) due to the increased acidity and the improved surface polarity and the three materials showed similar symmetric shapes and CV curves.

### 2.3.4 Surface modification

The modification of the surface of porous carbon material is very significant because carbons materials are usually used as catalysts support to enhance application behaviour. There are two main ways to functionalize the surface of carbons: deposition nanoparticles and functional group modification.

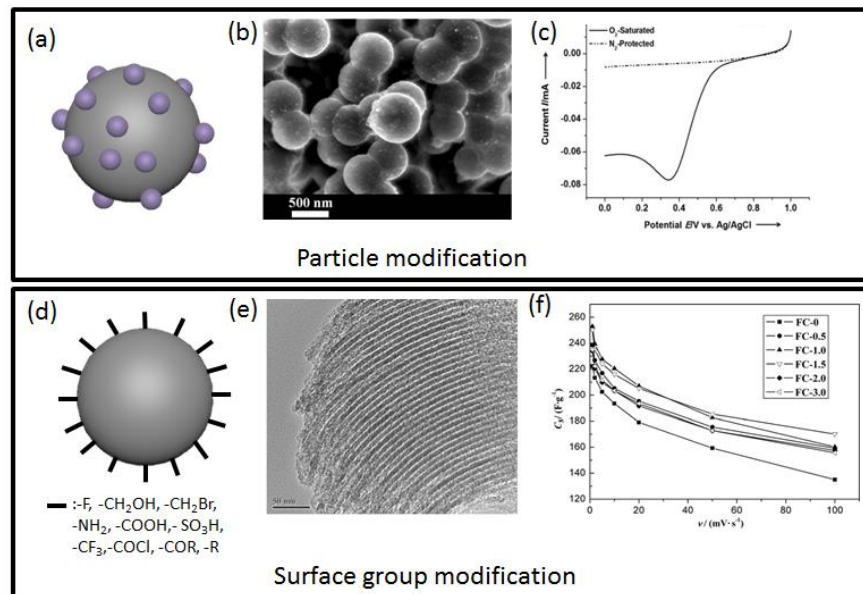


**Figure 2.5.** Surface modification of porous carbon materials (a): illustration of particle modified carbons; (b) TEM image of Pt/carbon spheres;<sup>55</sup> (c) linear-sweep voltammograms of Pt/carbon spheres for the oxygen reduction reaction (ORR) in an O<sub>2</sub>-saturated and O<sub>2</sub>-free (under N atmosphere) 0.5m H<sub>2</sub>SO<sub>4</sub> solution at room temperature at a scan rate of 10 mVs<sup>-1</sup>; <sup>55</sup>(d) illustration of surface group modified carbons; (e) (f) TEM image and cyclic voltammogram of mesoporous carbon CMK-3 after oxidation in HNO<sub>3</sub>.<sup>154</sup>

### 2.3.4.1 Nanoparticle modification

Nanoparticles deposition on the surface of carbons is often considered as a very effective method to adjust the interfacial properties and improve the interaction among molecules. An illustration of particle modified carbons was shown in **Figure 2.5a**. Due to the reliability of surface modification in electrical process, electron conductivity and electrochemical activity can be improved through incorporation of nanoparticles on the surface of porous carbon materials.

Many methodologies have been developed to modify carbon materials through combining the secondary phase within carbon structure. Two main ways are commonly used to incorporate secondary particles into carbon framework: impregnation metal salt

precursors with carbon framework and incorporation hard or soft template with metal salt precursors with the following template removal process. The first technique is direct loading of nanoparticles on the surface of carbon framework through impregnation methods. Due to cheap and simple synthesis, impregnation method is widely utilized. After mixing metal salt precursors with carbon frameworks, drying and calcination process, metal oxides such as iron oxide, copper oxide, nickel oxide, cobalt oxide, manganese oxide, and zinc oxide are loaded on the surface of porous carbons.<sup>155-159</sup> Zhao et al. synthesized SnO loaded ordered mesoporous carbon materials through deposition method by using SnCl<sub>2</sub> and phosphorus ester OP(OCH<sub>3</sub>). Compared with other hydrophilic phosphorus precursors such as PCl<sub>3</sub> and H<sub>3</sub>PO<sub>4</sub>, the use of hydrophobic OP(OCH<sub>3</sub>) facilitates precursor impregnation and uniform formation of SnO. The synthesized material presented better cycle-ability as negative electrodes for lithium-ion batteries than those discrete SnO<sub>2</sub> nanoparticles.<sup>160</sup> In addition, Pt nanoparticles (about 6 nm) could be loaded on the surface of carbon spheres (**Figure 2.5b**) derived from monodisperse resorcinol and formaldehyde (RF) resin polymer. **Figure 2.5c** showed that an onset potential about 0.6 V in linear sweep voltammograms under the O<sub>2</sub> atmosphere for the oxygen reduction reaction was presented by using this composite material, indicating carbon spheres could become an excellent candidate of support materials.<sup>55</sup> The second method is a direct, one-port, co-assembly method through incorporation of carbon precursor, metal precursor and hard template such as SBA-15 or soft template such as block copolymer. Jaroniec et al. prepared mesoporous carbon materials with ultra-thin pore walls and highly dispersed nickel nanoparticles. They used SBA-15 as a hard template, nickel nitrate hexahydrate [Ni(NO<sub>3</sub>)<sub>2</sub>·6H<sub>2</sub>O] as a nickel source and 2,3-dihydroxynaphthalene (DHN) as a carbon source. Additionally, the nickel nanoparticles with uniform size about 3 nm were homogeneously distributed on the tubular carbon walls.<sup>161</sup> For example, Zhao et al. synthesized ordered mesoporous carbon materials with iron-oxide nanoparticles through a chelate-assisted multicomponent co-assembly method by using acetyl-acetone as a chelating precursor, iron nitrates as metal precursor and phenolic resol as a carbon source and copolymer Pluronic F127 as soft template. 2-D hexagonally pore structure with uniform pore size (about 4 nm) and high surface area (approximately 500 m<sup>2</sup>/g) and highly dispersed iron

oxide nanoparticles were generated after carbonization. They also found the amount of acetyl-acetone could control the particle size of iron oxide and the synthesized iron/carbon material showed excellent catalytic performance, high stability and high selectivity in Fischer-Tropsch Synthesis due to high porosity of carbon framework and semiexposed structure of iron-oxide nanoparticles.<sup>162</sup>

#### 2.3.4.2 Functional group modification

Functional groups on the surface of carbon materials are treated as anchoring sites for metal catalysts and can assist the metal adsorption on the carbon surface. This usually leads to high dispersion of metallic species on the surface and enhanced chemical performance in fuel cells.<sup>7</sup> Five main methods are usually used for functional group modification of carbon surface involving oxidation, KOH activation, sulphonation, halogenation, polymer decoration and grafting. An illustration of surface group modified carbons was shown in **Figure 2.5d**.

Oxygen containing functional groups such as anhydride, carboxylic acid, ether, ketone, phenol are introduced to carbon surface through covalent, electrostatic and hydrogen bonding interactions, resulting in the enhanced wettability of the pores by polar solvents and electrochemical capacitance of porous carbon material.<sup>163</sup> Oxidizing gases such as air oxygen and ozone and oxidizing solutions such as nitric acid and hydrogen oxide are usually used for oxidation of carbon surface.<sup>164, 165</sup> Because excessive oxidation results in structural collapse of carbon framework, the oxidation conditions must be chosen carefully. For example, carboxyl-group and hydroxyl-group modified mesoporous carbons were synthesized through oxidation treatment of CMK-3 in nitric acid solutions. The ordered mesoporous carbon structures were maintained after acid treatment, as confirmed from TEM image in **Figure 2.5e**. It could be also clearly seen from **Figure 2.5f** that the capacitance of all the materials decreased with the increase of scan rate and FC-1.5 exhibited the highest specific capacitance among the test samples, indicating the optimum oxidation time is 1.5 hour.<sup>154</sup> In addition, functionalization by concentrated treatment acid induced the formation of oxygen-containing functional groups, resulting in strong binding between Pt nanoparticles and carbon surface and further improved

electro-catalytic activity in methanol fuel cells.<sup>166</sup> Surface oxidation was also considered to be the cause of micropore generation in shorter oxidation time, leading to increased surface area, pore size and better capacitance.<sup>154</sup> But the electronic conductivity of porous carbons can also be decreased via surface oxidation, which is disadvantageous when porous carbons were used as electrodes in the area of fuel cell.<sup>40</sup>

The carbon surface can be modified through functional group grafting method via organic chemical reaction. Firstly, after introduction of carboxyl groups, acyl chloride groups, amino groups, hydroxyl groups, bromine groups, thiol groups could be converted through organic chemical reaction such as substitution, esterification, reduction and hydrolysis reaction.<sup>167, 168</sup> For example, nitric acid was used to treat microporous carbons and macroporous carbons to produce carboxyl groups. After that, the functionalized carbons were treated with thionyl chloride (SOCl<sub>2</sub>), followed by immobilization of diamine compounds (ethylenediamine (EDA) and hexamethylenediamine (HMDA)). Although the BET surface area of amino-immobilized microporous carbon decreased largely compared with unfunctionalized microporous carbon, mesoporous carbon showed similar BET surface area and pore volume after functionalized diamine.<sup>167</sup> Secondly, in order to maintain carbon frameworks and surface smoothness in the process of carbon oxidation, reductive compounds such as diazonium salts, isoamyl nitrite or hydrophosphorus acid have been used directly to functionalize the carbon surface.<sup>169-173</sup> For example, Pinson et al. grafted aryl groups on the carbon surface through electrochemical reduction of diazonium salts and this method could be used to covalently attached a large number of diazonium salts. Alternation of the texture of carbon surface can also occur through KOH activation,<sup>174</sup> sulphonation,<sup>175, 176</sup> halogenation,<sup>138, 177</sup> polymer decoration<sup>178</sup> method.

### 2.3.5 Graphitization degree

Graphitic carbon materials have various advantages such as high thermal and chemical stability, great electronic conductivity and excellent field emission behaviour. Therefore, exceptional graphitization degree for nanoporous carbon materials can enhance their performances in direct methanol fuel cell, lithium ion battery and electrochemical

catalysts.<sup>179-181</sup> Recently, a large number of porous carbon materials with a graphitic structure have been synthesized through four main different methods.

Firstly, to generate porous carbons with graphitic structure, carbon precursors such as mesophase pitch, acenaphthene, furfuryl alcohol have been employed to infiltrate the pores of mesoporous templates.<sup>182-185</sup> For example, Johnson et al. reported that mesoporous carbon prepared from furfural alcohol (FA) showed higher graphitization degree than that derived from mesophase pitch (MP). It indicated that FA-made carbons presented higher electrochemical stability in oxygen reduction reaction than MP-made carbons.<sup>182</sup> In addition, the effect of thermal treatment and different carbon precursors for graphitization degree were investigated. Heat treatment resulted in a gradual shrinking of structure and fracturing of pore walls and the carbons prepared from polyaromatic and acenaphthene and mesophase presented higher graphitic degree than that synthesized from furfuryl alcohol. But time-consuming and repeated infiltration and polymerization process is necessary to obtain ordered carbon materials. In addition, during high-temperature carbonization, a great deal of small molecules such as water will be emitted, deteriorating the pore structure of the template and the final carbon products.<sup>186, 187</sup>

Secondly, the catalytic graphitization is an effective method to synthesize graphitic carbon with high crystallinity in mild conditions. With the help of catalysts (Fe, Ni and Co), relatively low pyrolysis temperature will be needed to prepare porous carbon materials with high graphitic structure by using mesoporous silica incorporated with metal salts as templates.<sup>110, 180, 188-195</sup> For example, a solid-state method by using metal phthalocyanines and SBA 15 was employed to prepare highly graphitic ordered mesoporous carbon materials. The degree of graphitization was enhanced by metal catalysts and the pore and graphitic structure remained complete during heat treatment, leading to high oxidative stability and capacitance.<sup>195</sup> In addition, the carbon materials synthesized from soft template method showed high graphitization degree in the presence of metal salts under 900 °C heat treatment, resulting in superior capacitive performance (155 F/g) over a wide range of scan rates, even up to 200 mV/s. But the

main disadvantage for this method is that synthesis of template is usually a time-consuming and high-costly process.

Thirdly, chemical vapour deposition is based on incorporating gaseous carbon precursors into silica template with the advantages of high degree of pore filling, simple control of pyrolytic carbon and easy formation of graphitic pore walls.<sup>196-198</sup> For example, two-dimensional hexagonally ordered mesoporous CMK-5 carbon materials were prepared by chemical vapour deposition of ferrocene in soft template SBA-15. Graphitization degree of CMK-5 was improved below the pyrolysis temperature of 850°C, but partial collapse of ordered CMK-5 occurred at above 850°C with the formation of entangled graphitic ribbons.<sup>197</sup> But the use of the template is still the shortcoming of this process.

Lastly, incorporation of ordered mesoporous carbon materials with other highly conductive carbon materials such as reduced graphene oxide can also enhance the graphitization degree.<sup>199-201</sup> For example, composite materials containing ordered mesoporous carbons (OMC) and reduced graphene oxide (RGO) were prepared through a solvent evaporation-induced self-assembly (EISA) method with Pluronic F127 as template. Ordered porous carbons were considered as supporting framework, avoiding the agglomeration of RGO and RGO could be connected by dispersed carbon nanoparticles to facilitate the electron transfer. Compared with the Pt loading on OMC-RGO, the amount of Pt loading on OMC was much less due to less functionalized groups for adsorption of the platinum ions on the surface of OMC.<sup>199</sup>

### 2.3.6 Morphology effect

In addition to porous structure, heteroatom-doped effect, surface modification, graphitization effect, carbon nanoparticles with controlled morphologies also have great advantages on adsorption, catalysts, drug delivery and energy storage/conversion. These were derived from porous structure, exceptional properties of meso-channels and quantum effect on nanoscales. Many efforts have been made to design carbon spheres, hollow spheres, York-shell structure, fibres, rods and monoliths as shown in **Figure 2.6**.

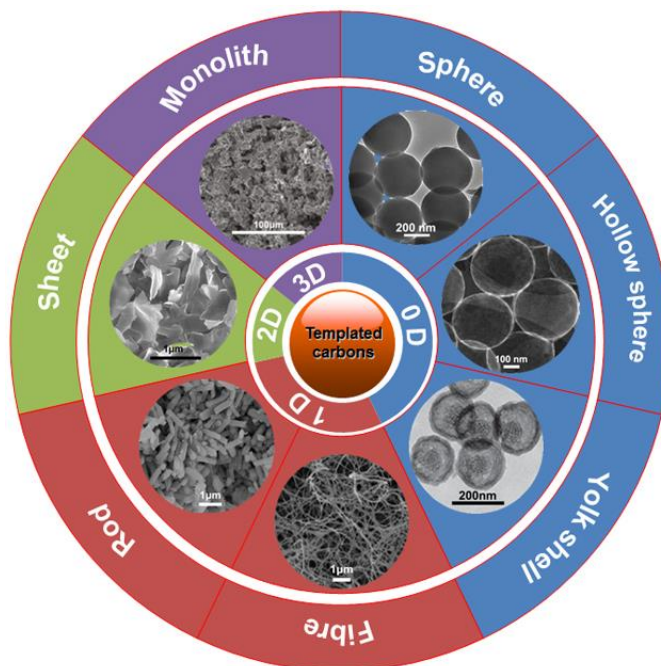


**Figure 2.6.** Tuned carbon nanostructures: (a) spheres,<sup>55</sup> (b) hollow spheres,<sup>202</sup> (c) yolk-shell nanoparticles,<sup>203</sup> (d) fibres,<sup>204</sup> (e) rods<sup>34</sup> (f) sheets<sup>205</sup> (g) monoliths<sup>206</sup>.

### 2.3.6.1 Spheres

Hard template method by filling and etching silica template and soft template method by organic-inorganic self-assembly are two main techniques for preparation of carbon spheres. Compared with hard template method, fewer synthetic steps, less time and expenses were required for soft template method. Recently, the extension of the Stober method was used for the preparation of monodisperse resorcinol and formaldehyde (RF) resin polymer spheres with uniform and controllable particle size and the following carbonization induced the formation of mesoporous carbon.<sup>55</sup> This efficient, facile, general and environmental-friendly method revealed that various different morphological carbons could be designed and synthesized. In addition, highly ordered mesoporous polymers with tuneable particle size were prepared through soft template method and porous carbon spheres could also be achieved through carbonization of the polymer spheres. This carbon material was further investigated as a cathode material for Li-S batteries and showed high initial discharge capability and good recyclability.<sup>52</sup>

### 2.3.6.2 Hollow spheres

Hard template method was widely used to prepare hollow carbon spheres. A carbon precursor was usually coated on the surface of template core for the formation of core-shell structure and the following carbonization and core-removing process lead to the generation of hollow carbon spheres. Dai et al. has developed a facile synthesis method of hollow carbon with dopamine as carbon source due to the nature of dopamine polymerization and high carbonization yield of polydopamine.<sup>202</sup> Double-shelled hollow carbon spheres could be obtained with hollow SnO<sub>2</sub> sphere as hard template. Due to the strong interaction between carbon and sulphur and the excellent encapsulation ability of double-shelled hollow carbon spheres, a large quantity of sulphur was encapsulated effectively in the double shell, suppressing the problem of polysulfides diffusion and volume variation. This also led to excellent electrochemical performance and great cycling ability as a cathode material for lithium-sulphur batteries.<sup>207</sup> Benzene or acetonitrile could also be used as carbon source for the generation of various hollow carbon spheres through chemical vapour deposition (CVD) method. The relative large silica spheres, short CVD time and high CVD temperature favoured the formation of hollow carbon spheres.<sup>208</sup>

### 2.3.6.3 York-shell nanoparticles

York shell structures are considered as promising functional materials in wide areas such as catalysts, drug delivery, lithium ion battery and biosensors because of easily fabrication of the composition of materials and simple tailored properties.<sup>209, 210</sup> York shell nanoparticles with a hollow space between the freely movable core and the protective shell could be synthesized by many methods such as selective dissolution, soft template, ship-in-bottle, Ostwald ripening or galvanic replacement process and kirkendall diffusion.<sup>211</sup> Recently, monodisperse Ag@C nanoparticles were prepared by carbonization of Ag, AgBr@RF york-shell nanoparticles which were synthesized by the extended stober method. Altering the concentration of the resorcinol and formaldehyde precursors and calcination atmosphere could tune the shape and thickness of the shell. Other type york shell structural material with metal core and carbon shell could also be

synthesized by this simple one-pot synthesis.<sup>71</sup> Additionally, a hierarchical porous yolk-shell structured carbons with a mesoporous carbon core and a microporous carbon shell was achieved through facile stober coating method, showing the maximum specific capacitance of 159 F/g among the synthesized carbons.<sup>203</sup>

#### 2.3.6.4 Fibres

Carbon fibres have attracted tremendous attentions in the area of catalysis, adsorption, biomedicine, energy storage and conversion due to high thermal stability, good biocompatibility, and abundant electronic and excellent mechanical properties. Many methods such as chemical vapour deposition, electrospinning and the template techniques have been utilized to fabricate them.<sup>212</sup> Carbon nanofibers could be obtained through direct template-based synthesis method by using solvent-free infiltration of the mixture of the tri-block copolymer Pluronic F127 as a structure-directing agent and phloroglucinol as a carbon source into porous alumina. This method indicated that prior to the infiltration process the disposal of the solvents avoided presence of macroscopic phase separation and hydrodynamic instabilities when the solvents were evaporated from the pores. Etching alumina generated 60 nm carbon fibers with helical mesopores.<sup>213</sup> In addition, carbon nanofibers with large pore (> 10 nm) on tube wall could be achieved. Aluminium oxide (AAO) provided the template for the growth of carbon fibre and the self-assembly of block copolymer/carbonhydrates were responsible for the formation of nanopores inside AAO pore channels.<sup>214</sup> Recently, an effective and large-scale method for the synthesis of heteroatom-doped carbon fibres was reported by using bacterial cellulose as the carbon source. The large number of functional groups on the surface of bacterial cellulose made it easy for P, N/P and B/P doping through pyrolysis the mixture of bacterial cellulose and  $H_3PO_4$ ,  $NH_4H_2PO_4$  and  $H_3BO_3/H_3PO_4$ . The prepared carbon fibers showed superior supercapacitive behaviour (186.03 kW/kg).<sup>204</sup>

#### 2.3.6.5 Rods

Hexagonally ordered porous carbon nanorods (CMK-3) were firstly synthesized with SBA-15 as hard template, sucrose as carbon source and sulphuric acid as the

carbonization catalyst. This ordered porous structure of CMK-3 showed an inverse carbon framework without structure transformation in the process of etching silica template compared with CMK-1.<sup>215</sup> Ordered mesoporous carbon nanorods (MWCCK-3) with large pore size (about 9 nm) and narrow size distribution could also be formed by using microwave-assisted synthesis of SBA-15 (MWSBA-15) which needed much less reaction time (less than 5 hour) than the conventional hydrothermal method (72 hour). This temperature-programmed microwave system provided homogeneous heat to improve the thermal stability of mesoporous silica template, facilitating the synthesis of SBA-15 with large pore size and narrow pore size distribution.<sup>34</sup>

#### 2.3.6.6 Sheets

Carbon nanosheets were different from graphene or graphene-based sheets because very small amount of graphene were presented in the obtained carbon sheets with a graphene inner layer and a carbon coating on both sides.<sup>205</sup> Ionic liquids were utilized for the synthesis of nitrogen-doped carbon nanosheets and changing the ratio of the raw materials could precisely control the thickness of the carbon layer. Excellent rate capability, high specific capacitance (341 F/g) and good cycling ability (over 35000 cycles) could be reached by using these materials when used as electrodes for supercapacitors.<sup>205</sup> An industrial production of porous carbon sheets could also be obtained through a graphene-directed and catalysis-free polymer synthesis and following thermal carbonization by using Schiff base-type polymer as precursors. The produced materials with high surface area and nitrogen content presented outstanding supercapacitive performance (424 F/g).<sup>216</sup> Graphene oxides and poly(benzoxazineco-resol) were used as shape-directing agent and carbon precursor for rapid fabrication of sandwich-type microporous carbon nanosheets with high surface area (1293 m<sup>2</sup>/g), narrow pore distribution (0.8 nm) and controlled layer thickness (about 17 nm). Such behaviours provided the fast diffusion of organic electrolytes, leading to superior gravimetric capacitance (103 F/g).<sup>217</sup>

#### 2.3.6.7 Monoliths

Due to escaping from the excessive pressure drop in fixed bed adsorber and dusting problems, carbon monoliths have attracted tremendous attention to reach daily needs for practical applications.<sup>218</sup> In order to enhance the performance of CO<sub>2</sub> capture and storage, amine groups were introduced into carbon materials through post-modification, copolymerization and direct pyrolysis of amine-containing precursors. Lu et al. designed and synthesized nitrogen-doped carbon monolith through direct pyrolysis of copolymer of resorcinol, formaldehyde and lysine as nitrogen source with higher CO<sub>2</sub>-adsorption capacity (3.13 mmol g<sup>-1</sup>) than melamine-derived mesoporous carbon (2.25 mmol g<sup>-1</sup>) at room temperature. This was due to the acid-base interaction between basic nitrogen groups in monolithic carbons and CO<sub>2</sub>.<sup>219</sup> A rapid and large-scale synthesis of hierarchical carbon monoliths with interconnected macroporous and ordered mesopore structure through soft template method was reported. The presence of lysine was proved to catalyze polymerization of resorcinol and formaldehyde in 15 mins at 90 °C and promoted the formation of mesostructured. Changing the amount of F127 copolymer could adjust the total pore volume and steam activation could also increase surface area up to 2422 m<sup>2</sup>/g.<sup>220</sup> In addition, superior capture, separation ability, high mechanical strength and excellent selectivity of CO<sub>2</sub> and facile regeneration could be achieved by using nitrogen-containing carbon monoliths. They were synthesized through a rapid and scalable self-assembly of poly(benzoxazine-co-resol) and following carbonization process.<sup>206</sup>

## **2.4. Applications for carbon materials**

Nanoporous carbon materials have the advantages such as chemical stability, electronic conductivity and absorption capabilities, so they have become quite promising materials in the energy and environment-related area. In this section, applications of porous carbon will be concluded into four parts: catalysts, batteries and capacitors/supercapacitors, which will provide perspectives for future investigations.

### **2.4.1 Metal-free electrocatalyst for oxygen reduction reaction**

Numerous attentions have been focused on fuel cells due to directly conversion chemical energy into electricity with no combustion process and high energy conversion efficiency. Among various types of fuel cells, direct methanol fuel cells and proton exchange membrane fuel cells have drawn much attention because of low operation temperature, abundant fuel supplies, small dimensions and little pollution during reaction.<sup>2</sup> This kind of fuel cells consists of oxygen reduction reaction (ORR) at cathode and hydrogen or methanol oxidation reaction at anode. The rate determining step is the process of the reduction of oxygen and the electrochemical reactions are usually accelerated with the assistance from electrocatalysts.<sup>3</sup> The ORR process occurs in two pathways: a) four-electron reduction of oxygen to water in acid condition or to hydroxyl ions in basic condition; b) two-electron reduction of oxygen to hydrogen peroxide in acid condition or  $\text{HO}_2^-$  in basic condition.<sup>221</sup> An illustration of oxygen reduction reaction with four-electron pathways by using cobalt–nitrogen-doped porous carbon material was shown in **Figure 2.7a**.

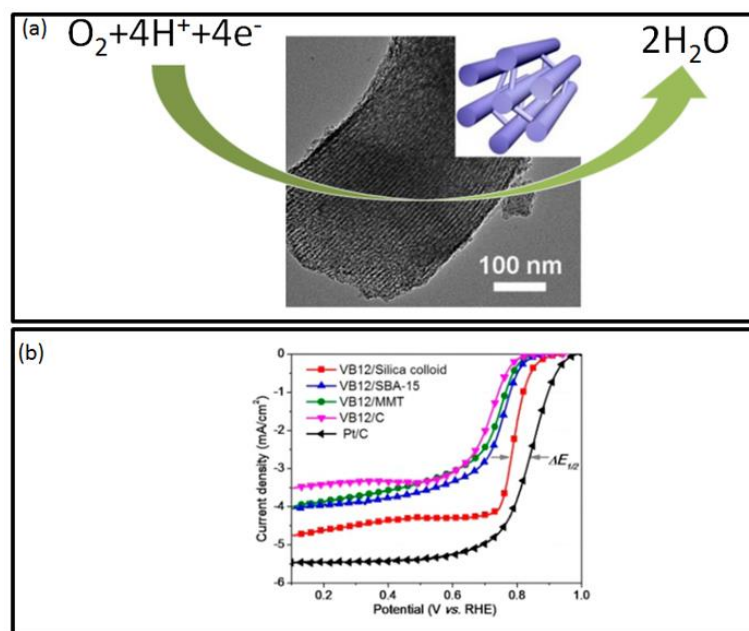


**Figure 2.7.** (a) TEM image with the inset of model illustration of cobalt–nitrogen-doped porous carbon material and illustration of oxygen reduction reaction (b) ORR polarization plots of various cobalt–nitrogen-doped porous carbon.<sup>222</sup>

Electrocatalysts are designed to facilitate electron transfer pathways to optimize the produced electricity.<sup>4</sup> However, high cost of commercial electrocatalysts such as platinum particles loaded activated carbons or carbon blacks and the low durability are still two major problems towards large scale productions. In addition, commercial materials usually suffered from some deactivation problems such as the susceptibility to carbon monoxide and methanol poisoning.<sup>4</sup> To address these problems, a lot of metal-free and nonprecious metal-doped carbons with high surface area, ordered structure and tuneable pores have been designed for oxygen reduction reactions. This was attributed to large number of active sites and enhanced mass-transport properties due to mesoporous structures in the carbons.

Hetero-atoms doped porous carbons are quite promising because of the enhanced porosity and the tailored electronic structure through the incorporation of heteroatoms into the carbon matrix. B-,<sup>118</sup> N-,<sup>223-226</sup> F-,<sup>119</sup> P-,<sup>120</sup> S-,<sup>121</sup> NP,<sup>152</sup> NS<sup>153</sup>-doped porous carbons with ordered mesoporous structure and high surface area have been prepared and showed superior electrochemical properties than undoped carbons and commercial Pt/C. For example, a series of nitrogen-doped porous carbon materials derived from the templates of silica nanoparticles, SBA-15, and montmorillonite were prepared and **Figure 2.7b** also showed all the three template carbons showed better activity than Pt/C with the regard of onset potential and half-wave potential.<sup>222</sup>

#### **2.4.2 Batteries (Na-ion sulphur batteries, Na-ion battery, Li-air battery)**

Energy storage has been recognized as one of most significant energy challenges and received worldwide concern and increasing research interest.<sup>5</sup> Batteries, as the most convenient form of energy storage, have played a very significant role in electric vehicles (EVs), hybrid electrical vehicles (HEVs), or car powered by other portable devices to provide abundant power and high energy density and at the same time could avoid the utilization of internal combustion engines. But several factors such as low energy and power densities, poor durability, high cost and poor safety have restricted the development of batteries.<sup>211</sup> Therefore, intensive efforts have been focused on designing next-generation batteries such as lithium ion batteries, lithium sulphur

batteries, lithium air batteries, sodium ion batteries and sodium sulphur batteries with enhanced power density, cycling life and charge/discharge rate capability.

#### 2.4.2.1 Lithium ion batteries

Because lithium is the lightest metal in the periodical table and thus can provide high energy density per electron, rechargeable lithium ion batteries are designed for the storage and conversion of electrochemical energy. The basic principle of lithium ion batteries is based on  $\text{Li}^+$  intercalation/conversion reactions. When the cell is discharged, lithium ions extract from the anode, pass through the electrolyte and intercalate into the cathode. In the meantime, the electrons pass through the external circuit to the cathode.<sup>227</sup> Carbonaceous materials are usually used as anode materials in the commercial rechargeable lithium batteries. Various carbon structures such as carbon nanofibers,<sup>228</sup> hollow nanospheres,<sup>229</sup> and carbon monoliths<sup>230 231</sup> have been designed to enhance lithiation capability and cycling stability because the transportation length of lithium ions will be shorten through porous structures and electrode/electrolyte interface for the charge-transfer reaction would also be improved. Doping non-carbon elements such as nitrogen in the porous carbon structures is another method to enhance the electrochemical performance. Nitrogen-doped porous carbons with high surface area ( $2381 \text{ m}^2/\text{g}$ ) and high nitrogen doping (about 16%) were produced through KOH activation of poly-pyrrole nano-fibre webs. The material showed excellent capacity, rate capability and stable stability when utilized as anode material for  $\text{Li}^+$  ion batteries. In addition, the specific capacity of this material could reach  $943 \text{ mAh/g}$  even at  $2 \text{ A/g}$  after 600 cycles because of the reduced transport length and facile transport channel of Lithium ions and high nitrogen doping.<sup>232</sup>

#### 2.4.2.2 Lithium sulphur batteries

Lithium sulphur batteries consist of a lithium metal anode and a sulphur cathode. The cathode involves the reaction of  $\text{S}_8 + 16 \text{ Li}^+ + 16 \text{ e}^- \leftrightarrow 8 \text{ Li}_2\text{S}$ , which provides high theoretical capacity of  $1672 \text{ mAh/g}$ . However, some shortcomings still hindered the development of lithium sulphur batteries because the poor electrical conductivity of

sulphur, the dissolution and shuttling effects of lithium polysulfides in organic liquid electrolytes resulted in poor coulombic efficiency, low utilization and poor cycle stability.<sup>233, 234</sup> In order to solve these problems, porous carbon materials have also been investigated as host for sulphur because porous carbon materials can strongly absorb polysulfides and buffer the volume expansion. Recently, various carbon hosts such as microporous carbons,<sup>235</sup> mesoporous carbons,<sup>236</sup> hierarchical porous carbons,<sup>237</sup> hollow carbon spheres,<sup>207</sup> carbon fibers,<sup>238</sup> nitrogen-doped carbons<sup>239</sup> have also been designed to overcome those drawbacks. Nazar et al. designed and synthesized polymer-modified mesoporous carbon-sulphur composites with reversible capacities up to 1320 mAh/g and good cycling ability. This superior performance was attributed to mesoporous structure of carbon hosts which provided more active sites between lithium ions and sulphur, constrained the growth of sulphur, generated more electrical contact area with sulphur and aided in trapping the formed polysulphides during reaction. The use of polymer on the carbon surface assisted the restriction of diffusion of large anions out of electrodes, leading to excellent electrochemical performance.<sup>236</sup> They also used mesoporous silica SBA-15 as polysulphide reservoir based on the design principle of drug delivery, which was incorporated in carbon/sulphur materials. This kind of materials provided superior adsorption and desorption ability of poly-sulphur ions, leading to the enhanced cycling ability and coulombic efficiency compared with CMK-3/sulphur composites.<sup>240</sup>

#### 2.4.2.3 Lithium-air batteries

Lithium-air batteries is also one of the most significant energy storage system and its capacities are theoretically calculated to be ten times higher than that of traditional lithium ion batteries.<sup>241</sup> Schematic cell configuration for the one type of Li-air battery was shown in **Figure 2.8a**. They usually involved a porous oxygen-breathing electrode as the cathode and a lithium metal as the anode. During the discharge process, lithium ions transport from the anode to the cathode and react with oxygen to form  $\text{Li}_2\text{O}$  or  $\text{Li}_2\text{O}_2$  inside the porous cathode material. At the same time, the electrons pass through the external circuit to the cathode. During charge process, oxygen will be released through decomposition of  $\text{Li}_2\text{O}$  or  $\text{Li}_2\text{O}_2$  through oxygen evolution reaction.<sup>242</sup> Large

surface area and high pore volume are necessary for superior electrochemical performance of lithium-air batteries because large surface area would provide more active sites and high pore volume could be related to the more accumulated discharge products.<sup>243</sup> For example, bimodal porous carbons with inter pore size about 28 nm (as shown in **Figure 2.8b**) have been synthesized by Xia et al. and exhibited about 40% higher discharge capacity than the commercial carbons (as shown in **Figure 2.8c**). The main factor was ascribed to large pore volume and ultra-large mesoporous structures.<sup>244</sup> In addition, the porous structure of carbon materials also affected the charge and discharge behaviour of lithium batteries. If the pore size is too small, the pores would be blocked by either electrolyte or lithium oxide. On the contrary, for large pores, electrochemical polarization would be caused by the growing lithium oxide because of poor conductivity, leading to the termination of discharge process.<sup>245</sup> Recently, nitrogen-enriched mesoporous carbon materials showed 1.73 times higher discharge ability (about 4500 mAh/g) than commercial carbons (BP 2000). More solid products were held in the large mesopores with suitable size. The interconnected macropore channels and low affinity to organic electrolytes facilitated oxygen diffusion, leading to high electrochemical performance of lithium-air batteries.

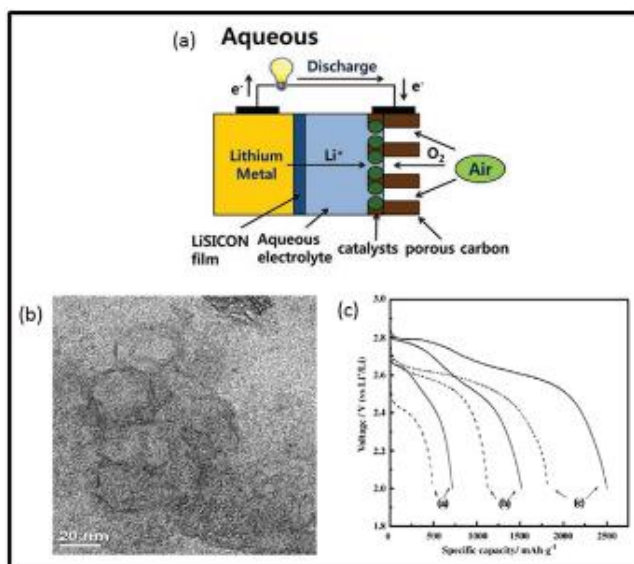


**Figure 2.8.** (a) Schematic cell configurations for the one type of Li-air battery.<sup>246</sup> (b) TEM image mesoporous carbons (MC) and (c) the discharge curve of MC (solid) and Super P carbon black (dash) at 0.5 mA/cm<sup>2</sup>, 0.2 mA/cm<sup>2</sup>, 0.1 mA/cm<sup>2</sup>.<sup>244</sup>

#### 2.4.2.4 Na-ion batteries

Rechargeable sodium ion batteries have also attracted lots of attention due to abundant supply and low cost for replacement to lithium ion batteries.<sup>247</sup> Due to larger radius than lithium ions, sodium ions have stronger coordination in the host lattices and are hard to be hosted in the interstitial space of most materials' crystallographic structure. Porous carbons have been investigated as anode materials because porous structure and large interlayer distance facilitated insertion and extraction of sodium ions.<sup>248</sup> The reversible sodium capacity of these carbons is usually between 100 and 300 mAh/g.<sup>249-252</sup> Tirado et al reported that carbon microspheres which were prepared from resorcinol/formaldehyde mixture exhibited high reversible capability (about 285 mAh/g). This was attributed to the interaction between the porous carbon structure and reversible inserted sodium ions.<sup>252</sup> Recently, Liu et al. also reported large mesopore and micropore in the carbon spheres and the connectivity and conductivity of the mesoporous network were also responsible for good electrochemical performance for sodium batteries such as a high initial capacity (410 mAh/g) and a good retention (125 mAh/g after 100 cycles).<sup>253</sup>

#### 2.4.2.5 Na-sulphur batteries

Sodium-sulphur (Na-S) batteries are one type of molten salt battery including the molten sodium and molten sulphur separated by beta-alumina solid electrolytes.<sup>254</sup> Due to reasonable power and energy densities, stability, abundance and low price, sodium sulphur batteries have become a sustainable and environmental-friendly technology. But sodium sulphur batteries still met with the difficulties as lithium sulphur batteries such as shuttling effect of polysulphides and low electric conductivity of sulphur.<sup>236</sup> High operation temperatures (above 300 °C) also restricted the application of lithium sulphur batteries. Choi et al. recently designed carbon-sulphur composite fibres which can be performed at room temperature with good sodiation and desodiation activity (about 500 cycles) and high rate performance. This was attributed to the stable atomic configuration of sulphur in the calcined polyacrylonitrile matrix overcoming the

shortcomings of lithium sulphur batteries and the fibre structure facilitating the sodiation and desodiation process.<sup>255</sup>

### 2.4.3 Supercapacitors

Supercapacitors have become one of the dominate power supplies with high energy and power densities and long cycling life and thus been considered as an excellent candidate for alternative batteries. A representation of an electrochemical double layer capacitor (in its charged state) was shown in **Figure 2.9a**.<sup>256</sup> Electrochemical capacitors can accumulate electrical energy due to formation of electrical double layer between electrodes and electrolytes. They can be classified into two categories: electrical double-layer capacitors (EDLCs) with a non-Faradic process based on carbon materials such as activated carbon, graphene, carbon nanotubes and carbon nanofibers and pseudo-capacitors with a Faradic process using  $\text{RuO}_2$ ,  $\text{MnO}_2$ ,  $\text{Co}_3\text{O}_4$  and conducting polymers.<sup>257</sup> To acquire superior electrochemical behaviour of super-capacitor, it is highly desirable to design carbon materials with optimal porous structure, high surface area, tuneable surface functionalities, appropriate wettability and excellent stability and electronic conductivity.<sup>42, 258, 259</sup>

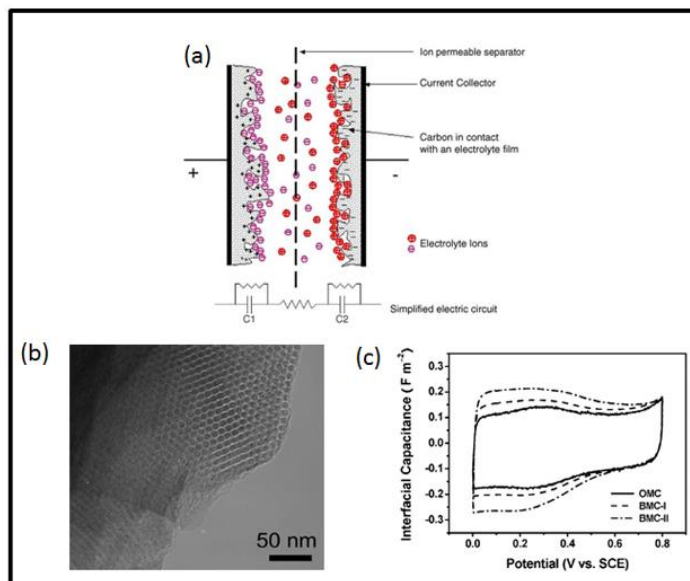


**Figure 2.9.** (a) Representation of an electrochemical double layer capacitor (in its charged state).<sup>256</sup> (b) SEM image and (c) cyclic voltammogram of carbon spheres.<sup>128</sup>

Micro-porous and macro-porous carbons were designed to enhance the capacitance through increasing surface area to facilitate ion transportation when carbon materials were used as electrode materials.<sup>260-263</sup> An ordered mesoporous carbon material, templated from Na–Y zeolite via nanocasting method, exhibited a narrow pore-size distribution within the micropore range. A large gravimetric capacitance (340 F/g) and better electrical performance than commercial carbon were shown by using this carbon material in aqueous solution. The adequate pore-size distribution and ordered structure make ions diffusion easy in the channels, indicating the enhanced electrochemical performance is not only derived from pore shape and pseudocapacitive effects but also from the pore shape and void tortuosity. In addition, the presence of nitrogen and oxygen functional groups on the surface of synthesized carbons led to a pseudocapacitive effect to facilitate electron transfer in acidic atmosphere.<sup>260</sup>

The electrochemical capacitance of carbon electrodes could be also be improved via surface modification of porous carbon materials with heteroatoms such as B,<sup>128</sup> P,<sup>264</sup>N,<sup>265, 266</sup> and S.<sup>267</sup> The hetero atom such as nitrogen on the carbon surface could lead to the pseudocapacitance interaction which is usually related to a charge or mass transfer between the electrode material and the ions of the electrolyte.<sup>266</sup> More protons could be attracted by introducing electron donor and charge-density of the space-charge layer could be enhanced to strengthen the redox reactions.<sup>266</sup>For example, Cheng et al. prepared boron-doped ordered mesoporous carbons with a diameter of about 7 nm (as shown in **Figure 2.9b**) by using sucrose as a carbon source and boric acid as a boron source through hard template method (mesoporous SBA-15). They also found interfacial capacitance of the boron-doped carbon increased about 1.6 times higher than non-doped material in both acidic (as shown in **Figure 2.9c**) and alkaline conditions, because low-level boron doping improved oxygen chemisorption on the surface and increased charge carrier concentration and Fermi level density of states.<sup>128</sup>

Coating of the porous carbon surface with conducting polymer such as polyaniline (PANI)<sup>268-270</sup> could also affect the electrochemical performances. Three dimensionally ordered macroporous carbons with a thin layer PANI coating were fabricated to improve the electrical performance. An excellent capacitance of 1490 F/g, great rate performance

and cycling ability were observed because the carbon matrix provided 3D interconnected microporous structure for fast ion transportation, good electrical conductivity, large surface area for deposition of PANI and a thin PANI coating layer endowed the pseudocapacitive contribution for the enhanced behaviour.<sup>269</sup> However, the decreased surface area and conductivity of carbons, the blockage of porous structure, strong swelling capability, weak surface adhesive ability and shortened cycling life could also occur when polymers were coated on the surface of carbon template.<sup>269, 271</sup>

### **2.5. Summary and future development**

Porous carbon nanocomposites for energy storage and conversion were reviewed in this literature review. At the first part for material preparation, hard template method, soft template method and hard-soft template method are three main common strategies to prepare ordered porous carbon materials. In the following part, six different aspects including composition, porous structure, doping effect, graphitization degree, morphology control and surface modification are deeply discussed for the design and fabrication of porous carbon composites. Moreover, carbon precursors, porous structures, pore sizes, pore volumes and surface areas are summarized in tables. It is obvious that porous carbons with tuneable pore size, porous structure and morphologies can be achieved through template methods. Different compositions including inorganic and metal/metal oxide carbon composites are also presented. Then porous carbon materials are then introduced according to pore size classification. Pore size is of great importance to electrochemical reactions for energy storage devices and electroconductivity for fuel cells because micro-porous carbons could provide high surface area to enhance reaction rate, while macro-porous carbon materials could facilitate mass transfer and diffusion of reactants and products in the reaction. With regard to the introduction of heteroatoms in the carbon matrix, monodoped, dual doped and multi-doped porous carbons from template methods for oxygen reduction reaction in fuel cells are reviewed. Recent investigations for this field reported that hetero-atoms doped porous carbons showed superior electrochemical properties than undoped carbons and commercial Pt/C because of the enhanced porosity and the tailored electronic structure through the incorporation of heteroatoms into the carbon matrix. Therefore, these heteroatom-doped porous carbons can be considered as metal-free electro-catalysts to

pave new ways to substitute the commercial Pt/C materials for cathode electrodes. Surface modification towards the functionalization of porous carbons is necessary because carbons materials are usually used as catalysts support to improve the metal dispersion and adsorption of metallic species on the carbon surface, leading to the enhanced electrical conductivity and application behaviour.

Tremendous developments have been made to the preparation of nanoporous carbons with uniform structure and morphology from template methods, but there are still lots of promising and heart-stirring opportunities for the advancement of modifying porous carbons to optimize their performance in energy-related applications. In terms of synthesis method, it is hard to avoid the hard-template etching by acid or base solution and reach the requirement of template recycling. In addition, the synthesis of microporous carbons by using soft template method is still a challenge. In order to find an environmental-friendly way for the preparation of ordered porous carbons with tuneable pore size (especially for less than 2 nm), porous structure and morphology, new templates will be explored. Additionally, the relationship among pore size, heteroatom doped effect, graphitization degree, surface modification and morphology need to be further understood to fabricate superior electrochemical devices. To improve electrochemical performance and electrocapitance, it is desirable to design hierarchical structural carbon materials with different levels of porosity into carbon framework due to the enhanced mass diffusion, electron transportation, surface area and pore volume. In addition to the materials preparation, the utilization of environmentally friendly, low cost and abundant raw carbon precursors is highly desirable for further advancement of rechargeable electrochemical energy storage and conversion devices. What is more, the prepared carbon nanocomposites can not only be used in energy-related applications, but also can be operated in the area of gas separation, absorption and storage or supports for bio-molecular immobilization in the field of biosensing.

## 2.6 References

1. R. D. Cortright, R. R. Davda and J. A. Dumesic, *Nature*, 2002, **418**, 964-967.
2. R. F. Service, *Science*, 2002, **296**, 1222-1224.
3. Y. Y. Shao, J. H. Sui, G. P. Yin and Y. Z. Gao, *Appl. Catal., B*, 2008, **79**, 89-99.

4. L. P. Zhang and Z. H. Xia, *J. Phys. Chem. C*, 2011, **115**, 11170-11176.
5. C. Liu, F. Li, L.-P. Ma and H.-M. Cheng, *Adv. Mater.*, 2010, **22**, E28-E62.
6. S. J. C. Cleghorn, X. Ren, T. E. Springer, M. S. Wilson, C. Zawodzinski, T. A. Zawodzinski and S. Gottesfeld, *Int. J. Hydrogen Energy*, 1997, **22**, 1137-1144.
7. J. Tang, J. Liu, N. L. Torad, T. Kimura and Y. Yamauchi, *Nano Today*, 2014, **9**, 305-323.
8. F. Beguin, V. Presser, A. Balducci and E. Frackowiak, *Adv. Mater.*, 2014, **26**, 2219-2251.
9. W. Chaikittisilp, K. Ariga and Y. Yamauchi, *J. Mater. Chem. A*, 2013, **1**, 14-19.
10. H. Nishihara and T. Kyotani, *Adv Mater*, 2012, **24**, 4473-4498.
11. L. Chuenchom, R. Kraehnert and B. M. Smarsly, *Soft Matter*, 2012, **8**, 10801-10812.
12. S. L. Candelaria, Y. Y. Shao, W. Zhou, X. L. Li, J. Xiao, J. G. Zhang, Y. Wang, J. Liu, J. H. Li and G. Z. Cao, *Nano Energy*, 2012, **1**, 195-220.
13. Y. D. Xia, Z. X. Yang and R. Mokaya, *Nanoscale*, 2010, **2**, 639-659.
14. M.-M. Titirici, R. J. White, N. Brun, V. L. Budarin, D. S. Su, F. del Monte, J. H. Clark and M. J. MacLachlan, *Chem. Soc. Rev.*, 2015, **44**, 250-290.
15. F. Rodriguezreinoso and M. Molinasabio, *Carbon*, 1992, **30**, 1111-1118.
16. T. Kyotani, *Bull. Chem. Soc. Jpn.*, 2006, **79**, 1322-1337.
17. S.-W. Woo, K. Dokko, H. Nakano and K. Kanamura, *J. Mater. Chem.*, 2008, **18**, 1674-1680.
18. Y. Meng, D. Gu, F. Q. Zhang, Y. F. Shi, H. F. Yang, Z. Li, C. Z. Yu, B. Tu and D. Y. Zhao, *Angew. Chem. Int. Ed.*, 2005, **44**, 7053-7059.
19. Z. Y. Wang, E. R. Kiesel and A. Stein, *J. Mater. Chem.*, 2008, **18**, 2194-2200.
20. J. S. Lee, S. H. Joo and R. Ryoo, *J. Am. Chem. Soc.*, 2002, **124**, 1156-1157.
21. S. H. Joo, S. J. Choi, I. Oh, J. Kwak, Z. Liu, O. Terasaki and R. Ryoo, *Nature*, 2001, **412**, 169-172.
22. H. F. Yang and D. Y. Zhao, *J. Mater. Chem.*, 2005, **15**, 1217-1231.
23. F. Lu, S. H. Wu, Y. Hung and C. Y. Mou, *Small*, 2009, **5**, 1408-1413.
24. C. D. Liang and S. Dai, *J. Am. Chem. Soc.*, 2006, **128**, 5316-5317.

25. F. Q. Zhang, D. Gu, T. Yu, F. Zhang, S. H. Xie, L. J. Zhang, Y. H. Deng, Y. Wan, B. Tu and D. Y. Zhao, *J. Am. Chem. Soc.*, 2007, **129**, 7746-7747.
26. L. Liu, F. Y. Wang, G. S. Shao and Z. Y. Yuan, *Carbon*, 2010, **48**, 2089-2099.
27. Y. Huang, H. Q. Cai, D. Feng, D. Gu, Y. H. Deng, B. Tu, H. T. Wang, P. A. Webley and D. Y. Zhao, *Chem. Commun.*, 2008, **23**, 2641-2643.
28. C. D. Liang, Z. J. Li and S. Dai, *Angew. Chem. Int. Ed.*, 2008, **47**, 3696-3717.
29. B. T. Holland, C. F. Blanford and A. Stein, *Science*, 1998, **281**, 538-540.
30. A. A. Zakhidov, R. H. Baughman, Z. Iqbal, C. X. Cui, I. Khayrullin, S. O. Dantas, I. Marti and V. G. Ralchenko, *Science*, 1998, **282**, 897-901.
31. Y. H. Deng, C. Liu, T. Yu, F. Liu, F. Q. Zhang, Y. Wan, L. J. Zhang, C. C. Wang, B. Tu, P. A. Webley, H. T. Wang and D. Y. Zhao, *Chem. Mater.*, 2007, **19**, 3271-3277.
32. S. Kang, J. S. Yu, M. Kruk and M. Jaroniec, *Chem. Commun.*, 2002, **16**, 1670-1671.
33. B. Z. Fang, J. H. Kim, M. Kim and J. S. Yu, *Chem. Mater.*, 2009, **21**, 789-796.
34. L. C. Sang, A. Vinu and M. O. Coppens, *J. Mater. Chem.*, 2011, **21**, 7410-7417.
35. J. S. Yu, S. Kang, S. B. Yoon and G. Chai, *J. Am. Chem. Soc.*, 2002, **124**, 9382-9383.
36. H. I. Lee, J. H. Kim, D. J. You, J. E. Lee, J. M. Kim, W. S. Ahn, C. Pak, S. H. Joo, H. Chang and D. Seung, *Adv. Mater.*, 2008, **20**, 757-762.
37. Z. B. Lei, Y. Xiao, L. Q. Dang, M. Lu and W. S. You, *Micropor. Mesopor. Mat.*, 2006, **96**, 127-134.
38. A. Taguchi, J. H. Smatt and M. Linden, *Adv. Mater.*, 2003, **15**, 1209-1211.
39. B. L. Su, A. Vantomme, L. Surahy, R. Pirard and J. P. Pirard, *Chem. Mater.*, 2007, **19**, 3325-3333.
40. Z. Y. Wang, F. Li, N. S. Ergang and A. Stein, *Chem. Mater.*, 2006, **18**, 5543-5553.
41. T. Morishita, Y. Soneda, T. Tsumura and M. Inagaki, *Carbon*, 2006, **44**, 2360-2367.
42. D.-W. Wang, F. Li, M. Liu, G. Q. Lu and H.-M. Cheng, *Angew. Chem. Int. Ed.*, 2008, **47**, 373-376.

43. J. Liang, Y. Zheng, J. Chen, J. Liu, D. Hulicova-Jurcakova, M. Jaroniec and S. Z. Qiao, *Angew. Chem. Int. Ed.*, 2012, **51**, 3892-3896.
44. C. D. Liang, K. L. Hong, G. A. Guiochon, J. W. Mays and S. Dai, *Angew. Chem. Int. Ed.*, 2004, **43**, 5785-5789.
45. S. Tanaka, N. Nishiyama, Y. Egashira and K. Ueyama, *Chem. Commun.*, 2005, **16**, 2125-2127.
46. F. Zhang, Y. Meng, D. Gu, Yan, C. Yu, B. Tu and D. Zhao, *J. Am. Chem. Soc.*, 2005, **127**, 13508-13509.
47. J. Y. Zhang, Y. H. Deng, J. Wei, Z. K. Sun, D. Gu, H. Bongard, C. Liu, H. H. Wu, B. Tu, F. Schuth and D. Y. Zhao, *Chem. Mater.*, 2009, **21**, 3996-4005.
48. Y. H. Deng, Y. Cai, Z. K. Sun, D. Gu, J. Wei, W. Li, X. H. Guo, J. P. Yang and D. Y. Zhao, *Adv. Funct. Mater.*, 2010, **20**, 3658-3665.
49. Y. H. Deng, J. Liu, C. Liu, D. Gu, Z. K. Sun, J. Wei, J. Y. Zhang, L. J. Zhang, B. Tu and D. Y. Zhao, *Chem. Mater.*, 2008, **20**, 7281-7286.
50. Y. Fang, D. Gu, Y. Zou, Z. X. Wu, F. Y. Li, R. C. Che, Y. H. Deng, B. Tu and D. Y. Zhao, *Angew. Chem. Int. Ed.*, 2010, **49**, 7987-7991.
51. T. Yang, J. Liu, R. Zhou, Z. Chen, H. Xu, S. Z. Qiao and M. J. Monteiro, *J. Mater. Chem. A*, 2014, **2**, 18139-18146.
52. J. Liu, T. Yang, D.-W. Wang, G. Q. Lu, D. Zhao and S. Z. Qiao, *Nat. Commun.*, 2013, **4**, 2798-2805.
53. N. W. Li, M. B. Zheng, S. Q. Feng, H. L. Lu, B. Zhao, J. F. Zheng, S. T. Zhang, G. B. Ji and J. M. Cao, *J. Phys. Chem. C*, 2013, **117**, 8784-8792.
54. W. Stöber, A. Fink and E. Bohn, *J. Colloid Interface Sci.*, 1968, **26**, 62-69.
55. J. Liu, S. Z. Qiao, H. Liu, J. Chen, A. Orpe, D. Y. Zhao and G. Q. Lu, *Angew. Chem. Int. Ed.*, 2011, **50**, 5947-5951.
56. A.-H. Lu, G.-P. Hao and Q. Sun, *Angew. Chem. Int. Ed.*, 2011, **50**, 9023-9025.
57. X. H. Zhang, Y. A. Li and C. B. Cao, *J. Mater. Chem.*, 2012, **22**, 13918-13921.
58. J. Choma, D. Jamiola, K. Augustynek, M. Marszewski, M. Gao and M. Jaroniec, *J. Mater. Chem.*, 2012, **22**, 12636-12642.
59. Z. A. Qiao, B. K. Guo, A. J. Binder, J. H. Chen, G. M. Veith and S. Dai, *Nano Lett.*, 2013, **13**, 207-212.

60. B. Y. Guan, X. Wang, Y. Xiao, Y. L. Liu and Q. S. Huo, *Nanoscale*, 2013, **5**, 2469-2475.
61. J. Zang, T. An, Y. Dong, X. Fang, M. Zheng, Q. Dong and N. Zheng, *Nano Res.*, 2015, **8**, 2663-2675.
62. J. C. Song, F. F. Xue, Z. Y. Lu and Z. Y. Sun, *Chem. Commun.*, 2015, **51**, 10517-10520.
63. R. Liu, Y.-W. Yeh, V. H. Tam, F. Qu, N. Yao and R. D. Priestley, *Chem. Commun.*, 2014, **50**, 9056-9059.
64. R. Liu, F. Qu, Y. Guo, N. Yao and R. D. Priestley, *Chem. Commun.*, 2014, **50**, 478-480.
65. T. Y. Yang, J. Liu, R. F. Zhou, Z. G. Chen, H. Y. Xu, S. Z. Qiao and M. J. Monteiro, *J. Mater. Chem. A*, 2014, **2**, 18139-18146.
66. H. Tian, M. Saunders, A. Dodd, K. O'Donnell, M. Jaroniec, S. Liu and J. Liu, *J. Mater. Chem. A*, 2016, **4**, 3721-3727.
67. X. Fang, J. Zang, X. Wang, M.-S. Zheng and N. Zheng, *J. Mater. Chem. A*, 2014, **2**, 6191-6197.
68. N. Liu, H. Wu, M. T. McDowell, Y. Yao, C. Wang and Y. Cui, *Nano Lett.*, 2012, **12**, 3315-3321.
69. Z. Wei Seh, W. Li, J. J. Cha, G. Zheng, Y. Yang, M. T. McDowell, P.-C. Hsu and Y. Cui, *Nat. Commun.*, 2013, **4**, 1331-1337.
70. J. Liu, T. Y. Yang, D. W. Wang, G. Q. M. Lu, D. Y. Zhao and S. Z. Qiao, *Nat. Commun.*, 2013, **4**, 2798-2805.
71. T. Yang, J. Liu, Y. Zheng, M. J. Monteiro and S. Z. Qiao, *Chem. Eur. J.*, 2013, **19**, 6942-6945.
72. T. Yang, R. Zhou, D.-W. Wang, S. P. Jiang, Y. Yamauchi, S. Z. Qiao, M. J. Monteiro and J. Liu, *Chem. Commun.*, 2015, **51**, 2518-2521.
73. J. Zhang, K. Wang, Q. Xu, Y. Zhou, F. Cheng and S. Guo, *ACS Nano*, 2015, **9**, 3369-3376.
74. Z. Liu, X.-Y. Yu and U. Paik, *Adv. Energy Mater.*, 2016, **6**, 1502318-1502323.
75. Y. Zhao, J. Li, C. Wu, Y. Ding and L. Guan, *ChemPlusChem*, 2012, **77**, 748-751.

76. C. Lei, F. Han, Q. Sun, W.-C. Li and A.-H. Lu, *Chem. Eur. J.*, 2014, **20**, 139-145.
77. E. Kang, Y. S. Jung, A. S. Cavanagh, G.-H. Kim, S. M. George, A. C. Dillon, J. K. Kim and J. Lee, *Adv. Funct. Mater.*, 2011, **21**, 2430-2438.
78. B. Lim, J. Jin, J. Yoo, S. Y. Han, K. Kim, S. Kang, N. Park, S. M. Lee, H. J. Kim and S. U. Son, *Chem. Commun.*, 2014, **50**, 7723-7726.
79. H. Zhang, L. Zhou, O. Noonan, D. J. Martin, A. K. Whittaker and C. Yu, *Adv. Funct. Mater.*, 2014, **24**, 4337-4342.
80. Y. Dai, L. Chen, V. Babayan, Q. Cheng, P. Saha, H. Jiang and C. Li, *J. Mater. Chem. A*, 2015, **3**, 21337-21342.
81. J. Zhang, K. Wang, S. Guo, S. Wang, Z. Liang, Z. Chen, J. Fu and Q. Xu, *ACS Appl. Mater. Interfaces.*, 2014, **6**, 2192-2198.
82. O. M. Yaghi and H. Li, *J. Am. Chem. Soc.*, 1995, **117**, 10401-10402.
83. B. Liu, H. Shioyama, T. Akita and Q. Xu, *J. Am. Chem. Soc.*, 2008, **130**, 5390-5391.
84. X. Li, Y. Fang, X. Lin, M. Tian, X. An, Y. Fu, R. Li, J. Jin and J. Ma, *J. Mater. Chem. A*, 2015, **3**, 17392-17402.
85. W. Xia, A. Mahmood, R. Zou and Q. Xu, *Energy Environ. Sci.*, 2015, **8**, 1837-1866.
86. H. Yang, S. J. Bradley, A. Chan, G. I. N. Waterhouse, T. Nann, P. E. Kruger and S. G. Telfer, *J. Am. Chem. Soc.*, 2016, **138**, 11872-11881.
87. J. Tang, R. R. Salunkhe, J. Liu, N. L. Torad, M. Imura, S. Furukawa and Y. Yamauchi, *J. Am. Chem. Soc.*, 2015, **137**, 1572-1580.
88. Z. Lei, Y. Zhang, H. Wang, Y. Ke, J. Li, F. Li and J. Xing, *J. Mater. Chem.*, 2001, **11**, 1975-1977.
89. Y. Zhao, X. Li, J. Liu, C. Wang, Y. Zhao and G. Yue, *ACS Appl. Mater. Interfaces.*, 2016, **8**, 6472-6480.
90. H. Li, Y. Su, W. Sun and Y. Wang, *Adv. Funct. Mater.*, 2016, **26**, 8345-8353.
91. F. Zou, X. Hu, Z. Li, L. Qie, C. Hu, R. Zeng, Y. Jiang and Y. Huang, *Adv. Mater.*, 2014, **26**, 6622-6628.

92. Y. Chen, J. Wu, W. Yang, Y. Fu, R. Zhou, S. Chen, L. Zhang, Y. Song and L. Wang, *J. Alloys Compd.*, 2016, **688**, 211-218.
93. X. Ge, Z. Li, C. Wang and L. Yin, *ACS Appl. Mater. Interfaces.*, 2015, **7**, 26633-26642.
94. H. Hu, L. Han, M. Yu, Z. Wang and X. W. Lou, *Energy Environ. Sci.*, 2016, **9**, 107-111.
95. X. Zhu, M. Liu, Y. Liu, R. Chen, Z. Nie, J. Li and S. Yao, *J. Mater. Chem. A*, 2016, **4**, 8974-8977.
96. T. Chen, Y. Hu, B. Cheng, R. Chen, H. Lv, L. Ma, G. Zhu, Y. Wang, C. Yan, Z. Tie, Z. Jin and J. Liu, *Nano Energy*, 2016, **20**, 305-314.
97. P. X. Hou, H. Orikasa, T. Yamazaki, K. Matsuoka, A. Tomita, N. Setoyama, Y. Fukushima and T. Kyotani, *Chem. Mater.*, 2005, **17**, 5187-5193.
98. A. Corma, *Chem. Rev.*, 1997, **97**, 2373-2419.
99. T. Kyotani, T. Nagai, S. Inoue and A. Tomita, *Chem. Mater.*, 1997, **9**, 609-615.
100. X. J. Zhao, H. Y. Zhao, T. T. Zhang, X. C. Yan, Y. Yuan, H. M. Zhang, H. J. Zhao, D. M. Zhang, G. S. Zhu and X. D. Yao, *J. Mater. Chem. A*, 2014, **2**, 11666-11671.
101. Y. C. Zhao, L. Zhao, L. J. Mao and B. H. Han, *J. Mater. Chem. A*, 2013, **1**, 9456-9461.
102. J. Lee, S. Han and T. Hyeon, *J. Mater. Chem.*, 2004, **14**, 478-486.
103. R. Ryoo, S. H. Joo, M. Kruk and M. Jaroniec, *Adv. Mater.*, 2001, **13**, 677-681.
104. T. Kyotani, *Carbon*, 2000, **38**, 269-286.
105. F. Schuth, *Angew. Chem. Int. Ed.*, 2003, **42**, 3604-3622.
106. R. Ryoo, S. H. Joo and S. Jun, *J. Phys. Chem. B*, 1999, **103**, 7743-7746.
107. A. Vinu, M. Miyahara, V. Sivamurugan, T. Mori and K. Ariga, *J. Mater. Chem.*, 2005, **15**, 5122-5127.
108. K. Ariga, A. Vinu, M. Miyahara, J. P. Hill and T. Mori, *J. Am. Chem. Soc.*, 2007, **129**, 11022-11023.
109. J. Lee, K. Sohn and T. Hyeon, *J. Am. Chem. Soc.*, 2001, **123**, 5146-5147.
110. A. B. Fuertes and T. A. Centeno, *J. Mater. Chem.*, 2005, **15**, 1079-1083.

111. C. T. Kresge, M. E. Leonowicz, W. J. Roth, J. C. Vartuli and J. S. Beck, *Nature*, 1992, **359**, 710-712.
112. J. S. Beck, J. C. Vartuli, W. J. Roth, M. E. Leonowicz, C. T. Kresge, K. D. Schmitt, C. T. W. Chu, D. H. Olson, E. W. Sheppard, S. B. Mccullen, J. B. Higgins and J. L. Schlenker, *J. Am. Chem. Soc.*, 1992, **114**, 10834-10843.
113. D. Y. Zhao, J. L. Feng, Q. S. Huo, N. Melosh, G. H. Fredrickson, B. F. Chmelka and G. D. Stucky, *Science*, 1998, **279**, 548-552.
114. D. Y. Zhao, Q. S. Huo, J. L. Feng, B. F. Chmelka and G. D. Stucky, *J. Am. Chem. Soc.*, 1998, **120**, 6024-6036.
115. F. Q. Zhang, Y. Meng, D. Gu, Y. Yan, C. Z. Yu, B. Tu and D. Y. Zhao, *J. Am. Chem. Soc.*, 2005, **127**, 13508-13509.
116. S. B. Yoon, K. Sohn, J. Y. Kim, C. H. Shin, J. S. Yu and T. Hyeon, *Adv. Mater.*, 2002, **14**, 19-21.
117. T. Kyotani, L. F. Tsai and A. Tomita, *Chem. Mater.*, 1996, **8**, 2109-2113.
118. X. J. Bo and L. P. Guo, *Phys. Chem. Chem. Phys.*, 2013, **15**, 2459-2465.
119. H. Wang and A. Kong, *Mater. Lett.*, 2014, **136**, 384-387.
120. D. S. Yang, D. Bhattacharjya, S. Inamdar, J. Park and J. S. Yu, *J. Am. Chem. Soc.*, 2012, **134**, 16127-16130.
121. H. Wang, X. J. Bo, Y. F. Zhang and L. P. Guo, *Electrochim. Acta*, 2013, **108**, 404-411.
122. X. X. Wu and L. R. Radovic, *J. Phys. Chem. A*, 2004, **108**, 9180-9187.
123. C. E. Lowell, *J. Am. Ceram. Soc.*, 1967, **50**, 142-144.
124. D. H. Zhong, H. Sano, Y. Uchiyama and K. Kobayashi, *Carbon*, 2000, **38**, 1199-1206.
125. L. R. Radovic, M. Karra, K. Skokova and P. A. Thrower, *Carbon*, 1998, **36**, 1841-1854.
126. X. C. Zhao, A. Q. Wang, J. W. Yan, G. Q. Sun, L. X. Sun and T. Zhang, *Chem. Mater.*, 2010, **22**, 5463-5473.
127. X. C. Zhao, Q. Zhang, B. S. Zhang, C. M. Chen, A. Q. Wang, T. Zhang and D. S. Su, *J. Mater. Chem.*, 2012, **22**, 4963-4969.

128. D. W. Wang, F. Li, Z. G. Chen, G. Q. Lu and H. M. Cheng, *Chem. Mater.*, 2008, **20**, 7195-7200.
129. T. Wang, C. Zhang, X. Sun, Y. Guo, H. Guo, J. Tang, H. Xue, M. Liu, X. Zhang, L. Zhu, Q. Xie and J. He, *J. Power Sources*, 2012, **212**, 1-12.
130. Y. D. Xia and R. Mokaya, *Adv. Mater.*, 2004, **16**, 1553-1558.
131. Y. D. Xia and R. Mokaya, *Chem. Mater.*, 2005, **17**, 1553-1560.
132. G. P. Mane, S. N. Talapaneni, C. Anand, S. Varghese, H. Iwai, Q. M. Ji, K. Ariga, T. Mori and A. Vinu, *Adv. Funct. Mater.*, 2012, **22**, 3596-3604.
133. R. L. Liu, D. Q. Wu, X. L. Feng and K. Mullen, *Angew. Chem. Int. Ed.*, 2010, **49**, 2565-2569.
134. C.-M. Yang, C. Weidenthaler, B. Spliethoff, M. Mayanna and F. Schüth, *Chem. Mater.*, 2005, **17**, 355-358.
135. Y. X. Guo, J. P. He, T. Wang, H. R. Xue, Y. Y. Hu, G. X. Li, J. Tang and X. Sun, *J. Power Sources*, 2011, **196**, 9299-9307.
136. R. Silva, D. Voiry, M. Chhowalla and T. Asefa, *J. Am. Chem. Soc.*, 2013, **135**, 7823-7826.
137. L. Liu, Q. F. Deng, T. Y. Ma, X. Z. Lin, X. X. Hou, Y. P. Liu and Z. Y. Yuan, *J. Mater. Chem.*, 2011, **21**, 16001-16009.
138. Z. J. Li, G. D. Del Cul, W. F. Yan, C. D. Liang and S. Dai, *J. Am. Chem. Soc.*, 2004, **126**, 12782-12783.
139. F. Chamssedine, M. Dubois, K. Guerin, J. Giraudet, F. Masin, D. A. Ivanov, L. Vidal, R. Yazami and A. Hamwi, *Chem. Mater.*, 2007, **19**, 161-172.
140. Y. Wan, X. Qian, N. Q. Jia, Z. Y. Wang, H. X. Li and D. Y. Zhao, *Chem. Mater.*, 2008, **20**, 1012-1018.
141. P. F. Fulvio, S. S. Brown, J. Adcock, R. T. Mayes, B. K. Guo, X. G. Sun, S. M. Mahurin, G. M. Veith and S. Dai, *Chem. Mater.*, 2011, **23**, 4420-4427.
142. H. L. Wang, Q. M. Gao and J. Hu, *Micropor. Mesopor. Mat.*, 2010, **131**, 89-96.
143. Y. S. Shin, G. Fryxell, W. Y. Um, K. Parker, S. V. Mattigod and R. Skaggs, *Adv. Funct. Mater.*, 2007, **17**, 2897-2901.
144. P. Valle-Vigon, M. Sevilla and A. B. Fuertes, *Mater. Chem. Phys.*, 2013, **139**, 281-289.

145. M. Sevilla, A. B. Fuertes and R. Mokaya, *Int. J. Hydrogen Energy*, 2011, **36**, 15658-15663.
146. M. Sevilla and A. B. Fuertes, *Micropor. Mesopor. Mat.*, 2012, **158**, 318-323.
147. K. Kwon, S. A. Jin, C. Pak, H. Chang, S. H. Joo, H. I. Lee, J. H. Kim and J. M. Kim, *Catal. Today*, 2011, **164**, 186-189.
148. X. C. Zhao, Q. Zhang, C. M. Chen, B. S. Zhang, S. Reiche, A. Q. Wang, T. Zhang, R. Schlogl and D. S. Su, *Nano Energy*, 2012, **1**, 624-630.
149. J. Guo, Y. Luo, A. C. Lua, R. A. Chi, Y. L. Chen, X. T. Bao and S. X. Xiang, *Carbon*, 2007, **45**, 330-336.
150. E. A. Morris, D. W. Kirk, C. Q. Jia and K. Morita, *Environ. Sci. Technol.*, 2012, **46**, 7905-7912.
151. H. L. Guo and Q. M. Gao, *J. Power Sources*, 2009, **186**, 551-556.
152. H. L. Jiang, Y. H. Zhu, Q. Feng, Y. H. Su, X. L. Yang and C. Z. Li, *Chem. Eur. J.*, 2014, **20**, 3106-3112.
153. Z. Liu, H. G. Nie, Z. Yang, J. Zhang, Z. P. Jin, Y. Q. Lu, Z. B. Xiao and S. M. Huang, *Nanoscale*, 2013, **5**, 3283-3288.
154. H. F. Li, H. A. Xi, S. M. Zhu, Z. Y. Wen and R. D. Wang, *Micropor. Mesopor. Mat.*, 2006, **96**, 357-362.
155. H. Huwe and M. Froba, *Micropor. Mesopor. Mat.*, 2003, **60**, 151-158.
156. C. Minchev, H. Huwe, T. Tsoncheva, D. Paneva, M. Dimitrov, I. Mitov and M. Froba, *Micropor. Mesopor. Mat.*, 2005, **81**, 333-341.
157. H. F. Li, H. A. Xi, S. M. Zhu and R. D. Wang, *Mater. Lett.*, 2006, **60**, 943-946.
158. H. F. Li, S. M. Zhu, H. A. Xi and R. D. Wang, *Micropor. Mesopor. Mat.*, 2006, **89**, 196-203.
159. H. Huwe and M. Froba, *Carbon*, 2007, **45**, 304-314.
160. J. Fan, T. Wang, C. Yu, B. Tu, Z. Jiang and D. Zhao, *Adv. Mater.*, 2004, **16**, 1432-1436.
161. P. F. Fulvio, C. D. Liang, S. Dai and M. Jaroniec, *Eur. J. Inorg. Chem.*, 2009, **5**, 605-612.
162. Z. K. Sun, B. Sun, M. H. Qiao, J. Wei, Q. Yue, C. Wang, Y. H. Deng, S. Kaliaguine and D. Y. Zhao, *J. Am. Chem. Soc.*, 2012, **134**, 17653-17660.

163. P. Z. Cheng and H. S. Teng, *Carbon*, 2003, **41**, 2057-2063.
164. Y. Otake and R. G. Jenkins, *Carbon*, 1993, **31**, 109-121.
165. M. Eto and F. B. Growcock, *Carbon*, 1983, **21**, 135-147.
166. A. Guha, W. J. Lu, T. A. Zawodzinski and D. A. Schiraldi, *Carbon*, 2007, **45**, 1506-1517.
167. H. Tamai, K. Shiraki, T. Shiono and H. Yasuda, *J. Colloid Interface Sci.*, 2006, **295**, 299-302.
168. C. U. Pittman, Z. Wu, W. Jiang, G. R. He, B. Wu, W. Li and S. D. Gardner, *Carbon*, 1997, **35**, 929-943.
169. M. Delamar, R. Hitmi, J. Pinson and J. M. Saveant, *J. Am. Chem. Soc.*, 1992, **114**, 5883-5884.
170. Z. Li, W. Yan and S. Dai, *Langmuir*, 2005, **21**, 11999-12006.
171. Z. Li and S. Dai, *Chem. Mater.*, 2005, **17**, 1717-1721.
172. M. Pandurangappa, N. S. Lawrence and R. G. Compton, *Analyst*, 2002, **127**, 1568-1571.
173. G. G. Wildgoose, H. C. Leventis, I. J. Davies, A. Crossley, N. S. Lawrence, L. Jiang, T. G. J. Jones and R. G. Compton, *J. Mater. Chem.*, 2005, **15**, 2375-2382.
174. M. Choi and R. Ryoo, *J. Mater. Chem.*, 2007, **17**, 4204-4209.
175. X. Q. Wang, R. Liu, M. M. Waje, Z. W. Chen, Y. S. Yan, K. N. Bozhilov and P. Y. Feng, *Chem. Mater.*, 2007, **19**, 2395-2397.
176. J. B. Lee, Y. K. Park, O. B. Yang, Y. Kang, K. W. Jun, Y. J. Lee, H. Y. Kim, K. H. Lee and W. C. Choi, *J. Power Sources*, 2006, **158**, 1251-1255.
177. L. F. Wang, Y. Zhao, K. F. Lin, X. J. Zhao, Z. C. Shan, Y. Di, Z. H. Sun, X. J. Cao, Y. C. Zou, D. Z. Jiang, L. Jiang and F. S. Xiao, *Carbon*, 2006, **44**, 1336-1339.
178. S. G. Chen, Z. D. Wei, X. Q. Qi, L. C. Dong, Y. G. Guo, L. J. Wan, Z. G. Shao and L. Li, *J. Am. Chem. Soc.*, 2012, **134**, 13252-13255.
179. M. Kim, S. Hwang and J.-S. Yu, *J. Mater. Chem.*, 2007, **17**, 1656-1659.
180. D. Yuan, X. Yuan, W. Zou, F. Zeng, X. Huang and S. Zhou, *J. Mater. Chem.*, 2012, **22**, 17820-17826.

181. M. Ishikawa, T. Sugimoto, M. Kikuta, E. Ishiko and M. Kono, *J. Power Sources*, 2006, **162**, 658-662.
182. G. Gupta, D. A. Slanac, P. Kumar, J. D. Wiggins-Camacho, J. Kim, R. Ryoo, K. J. Stevenson and K. P. Johnston, *J. Phys. Chem. C*, 2010, **114**, 10796-10805.
183. K. P. Gierszal, M. Jaroniec, T.-W. Kim, J. Kim and R. Ryoo, *New J. Chem.*, 2008, **32**, 981-993.
184. H. Yang, Yan, Y. Liu, F. Zhang, R. Zhang, Y. YanMeng, M. Li, S. Xie, B. Tu and D. Zhao, *J. Phys. Chem. B*, 2004, **108**, 17320-17328.
185. T.-W. Kim, I.-S. Park and R. Ryoo, *Angew. Chem. Int. Ed.*, 2003, **42**, 4375-4379.
186. F. Zhang, Yan, H. Yang, Y. YanMeng, C. Yu, B. Tu and D. Zhao, *J. Phys. Chem. B*, 2005, **109**, 8723-8732.
187. F. Ehrburger-Dolle, I. Morfin, E. Geissler, F. Bley, F. Livet, C. Vix-Guterl, S. Saadallah, J. Parmentier, M. Reda, J. Patarin, M. Iliescu and J. Werckmann, *Langmuir*, 2003, **19**, 4303-4308.
188. C.-M. Yang, C. Weidenthaler, B. Spliethoff, M. Mayanna and F. Schüth, *Chem. Mater.*, 2004, **17**, 355-358.
189. X. Ji, P. S. Herle, Y. Rho and L. F. Nazar, *Chem. Mater.*, 2007, **19**, 374-383.
190. W. Zhu, J. Ren, X. Gu, M. U. Azmat, G. Lu and Y. Wang, *Carbon*, 2011, **49**, 1462-1472.
191. W. Gao, Y. Wan, Y. Dou and D. Zhao, *Adv. Energy Mater.*, 2011, **1**, 115-123.
192. J. Yuan, C. Giordano and M. Antonietti, *Chem. Mater.*, 2010, **22**, 5003-5012.
193. Z. L. Schaefer, M. L. Gross, M. A. Hickner and R. E. Schaak, *Angew. Chem.*, 2010, **122**, 7199-7202.
194. A. B. Fuertes and S. Alvarez, *Carbon*, 2004, **42**, 3049-3055.
195. K. T. Lee, X. L. Ji, M. Rault and L. F. Nazar, *Angew. Chem. Int. Ed.*, 2009, **48**, 5661-5665.
196. F. Su, J. Zeng, X. Bao, Y. Yu, J. Y. Lee and X. S. Zhao, *Chem. Mater.*, 2005, **17**, 3960-3967.
197. Z. Lei, S. Bai, Y. Xiao, L. Dang, L. An, G. Zhang and Q. Xu, *J. Phys. Chem. C*, 2008, **112**, 722-731.

198. W. H. Zhang, C. Liang, H. Sun, Z. Shen, Y. Guan, P. Ying and C. Li, *Adv. Mater.*, 2002, **14**, 1776-1778.
199. X. Sun, J. P. He, J. Tang, T. Wang, Y. X. Guo, H. R. Xue, G. X. Li and Y. O. Ma, *J. Mater. Chem.*, 2012, **22**, 10900-10910.
200. F. Su, X. S. Zhao, Y. Wang and J. Y. Lee, *Micropor. Mesopor. Mat.*, 2007, **98**, 323-329.
201. P. F. Fulvio, R. T. Mayes, X. Q. Wang, S. M. Mahurin, J. C. Bauer, V. Presser, J. McDonough, Y. Gogotsi and S. Dai, *Adv. Funct. Mater.*, 2011, **21**, 2208-2215.
202. R. Liu, S. M. Mahurin, C. Li, R. R. Unocic, J. C. Idrobo, H. J. Gao, S. J. Pennycook and S. Dai, *Angew. Chem. Int. Ed.*, 2011, **50**, 6799-6802.
203. T. Yang, R. Zhou, D. W. Wang, S. P. Jiang, Y. Yamauchi, S. Z. Qiao, M. J. Monteiro and J. Liu, *Chem. Commun.*, 2015, **51**, 2518-2521.
204. L. F. Chen, Z. H. Huang, H. W. Liang, H. L. Gao and S. H. Yu, *Adv. Funct. Mater.*, 2014, **24**, 5104-5111.
205. Z. Y. Jin, A. H. Lu, Y. Y. Xu, J. T. Zhang and W. C. Li, *Adv. Mater.*, 2014, **26**, 3700-3705.
206. G. P. Hao, W. C. Li, D. Qian, G. H. Wang, W. P. Zhang, T. Zhang, A. Q. Wang, F. Schuth, H. J. Bongard and A. H. Lu, *J. Am. Chem. Soc.*, 2011, **133**, 11378-11388.
207. C. F. Zhang, H. B. Wu, C. Z. Yuan, Z. P. Guo and X. W. Lou, *Angew. Chem. Int. Ed.*, 2012, **51**, 9592-9595.
208. F. B. Su, X. S. Zhao, Y. Wang, L. K. Wang and J. Y. Lee, *J. Mater. Chem.*, 2006, **16**, 4413-4419.
209. J. Liu, S. Z. Qiao, S. Budi Hartono and G. Q. Lu, *Angew. Chem. Int. Ed.*, 2010, **49**, 4981-4985.
210. J. Liu, H. Q. Yang, F. Kleitz, Z. G. Chen, T. Yang, E. Strounina, G. Q. Lu and S. Z. Qiao, *Adv. Funct. Mater.*, 2012, **22**, 591-599.
211. J. Liu, S. Z. Qiao, J. S. Chen, X. W. Lou, X. Xing and G. Q. Lu, *Chem. Commun.*, 2011, **47**, 12578-12591.
212. N. Suzuki, J. Liu and Y. Yamauchi, *New J. Chem.*, 2014, **38**, 3330-3335.

213. M. Steinhart, C. D. Liang, G. W. Lynn, U. Gosele and S. Dai, *Chem. Mater.*, 2007, **19**, 2383-2385.
214. A. T. Rodriguez, M. Chen, Z. Chen, C. J. Brinker and H. Y. Fan, *J. Am. Chem. Soc.*, 2006, **128**, 9276-9277.
215. S. Jun, S. H. Joo, R. Ryoo, M. Kruk, M. Jaroniec, Z. Liu, T. Ohsuna and O. Terasaki, *J. Am. Chem. Soc.*, 2000, **122**, 10712-10713.
216. X. D. Zhuang, F. Zhang, D. Q. Wu and X. L. Feng, *Adv. Mater.*, 2014, **26**, 3081-3086.
217. G. P. Hao, A. H. Lu, W. Dong, Z. Y. Jin, X. Q. Zhang, J. T. Zhang and W. C. Li, *Adv. Energy Mater.*, 2013, **3**, 1421-1427.
218. D. Qian, C. Lei, G. P. Hao, W. C. Li and A. H. Lu, *ACS Appl Mater. Inter.*, 2012, **4**, 6125-6132.
219. G. P. Hao, W. C. Li, D. Qian and A. H. Lu, *Adv. Mater.*, 2010, **22**, 853-857.
220. G. P. Hao, W. C. Li, S. A. Wang, G. H. Wang, L. Qi and A. H. Lu, *Carbon*, 2011, **49**, 3762-3772.
221. D. W. Wang and D. S. Su, *Energy Environ. Sci.*, 2014, **7**, 576-591.
222. H. W. Liang, W. Wei, Z. S. Wu, X. L. Feng and K. Mullen, *J. Am. Chem. Soc.*, 2013, **135**, 16002-16005.
223. T. Yang, J. Liu, R. Zhou, Z. Chen, H. Xu, S. Z. Qiao and M. J. Monteiro, *J. Mater. Chem. A*, 2014, **2**, 18139-18146.
224. M. Shen, C. Ruan, Y. Chen, C. Jiang, K. Ai and L. Lu, *ACS Appl Mater. Inter.*, 2015, **7**, 1207-1218.
225. G. Tao, L. Zhang, L. Chen, X. Cui, Z. Hua, M. Wang, J. Wang, Y. Chen and J. Shi, *Carbon*, 2015, **86**, 108-117.
226. J. Yan, H. Meng, F. Y. Xie, X. L. Yuan, W. D. Yu, W. R. Lin, W. P. Ouyang and D. S. Yuan, *J. Power Sources*, 2014, **245**, 772-778.
227. F. Cheng, Z. Tao, J. Liang and J. Chen, *Chem. Mater.*, 2008, **20**, 667-681.
228. C. C. Li, X. M. Yin, L. B. Chen, Q. H. Li and T. H. Wang, *J. Phys. Chem. C*, 2009, **113**, 13438-13442.
229. F. D. Han, Y. J. Bai, R. Liu, B. Yao, Y. X. Qi, N. Lun and J. X. Zhang, *Adv. Energy Mater.*, 2011, **1**, 798-801.

230. Y. S. Hu, P. Adelhelm, B. M. Smarsly, S. Hore, M. Antonietti and J. Maier, *Adv. Funct. Mater.*, 2007, **17**, 1873-1878.
231. K. T. Lee, J. C. Lytle, N. S. Ergang, S. M. Oh and A. Stein, *Adv. Funct. Mater.*, 2005, **15**, 547-556.
232. L. Qie, W.-M. Chen, Z.-H. Wang, Q.-G. Shao, X. Li, L.-X. Yuan, X.-L. Hu, W.-X. Zhang and Y.-H. Huang, *Adv. Mater.*, 2012, **24**, 2047-2050.
233. Y. Yang, G. Yu, J. J. Cha, H. Wu, M. Vosgueritchian, Y. Yao, Z. Bao and Y. Cui, *ACS Nano*, 2011, **5**, 9187-9193.
234. X. Tao, X. Chen, Y. Xia, H. Huang, Y. Gan, R. Wu, F. Chen and W. zhang, *J. Mater. Chem. A*, 2013, **1**, 3295-3301.
235. B. Zhang, X. Qin, G. R. Li and X. P. Gao, *Energy Environ. Sci.*, 2010, **3**, 1531-1537.
236. X. Ji, K. T. Lee and L. F. Nazar, *Nat. Mater.*, 2009, **8**, 500-506.
237. B. Ding, C. Yuan, L. Shen, G. Xu, P. Nie and X. Zhang, *Chem. Eur. J.*, 2013, **19**, 1013-1019.
238. G. Zheng, Y. Yang, J. J. Cha, S. S. Hong and Y. Cui, *Nano Lett.*, 2011, **11**, 4462-4467.
239. X.-G. Sun, X. Wang, R. T. Mayes and S. Dai, *ChemSusChem*, 2012, **5**, 2079-2085.
240. X. L. Ji, S. Evers, R. Black and L. F. Nazar, *Nat. Commun.*, 2011, **2**, 325-332.
241. Y. C. Lu, H. A. Gasteiger, M. C. Parent, V. Chiloyan and Y. Shao-Horn, *Electrochem. Solid-State Lett.*, 2010, **13**, A69-A72.
242. S. S. Zhang, D. Foster and J. Read, *J. Power Sources*, 2010, **195**, 1235-1240.
243. J. Xiao, D. H. Mei, X. L. Li, W. Xu, D. Y. Wang, G. L. Graff, W. D. Bennett, Z. M. Nie, L. V. Saraf, I. A. Aksay, J. Liu and J. G. Zhang, *Nano Lett.*, 2011, **11**, 5071-5078.
244. X.-h. Yang, P. He and Y.-y. Xia, *Electrochem. Commun.*, 2009, **11**, 1127-1130.
245. Y. N. Zhang, H. M. Zhang, J. Li, M. R. Wang, H. J. Nie and F. X. Zhang, *J. Power Sources*, 2013, **240**, 390-396.
246. J. S. Lee, S. T. Kim, R. Cao, N. S. Choi, M. Liu, K. T. Lee and J. Cho, *Adv. Energy Mater.*, 2011, **1**, 34-50.

247. M. D. Slater, D. Kim, E. Lee and C. S. Johnson, *Adv. Funct. Mater.*, 2013, **23**, 947-958.
248. Y. K. Sun, Z. H. Chen, H. J. Noh, D. J. Lee, H. G. Jung, Y. Ren, S. Wang, C. S. Yoon, S. T. Myung and K. Amine, *Nat. Mater.*, 2012, **11**, 942-947.
249. K. Tang, L. J. Fu, R. J. White, L. H. Yu, M. M. Titirici, M. Antonietti and J. Maier, *Adv. Energy Mater.*, 2012, **2**, 873-877.
250. S. Wenzel, T. Hara, J. Janek and P. Adelhelm, *Energy Environ. Sci.*, 2011, **4**, 3342-3345.
251. Y. L. Cao, L. F. Xiao, M. L. Sushko, W. Wang, B. Schwenzer, J. Xiao, Z. M. Nie, L. V. Saraf, Z. G. Yang and J. Liu, *Nano Lett.*, 2012, **12**, 3783-3787.
252. R. Alcantara, P. Lavela, G. F. Ortiz and J. L. Tirado, *Electrochem. Solid-State Lett.*, 2005, **8**, A222-A225.
253. J. Liu, H. Liu, T. Y. Yang, G. X. Wang and M. O. Tade, *Chin. Sci. Bull.*, 2014, **59**, 2186-2190.
254. K. B. Hueso, M. Armand and T. Rojo, *Energy Environ. Sci.*, 2013, **6**, 734-749.
255. T. H. Hwang, D. S. Jung, J.-S. Kim, B. G. Kim and J. W. Choi, *Nano Lett.*, 2013, **13**, 4532-4538.
256. A. G. Pandolfo and A. F. Hollenkamp, *J. Power Sources*, 2006, **157**, 11-27.
257. G.-H. An and H.-J. Ahn, *Carbon*, 2013, **65**, 87-96.
258. P. Simon and Y. Gogotsi, *Nat. Mater.*, 2008, **7**, 845-854.
259. J. Huang, B. G. Sumpter and V. Meunier, *Angew. Chem. Int. Ed.*, 2008, **47**, 520-524.
260. C. O. Ania, V. Khomenko, E. Raymundo-Piñero, J. B. Parra and F. Béguin, *Adv. Funct. Mater.*, 2007, **17**, 1828-1836.
261. C. Largeot, C. Portet, J. Chmiola, P.-L. Taberna, Y. Gogotsi and P. Simon, *J. Am. Chem. Soc.*, 2008, **130**, 2730-2731.
262. J. Chmiola, C. Largeot, P.-L. Taberna, P. Simon and Y. Gogotsi, *Angew. Chem. Int. Ed.*, 2008, **47**, 3392-3395.
263. J. Chmiola, G. Yushin, Y. Gogotsi, C. Portet, P. Simon and P. L. Taberna, *Science*, 2006, **313**, 1760-1763.

264. D. Hulicova-Jurcakova, A. M. Puziy, O. I. Poddubnaya, F. Suarez-Garcia, J. M. D. Tascon and G. Q. Lu, *J. Am. Chem. Soc.*, 2009, **131**, 5026-+.
265. D. Hulicova, J. Yamashita, Y. Soneda, H. Hatori and M. Kodama, *Chem. Mater.*, 2005, **17**, 1241-1247.
266. D. Hulicova-Jurcakova, M. Kodama, S. Shiraishi, H. Hatori, Z. H. Zhu and G. Q. Lu, *Adv. Funct. Mater.*, 2009, **19**, 1800-1809.
267. H.-K. Jeong, M. Jin, E. J. Ra, K. Y. Sheem, G. H. Han, S. Arepalli and Y. H. Lee, *ACS Nano*, 2010, **4**, 1162-1166.
268. L. Z. Fan, Y. S. Hu, J. Maier, P. Adelhelm, B. Smarsly and M. Antonietti, *Adv. Funct. Mater.*, 2007, **17**, 3083-3087.
269. L. L. Zhang, S. Li, J. Zhang, P. Guo, J. Zheng and X. S. Zhao, *Chem. Mater.*, 2009, **22**, 1195-1202.
270. S. R. Sivakkumar, W. J. Kim, J.-A. Choi, D. R. MacFarlane, M. Forsyth and D.-W. Kim, *J. Power Sources*, 2007, **171**, 1062-1068.
271. F. Fusalba, H. A. Ho, L. Breau and D. Bélanger, *Chem. Mater.*, 2000, **12**, 2581-2589.

*Every reasonable effort has been made to acknowledge the owners of copyright material. I would be pleased to hear from any copyright owner who has been omitted or incorrectly acknowledged.*

---

# Chapter 3. Triconstituent Co-assembly Synthesis of N, S-Doped Carbon-Silica Nanospheres with Smooth and Rough Surfaces

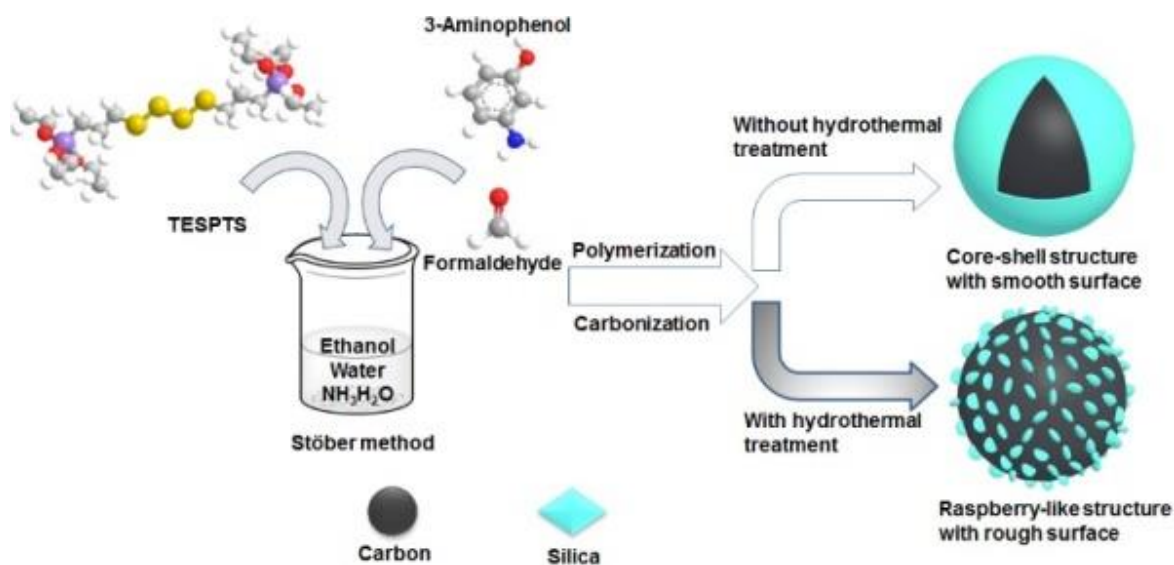
## 3.1 Introduction

The design and synthesis of nanoparticles with controllable surface properties are of great importance for various applications such as drug delivery, catalysis, energy storage and conversion.<sup>1-5</sup> Learning from nature, in particular from virus and pollen morphology, the raspberry-like nanoparticles with rough surface have attracted a widespread interest due to their unique structure and functionality such as exceptional morphology, large specific surface area, surface coarseness, and large light scattering. Although raspberry-like nanoparticles have been designed and synthesized for specific applications, e.g., self-cleaning,<sup>6</sup> drug delivery,<sup>7</sup> catalysis,<sup>8</sup> optical and electrical devices,<sup>9</sup> and heavy metals removal,<sup>10</sup> it is still a great challenge to fabricate in a simple and effective way various multifunctional raspberry-like porous nanospheres such as carbon-silica composite particles.

To date, the Stöber method has been developed for a one-pot synthesis of silica, phenolic resin (PR) and carbon spheres.<sup>11-13</sup> Recently, this facile method has been extended to prepare highly monodispersed and core-shell structured silica-resorcinol-formaldehyde spheres and silica-carbon spheres.<sup>14-26</sup> To improve the conductivity and catalytic activity, heteroatoms such as nitrogen have been doped into the carbon framework.<sup>27,28</sup> However, the resultant silica-carbon spheres are not richly functionalized, which limits their

practical applications. In addition, it is desirable to design carbon-silica composite particles with controllable surface roughness.

In this contribution, we report triconstituent co-assembly of 3-aminophenol (AP), formaldehyde, and bis[3-(triethoxysilyl)propyl]tetrasulfide (TESPTS) for a facile synthesis of PR polymer-silica nanospheres with smooth and rough surfaces. Carbonization of these spheres generates the carbon-silica nanospheres. The raspberry-like carbon-silica nanospheres are composed of carbon cores decorated with many silica nanoparticles on the surface. As illustrated in **Scheme 3.1**, our approach is based on the Stöber method involving simultaneously polymerization of PR and condensation of TESPTS in aqueous alcohol solution with addition of ammonia catalyst. Hydrothermal treatment of PR polymer-silica core-shell nanoparticles plays a key role in developing the surface roughness due to the enhanced condensation degree of TESPTS.



**Scheme 3.1.** Synthesis of polymer-silica and carbon-silica core-shell spheres functionalized with N, S-species.

## 3.2 Experimental Section

### 3.2.1 Materials

Formaldehyde (37% solution), aqueous ammonia (25% solution), ethanol (undenatured, 95-100%), 3-aminophenol (99%) and bis[3-(triethoxysilyl)propyl] tetrasulfide (TESPTS,  $\geq 90\%$ ) were purchased from Sigma-Aldrich and used as received without any further purification. Washing was achieved with ultrapure water and reagent grade ethanol where required. Ultrapure water was used for solution preparations.

### 3.2.2 Synthesis of N, S-dual functionalized polymer-silica spheres

Typically, ammonia aqueous solution ( $\text{NH}_3 \cdot \text{H}_2\text{O}$ , 0.6 mL, 25 wt%) was mixed with a solution containing absolute ethanol (EtOH, 24 mL) and deionized water ( $\text{H}_2\text{O}$ , 114 mL), then stirred for 30 min. Subsequently, 3-aminophenol (1.2 g) was added and continually stirred for 30 min. Then 5.28 mL bis[3-(triethoxysilyl)propyl] tetrasulfide (TESPTS) and formaldehyde solution (1.68 mL) were added to the reaction solution and stirred for 24 h at 30 °C. The mixture was separated into two equal parts. The first part of the mixture named N,S-dual functionalized polymer silica spheres without hydrothermal treatment (N,S-PSS) was separated directly and washed with Di-water and ethanol 3 times. The second part was transferred to a hydrothermal reactor which was then placed into an oven for 24 h at 100 °C. Then the remained materials N, S-dual functionalized polymer silica spheres after hydrothermal treatment (N, S-PSR) were washed with Di-water and ethanol 3 times.

### 3.2.3 Synthesis of N, S-dual functionalized carbon-silica spheres

N,S-PSS and N,S-PSR were calcinated under  $\text{N}_2$  flow in the tube furnace using a heating rate of 1 °C  $\text{min}^{-1}$  up to 350 °C, dwell for 2 h, and resuming heating rate at 1 °C  $\text{min}^{-1}$  up to 700 °C and dwell for 4 h to achieve N,S-dual functionalized carbon-silica spheres named of N,S-dual functionalized carbon-silica spheres without hydrothermal

treatment (N,S-CSS) and N,S-dual functionalized carbon-silica spheres with hydrothermal treatment (N,S-CSR-1), respectively. N,S-CSS-900 was prepared through calcination of N,S-PSS under N<sub>2</sub> flow in the tube furnace using a heating rate of 1 °C min<sup>-1</sup> up to 350 °C, dwell for 2 h, and resuming heating rate at 1 °C min<sup>-1</sup> up to 900 °C and dwell for 4 h.

### 3.2.4 Synthesis of silica nanoparticles

N,S-dual functionalized carbon-silica spheres were calcinated in muffle furnace using a heating rate of 1 °C min<sup>-1</sup> up to 350 °C, dwell for 2 h, and resuming heating rate at 1 °C min<sup>-1</sup> up to 700 °C and dwell for 4 h to achieve silica nanoparticles.

### 3.2.5 Characterisation

The sample morphology was characterized by using a transmission electron microscope (TEM, JEOL EM-2100) and a scanning electron microscope (SEM, Zeiss Neon). High Angle Annular Dark Field Scanning Transmission Electron Microscopy (HAADF-STEM) imaging and element mapping were carried out using a FEI Titan G2 80-200 TEM/STEM with ChemiSTEM Technology operating at 200 kV. The element maps were obtained by energy dispersive X-ray spectroscopy using the Super-X detector on the Titan with a probe size ~1 nm and a probe current of ~0.4 nA. Nitrogen adsorption and desorption analyses were performed on Micromeritics TriStar II Surface Area and Porosity Analyser. The specific surface area was calculated by the Brunauer–Emmett–Teller (BET) method. Nonlocal density functional theory (NLDFT) was utilized to obtain the pore volume and pore size distribution. Prior to measurements in the nitrogen sorption analysers, the samples were degassed at 250 °C overnight.

### 3.2.6 CO<sub>2</sub> adsorption

The carbon dioxide adsorption isotherm was obtained at 0 °C using a carbon dioxide sorption instrument (Micromeritics Gemini 2360 Surface Area Analyser). Prior to

measurements in the carbon dioxide sorption analysers, the samples were degassed at 250 °C overnight.

### 3.2.7 Electrochemical measurement

3 mg carbon-silica powder was dispersed in 3 ml 0.2 % Nafion aqueous solution by ultrasonication. 10  $\mu$ L of the dispersion was dipped onto the glassy carbon electrode (5 mm in diameter) and dried under ambient condition. The electrode was then used as the working electrode in a 3-electrode electrochemistry system. In the system, a Ag/AgCl electrode (in 3M KCl) and a Pt wire were used as the reference electrode and the counter electrode respectively. 6 M KOH aqueous solutions were used as the electrolyte. Cyclic voltammetry (CV) was applied to the working electrode between 0 V and -0.8 V at scanning rate between 10 mV/s and 500 mV/s.

### 3.3 Results and discussion

The observed difference in the polymerization rate of APF and TESPTS, namely the much faster polymerization rate of APF than that of TESPTS, causes the initial formation of the  $\text{NH}_4^+$  modified phenol resin cores, which electrostatically attract negatively charged silica nanoparticles by forming the raspberry-like polymer-silica spheres. Subsequently, the carbon-silica core-shell spheres can be obtained by pyrolysis of PR polymer-silica spheres under  $\text{N}_2$  atmosphere as shown in **Scheme 3.1**. Moreover, the silica hollow capsules can be generated by burning off the carbon-silica particles in air. This approach combines two merits: (i) multi-step assembling and coating processes are combined into one-step process and also (ii) multi-functional groups and the desired surface roughness can be achieved at the same time.

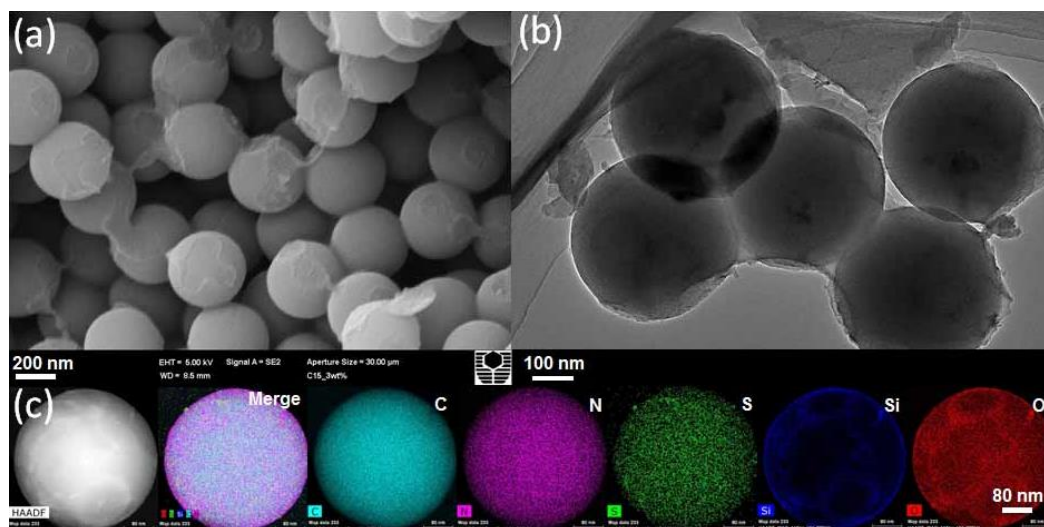


**Figure 3.1.** (a) SEM image, (b) TEM image, (c) STEM and EDS mapping of carbon-silica spheres with N,S-species (N,S-CSS) obtained without hydrothermal treatment.

As shown in **Figure 3.1a**, the scanning electron microscope (SEM) image shows that N,S- functionalized carbon-silica spheres (N,S-CSS) obtained without hydrothermal treatment exhibit uniform spherical morphology with relatively smooth surface and the average particle size of about 400 nm. A transmission electron microscope (TEM) image (**Figure 3.1b**) confirms that N, S-CSS spheres are very uniform. The scanning transmission electron microscope (STEM) and the corresponding energy dispersive X-ray spectroscopy (EDS) mapping (**Figure 3.1c**) were obtained to identify the distribution of silica and carbon. As shown in **Figure 3.1c**, nitrogen atoms are homogeneously distributed in the carbon framework and the silica shell formed on the surface of the carbon core is thin, indicating the carbon-silica core-shell structure.

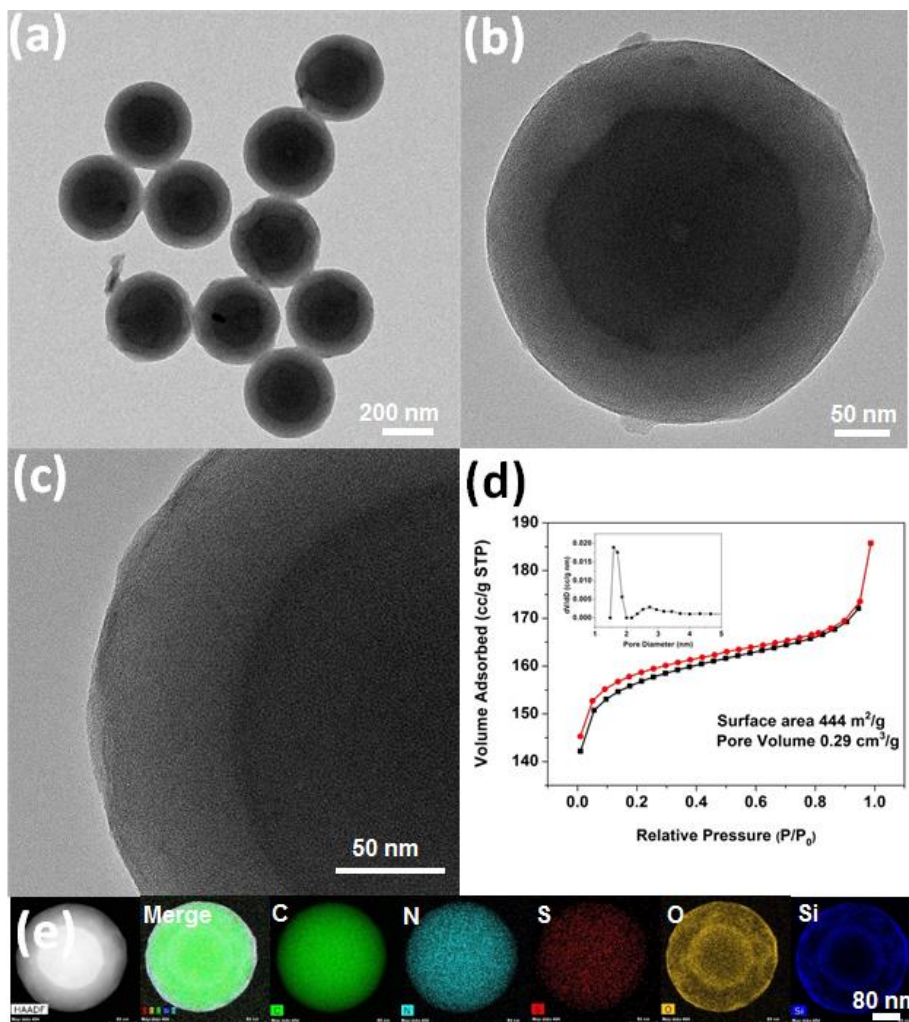


**Figure 3.2.** (a) (b) (c) TEM images, (d)  $N_2$  adsorption-desorption isotherms curve and the inset pore size distribution curve, (e) STEM and EDS mapping of N,S-dually functionalized carbon-silica obtained before hydrothermal treatment with the following calcination at  $900\text{ }^\circ\text{C}$  (N,S-CSS-900).

After higher temperature calcination at  $900\text{ }^\circ\text{C}$  of N,S-PSS, uniform core-shell structured and spherical carbon-silica composite materials with smooth surface (N,S-CSS-900) are achieved and the average particle size is about  $355\text{ nm}$  (as shown in **Figure 3.2a**). From **Figure 3.2b and 3.2c**, the diameter of the shell is about  $50\text{ nm}$  and the diameter of core is about  $255\text{ nm}$ . As shown in **Figure 3.2d**,  $N_2$  adsorption-desorption isotherms measured for the N, S-CSS-900 spheres represent a combination

of type I and type IV isotherms, indicating their micropores and mesopores in N, S-CSS-900. Non-local density functional theory (NLDFT) is used to provide the detailed information about the micro and mesopore size distribution. From inset figure in Figure 2d, a bimodal pore size distribution centered at 1.6 and 2.8 nm was observed, confirming micro-mesoporous structure.<sup>25, 29</sup> The Brunauer-Emmett-Teller (BET) surface area and the pore volume obtained on the basis of the aforementioned adsorption isotherms are 444 m<sup>2</sup>/g and 0.29 cm<sup>3</sup>/g, respectively. The scanning transmission electron microscope (STEM) and the corresponding energy dispersive X-ray spectroscopy (EDS) mapping (Figure 3.2e) were obtained to identify the distribution of silica and carbon. As shown in Figure 3.2e, it is interesting to find that the double-layered silica shell formed on the surface of the inner and outer carbon core, indicating the carbon-silica core-shell structure.

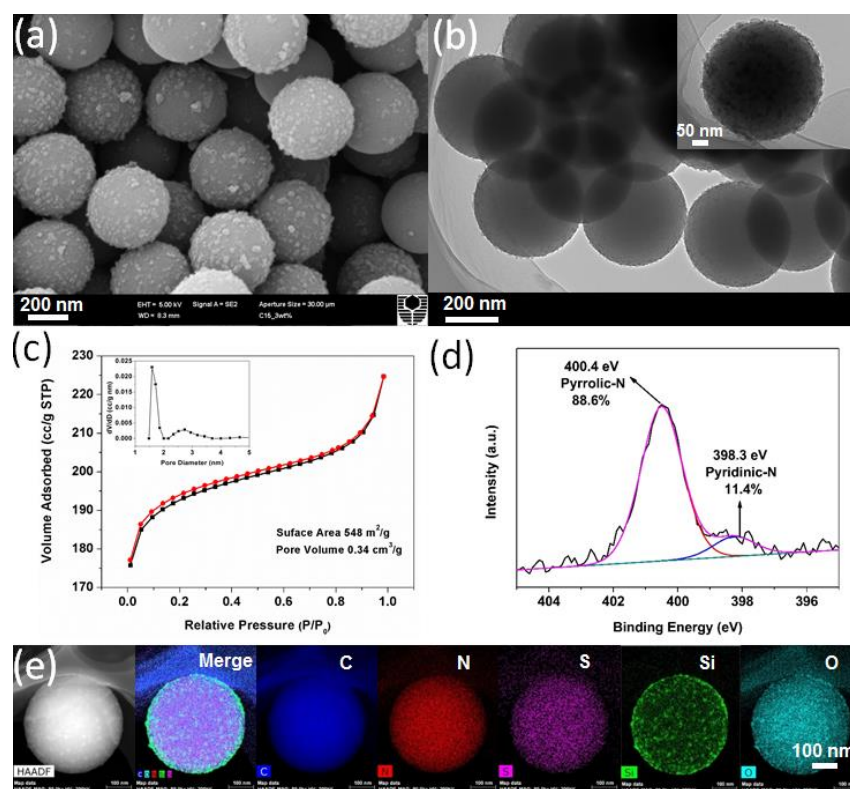


**Figure 3.3.** (a) SEM image, (b) TEM image, (c) N<sub>2</sub> adsorption-desorption isotherms and the inset pore size distribution curve, (d) high resolution XPS spectrum of N 1s and (e) STEM and EDS mapping of N,S-dually functionalized carbon-silica obtained after hydrothermal treatment (N,S-CSR-1) of N,S-CSR spheres.

An additional hydrothermal treatment of the N,S-dually functionalized carbon-silica spheres (N,S-CSR-1) resulted in the raspberry-like spheres (**Figure 3a**), which is confirmed by the TEM images shown in **Figure 3b**. The silica nanoparticles which decorated on the carbon cores are of about 20 nm. As shown in Figure 3c, N<sub>2</sub> adsorption-desorption isotherms measured for the N, S-CSR-1 spheres represent a combination of type I and type IV isotherms, indicating their micropores and mesopores in N, S-CSR-1. Micro-mesoporous structure was also confirmed by non-local density functional theory (NLDFT).<sup>25, 29</sup> From inset figure in **Figure 3c**, a similar bimodal pore size distribution centered at 1.6 and 2.8 nm with N, S-CSS-900 was observed. The Brunauer-Emmett-Teller (BET) surface area and the pore volume obtained on the basis of the aforementioned adsorption isotherms are 548 m<sup>2</sup>/g and 0.34 cm<sup>3</sup>/g, respectively.

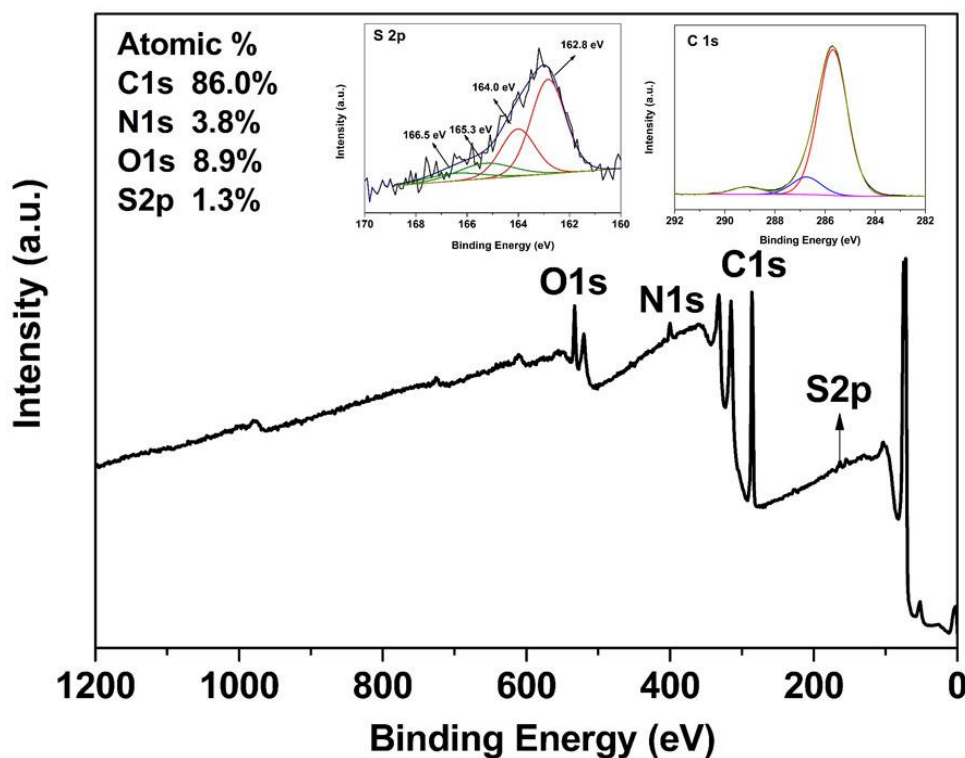


**Figure 3.4.** XPS survey spectra, high resolution C1s spectra (insert figure) and high resolution S2p spectra (insert figure).

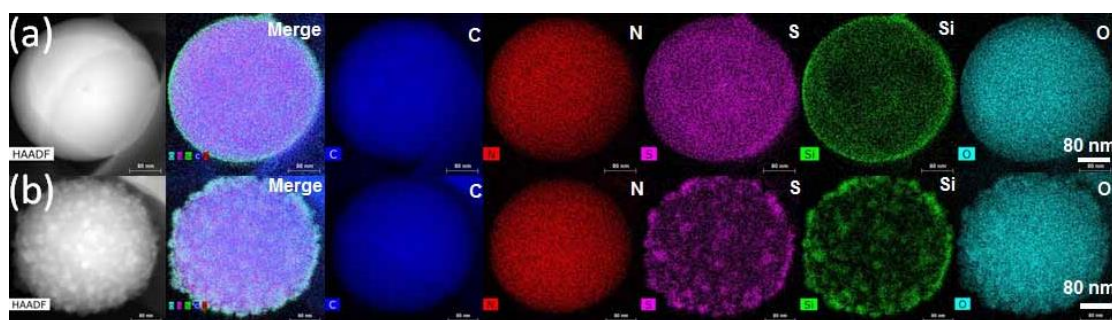


**Figure 3.5.** (a) STEM and EDS mapping of N, S-dual functionalized polymer-silica spheres without hydrothermal treatment (N,S-PSS). (b) STEM and EDS mapping of N,S-dual functionalized polymer-silica spheres after hydrothermal treatment (N,S-PSR).

The X-ray photoelectron spectroscopy (XPS) (**Figure 3.4**) pattern exhibits four typical peaks for C1s, N1s, O1s and S2P on the survey spectrum with the corresponding content of each element of 86.0 %, 3.8%, 8.9% and 1.3%, respectively. The XPS high resolution narrow scan (**Figure 3.3d**) displays two overlapping N1s peaks corresponding to pyridinic nitrogen (398.3 eV) and pyrrolic nitrogen (400.4 eV) with the relative concentration of each of about 11.4% and 88.6%, respectively.<sup>30</sup> S 2p<sub>3/2</sub> and 2p<sub>1/2</sub> doublet peak was recorded and unfolded with an energy separation of 1.2 eV and relative peak intensities of 2:1. The binding energy of S 2p<sub>1/2</sub> peak at 162.8 eV is probably attributed to C–S species in the silica precursors.<sup>31</sup> The signals of the binding energy at 165.3 -166.5 eV are also observed indicating that S constituents were oxidized into sulfite functional groups.<sup>32</sup> Interestingly, the particle size of N,S-CSS (400 nm) did not change during hydrothermal treatment process, which resulted in the raspberry-like N,S-CSR-1 core-shell spheres with silica shells consisting of a large number of silica nanoparticles present on the surface of carbon cores. To determine the dispersion of elements in N, S-CSR-1, the EDS mapping of N, S-CSR-1 has been used to reveal that the small clusters grown on the surface of carbon spheres are silica by polycondensation of TESPTS (**Figure 3.3e**). Similarly, a nanoparticles. These small nanoparticles are derived upon hydrothermal treatment of silica generated thin silica layer was formed on

the surface of polymer spheres (**Figure 3.5a**), which upon hydrothermal treatment was converted to silica nanoparticles (**Figures 3b and 3.5b**).

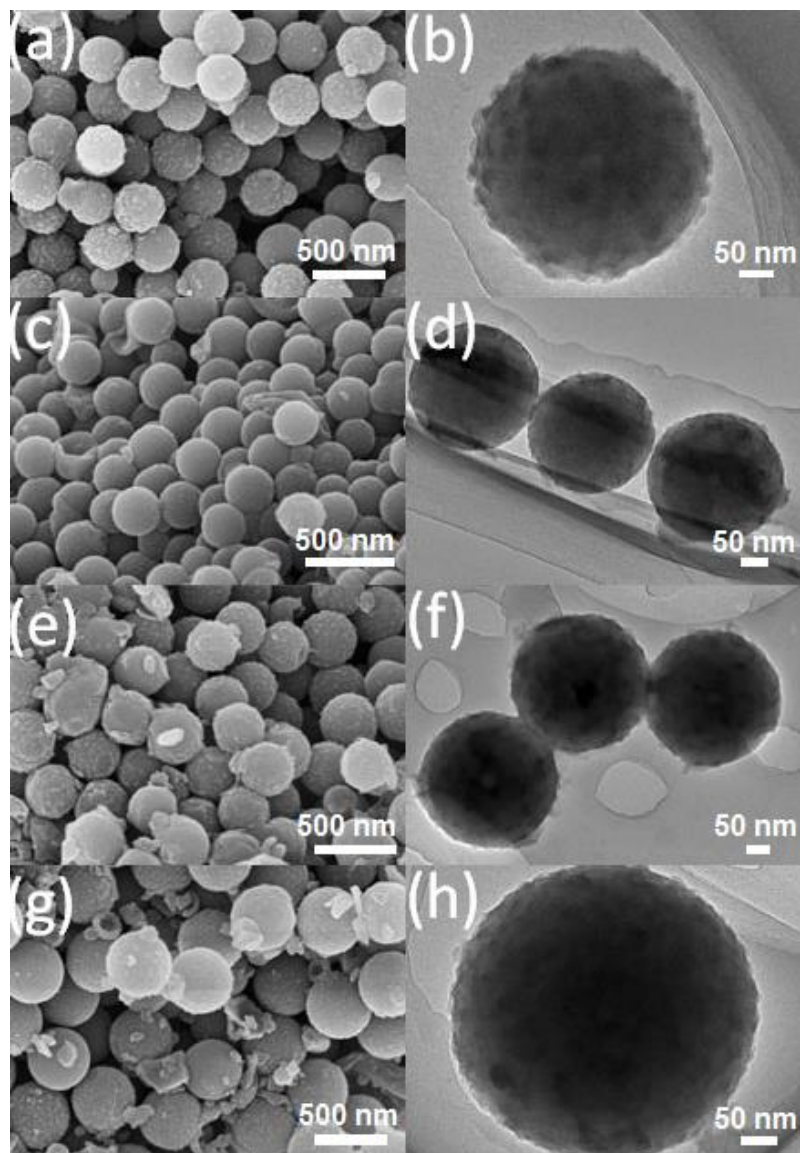


**Figure 3.6.** SEM and TEM images of N,S-CSR-2 (a) (b); N,S-CSR-3(c)(d); N,S-CSR-4(e)(f); N,S-CSR-5(g)(h).

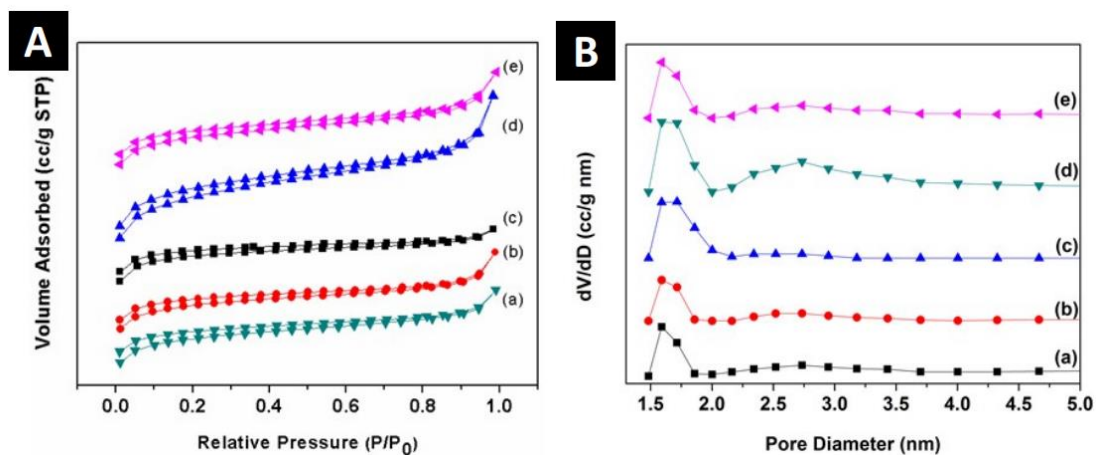


**Figure 3.7.** (A) N<sub>2</sub> adsorption-desorption isotherms and (B) nonlocal density functional theory (NLDFT) pore size distributions of (a) N,S-CSR-4; (b) N,S-CSR-2; (c) N,SCSS; (d) N,S-CSR-3; (e) N,S-CSR-5.

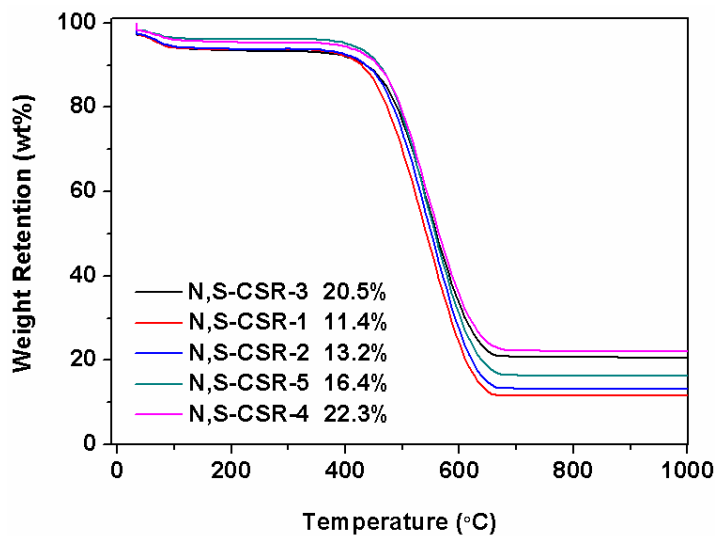


**Figure 3.8.** TG profiles of N, S-CSR-1, N,S-CSR-2, N,S-CSR-3, N,S-CSR-4 and N,S-CSR-5.

In order to tailor the particle size and the N and S contents, the TESPTS/AP molar ratio was varied. The nitrogen sorption isotherms of the other carbon-silica materials are shown in **Figure 3.7** and the results of the surface area, pore size and pore volume are

listed in Table S1. As shown in Figure 3.7A, all the samples show type-I isotherms with micro-mesoporous structure. Similar pore size distribution about 1.6 nm and 2.8nm is also presented in Figure 3.7B. The specific surface area of these particles varies from 300 m<sup>2</sup>/g to 550 m<sup>2</sup>/g. The smallest surface area obtained for N, S-CSR-4 is mainly derived from the relatively high residual content (22.3%) in comparison to other samples (see Figure 3.8). The rest of the other carbon-silica samples possess relatively high surface area because of comparatively high carbon content. The highest surface area of N, S-CSR-1 can be due to the highest carbon content (88.6%) among all five samples. As the amount of TESPTS increases as evidenced by the molar ratio of TESPTS/AP varying from 0.48 to 1.92, the size of monodisperse carbon- silica spheres decreases from 465 nm to 270 nm (see Figure 3.6, Table 3.1 and Figure 3.9). This is probably associated with the fact that with decreasing concentration of 3-aminophenol, the polymerization rate is reduced and the smaller resin particles are produced. Additionally, the TEM and SEM images of N, S-CSR-3 (Figure 3.6) show smoother surface than that of other samples, indicating that higher concentration of TESPTS leads to the formation of thicker silica layer with smaller silica nanoparticles.

**Table 3.1.** Physical properties of N, S-dual functionalized carbon-silica spheres.

Sample	BET surface area (m <sup>2</sup> /g) <sup>a</sup>	Pore volume (cm <sup>3</sup> /g) <sup>b</sup>	Pore size (nm) <sup>a</sup>	Particle size (nm) <sup>c</sup>	Molar ratio (TESPTS: AP)	Weight retention	Molar ratio (S:N) <sup>d</sup>
N,S-CSS	397	0.24	1.7, 2.6	400	0.96	N/A	N/A
N,S-CSS-900	444	0.29	1.6, 2.8	355	0.96	N/A	N/A
N,S-CSR-1	548	0.35	1.6, 2.8	400	0.96	11.4%	3.84
N,S-CSR-2	334	0.22	1.6,2.8	355	0.64	13.2%	2.56
N,S-CSR-3	485	0.33	1.6,2.8	270	1.92	20.5%	7.68
N,S-CSR-4	300	0.19	1.6,2.8	345	1.44	22.3%	5.76
N,S-CSR-5	346	0.23	1.6,2.8	465	0.48	16.4%	1.92

<sup>a</sup> Specific surface area was calculated by BET modelling. <sup>b</sup> Nonlocal density functional theory (NLDFT) was utilized to obtain the pore volume and pore size distribution. <sup>c</sup> Mean particle size was estimated by SEM and TEM analysis. <sup>d</sup> theoretical molar ratio S/N.

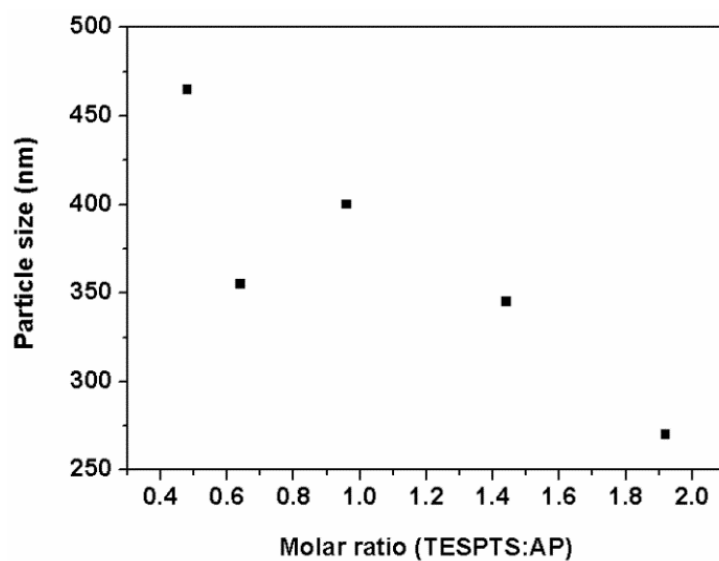
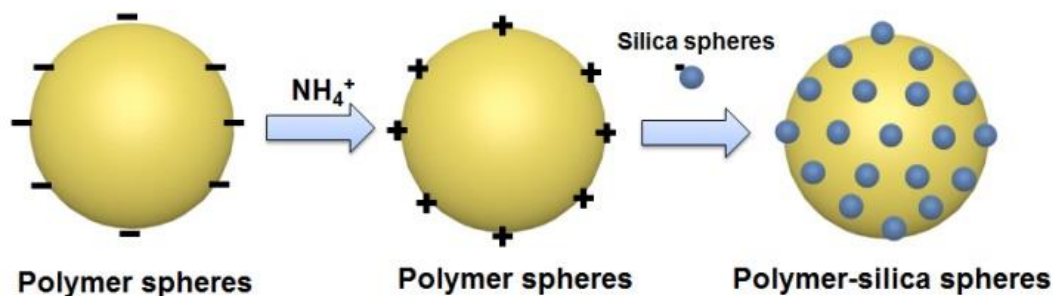


**Figure 3.9.** The relationship between particle size of N,S-dual functionalized carbon-silica and molar ratio of TESPTS/AP.



**Scheme 3.2.** Mechanism illustration of formation mechanism of polymer-silica sphere.

Based on the above presented observations, the proposed mechanism of the formation of N, S-dually functionalized carbon-silica spheres and the corresponding polymer-silica spheres can be explained as shown in **Scheme 3.1** and **Scheme 3.2**, respectively. In the first step, the negatively charged PR spheres are formed rapidly in the presence

of ammonia in ethanol/water mixture and a stable colloidal suspension is obtained. Then the surface of PR spheres is covered with  $\text{NH}_4^+$  ions to inhibit their further aggregation. At the same time, due to the relatively slow hydrolysis and condensation of TESPTS silane,<sup>33</sup> the formation of cross-linked silica particles requires longer reaction time or higher reaction temperature. In the next step, due to the strong electrostatic interaction between silicate anions and  $\text{NH}_4^+$  ions on the surface of polymer spheres, a thin layer of silica is formed on the surface of polymer spheres. It is also well-known that the hydroxyl groups present in phenolic resin can react with silane oligomer species. As a result, a cooperative condensation and cross-linking reaction occurs between silicate oligomers and phenolic resin. After carbonization of phenolic resin-silica nanoparticles, N, S-dually functionalized carbon-silica spheres are obtained.<sup>34</sup>

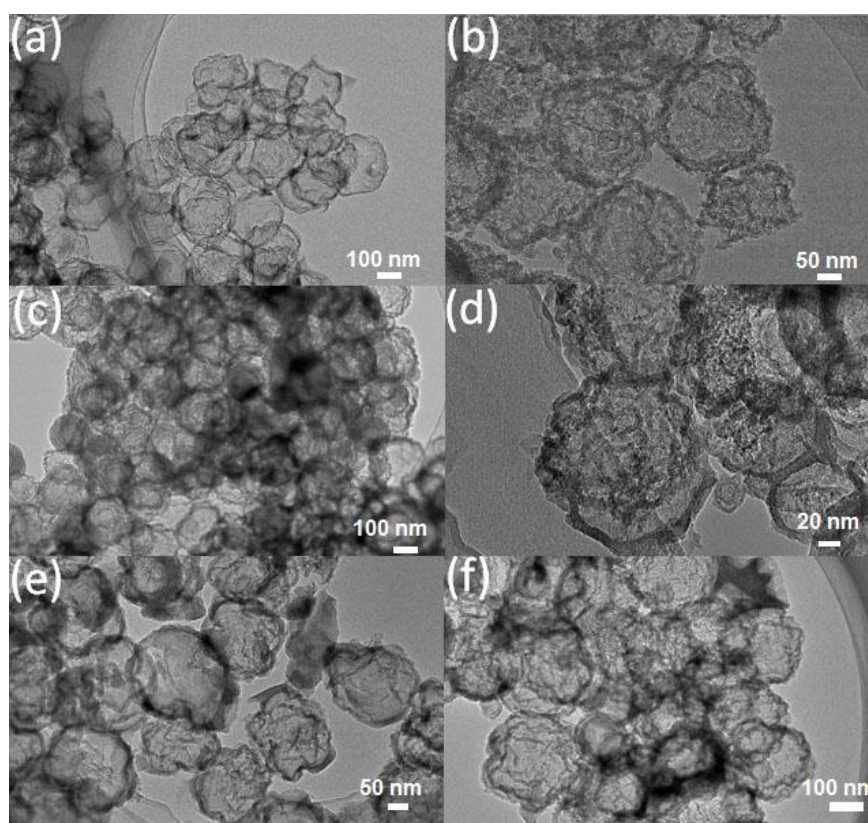


**Figure 3.10.** TEM images of air-annealing effect of N,S-CSS-silica (a); N,S-CSR-1-silica (b); N,S-CSR-2-silica (c); N,S-CSR-3-silica (d); N,S-CSR-4-silica (e); N,S-CSR-5-silica(f)

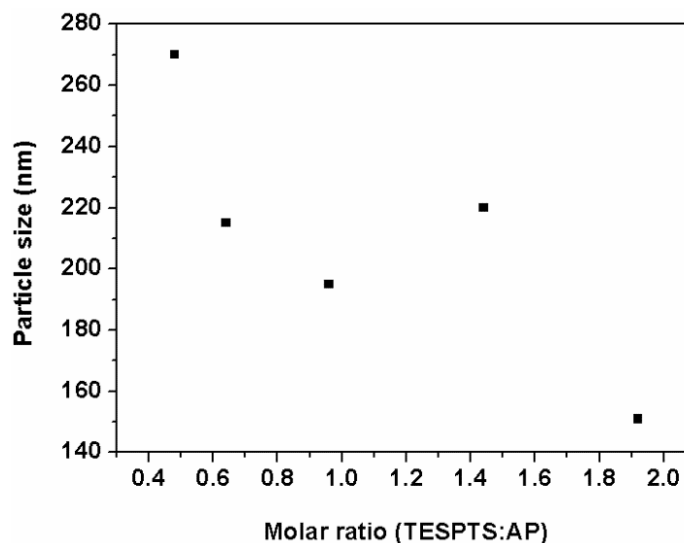


**Figure 3.11.** The relationship between particle size of hollow silica and molar ratio of TESPTS/AP.

**Table 3.2.** Particle size and shell thickness of silica samples.

Samples	Mean particle size (nm)	Mean shell thickness (nm)	Contraction percentage (%)
N,S-CSS-silica	210	8	48
N,S-CSR-1-silica	195	20	51
N,S-CSR-2-silica	215	13	39
N,S-CSR-3-silica	151	9	44
N,S-CSR-4-silica	220	15	36
N,S-CSR-5-silica	270	18	42

To further confirm the carbon core and silica shell structure, the N, S-functionalized carbon-silica core-shell spheres were calcined in air to remove the carbon core. Figures **3.10a** and **3.10b** show the TEM images of N, S-CSS-silica and N, S-CSR-1-silica, respectively. Uniform hollow silica capsules with particle size of about 210 nm and the

shell thickness of about 8 nm are observed in the case of N,S-CSS-silica (**Figure 3.10a**), indicating that the calcination in air resulted in the formation of hollow structure. Particularly, the dimension of the hollow spheres decreased tremendously as compared with the solid spherical structure of N, S-CSS (**Figure 3.10b**). This decrease can be attributed to the shrinkage of the shell and pore during calcination. As presented in **Figure 3.10b** and **Table 3.2**, the hydrothermally-treated silica nanoparticles (N, S-CSR-1-silica) exhibit raspberry-like structure. The diameter of hollow silica spheres is of about 195 nm and the shell thickness is of about 20 nm. Hydrothermal treatment causes also an increase in the surface roughness, wall thickness and structural shrinkage of hollow silica spheres. Note that the mean particle size and the mean shell thickness can be also adjusted by adjusting the molar concentrations of TESPTS and 3-aminophenol. As the amount of TESPTS increases as evidenced by variation of the molar ratio of TESPTS/AP from 0.48 to 1.92, the size of hollow silica spheres tends to decrease from 270 nm to 151 nm (see **Figures 3.10, 3.11**, and **Table 3.2**). This is consistent with the trend of the particle size of N, S- functionalized carbon-silica spheres, confirming that the formation of core-shell structures with carbon cores and silica shells.

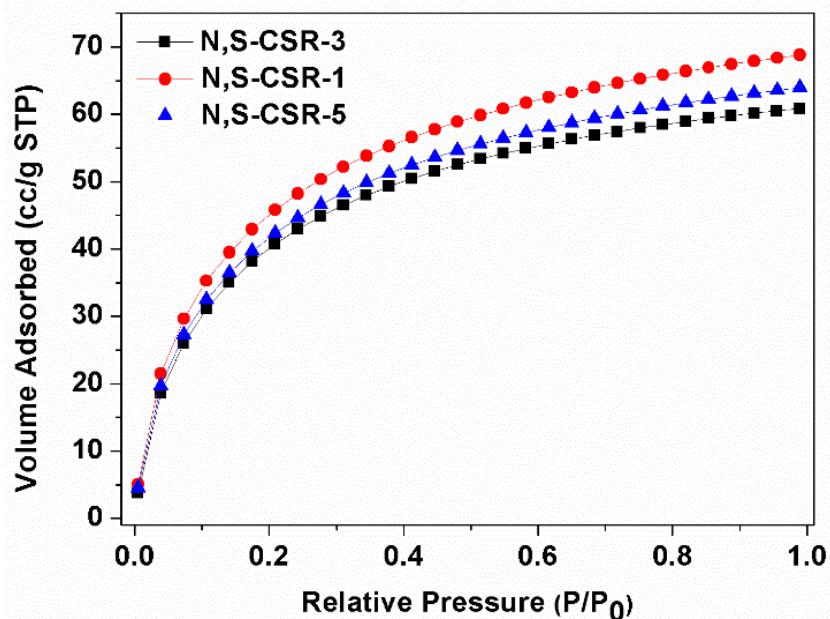


**Figure 3.12.** CO<sub>2</sub> adsorption isotherms ( $T = 0 \pm 1$  °C) measured for N,S- functionalized carbon-silica spheres N,S-CSR-1, N,S-CSR-3, N,S-CSR-5.

The CO<sub>2</sub> capture has attracted a great attention in recent years due to the need of reducing the concentration of greenhouse gases that cause the observed climate changes. The CO<sub>2</sub> adsorption isotherms measured on N, S-CSR-1 spheres with largest surface area (548 m<sup>2</sup>/g) and highest nitrogen content show highest capacity of 67 cm<sup>3</sup>/g at 0 ± 1 °C and 1.0 bar (**Figure 3.12**). After increasing the molar amount of TESPTES and decreasing the molar amount of 3-aminophenol, the CO<sub>2</sub> uptakes obtained for N,S-CSR-3 and N,S-CSR-5 are smaller, 64 cm<sup>3</sup>/g and 60 cm<sup>3</sup>/g at 0 ± 1 °C and 1.0 bar, respectively (**Figure 3.12**). This implies that the smaller surface area with fewer exposed N-containing basic sites can significantly reduce the CO<sub>2</sub> capacity.<sup>35-36</sup>

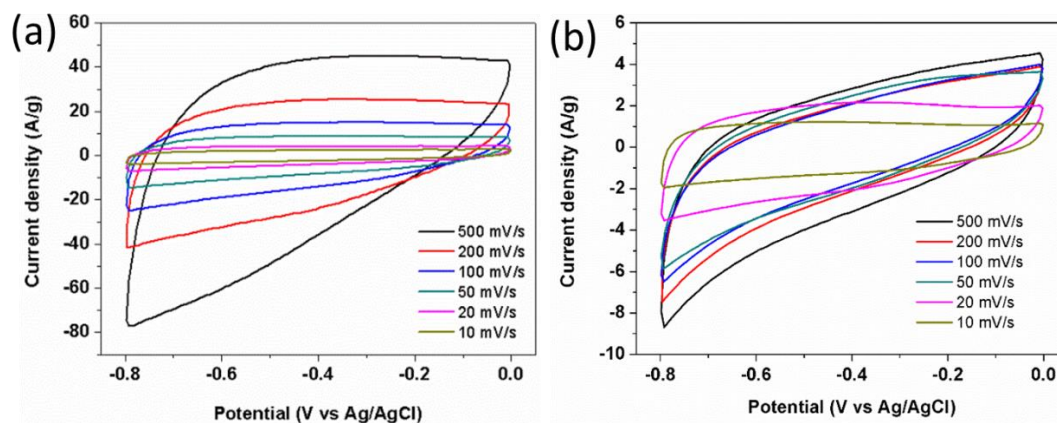


**Figure 3.13.** CV profiles of N,S-CSS (a) and N,S-CSR-1 (b) measured in basic conditions.

Inspired by high surface area and high nitrogen content of the carbon-silica core-shell spheres, we studied their electrochemical properties by a cyclic voltammetry (CV). The particle size, surface area, microporosity and nitrogen-doping usually have a great impact on the capacitance.<sup>37-38</sup> **Figure 3.13** shows the CV curves recorded for N,S-CSS and N,S-CSR-1 using a three-electrode system in the range from -0.8 V to 0.0 V (vs Ag/AgCl) at different scan rates. It can be observed that the cyclic voltammetry (CV) plots measured for N,S-CSS under basic conditions (6 M KOH) exhibit a nearly rectangular shape at a voltage scan rate up to 200 mV/s, revealing a double-layer capacitance performance and outstanding high rate capability. The specific capacitance of N, S-CSS is 221 F/g (**Figure 3.11** and **Table 3.3**) because of high surface area and

nitrogen doping in the carbon framework. Although the surface area of N, S-CSR-1 is higher than the surface area of N, S-CSS, the former exhibits lower capacitance (about 111 F/g) than that of N, S-CSS (**Figure 3.11** and **Table 3.3**). This is probably due to the fact that the hydrothermal treatment resulted in the formation of more nucleated and non-conductive silica nanoparticles on the surface of carbon spheres making ion transportation and diffusion in the carbon spheres of N, S-CSR-1 more difficult than that in N, S-CSS.

**Table 3.3.** Capacitances of N, S-CSS and N, S-CSR-1 measured in the basic conditions (6mol/L KOH).

Samples	10 mV/s	20 mV/s	50 mV/s	100 mV/s	200 mV/s	500 mV/s
N,S-CSS	221	192	157	131	109	75
N,S-CSR-1	111	92	47	23	12	6

### 3.4 Conclusions

In summary, we have successfully synthesized polymer-silica nanospheres using the extended Stöber method via triconstituent co-assembly of 3-aminophenol, formaldehyde, and TESPTS. Further carbonization of the resulting polymer-silica spheres generated N, S-functionalized carbon-silica nanospheres. Moreover, this study shows that the particle size of monodisperse carbon-silica spheres and hollow silica spheres can be tailored through adjusting the molar ratio of TESPTS/PR. It is shown that the prepared carbon-silica spheres exhibit excellent performance as adsorbents for CO<sub>2</sub> capture (67 cm<sup>3</sup>/g at 0 ± 1 °C and 1.0 bar) and as supercapacitor electrode with high specific capacitance in basic media (221 F/g, 6 M KOH) due to high surface area and nitrogen-doping. Therefore, it is anticipated that N, S- functionalized carbon-silica spheres are very promising not only as supercapacitor electrodes and CO<sub>2</sub> adsorbents but also in other multi-purpose applications such as catalyst supports, drug delivery carriers and hard templates. Our method allows for control of the growth of silica

nanoparticles onto carbon cores to obtain the core-shell carbon-silica spheres and for tailoring their surface functionality, roughness, and porous structures; all these properties cannot be achieved by using the currently existing synthetic methods.

### 3.5 References

1. J. Liu, S. Z. Qiao, Q. H. Hu and G. Q. Lu, *Small*, 2011, **7**, 425-443.
2. J. Liu, S. Z. Qiao, J. S. Chen, X. W. Lou, X. Xing and G. Q. Lu, *Chem. Commun.*, 2011, **47**, 12578-12591.
3. A. Guerrero-Martinez, J. Perez-Juste and L. M. Liz-Marzan, *Adv. Mater.*, 2010, **22**, 1182-1195.
4. J. Liu, N. P. Wickramaratne, S. Z. Qiao and M. Jaroniec, *Nat. Mater.*, 2015, **14**, 763-774.
5. G.-H. Wang, J. Hilgert, F. H. Richter, F. Wang, H.-J. Bongard, B. Spliethoff, C. Weidenthaler and F. Schüth, *Nat. Mater.*, 2014, **13**, 293-300.
6. X. Li and J. He, *ACS Appl. Mater. Interfaces*, 2013, **5**, 5282-5290.
7. Y. Ahmad Nor, Y. Niu, S. Karmakar, L. Zhou, C. Xu, J. Zhang, H. Zhang, M. Yu, D. Mahony, N. Mitter, M. A. Cooper and C. Yu, *ACS Cent. Sci.*, 2015, **1**, 328-334.
8. S. S. Acharyya, S. Ghosh and R. Bal, *ACS Appl. Mater. Interfaces*, 2014, **6**, 14451-14459.
9. X. Du, X. M. Liu, H. M. Chen and J. H. He, *J. Phys. Chem. C*, 2009, **113**, 9063-9070.
10. R. Demir-Cakan, N. Baccile, M. Antonietti and M.-M. Titirici, *Chem. Mater.*, 2009, **21**, 484-490.
11. W. Stöber, A. Fink and E. Bohn, *J. Colloid Interf. Sci.*, 1968, **26**, 62-69.

12. J. Liu, S. Z. Qiao, H. Liu, J. Chen, A. Orpe, D. Zhao and G. Q. Lu, *Angew. Chem. Int. Edit.*, 2011, **50**, 5947-5951.
13. A. H. Lu, G. P. Hao and Q. Sun, *Angew. Chem. Int. Edit.*, 2011, **50**, 9023-9025.
14. A. B. Fuertes, P. Valle-Vigon and M. Sevilla, *Chem. Commun.*, 2012, **48**, 6124-6126.
15. X. H. Zhang, Y. A. Li and C. B. Cao, *J. Mater. Chem.*, 2012, **22**, 13918-13921.
16. J. Choma, D. Jamiola, K. Augustynek, M. Marszewski, M. Gao and M. Jaroniec, *J. Mater. Chem.*, 2012, **22**, 12636-12642.
17. Z. A. Qiao, B. Guo, A. J. Binder, J. Chen, G. M. Veith and S. Dai, *Nano Lett.*, 2013, **13**, 207-212.
18. B. Guan, X. Wang, Y. Xiao, Y. Liu and Q. Huo, *Nanoscale*, 2013, **5**, 2469-2475.
19. J. Zang, T. An, Y. Dong, X. Fang, M. Zheng, Q. Dong and N. Zheng, *Nano Res.*, 2015, **8**, 2663-2675.
20. J.-C. Song, F.-F. Xue, Z.-Y. Lu and Z.-Y. Sun, *Chem. Commun.*, 2015, **51**, 10517-10520.
21. R. Liu, Y. W. Yeh, V. H. Tam, F. Qu, N. Yao and R. D. Priestley, *Chem. Commun.*, 2014, **50**, 9056-9059.
22. R. Liu, F. Qu, Y. Guo, N. Yao and R. D. Priestley, *Chem. Commun.*, 2014, **50**, 478-480.
23. S. Mezzavilla, C. Baldizzone, K. J. Mayrhofer and F. Schuth, *ACS Appl. Mater. Interfaces*, 2015, **7**, 12914-12922.
24. X. Ma, L. Gan, M. Liu, P. K. Tripathi, Y. Zhao, Z. Xu, D. Zhu and L. Chen, *J. Mater. Chem. A*, 2014, **2**, 8407-8415.

25. P. K. Tripathi, M. Liu, Y. Zhao, X. Ma, L. Gan, O. Noonan and C. Yu, *J. Mater. Chem. A*, 2014, **2**, 8534-8544.
26. M. Liu, X. Ma, L. Gan, Z. Xu, D. Zhu and L. Chen, *J. Mater. Chem. A*, 2014, **2**, 17107-17114.
27. D. Zhu, Y. Wang, L. Gan, M. Liu, K. Cheng, Y. Zhao, X. Deng and D. Sun, *Electrochim. Acta*, 2015, 158, 166-174.
28. Y. Zhao, M. Liu, X. Deng, L. Miao, P. K. Tripathi, X. Ma, D. Zhu, Z. Xu, Z. Hao and L. Gan, *Electrochim. Acta*, 2015, 153, 448-455.
29. M. Liu, J. Qian, Y. Zhao, D. Zhu, L. Gan and L. Chen, *J. Mater. Chem. A*, 2015, **3**, 11517-11526.
30. T. Y. Yang, J. Liu, R. F. Zhou, Z. G. Chen, H. Y. Xu, S. Z. Qiao and M. J. Monteiro, *J. Mater. Chem. A*, 2014, **2**, 18139-18146.
31. S. A. Wohlgemuth, F. Vilela, M. M. Titirici and M. Antonietti, *Green Chem.*, 2012, **14**, 741-749.
32. S. Gupta, B. R. Weiner and G. Morell, *J. Mater. Res.*, 2003, **18**, 363-381.
33. J. Liu, Q. H. Yang, L. Zhang, D. M. Jiang, X. Shi, J. Yang, H. Zhong and C. Li, *Adv. Funct. Mater.*, 2007, **17**, 569-576.
34. R. Liu, Y. Shi, Y. Wan, Y. Meng, F. Zhang, D. Gu, Z. Chen, B. Tu and D. Zhao, *J. Am. Chem. Soc.*, 2006, **128**, 11652-11662.
35. M. Sevilla, P. Valle-Vigon and A. B. Fuertes, *Adv. Funct. Mater.*, 2011, **21**, 2781-2787.
36. W. Xing, C. Liu, Z. Y. Zhou, L. Zhang, J. Zhou, S. P. Zhuo, Z. F. Yan, H. Gao, G. Q. Wang and S. Z. Qiao, *Energy Environ. Sci.*, 2012, **5**, 7323-7327.

37. D. W. Wang, F. Li, M. Liu, G. Q. Lu and H. M. Cheng, *Angew. Chem. Int. Edit.*, 2008, **47**, 373-376.
38. T. Yang, R. Zhou, D. W. Wang, S. P. Jiang, Y. Yamauchi, S. Z. Qiao, M. J. Monteiro and J. Liu, *Chem. Commun.*, 2015, **51**, 2518-2521.

*Every reasonable effort has been made to acknowledge the owners of copyright material. I would be pleased to hear from any copyright owner who has been omitted or incorrectly acknowledged.*

---

# Chapter 4. Fabrication of core-shell, yolk-shell and hollow Fe<sub>3</sub>O<sub>4</sub>@carbon microboxes for high-performance lithium-ion batteries

## 4.1 Introduction

As one of the typical energy storage and supplemental devices, rechargeable lithium ion batteries (LIBs) are very promising towards sustainable energy.<sup>1-3</sup> In the past decade, enormous efforts have been undertaken toward advanced electrode materials. Fe<sub>3</sub>O<sub>4</sub>-based nanomaterials with special morphologies and structures have been used as anode materials with superior performance because of their high theoretical capacity (924 mA h g<sup>-1</sup>), low cost, low toxicity and natural abundance of iron.<sup>4-5</sup> However, a large volume expansion during lithiation, poor electronic conductivity and ion diffusion ability are the major problems that restrict the practical applications of these anode materials.<sup>6-7</sup> Design and fabrication of nanoparticles with special morphologies and tailored properties have been reported to enhance the cycle performance and rate capability.<sup>8-28</sup> For example, in the case of hollow structured Fe<sub>3</sub>O<sub>4</sub>-based nanomaterials, a sufficiently large space can be provided to facilitate the drastic volume expansion and short diffusion paths can also be created to promote lithium-ion transportation in the hollow structure.<sup>29-30</sup> In particular, the design of special core-shell and yolk-shell nanostructures is an alternative efficient strategy to improve the cycling performance.<sup>31-35</sup> An adequately designed interior space has been proven to be crucial for accommodation of large volume change of the Fe<sub>3</sub>O<sub>4</sub> active materials, and the particle aggregation can also be hindered by using protective shells. However, the synthesis of the above structured

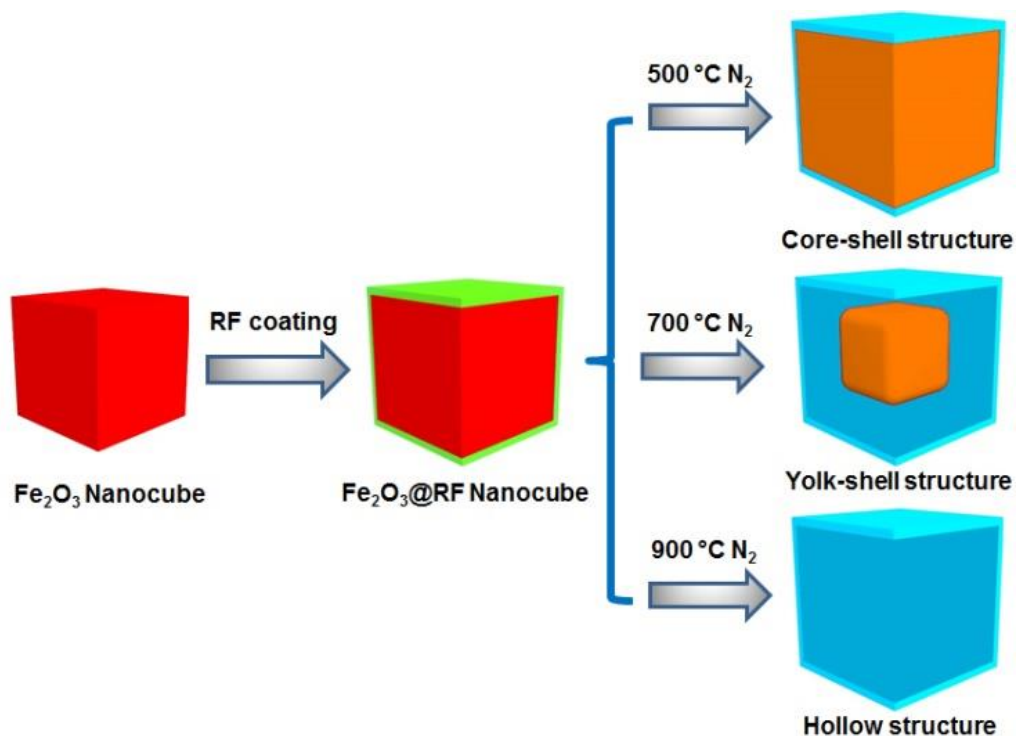
materials involves multiple steps; thus, there is still a challenge to fabricate nanoparticles with different compositional and morphological core and shells at the same scale. In addition, a deep understanding of the relationship between the structure of nanoparticle including core-shell, yolk-shell and hollow structures and electrochemical performance is rarely discussed.

Hollow and yolk-shell structured materials with tailored physical and chemical properties have shown a great potential for a variety of applications including catalysis, drug delivery, energy storage and conversion.<sup>36-40</sup> Recently, we have successfully prepared nitrogen-doped carbon nanocapsules with mesoporous carbon shells<sup>41</sup> and macroporous voids. In addition, hierarchical mesoporous yolk-shell structured carbon nanospheres (YSCNs) with ordered mesoporous carbon cores and microporous carbon shells<sup>42</sup> have been also synthesized via an extended Stöber method. The versatile coating techniques for fabrication of various carbon spheres along with our well-established carbon spheres library<sup>37, 43-45</sup> allowed us to design and synthesise core-shell, yolk-shell structured metal oxides carbon composites with unique core@void@shell structures. This approach can also be further utilized for the preparation of other core-shell structures with various morphologies, such as polymer@polymer,<sup>42</sup> Ag@polymer<sup>44</sup> and  $\alpha$ -Fe<sub>2</sub>O<sub>3</sub> nanospindle@ polymer.<sup>46</sup> In addition, the microbox-type structures have been shown to exhibit an excellent performance in energy storage, however the available literature on their synthesis is very limited.<sup>47-49</sup>

To create active sites and further enhance the conductivity, catalytic activity and the interaction between carbon composites and reactants, doping heteroatoms such as nitrogen is usually used.<sup>41</sup> Two different routes are usually employed to prepare N-doped carbon nanocomposites: a) direct pyrolysis of nitrogen-containing precursors such as melamine foam, carbon nitride and polymer framework,<sup>37,41</sup> and b) post-synthesis incorporation of nitrogen atoms into carbon framework via chemical vapour deposition (CVD),<sup>50</sup> or thermal treatment in ammonia or polyaniline.<sup>50,51</sup>

Herein, we report a one-step Stöber coating method to synthesize unique core-shell, yolk-shell structured Fe<sub>3</sub>O<sub>4</sub>@carbon microboxes by using Fe<sub>2</sub>O<sub>3</sub> cube as a core material.

These nanoparticles were used to fabricate anode and examine the lithium storage capability; electrochemical testing of this anode showed an excellent cycling performance, high rate capability, and high Coulombic efficiency. The particles studied combine the advantages of core-shell structures and conductive carbon shells acting as buffer layers. This study provides some guidelines for selection of proper polymer coatings and calcination conditions to achieve the desired structure and functionality of nanomaterials for fabrication of lithium ion battery electrodes, and to investigate the relationship between the structure of particles and the performance of these electrodes.



**Scheme 4.1** Synthetic illustration for the preparation of core-shell structure, yolk-shell structure and hollow structures of Fe<sub>3</sub>O<sub>4</sub>@carbon (Red, green, brown and blue colours refer to Fe<sub>2</sub>O<sub>3</sub> nanocube, polymer layer, Fe<sub>3</sub>O<sub>4</sub> nanoparticles and carbon layer, separately). Note: darker blue colour in the scheme denotes an empty space; in the core-shell particles there is no space between core and shell, while in the yolk shell particles there is space between yolk and shell.

## 4.2 Experimental Section

### 4.2.1 Materials

The following chemicals were used in this work: formaldehyde (37% solution), aqueous ammonia (25% solution), ethanol (95-100%), 3-aminophenol (99%), ferric chloride ( $\text{FeCl}_3$ ) and sodium hydroxide (NaOH), all were purchased from Sigma-Aldrich and used as received without any further purification. Washing was achieved with ultrapure water and if needed the reagent grade ethanol was applied. Ultrapure water was used for solution preparations.

#### 4.2.2 Synthesis of $\text{Fe}_2\text{O}_3$ nanocubes

The  $\text{Fe}_2\text{O}_3$  nanocubes were synthesized through a simple precipitation method. In a typical synthesis, 50 mL of 5.4 M NaOH solution was mixed with 50 mL of 2.0 M  $\text{FeCl}_3$  solution under continuous stirring at 75 °C. The resultant  $\text{Fe}(\text{OH})_3$  gel was continually stirred at the same temperature for 10 min, and transferred to a hydrothermal reactor, which was then placed into an oven for 4 days at 100 °C. The red product was collected and washed with DI-water and ethanol three times before drying at 80 °C overnight.

#### 4.2.3 Synthesis of $\text{Fe}_2\text{O}_3$ @polymer core@shell structures (FP)

In a typical synthesis, CTAB (0.1 g) was dissolved in a mixture of water (20 mL) and ethanol (8 mL). Then, an aqueous solution of ammonia ( $\text{NH}_4\text{OH}$ , 0.2 mL, 25 wt%) was added and stirred at room temperature for 0.5 h, followed by addition of  $\text{Fe}_2\text{O}_3$  nanocubes (0.1 g). After stirring for 0.5 h, 3-aminophenol (0.04 g) was added into the above suspension. After stirring for additional 30 min, a solution of formaldehyde (0.056 mL) was added. The mixture was stirred for 24 h at room temperature and subsequently heated for 24 h at 100 °C under static conditions in a Teflon-lined autoclave. The solid product was recovered by centrifugation and dried at 100 °C for 24 h. Subsequent variations of the synthesis process involved altering 3-aminophenol and formaldehyde to adjust the thickness of polymer coating; the resulting materials are denoted by FP-X, where X = 10, 23, 43 and 233 is the thickness of polymer expressed in nanometer scale.

#### 4.2.4 Synthesis of Fe<sub>3</sub>O<sub>4</sub>@carbon core@shell structures (FC)

The obtained Fe<sub>2</sub>O<sub>3</sub>@polymer core@shell structures were carbonized under N<sub>2</sub> flow in the tube furnace using a heating rate of 1 °C min<sup>-1</sup> up to 350 °C, kept for 2 h at that temperature, heated again with the heating rate at 1 °C min<sup>-1</sup> up to 700 °C and dwelled for 4 h to achieve Fe<sub>2</sub>O<sub>3</sub>@carbon core@shell structures. Subsequent variations of the synthesis process involved various calcination temperatures: 700, 800 and 900 °C; the resulting samples are denoted as FC-X-Y, where X and Y refer to the thickness of polymer coating and calcination temperature, respectively.

#### 4.2.5 Cell assembly and electrochemical testing

The electrodes were prepared by mixing the active materials, carbon black (CB), and poly(vinylidene fluoride) (PVDF) used as a binder, at the weight ratio of 7:2:1. The mixture was dispersed in *n*-methyl pyrrolidone (NMP) solvent and then the slurry was uniformly pasted onto Cu foils. The electrodes were dried at 120 °C in a vacuum oven for 12 h and subsequently pressed at a pressure of 200 kg cm<sup>-2</sup>. CR2032-type coin cells were assembled in a glove box for electrochemical measurements. A non-aqueous solution of 1 M LiPF<sub>6</sub> in an ethylene carbonate (EC), diethyl carbonate (DEC), and dimethyl carbonate (DMC) mixture (1:1:1) was used as the electrolyte. Li metal disks were used as the counter electrodes. The cells were galvanostatically charged and discharged in a current density range of 0.1 A g<sup>-1</sup> within the voltage range of 0.01–3.0 V. For the high rate testing, the charge/discharge current gradually increased from 0.1 to 0.2, 0.5, 1, 2, and 5 A g<sup>-1</sup> (corresponding approximately to 0.1, 0.2, 0.5, 1, 2 and 5 C, respectively), then decreased to 1 and 0.1 A g<sup>-1</sup>, step by step. Cyclic voltammetry (CV) curves were collected on an electrochemistry workstation (CHI660C) at 0.1 mV s<sup>-1</sup> within a range of 0.01–3.0 V. For the electrochemical impedance spectroscopy (EIS) measurements, the excitation voltage applied to the cells was 5 mV.

#### 4.2.6 Materials characterization

The sample morphology was characterized by using a transmission electron microscope (TEM, JEOL EM-2100) and a scanning electron microscope (SEM, Zeiss Neon). High Angle Annular Dark Field Scanning Transmission Electron Microscopy (HAADF-STEM) imaging and elemental mapping were carried out using a FEI Titan G2 80-200 TEM/STEM with ChemiSTEM Technology operating at 200 kV. The elemental maps were obtained by energy dispersive X-ray spectroscopy using the Super-X detector on the Titan with a probe size of  $\sim 1$  nm and a probe current of  $\sim 0.4$  nA. X-ray powder diffraction (XRD) analysis was performed on an X-ray diffractometer (Bruker D8 Advance) using Cu K $\alpha$  radiation at 40 kV and 30 mA. The BET specific surface area and single-point pore volume were obtained from nitrogen adsorption isotherms measured at  $-196$  °C using a gas sorption instrument (Micromeritics TriStar II Surface Area and Porosity Analyzer). Prior to nitrogen adsorption measurements, the samples were degassed at  $250$  °C overnight. X-ray photoelectron spectroscopy (XPS) measurements were performed on a Kratos Axis Ultra DLD spectrometer using a monochromatic AlK $\alpha$  (1486.6 eV) irradiation source operated at 150 W. The vacuum pressure of the analysis chamber of the spectrometer was maintained a  $5 \times 10^{-11}$  Torr or lower during analysis. The electron binding energy scale was calibrated for each sample by setting the main line of the C 1s spectrum to 284.5 eV. The XPS spectra were collected with a pass energy of 160 eV for the survey spectra and 40 eV for the high-resolution spectra. Data files were processed using CasaXPS software and interpreted using relative sensitivity factors provided by the instrument manufacturer (Kratos) as a guide. Background subtractions using a Shirley background were applied to all high-resolution spectra. Each high-resolution spectra were fitted with a Gaussian-Lorentzian (70%-30%) line shape with the full-width half maximum (FWHM) constrained to values considered reasonable for each element. In the case of the Fe 2p spectra, for which the interpretation of Fe oxidation states is known to be complicated by complex multiplet splitting, a simplified approach was used to obtain the approximate Fe<sup>2+</sup>/Fe<sup>3+</sup> ratios. Briefly, the broad peak shapes were used to quantify Fe<sup>2+</sup> and Fe<sup>3+</sup> components, with the shake-up satellites used as approximate guides for the positioning of the main 2p peaks.

### 4.3 Results and discussion

The proposed synthetic strategy for the preparation of core-shell and yolk-shell structured  $\text{Fe}_3\text{O}_4$ @carbon microboxes is illustrated in **Scheme 4.1**. Firstly, uniform  $\text{Fe}_2\text{O}_3$  microcubes were coated with aminophenol resin polymer to obtain  $\text{Fe}_2\text{O}_3$ @polymer core-shell structures. In the subsequent step, this structure can be converted into core-shell and yolk-shell structured  $\text{Fe}_3\text{O}_4$ @carbon and hollow carbon cages under  $\text{N}_2$  atmosphere through varying the calcination temperature. A co-precipitation method was used to synthesize the uniform  $\text{Fe}_2\text{O}_3$  microcubes with an average size of about 650 nm and rough surface (**Figure 4.1a-4.1b**), which is also confirmed by TEM imaging (**Figure 4.1c and 4.1d**). Then, the as-synthesized  $\text{Fe}_2\text{O}_3$  microcubes were successfully coated with a uniform and smooth layer (**Figure 4.1e and 4.1f**) of aminophenol resin polymer (APF) with a thickness of around 23 nm as shown in **Figure 4.1g-4.1h**.

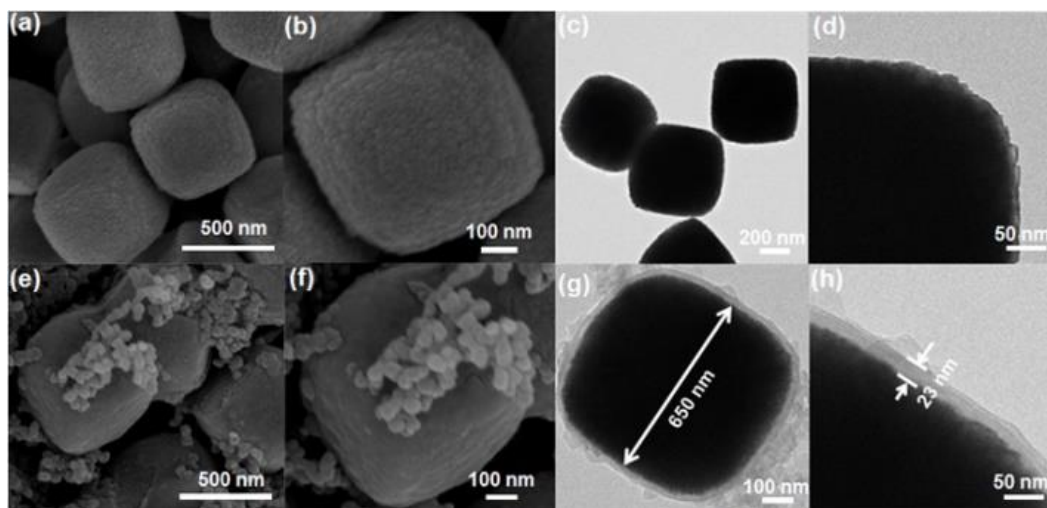


**Figure 4.1.** SEM images (a)(b) and TEM images (c)(d) of  $\text{Fe}_2\text{O}_3$  cubes, SEM images (e)(f) and TEM images (g)(h) of FP-23.

In the next step, these core-shell structured FP-23 nanoparticles were transformed into  $\text{Fe}_3\text{O}_4$ @carbon core-shell structures after carbonization in  $\text{N}_2$  atmosphere in  $500^\circ\text{C}$ , as shown in **Figure 4.2a-4.2d**. FC-23-500 nanoparticles present a core-shell structure with

carbon shell thickness of about 15 nm. After elevating temperature to 700 °C, hollow voids were created between the carbon shells and Fe<sub>3</sub>O<sub>4</sub> cores (as shown in **Figure 4.2e and 4.2f**). It also can be easily observed that some small impurities decorated on the surface of FC-23-700 nanoparticles are carbon nanospheres, which are derived from the side reaction of resin self-polymerization during the Stöber coating procedures. The TEM images of FC-23-700 in **Figure 4.2g and 4.2h** also confirm the formation of yolk-shell structures with shell thickness of about 12 nm. This indicates that by increasing temperature to 700 °C the core material is gradually released from the carbon shells to form large internal voids between the cores and carbon shells, which results in converting the core-shell structure of FC-23-500 to the yolk-shell structure of FC-23-700. The resulting yolk-shell structure of Fe<sub>3</sub>O<sub>4</sub>@carbon-23-700 was further examined by investigating elemental distribution through scanning transmission electron microscope (STEM) and the corresponding energy dispersive X-ray spectroscopy (EDS) mapping, as shown in **Figure 4.2i**. As can be seen the elemental iron is well distributed in the core and carbon element is uniformly distributed on the entire carbon box, further supporting that the formation of yolk shell structures.

Hollow carbon boxes with shell thickness of about 8 nm (**Figure 4.2j**) can be achieved after elevating temperature to 900°C, indicating that all the core material is escaped from carbon shells. This can be attributed to in situ reduction-carbonization of Fe<sub>2</sub>O<sub>3</sub> cubes coated with nitrogen-doped carbon at high temperatures causing iron escape from carbon shells. Scanning transmission electron microscope (STEM) and the corresponding energy dispersive X-ray spectroscopy (EDS) mapping was used to investigate the distribution of each element. As can be seen from **Figure 4.2k** for FC-23-900, the carbon, nitrogen and oxygen atoms are homogeneously distributed in the carbon box framework. Moreover, all the irons escaped from carbon boxes and only a small amount of iron can be found on the outer layers of carbon boxes.

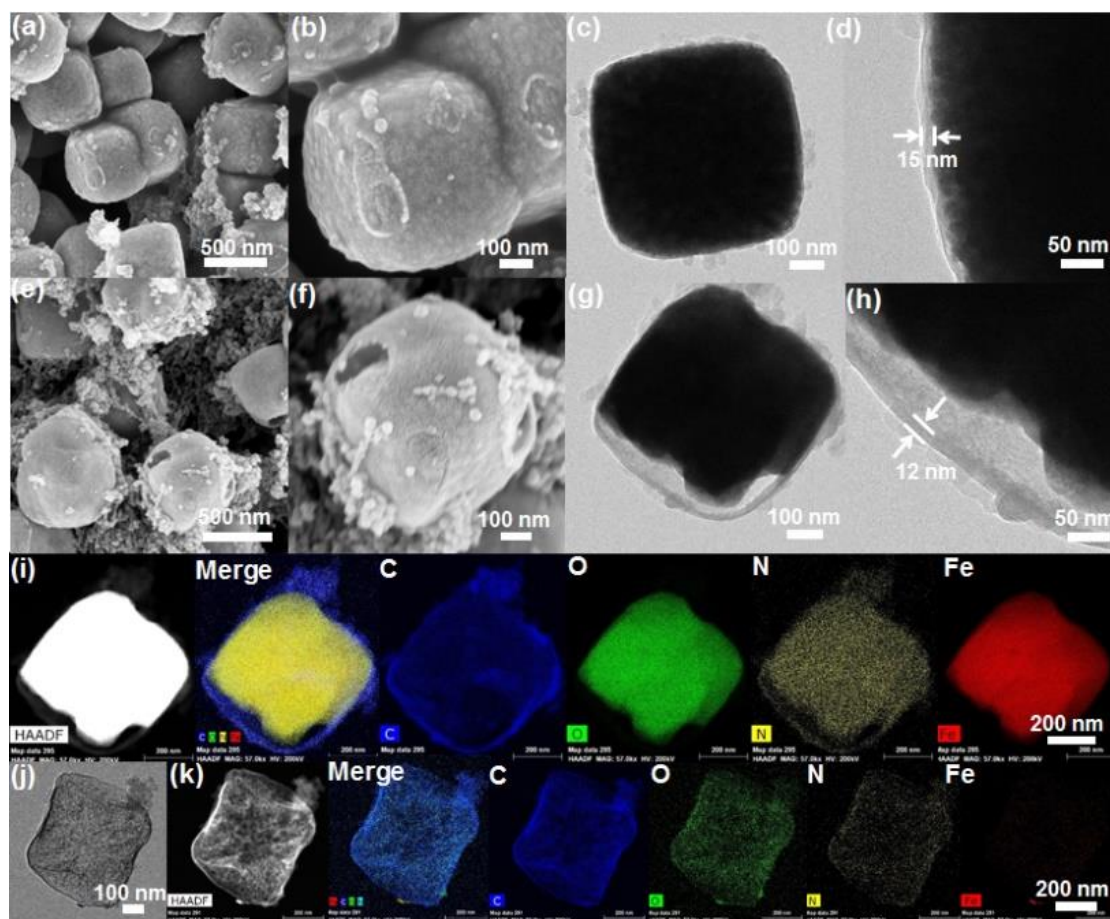


**Figure 4.2.** SEM images (a)(b) and TEM images (c)(d) of FC-23-500; SEM images (e)(f) and TEM images (g)(h), HAADF image, STEM and EDS elemental mapping (i) of FC-23-700; TEM images (j), HAADF image, STEM and EDS mapping (k) of FC-23-900.

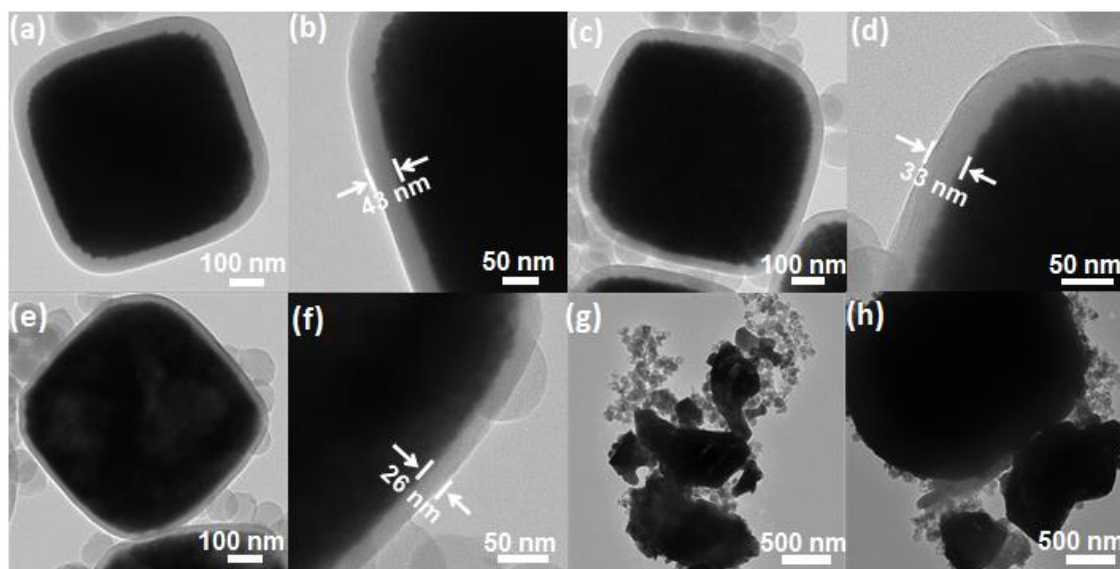


**Figure 4.3.** TEM images of FP-43 (a)(b), FC-43-500 (c)(d), FC-43-700 (e)(f) and FC-43-900 (g)(h).

It is also worth mentioning that the structure parameters of the obtained  $\text{Fe}_2\text{O}_3$ @polymer core-shell structures are highly tuneable. As one of the advantages of the RF coating strategy, the thickness of aminophenol resin polymer can be adjusted from 10 to 233 nm by controlling the amount of aminophenol and formaldehyde while keeping other synthetic parameters unchanged. After calcination of FP-43 with the shell thick of 43 nm (**Figure 4.3a** and **4.3b**) in nitrogen atmosphere at 500 and 700 °C, the carbon shell of the obtained FC-43-500 shrank to 33 nm (**Figure 4.3c** and **4.3d**) and 26 nm (**Figure 4.3e** and **4.3f**), respectively. Elevating the calcination temperature to 900 °C results in the release of elemental iron from the core and the damage of the core-shell structure, as shown in **Figure 4.1g** and **4.1h**. A similar phenomenon is also observed when the thickness of aminophenol polymer is increased to 233 nm, as shown in **Figure 4.4**. Moreover, the thickness of carbon layer decreases to 152 nm and 110 nm with increasing temperature to 500°C and 700°C, respectively. Higher calcination temperature at 900 °C results in the collapse of core-shell structure. However, after coating a polymer layer of about 10 nm on the core surface (**Figure 4.5a** and **4.5b**) and carbonizing it at 500°C (**Figure 4.5c** and **4.5d**) and 700°C (**Figure 4.5e** and **4.5f**), only

bulk composite materials with carbon nanoparticles present on the surface are formed because the core  $\text{Fe}_2\text{O}_3$  materials expand and their confinement within thin carbon shell is extremely difficult.

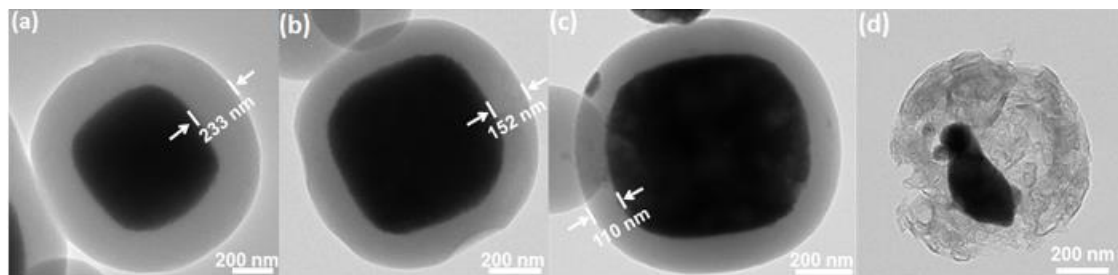


**Figure 4.4.** TEM images of FP-233 (a), FC-223-500 (b), FC-43-700 (c) and FC-43-900 (d).

The crystal structure and composition of FC nanoparticles was studied by the XRD analysis as shown in **Figure 4.2** and **Figure 4.3**. The complex XRD patterns at different calcination temperatures reflect the structural transformation from core-shell to yolk-shell and hollow carbon structures. Both XRD patterns of FC-23-500 and FC-43-500 (**Figure 4.6**) exhibit the typical peaks of  $\text{Fe}_3\text{O}_4$  (JCPD No. 65-3107) and no additional peaks are found, revealing that  $\text{Fe}_2\text{O}_3$  core materials are totally converted into  $\text{Fe}_3\text{O}_4$ . When the carbonization temperature goes to  $700^\circ\text{C}$ , new phase  $\text{Fe}_3\text{C}$  (JCPDS No. 89-2867) appears in FC-23-700 and FC-43-700. This indicates that  $\text{Fe}_2\text{O}_3$  cubes are simultaneously reduced by a carbon precursor and finally converted to metallic iron, which can fuse and escape from the relatively thin carbon shell. Increasing the carbonization temperature to  $900^\circ\text{C}$  results in the formation of metallic iron in FC-23-900. However, as compared with FC-23-900, the XRD pattern of FC-43-900 shows additional peaks, which can be ascribed to  $\text{Fe}_3\text{C}$  and  $\text{Fe}_3\text{O}_4$ . This is probably due to the fact that the relatively thick polymer coating impedes the heat transfer from the carbon shell to the core material and further restricts the reduction ability of the carbon layer.

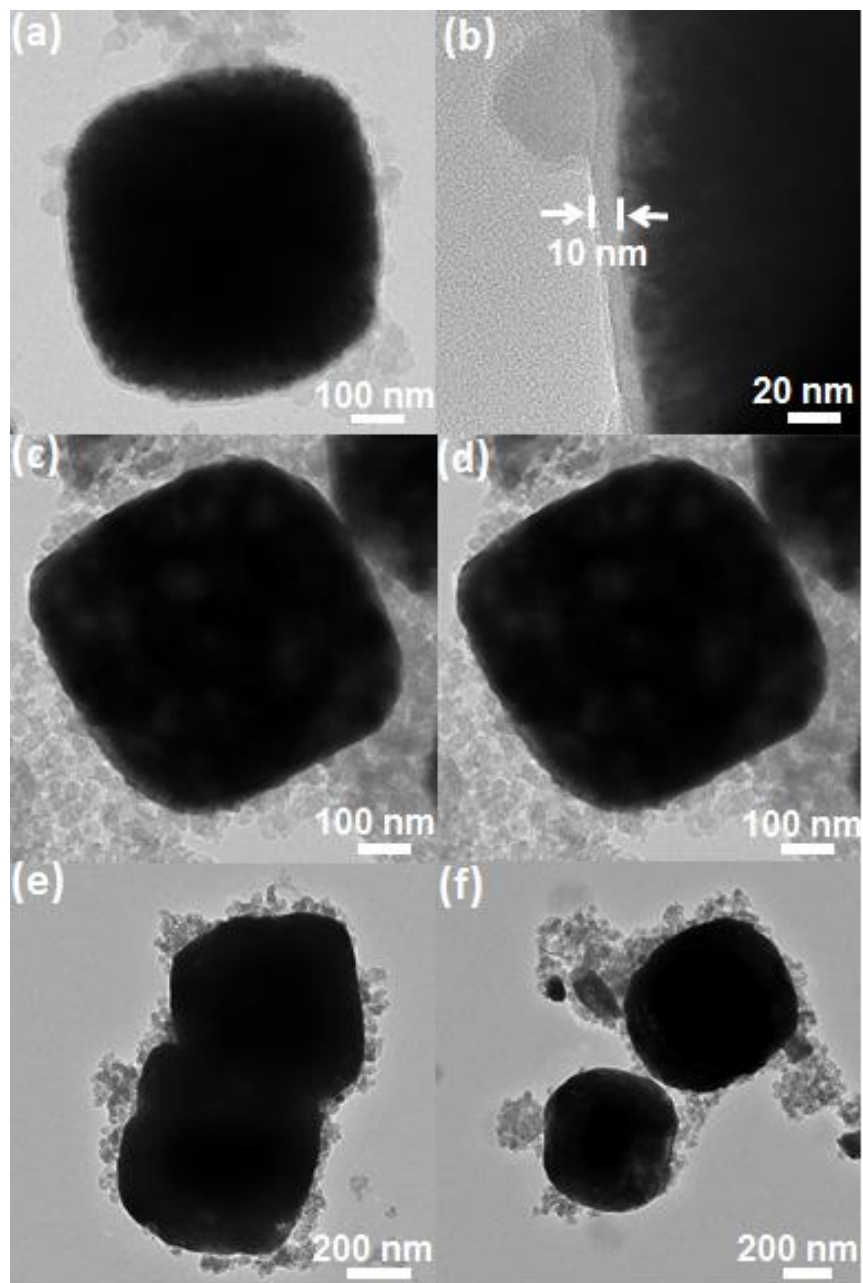


**Figure 4.5.** TEM images of FP-10 (a)(b), FC-10-500 (c)(d) and FC-10-700 (e)(f).

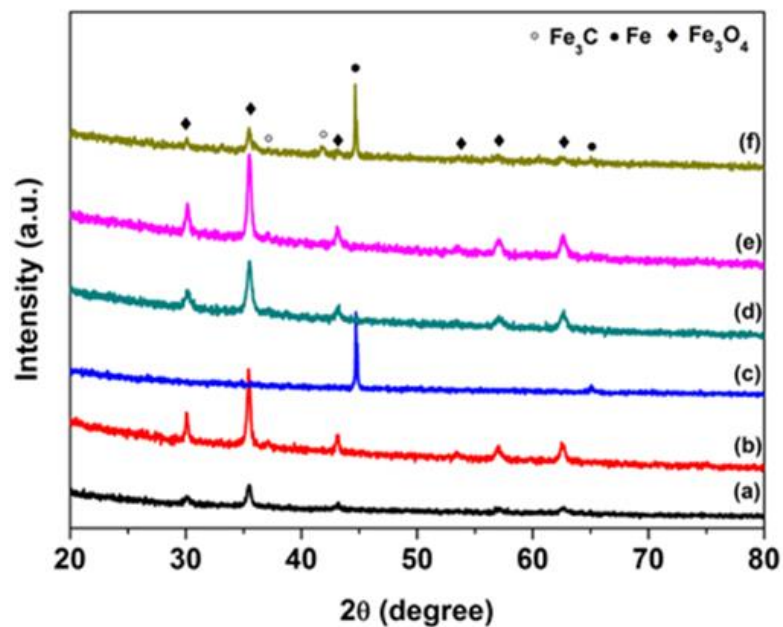


**Figure 4.6.** XRD patterns of FC-23-500 (a), FC-23-700 (b), FC-23-900(c), FC-43-500 (d), FC-43-700 (e) and FC-43-900 (f).

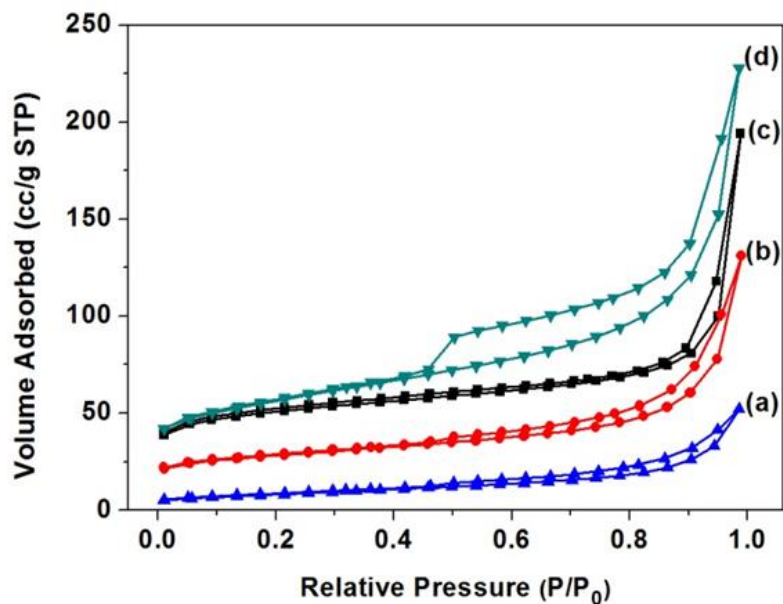


**Figure 4.7.** N<sub>2</sub> adsorption-desorption isotherms and of (a) FC-23-900; (b) FC-23-700; (c) FC-23-500; (d) FC-43-700.

The surface areas of FC-23-500, FC-23-700, FC-23-900 and FC-43-700 are determined by nitrogen adsorption measurements and the results are shown in **Figure 4.7** and **Table 4.1**. As shown in **Figure 4a**, the nitrogen adsorption isotherms of four samples are type IV with a distinct hysteresis loop, indicating the presence of mesopores.<sup>52</sup> Note that these isotherms show a rapid increase in the adsorbed volume at the relative pressures close to one, which is characteristic for type II isotherms observed for nonporous and macroporous materials. As presented in Table S1, the Brunauer–Emmett–Teller (BET) surface area and the pore volume obtained on the basis of the adsorption isotherm for FC-23-500 are  $156 \text{ m}^2 \text{ g}^{-1}$  and  $0.3 \text{ cm}^3 \text{ g}^{-1}$ , respectively. As the calcination temperature increases to 700 and 900 °C, the BET surface area and pore volume decrease respectively to  $90 \text{ m}^2 \text{ g}^{-1}$  and  $0.2 \text{ cm}^3 \text{ g}^{-1}$  for FC-23-700, and  $30 \text{ m}^2 \text{ g}^{-1}$  and  $0.08 \text{ cm}^3 \text{ g}^{-1}$  for FC-23-900, which is probably due to the change of microstructure, increased crystallinity and iron particle sintering and agglomeration.<sup>53</sup> After increasing carbon layer thickness, the FC-43-500 nanoparticles show higher BET surface area and higher pore volume ( $184 \text{ m}^2 \text{ g}^{-1}$  and  $0.35 \text{ cm}^3 \text{ g}^{-1}$ ) than FC-23-500 because of the larger amount of carbon in FC-43-500 nanoparticles, and consequently larger amount of fine pores in the carbon shells.

**Table 4.1.** Physical properties of FC.

Sample	BET surface area ( $\text{m}^2/\text{g}$ ) <sup>a</sup>	Pore volume ( $\text{cm}^3/\text{g}$ ) <sup>b</sup>	Layer thickness(nm) <sup>c</sup>
FC-23-500	156	0.30	15
FC-23-700	90	0.21	12
FC-23-900	30	0.08	8
FC-43-700	184	0.35	26

<sup>a</sup> Specific surface area was calculated by the BET method. <sup>b</sup> The pore volume was evaluated by using the adsorption value at  $P/P_0 \sim 0.99$ . <sup>c</sup> The mean layer thickness was estimated by TEM analysis.

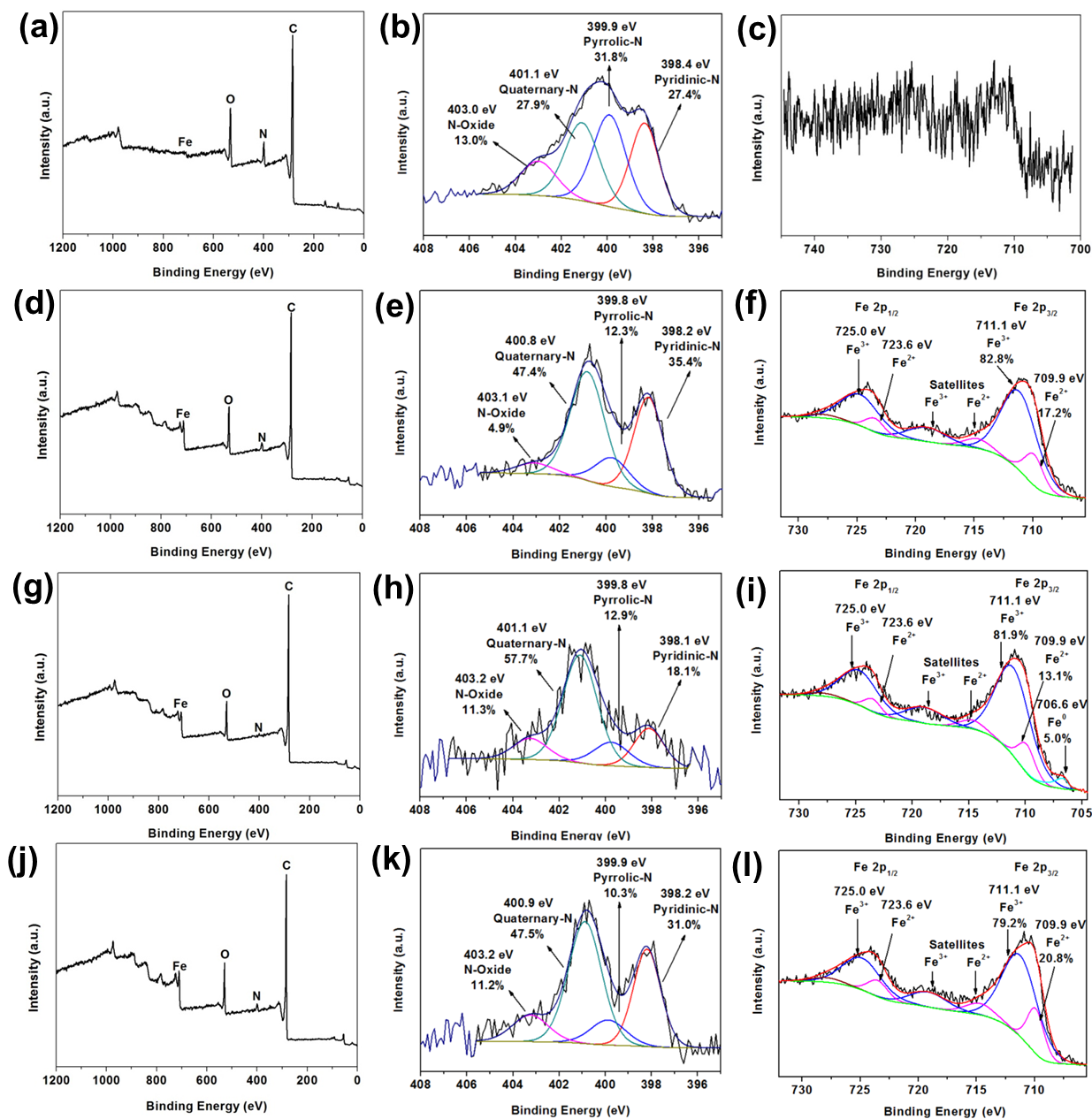


**Figure 4.8.** Survey XPS spectra (a)(d)(g)(j), high resolution N 1s XPS spectra (b)(e)(h)(k), high resolution Fe 2p XPS spectra (c)(f)(i)(l) of FC-23-500, FC-23-700, FC-23-900 and FC-43-700, respectively.

**Figures 4.8** illustrate the X-ray photoelectron spectroscopy (XPS) survey spectra of FC-23-500, FC-23-700, FC-23-900 and FC-43-700 with the corresponding high resolution spectra of N 1s and Fe 2p, respectively. As shown in **Figure 4.8a**, only trace amount of Fe can be detected (about 0.1 at.%; **Table 4.2**), indicating that nearly all Fe<sub>3</sub>O<sub>4</sub> nanoparticles are successfully embedded in carbon boxes. The XPS high resolution narrow scan (**Figure 4.8b**) presents four overlapping N1s peaks corresponding to pyridinic nitrogen (398.4 eV), pyrrolic nitrogen (399.9 eV), quaternary nitrogen (401.1 eV), and pyridine-oxide (403.0 eV)<sup>54</sup> with the relative concentration of about 27.4%, 31.8%, 27.9% and 13.0%, respectively (**Table 4.3**). Similarly, the Fe2p peak (**Figure 4.8c**) is very weak after carbonization. The XPS survey spectra in **Figure 4.8d, 4.8g and 4.8j** confirm also the presence of C, N, Fe, and O elements in the nanoparticles studied. The deconvoluted Fe 2p<sub>3/2</sub> spectra are presented in **Figures 4.8f, 4.8i and 4.8l**. As expected, a mixture of Fe<sup>2+</sup> and Fe<sup>3+</sup> can be observed across all samples which is consistent with the presence of Fe<sub>3</sub>O<sub>4</sub>. However, the ratios of Fe<sup>2+</sup>: Fe<sup>3+</sup> are somewhat lower than expected, which suggests the coexistence of Fe<sub>2</sub>O<sub>3</sub>. While the XRD analysis (**Figure 4.6**) shows only the presence of Fe<sub>3</sub>O<sub>4</sub>, the XRD and XPS patterns are very different. The XRD technique probes the bulk, while XPS probes only the top few nanometers of the samples surface (typically 2-5 nm). Hence, the discrepancy between the XRD and XPS results is not surprising as it is entirely possible that Fe<sub>2</sub>O<sub>3</sub> is only present on the surface, while the bulk of nanoparticles contains predominantly Fe<sub>3</sub>O<sub>4</sub>. The surface sensitivity of XPS is also an important factor that indicates that iron nanoparticles can be leached out of the carbon boxes, as confirmed by TEM images and XRD results, because photoelectrons emitted from any material within the box would be severely attenuated by the thickness of the carbon layer. In other words, XPS is incapable of probing any material within the carbon box. The deconvoluted Fe 2p spectrum of FC-23-900 (**Figure 4.8i**), reveals also the presence of a small amount (about 5 at%) of metallic iron, which is consistent with the previously reported XRD data suggesting that iron migrates through the carbon box at higher temperatures.

**Table 4.2.** The chemical composition of FC-23-500, FC-23-700, FC-23-900 and FC-43-700 obtained by XPS analysis.

Sample	C (at.%)	N (at.%)	O (at.%)	Fe (at.%)
FC-23-500	81.5	7.4	11.0	0.1
FC-23-700	85.2	3.6	9.4	1.8
FC-23-900	89.1	1.1	8.0	1.8
FC-43-700	85.4	3.0	9.3	2.3

**Table 4.3.** The atomic percentage of pyridinic N, pyrrolic N, quaternary N and oxidized N of FC-23-500, FC-23-700, FC-23-900 and FC-43-700 obtained on the basis of high resolution N 1s XPS spectra.

Sample	Pyridinic N (at.%)	Pyrrolic N (at.%)	Quaternary N (at.%)	Oxidized N (at.%)
FC-23-500	27.4	31.8	27.9	13.0
FC-23-700	35.4	12.3	47.4	4.9
FC-23-900	18.1	12.9	57.7	11.3
FC-43-700	31.0	10.3	47.5	11.2

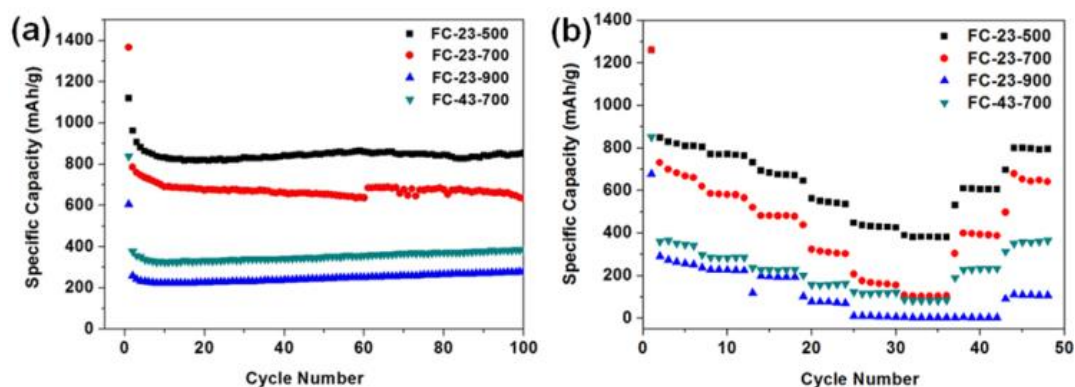


**Figure 4.9.** (a) Discharge capacity versus cycle number plots of FC-23-500, FC-23-700, FC-23-900 and FC-43-700 measured at a current density of  $0.1 \text{ Ag}^{-1}$ , (b) the rate capability of FC-23-500, FC-23-900 and FC-43-700 at different current densities between  $0.1$  and  $5 \text{ Ag}^{-1}$ .

**Figure 4.9a** shows the cycling performance of as-prepared anode materials for lithium ion batteries at low current density of  $0.1 \text{ Ag}^{-1}$ . Noticeably, FC-23-500 exhibits the best electrochemical performance, regarding both the specific capacity and retention. The initial specific discharge capacity of FC-23-500 is  $1120 \text{ mAh/g}$ , with a Coulombic efficiency of 86% (**Figure 4.10**). The excess of theoretical capacity in initial cycle is attributed to the irreversible capacity related to the decomposition of electrolyte to form a solid electrolyte interface (SEI) layer. High capacities of  $869 \text{ mAhg}^{-1}$  and  $857 \text{ mAh g}^{-1}$  after 50 and 100 cycles can be achieved, respectively, indicating an excellent capacity retention of FC-23-500. In contrast, FC-23-700 exhibits an initial discharge capacity of  $1366 \text{ mAh g}^{-1}$  and a lower Coulombic efficiency of 58%. The discharge capacity of FC-23-700 after 100 cycles is  $623 \text{ mAh g}^{-1}$ , which corresponds to 45.6% of its initial capacity. The FC-23-900 material has a low initial specific capacity of  $605 \text{ mAh g}^{-1}$ , owing to the low content of active material (iron oxide) in the composite. The discharge capacity of FC-23-900 after 100 cycles is only  $280 \text{ mAh g}^{-1}$ , demonstrating at this stage its unsuitability for practical applications in lithium ion batteries. The electrochemical performance of FC-43-700 was also investigated to compare the effect of coating thickness. It is obvious that the material with higher carbon content (FC-43-700) displays lower specific capacity, retaining  $351 \text{ mAhg}^{-1}$  after 50 cycles and  $380 \text{ mAhg}^{-1}$  after 100 cycles.

**Figure 4.9b** shows the rate capability of the FC-23-500, FC-23-700, FC-23-900 and FC-43-700 samples evaluated at the current densities in the range of  $0.1\text{--}5 \text{ Ag}^{-1}$ . The discharge capacity of the core-shell structured FC-23-500 remains at  $804, 759, 674, 527, 420$  and  $384 \text{ mAh g}^{-1}$  levels at the current densities of  $0.1, 0.2, 0.5, 1, 2$  and  $5 \text{ Ag}^{-1}$ , respectively. The FC-23-500 anode exhibits an excellent rate capability because it can deliver a high capacity of about  $384 \text{ mAhg}^{-1}$  at a high current of  $5 \text{ Ag}^{-1}$ . After decreasing the current density to  $0.1 \text{ Ag}^{-1}$ , the discharge capacity can recover to about  $800 \text{ mAh g}^{-1}$ , implying an excellent reversibility of FC-23-500. In comparison, the FC-23-700, FC-23-900 and FC-43-700 samples deliver inferior capacities at all testing currents. They display lower discharge capacities at high rate, namely,  $108, 3$  and  $88 \text{ mAh g}^{-1}$ , respectively, at the high current of  $5 \text{ Ag}^{-1}$ .

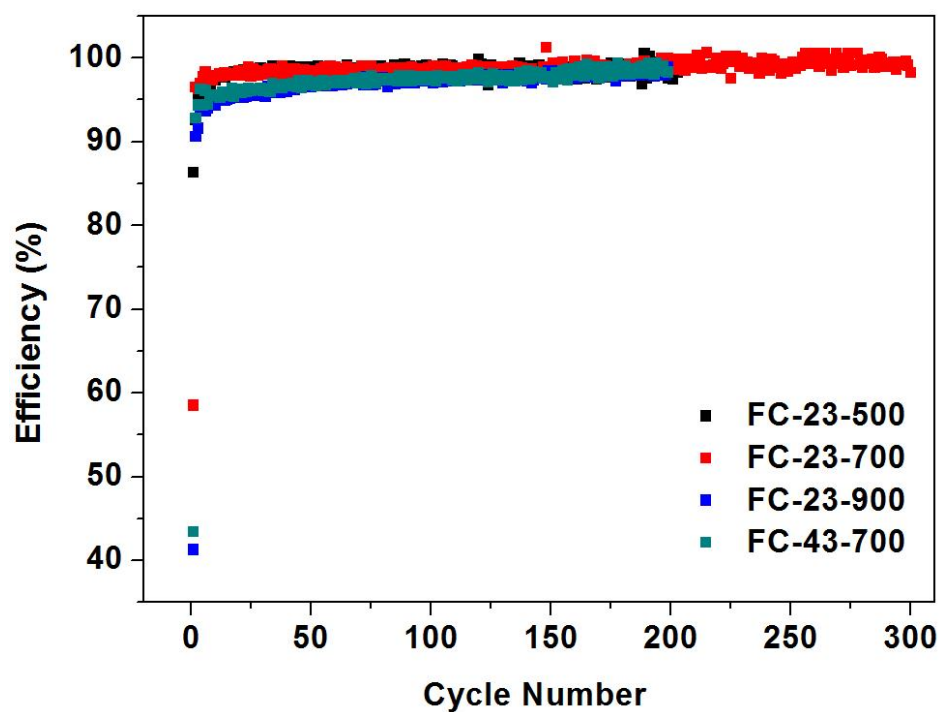


**Figure 4.10.** Coulombic efficiency curves of FC-23-500, FC-23-700, FC-23-900 and FC-43-700.

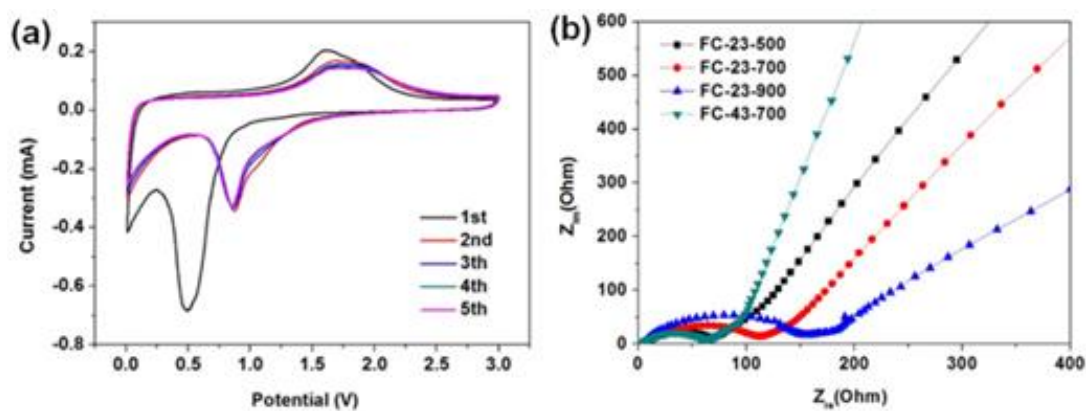


**Figure 4.11.** (a) Cyclic voltammograms of FC-23-500 at a scan rate of  $0.1 \text{ mVs}^{-1}$  between 0.01 and 3.0 V, (b) Nyquist plots of the electrodes composed of FC-23-500, FC-23-700, FC-23-900 and FC-43-700.

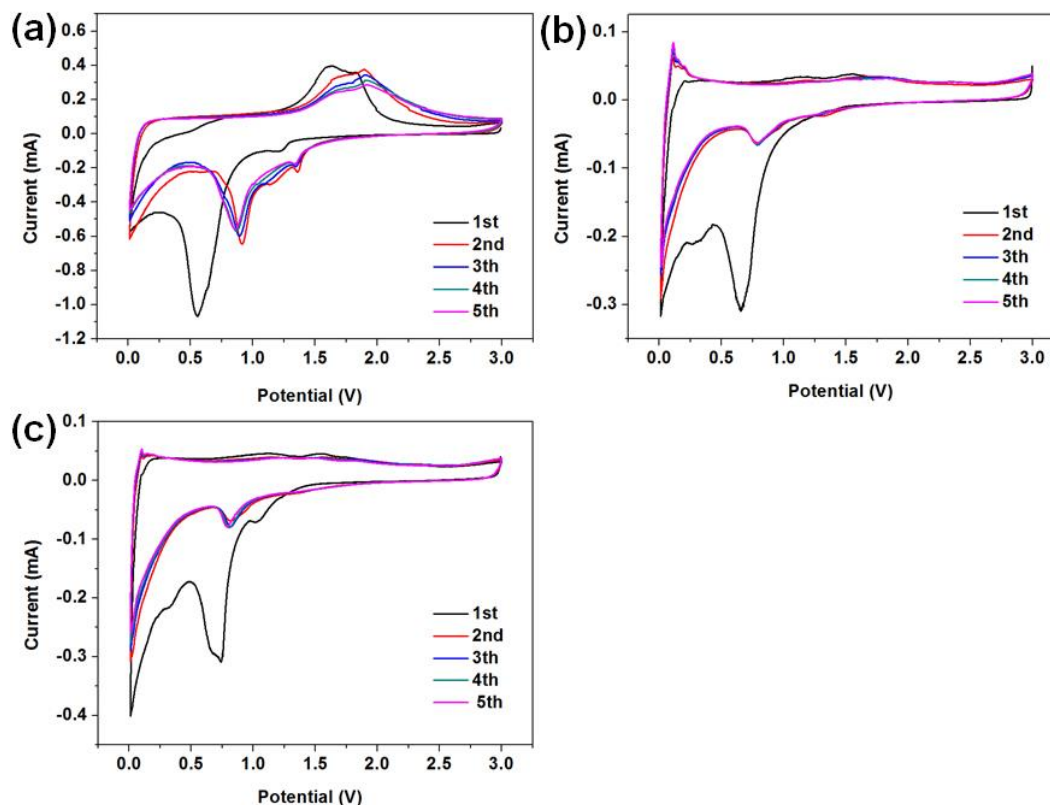


**Figure 4.12.** Cyclic voltammograms of FC-23-700 (a), FC-23-900 (b) and FC-43-700 (c) at a scan rate of  $0.1 \text{ mVs}^{-1}$  between 0.01 and 3.0 V.

**Figure 4.11a** shows the CV profile of FC-23-500 collected at a scan rate of  $0.1 \text{ mVs}^{-1}$  between 0.01 and 3.0 V. In the initial cathodic sweep, the broad peak appearing at about 0.5 V can be attributed to the reduction reaction of Fe ion to metallic Fe. In addition, this cathodic process is also associated with electrolyte decomposition to form the SEI layer and the reversible conversion reaction of lithium ion to form  $\text{Li}_2\text{O}$ . An anodic peak is present at about 1.7 V, corresponding to the reversible oxidation of Fe. In the subsequent cycles, the cathodic peak potential shifts to 0.85 V. The CV curves of FC-23-500 are identical from the second cycles, indicating high reversibility and good capacity retention. By contrast, the CV curves of other samples show either lower reactivity or worse reversibility (in **Figure 4.12**). **Figure 4.11b** shows the Nyquist plots of electrode materials measured at room temperature, which were collected by an

electrochemical impedance spectroscopy (EIS) method. All profiles represent a combination of a straight line in the low frequency region and a semicircle in the moderate frequency region. The straight line in the low frequency region implies a typical Warburg behaviour, which is related to the diffusion of lithium ions in the solid electrodes. The depressed semicircle in the moderate frequency region is attributed to the charge transfer process. The numerical value of the diameter of the semicircle on the  $Z_{re}$  axis gives an approximate indication of the charge transfer resistance ( $R_{ct}$ ). Therefore, as can be seen the trend of charge transfer resistance is in the following order: FC-23-500 < FC-23-700 < FC-23-900.

The above electrochemical data indicate that the core-shell structured FC-23-500 shows the best overall performance in terms of the specific capacity, long term retention and high rate performance. The significantly enhanced electrochemical performance of FC-23-500 can be attributed to the unique core-shell structure ensuring sufficient electrolyte/electrode contact area, strengthened structure over long term electrochemical processes and high dynamics for lithium diffusion. The FC-23-700 sample showed lower specific capacity, larger irreversible capacity and worse retention due to the fragmentation of outer carbon shells, causing inferior structural stability and additional side reaction during SEI formation. During the cycling, the broken outer carbon shells (**Figure 4.2f**) were unable to protect  $Fe_3O_4$  nanoparticles, which can leach out from these shells after long term cycling. The FC-23-900 material showed the lowest capacity, owing to the low content of active material (iron oxide) in the composite. Analysis of CV and EIS data demonstrate the same trend in the reactivity, reversibility and lithium ion diffusion kinetics, expressed by the following order: FC-23-500 > FC-23-700 > FC-23-900, which is consistent with the electrochemical behaviour of these materials.

#### 4.4 Conclusions

In summary, the  $Fe_3O_4$ -carbon composites with core-shell, yolk-shell and hollow microboxes were facilely synthesized by polymer coating of  $Fe_3O_4$  microboxes followed by carbonization at different temperatures. The core-shell structured  $Fe_3O_4$ -

carbon composites (FC-23-500) possess high specific surface area of  $156 \text{ m}^2 \text{ g}^{-1}$ , large pore volume of  $0.3 \text{ cm}^3 \text{ g}^{-1}$ , and the well-defined cube-like structure uniformly wrapped by N-doped carbon layer. The yolk-shell structured and hollow  $\text{Fe}_3\text{O}_4$ -carbon composites can only be achieved when the polymer thickness exceeding 23 nm. This study shows an excellent performance of these materials in lithium ion batteries. The core-shell structured FC-23-500 electrode delivers highly reversible capacity of  $857 \text{ mAh g}^{-1}$  at the current density of  $0.1 \text{ A g}^{-1}$  after 100 cycles. Moreover, this electrode showed a superior high-rate capability and achieved the reversible capacity of  $384 \text{ mAh g}^{-1}$  at the current density of  $5 \text{ A g}^{-1}$ . Due to an inadequate protective carbon shell and  $\text{Fe}_3\text{O}_4$  leaching out of the carbon shells, an inferior cycle performance and rate capability are observed when the yolk-shell and hollow nanoparticles are used as the electrodes. A great performance of the core-shell  $\text{Fe}_3\text{O}_4$ -carbon structures proves the importance of rational design and fabrication of core-shell particles with tunable structures, multi-chemical composition and improved functionalities.

#### 4.5 References

1. J. M. Tarascon and M. Armand, *Nature*, 2001, **414**, 359-367.
2. Y. Idota, T. Kubota, A. Matsufuji, Y. Maekawa and T. Miyasaka, *Science*, 1997, **276**, 1395-1397.
3. K. T. Nam, D. W. Kim, P. J. Yoo, C. Y. Chiang, N. Meethong, P. T. Hammond, Y. M. Chiang and A. M. Belcher, *Science*, 2006, **312**, 885-888.
4. G. Zhou, D. W. Wang, F. Li, L. Zhang, N. Li, Z. S. Wu, L. Wen, G. Q. Lu and H.-M. Cheng, *Chem. Mater.*, 2010, **22**, 5306-5313.
5. W. M. Zhang, X. L. Wu, J. S. Hu, Y. G. Guo and L. J. Wan, *Adv. Funct. Mater.*, 2008, **18**, 3941-3946.
6. S. H. Lee, S.-H. Yu, J. E. Lee, A. Jin, D. J. Lee, N. Lee, H. Jo, K. Shin, T. Y. Ahn, Y. W. Kim, H. Choe, Y. E. Sung and T. Hyeon, *Nano Lett.*, 2013, **13**, 4249-4256.
7. F.-X. Ma, H. Hu, H. B. Wu, C.-Y. Xu, Z. Xu, L. Zhen and X. W. Lou, *Adv. Mater.*, 2015, **27**, 4097-4101.
8. X. W. Lou, L. A. Archer and Z. C. Yang, *Adv. Mater.*, 2008, **20**, 3987-4019.

9. J. Liu, S. Z. Qiao, J. S. Chen, X. W. Lou, X. R. Xing and G. Q. Lu, *Chem. Commun.*, 2011, **47**, 12578-12591.
10. J. Liu, N. P. Wickramaratne, S. Z. Qiao and M. Jaroniec, *Nat. Mater.*, 2015, **14**, 763-774.
11. S. Xu, C. M. Hessel, H. Ren, R. Yu, Q. Jin, M. Yang, H. Zhao and D. Wang, *Energy Environ. Sci.*, 2014, **7**, 632-637.
12. J. Qi, X. Lai, J. Wang, H. Tang, H. Ren, Y. Yang, Q. Jin, L. Zhang, R. Yu, G. Ma, Z. Su, H. Zhao and D. Wang, *Chem. Soc. Rev.*, 2015, **44**, 6749-6773.
13. X. Lai, J. E. Halpert and D. Wang, *Energy Environ. Sci.*, 2012, **5**, 5604-5618.
14. J. Wang, N. Yang, H. Tang, Z. Dong, Q. Jin, M. Yang, D. Kisailus, H. Zhao, Z. Tang and D. Wang, *Angew. Chem. Int. Ed.*, 2013, **52**, 6417-6420.
15. H. Ren, R. Yu, J. Wang, Q. Jin, M. Yang, D. Mao, D. Kisailus, H. Zhao and D. Wang, *Nano Lett.*, 2014, **14**, 6679-6684.
16. J. Wang, H. Tang, L. Zhang, H. Ren, R. Yu, Q. Jin, J. Qi, D. Mao, M. Yang, Y. Wang, P. Liu, Y. Zhang, Y. Wen, L. Gu, G. Ma, Z. Su, Z. Tang, H. Zhao and D. Wang, *Nature Energy*, 2016, **1**, 16050-16058.
17. F. Wang, J. Wang, H. Ren, H. Tang, R. Yu and D. Wang, *Inorg. Chem. Front.*, 2016, **3**, 365-369.
18. H. Ren, J. Sun, R. Yu, M. Yang, L. Gu, P. Liu, H. Zhao, D. Kisailus and D. Wang, *Chem. Sci.*, 2016, **7**, 793-798.
19. J. Wang, H. Tang, H. Wang, R. Yu and D. Wang, *Inorg. Chem. Front.*, 2017, DOI: 10.1039/c6qm00273k.
20. L. Yu, H. B. Wu and X. W. D. Lou, *Acc. Chem. Res.*, 2017, **50**, 293-301.
21. L. Yu, H. Hu, H. B. Wu and X. W. Lou, *Adv. Mater.*, 2017, DOI: 10.1002/adma.201604563, 1604563-1604602.
22. Z. Li, H. B. Wu and X. W. Lou, *Energy Environ. Sci.*, 2016, **9**, 3061-3070.
23. Y. Boyjoo, M. Wang, V. K. Pareek, J. Liu and M. Jaroniec, *Chem. Soc. Rev.*, 2016, **45**, 6013-6047.
24. Y. Zhao, L. P. Wang, M. T. Sougrati, Z. Feng, Y. Leconte, A. Fisher, M. Srinivasan and Z. Xu, *Adv. Energy Mater.*, 2017, DOI: 10.1002/aenm.201601424, 1601424-1601494.

25. J. Lian, X. Duan, J. Ma, P. Peng, T. Kim and W. Zheng, *ACS nano*, **3**, 3749-3761.
26. Y. Cai, X. Li, L. Wang, H. Gao, Y. Zhao and J. Ma, *J. Mater. Chem. A*, 2015, **3**, 1396-1399.
27. X. Li, J. Xu, Z. Zhang, L. Mei, C. Cui, H. K. Liu and J. Ma, *J. Mater. Chem. A*, 2015, **3**, 3257-3260.
28. Lei Wang, Shuo Dou, Jiantie Xu, Hua Kun Liu, Shuangyin Wang, Jianmin Ma and Shi Xue Dou, *Chem. Commun.*, 2015, **51**, 11791-11794.
29. L. Zhang, H. B. Wu and X. W. Lou, *Adv. Energy Mater.*, 2014, **4**, 1300958.
30. J. Liu and D. Xue, *Nanoscale Res. Lett.*, 2010, **5**, 1525-1534.
31. N. Liu, H. Wu, M. T. McDowell, Y. Yao, C. Wang and Y. Cui, *Nano Lett.*, 2012, **12**, 3315-3321.
32. Y. Zhao, X. Li, J. Liu, C. Wang, Y. Zhao and G. Yue, *ACS Appl. Mater. Interfaces.*, 2016, **8**, 6472-6480.
33. S. Li, J. Niu, Y. C. Zhao, K. P. So, C. Wang, C. A. Wang and J. Li, *Nat. Commun.*, 2015, **6**, 7872-7878.
34. Z. W. Seh, W. Li, J. J. Cha, G. Zheng, Y. Yang, M. T. McDowell, P.-C. Hsu and Y. Cui, *Nat. Commun.*, 2013, **4**, 1331-1336.
35. A. H. Lu, X. Q. Zhang, Q. Sun, Y. Zhang, Q. W. Song, F. Schüth, C. Y. Chen and F. Cheng, *Nano Res.*, 2016, **9**, 1460-1469.
36. J. Liu, H. Q. Yang, F. Kleitz, Z. G. Chen, T. Y. Yang, E. Strounina, G. Q. Lu and S. Z. Qiao, *Adv. Funct. Mater.*, 2012, **22**, 591-599.
37. J. Liu, T. Y. Yang, D. W. Wang, G. Q. M. Lu, D. Y. Zhao and S. Z. Qiao, *Nat. Commun.*, 2013, **4**, 2798-2804.
38. H. Tian, M. Saunders, A. Dodd, K. O'Donnell, M. Jaroniec, S. Liu and J. Liu, *J. Mater. Chem. A*, 2016, **4**, 3721-3727.
39. J. Zhang, H. Hu, Z. Li and X. W. Lou, *Angew. Chem. Int. Ed.*, 2016, **55**, 3982-3986.
40. Z. G. Teng, X. D. So, Y. Y. Zheng, J. J. Zhang, Y. Liu, S. J. Wang, J. Wu, G. T. Chen, J. D. Wang, D. Y. Zhao and G. M. Lu, *J. Am. Chem. Soc.*, 2015, **137**, 7935-7944.
41. T. Yang, J. Liu, R. Zhou, Z. Chen, H. Xu, S. Z. Qiao and M. J. Monteiro, *J. Mater. Chem. A*, 2014, **2**, 18139-18146.

42. T. Yang, R. Zhou, D.-W. Wang, S. P. Jiang, Y. Yamauchi, S. Z. Qiao, M. J. Monteiro and J. Liu, *Chem. Commun.*, 2015, **51**, 2518-2521.
43. J. Liu, S. Z. Qiao, S. B. Hartono and G. Q. Lu, *Angew. Chem. Int. Edit.*, 2010, **49**, 4981-4985.
44. T. Yang, J. Liu, Y. Zheng, M. J. Monteiro and S. Z. Qiao, *Chem. Eur. J.*, 2013, **19**, 6942-6945.
45. J. Tang, J. Liu, C. Li, Y. Li, M. O. Tade, S. Dai and Y. Yamauchi, *Angew. Chem. Int. Ed.*, 2015, **54**, 588-593.
46. J. Zhang, K. Wang, Q. Xu, Y. Zhou, F. Cheng and S. Guo, *ACS Nano*, 2015, **9**, 3369-3376.
47. X.-Y. Yu, H. Hu, Y. Wang, H. Chen and X. W. Lou, *Angew. Chem. Int. Ed.*, 2015, **54**, 7395-7398.
48. Y. Dai, L. Chen, V. Babayan, Q. Cheng, P. Saha, H. Jiang and C. Li, *J. Mater. Chem. A*, 2015, **3**, 21337-21342.
49. Z. Liu, X.-Y. Yu and U. Paik, *Adv. Energy Mater.*, 2016, **6**, 1502318-1502323.
50. R. L. Liu, D. Q. Wu, X. L. Feng and K. Mullen, *Angew. Chem. Int. Ed.*, 2010, **49**, 2565-2569.
51. R. Silva, D. Voiry, M. Chhowalla and T. Asefa, *J. Am. Chem. Soc.*, 2013, **135**, 7823-7826.
52. H. Jiang, L. Yang, C. Li, C. Yan, P. S. Lee and J. Ma, *Energy Environ. Sci.*, 2011, **4**, 1813-1819.
53. K. Kiatkittipong, J. Scott and R. Amal, *ACS Appl. Mater. Interfaces*, 2011, **3**, 3988-3996.
54. X. Li, X. Pan, L. Yu, P. Ren, X. Wu, L. Sun, F. Jiao, X. Bao, *Nat. Commun.*, 2013, **5**, 3688-3695.

*Every reasonable effort has been made to acknowledge the owners of copyright material. I would be pleased to hear from any copyright owner who has been omitted or incorrectly acknowledged.*

---

# Chapter 5. Yolk-shell structured nanoreactors with ZnO core and microporous carbon shell

## 5.1. Introduction

Tremendous interests have been attracted on the design and fabrication of nanoparticles with desired morphologies and tailored properties.<sup>1-3</sup> Yolk-shell structured materials with tailored physical and chemical properties have showed great potentials in wide applications including catalysis, drug delivery and release, energy conversion and storage.<sup>4-8</sup> Yolk-shell nanoparticles (YSNs) with distinctive structures and tunable functionalities in both core and shell have been fabricated by selective-etching, soft-templating, Ostwald ripening, ship-in-bottle methods, galvanic-replacing and Kirkendall-effect methods.<sup>9-14</sup> However, most of the above mentioned methods involved multi-steps and it still remains an enormous challenge to engineer YSNs with different compositional, incompatible and morphological cores and shells.

As one of the presentative metal organic frameworks (MOFs), zeolite imidazolate frameworks (ZIFs) have been universally used for heterogeneous catalysts because they possess well-ordered pore size, brilliant chemical stability and well-manipulated morphologies.<sup>15-17</sup> The ZIF structure can tolerate with water, which is still a great problem for metal organic frameworks (MOFs) because of the strong coordination between the ligand and metal ions. Recent efforts have been made on fabricating YSNs based on ZIF template.<sup>18-25</sup> For examples, Li and coworkers designed and prepared hollow Zn/Co ZIF particles with superior hydrogenation activity and selectivity.<sup>24</sup> Lou et al. prepared box-in-box nanocage with improved capacitance and electrocatalytic

properties because of their unique reactivity and thermal behaviour.<sup>26</sup> However, these materials are limited to YSNs with similar compositional and morphological cores and shells and it is hard to control the shell structure and thickness. The main reason is that different materials with distinct physical and chemical properties are difficult to manipulate simultaneously during material synthesis. Besides, it is often very important to make active nanoparticles separate to preserve their chemical properties.

Herein, inspired by the extended StÖber method of synthesis colloidal polymer spheres,<sup>27</sup> we present a spontaneous phase transformation of ZIF-8@polymer core-shell structure to ZnO@polymer yolk-shell structure under mild solvent hydrothermal conditions. Coating resin polymer on the surface of ZIF-8 creates a “nanoreactor” to complete the phase transformation. Besides, this method could also be extended to control the morphology of inside ZnO core and the thickness and polymer shell. This unique synthetic strategy empowered the rational design of multifunctional catalyst with enhanced chemical properties and the void space inside the hollow shell provided enough space to host many cargos as a nanoreactor or nanocontainer for various applications.

## 5.2 Experimental section

### 5.2.1 Materials

The chemicals used in this work were provided as follows: formaldehyde (37%), ammonia solution (25%), ethanol (95-100%), 3-aminophenol (99%), methanol (99%), zinc nitrate hexahydrate ( $\text{Zn}(\text{NO}_3)_2 \cdot 6\text{H}_2\text{O}$ ) chloroplatinic acid hexahydrate ( $\text{H}_2\text{PtCl}_6 \cdot 6\text{H}_2\text{O}$ ), gold chloride trihydrate ( $\text{AuCl}_3 \cdot 3\text{H}_2\text{O}$ ), palladium chloride ( $\text{PdCl}_2$ ) and 2-methylimidazole were purchased from Sigma-Aldrich and used as received without any further purification. Reagent grade ethanol and ultrapure water were used for sample washings and solution preparations.

### 5.2.2 Synthesis of ZIF-8

Typically, 30 mL of methanol solution involving  $\text{Zn}(\text{NO}_3)_2 \cdot 6\text{H}_2\text{O}$  (0.89 g) was firstly prepared. 2-methylimidazole (1.97g) was dissolved in 20 mL of methanol and this mixture was poured into  $\text{Zn}(\text{NO}_3)_2$  solution. The mixed solution was kept stirring at room temperature for 24 h. The remaining white products were collected through centrifuging and washing with methanol a few times, and finally dried at 80 °C overnight.

### 5.2.3 Synthesis of ZnO@polymer (ZP)

Firstly, an aqueous solution containing 0.1 g CTAB, 20 mL water and 8 mL ethanol was prepared. Then, 0.2 mL aqueous solution of ammonia was added and kept stirring for 0.5 h, followed by the addition of 0.1g ZIF-8. After this mixture remained stirring for 0.5 h, 0.08 g 3-aminophenol was added into that solution. Followed by stirring for extra 30 min, 0.112 mL formaldehyde were added. Subsequently, the mixture continued stirring for 24 h at room temperature and afterwards hydrothermal treated for 24 h at 100 °C in a Teflon-lined autoclave. The remaining products were collected through centrifuging and washing and dried at 80 °C overnight. Subsequent variations to the synthesis process involved altering hydrothermal treatment time for 3h, 6h, 12h named as ZP-3h, ZP-6h and ZP-12h, hydrothermal temperature at 60 °C, 80 °C, 120 °C, 140 °C denoted as ZP-60, ZP-80, ZP-100, ZP-120 and ZP-140, and the amount of 3-aminophenol to 0.04 g and 0.12g indicated as ZP-1 and ZP-2.

### 5.2.4 Synthesis of ZnO@carbon (ZC)

The prepared ZnO@polymer composites were calcined in  $\text{N}_2$  atmosphere in a tube furnace with a ramping rate of 1 °C  $\text{min}^{-1}$  up to 350 °C, remain for 2 h, and resuming ramping rate at 1 °C  $\text{min}^{-1}$  up to 700 °C and remain for 4 h to achieve ZnO@carbon nanoparticles.

### 5.2.5 Synthesis of metal-loaded ZIF-8 (Au-ZIF-8, Pt-ZIF-8, and Pd-ZIF-8)

0.1 g ZIF-8 nanoparticles were dispersed in a solution containing  $\text{HAuCl}_4 \cdot 3\text{H}_2\text{O}$  (5.2 mg) and 1 ml methanol. Then, this suspension was sonicated for 5 mins. Followed by drying at  $100^\circ\text{C}$  for 0.5 h and 10 ml methanol was added, the mixture was sonicated for another 5 min and then a solution containing 40 mg  $\text{NaBH}_4$  and 1.0 ml methanol was quickly added to the mixture with vigorous stirring. The mixture remained stirring for extra 1.5 h. The product Au-loaded ZIF-8 (Au-ZIF-8) was collected by centrifuging and washing with ethanol several times and dried at  $100^\circ\text{C}$  overnight. The synthesis procedure of Pt-loaded ZIF-8 (Pt-ZIF-8) and Pd-loaded ZIF-8 (Pd-ZIF-8) is similar with that of Au-ZIF-8 through simply changing  $\text{HAuCl}_4 \cdot 3\text{H}_2\text{O}$  to  $\text{H}_2\text{PtCl}_6 \cdot 6\text{H}_2\text{O}$  or  $\text{Na}_2\text{PdCl}_4$  with the same addition amount.

### **5.2.6 Synthesis of metal-loaded ZnO@polymer (Au-ZnO@polymer, Pt-ZnO@polymer, and Pd-ZnO@polymer)**

Firstly, an aqueous solution containing CTAB (0.1 g), water (20 mL) and ethanol (8 mL) was prepared. Then, 0.2 mL ammonia solution was added and kept stirring for 0.5 h, followed by the addition of Au-ZIF-8. After this mixture remained stirring for 0.5 h, 0.08 g 3-aminophenol was added into that solution. Followed by stirring for extra 30 min, 0.112 mL formaldehyde were added. Subsequently, the mixture continued stirring for 24 h at room temperature and afterwards hydrothermal treated for 24 h at  $100^\circ\text{C}$  in a Teflon-lined autoclave. The remaining products were collected through centrifuging and washing and dried at  $80^\circ\text{C}$  for 24 h. The solid product (Au-ZIF-8@polymer) were recovered by centrifugation and dried at  $100^\circ\text{C}$  for 24 h. The synthesis procedure of Pt-ZIF-8@polymer, and Pd-ZIF-8@polymer is similar with that of Au-ZnO@polymer through simply changing Au-ZIF-8 to Pt-ZIF-8 or Pd-ZIF-8 with the same addition amount.

### **5.2.7 Synthesis of metal-encapsulated ZnO@carbon (Au, Pt and Pd-encapsulated ZnO@carbon)**

Metal-encapsulated ZnO@carbon were calcined in N<sub>2</sub> atmosphere in a tube furnace with a heating rate of 1 °C min<sup>-1</sup> up to 350 °C, remain for 2 h, and resuming heating rate at 1 °C min<sup>-1</sup> up to 700 °C and remain for 4 h to obtain Au-encapsulated ZnO@carbon, Pt-encapsulated ZnO@carbon and Pd-encapsulated ZnO@carbon .

### 5.2.8 Synthesis of ZIF-8 (without polymer coating)

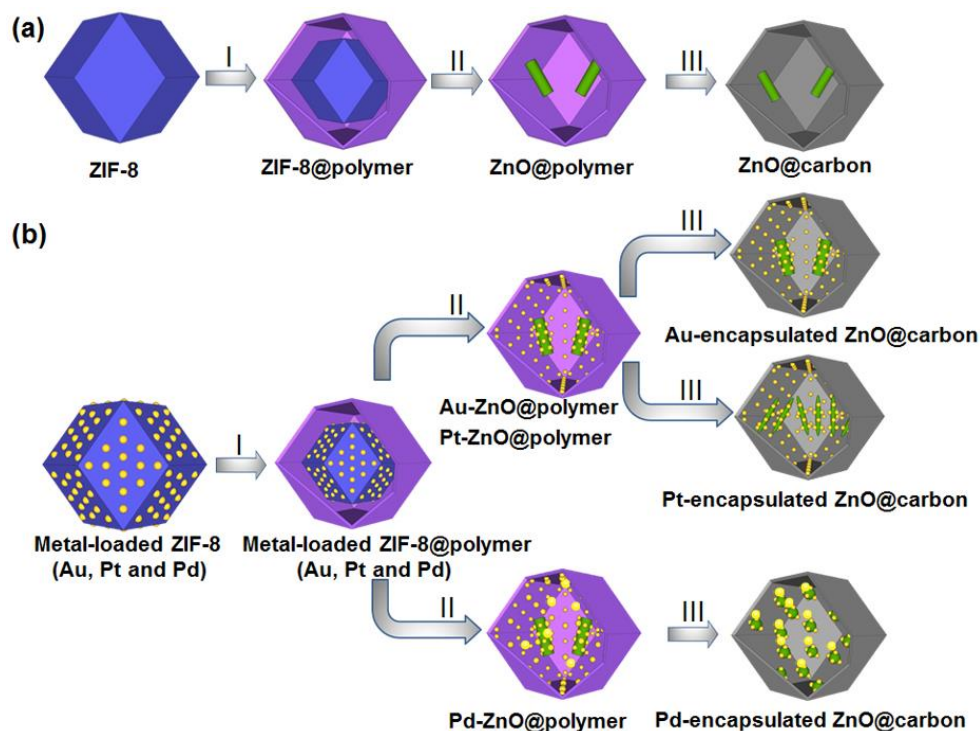
0.1 g CTAB was dissolved in an aqueous solution containing 20 mL water and 8 mL ethanol. Then, 0.2 mL ammonia solution was added and stirred at room temperature for 0.5 h, followed by addition of 0.1g ZIF-8. This suspension was kept stirring for 0.5 h at room temperature and afterwards hydrothermally treated for 24 h at 100 °C in a Teflon-lined autoclave. The remaining products were collected through centrifuging and washing with ethanol and dried at 80 °C for 24 h.

### 5.2.9 Materials Characterization

The sample structure was characterized through a transmission electron microscope (TEM, FEI Titan G2 80-200) with High Angle Annular Dark Field Scanning Transmission Electron Microscopy (HAADF-STEM) imaging and elemental distribution map which was operated at 200 kV. The element maps were achieved by energy dispersive X-ray spectroscopy with Super-X detector on the TEM equipment using a probe size about 1 nm and a probe current of approximately 0.4 nA. X-ray diffractometer (Bruker D8 Advance) was used to perform Powder X-ray powder diffraction (XRD) analysis with Cu K $\alpha$  radiation at 40 kV and 30 mA. Micromeritics TriStar II Surface Area and Porosity Analyzer was utilized to obtain the BET specific surface area and single-point pore volume from nitrogen adsorption isotherms measured at -196 °C. Before the measurement of nitrogen adsorption, the samples were degassed at 250 °C for 10 h. A Kratos Axis Ultra DLD spectrometer with a monochromatic AlK $\alpha$  (1486.6 eV) irradiation source which was operated at 150 W was used for X-ray photoelectron spectroscopy (XPS) measurements. During XPS measurements, the vacuum pressure of the analysis chamber of the spectrometer was maintained a 5 x 10<sup>-7</sup>

<sup>11</sup> Torr or lower. Samples were mounted for analysis by suspending a small amount of the powder sample in isopropanol, then drop casting the resultant mixture onto a 5mm x 10mm silicon wafer. The samples were allowed to gently dry under a heat lamp before being introduced into the ultra-high vacuum analytical chamber of the XPS instrument.

### 5.3 Results and discussion



**Scheme 5.1** Schematic illustration of the fabrication of yolk-shell structured ZnO@polymer (ZP) and metal-encapsulated ZnO@carbon: I) uniform coating of polymer onto the surface of ZIF-8 or metal-loaded ZIF-8; II) hydrothermal treatment of ZIF-8@polymer and metal-loaded ZIF-8@polymer; III) carbonization treatment in nitrogen atmosphere. (Blue, purple, yellow, green and gray colors mean ZIF-8, polymer layer, metal nanoparticles, ZnO nanoparticles and carbon layer, separately)

The synthesis strategy of yolk-shell structured ZnO/polymer (ZP) is schematically illustrated in **Scheme 5.1a**. Firstly, well-ordered ZIF-8 nanoparticles are prepared and

polymer layer is coated on the surface of these hard templates through extended StÖber method. Followed by hydrothermal treatment of ZIF-8@polymer core-shell structures, yolk-shell structured ZnO@polymer (ZP) nanoparticles are achieved. Carbonization of these yolk-shell structured ZP in nitrogen atmosphere can generate yolk-shell structured ZnO@carbon. The introduction of metal nanoparticles into yolk-shell structured ZnO@carbon is illustrated in Scheme 5.1b. A wet chemical reduction method is used to load metal nanoparticles (Au, Pt and Pd) on the ZIF-8 nanoparticles starting from corresponding metal salts. Aminophenol polymer layer is then coated on the surface of metal-ZIF-8 nanoparticles through the same extended StÖber coating method. Metal-encapsulated ZnO@carbon was then prepared via hydrothermal treatment of metal-ZIF-8@polymer and the following carbonization method.

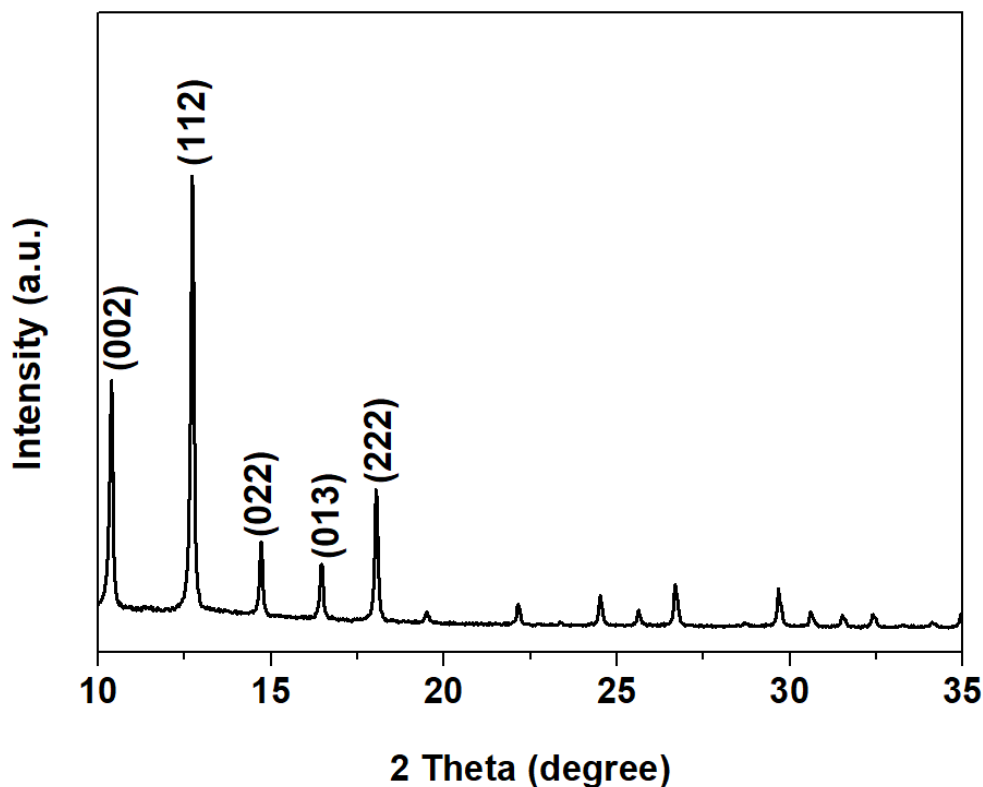
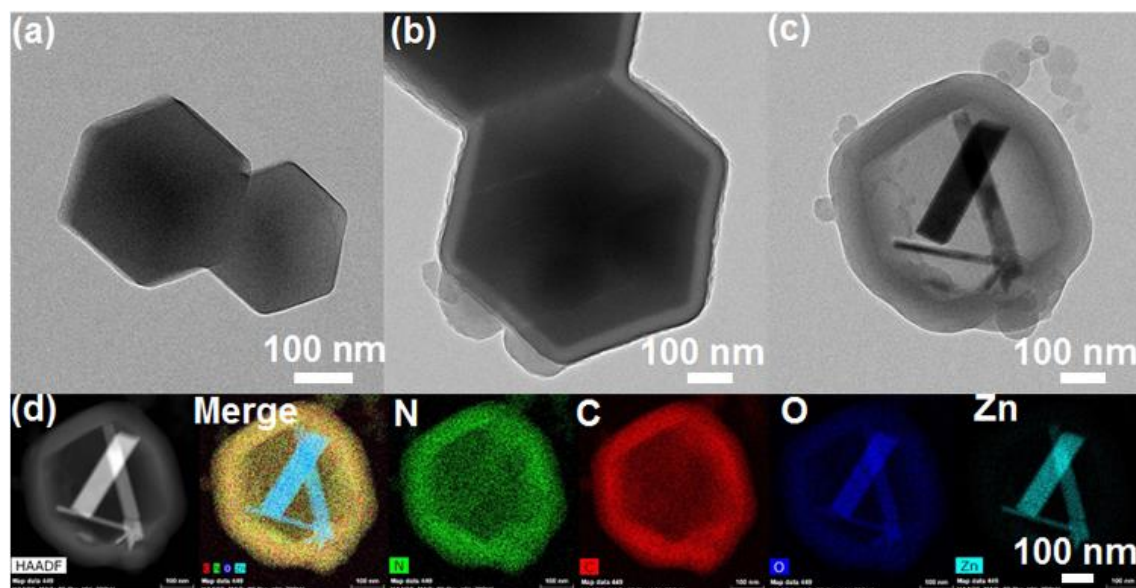


Figure 5.1. XRD patterns of ZIF-8.



**Figure 5.2.** TEM images of ZIF-8(a), ZIF-8@polymer before hydrothermal treatment (b). (c)TEM, (d) STEM and EDS mapping of ZP-100.

The structures formed at different procedures are characterized by XRD, TEM and HAADF-STEM imaging and element mapping. The XRD diffraction patterns in **Figure 5.1** exhibit the characteristic peaks (011), (002), (112), (022), (013) and (222), which can be indexed to the unit cell of the SOD-type ZIF-8 structure and in agreement well with previous literatures.<sup>25, 28</sup> A polyhedral shape with average particle size about 300 nm and a smooth surface is presented in TEM image (**Figure 5.2a**). After generation of ZIF-8@polymer core-shell structure with shell thickness approximately 42 nm, the particles still remain polyhedral structure but with a rougher surface, as shown in **Figure 5.2b**. Subsequent hydrothermal treatment for 24 hour of ZIF-8@polymer nanoparticles (**Figure 5.2c**) induced the generation of yolk-shell structured nanoparticles with inner diameters about 365 nm and increased shell thickness  $\sim 70$  nm. Noticeably, it is also very interesting to find nanoribbons are generated in the hollow polymer shell. The scanning transmission electron microscopy (STEM) and the corresponding energy dispersive X-ray spectroscopy (EDS) elemental mapping (**Figure 5.2d**) are obtained to identify the distribution of nitrogen, carbon, zinc and oxygen in this hollow structure. Elemental carbon and nitrogen are homogeneously distributed in the carbon shell, but zinc and most oxygen atoms only are present in the core materials, confirming elemental

zinc were confined in the hollow carbon shell. In order to investigate the effect of polymer layer in the synthesis of ZIF-8@polymer, ZIF-8 nanoparticles are prepared without polymer coating. **Figure 5.3** shows that irregularly shaped nanoparticles with decreased average particle size about 110 nm are only generated and nanoribbons are not observed, indicating that the polymer coating has a great influence on the formation of nanoribbons. For clarity, the TEM specimen of ZP nanoparticles is carefully tilted by rotation around the axis of the holder to  $-30^\circ$  and  $+30^\circ$ , as illustrated in **Figure 5.4**. The TEM images with multiple views reveal that the nanoribbon cores were indeed attached the inner shell.

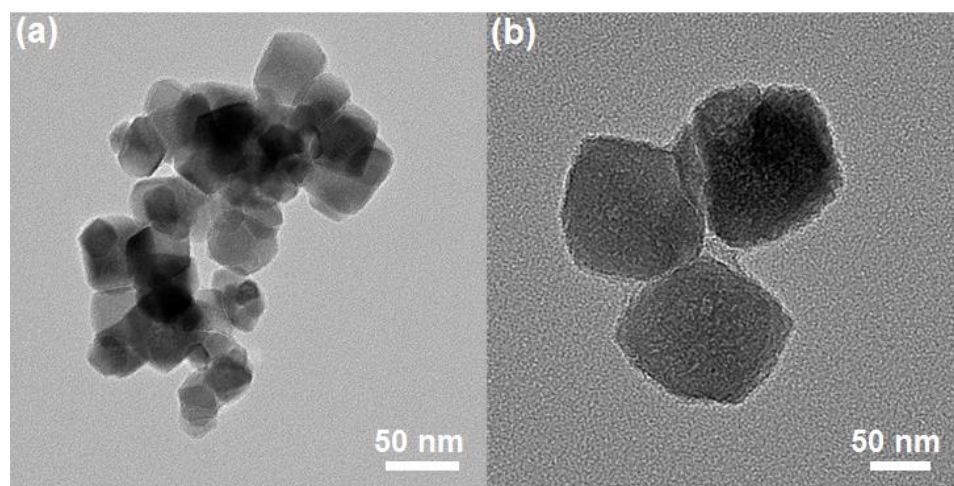


**Figure 5.3.** TEM images of ZIF-8 (without polymer coating).

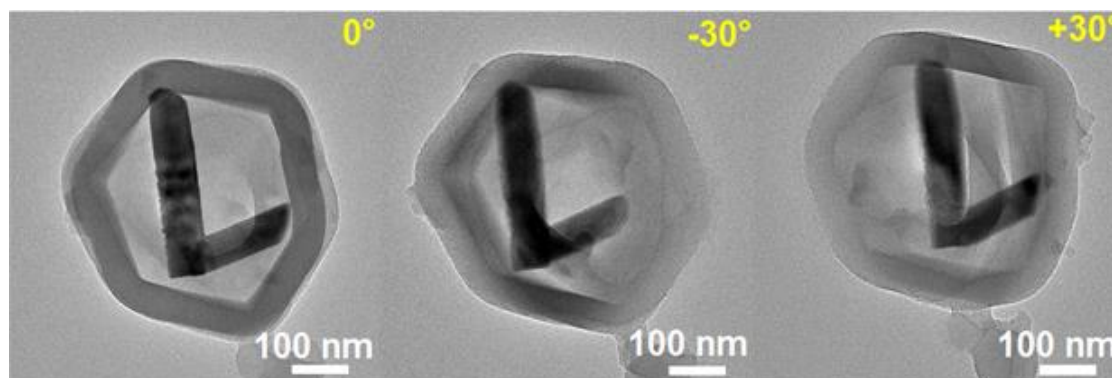


**Figure 5.4.** TEM images of ZP with the sample holder tilted to  $-30^\circ$ ,  $0^\circ$ ,  $+30^\circ$  by rotation around the axis of the holder.

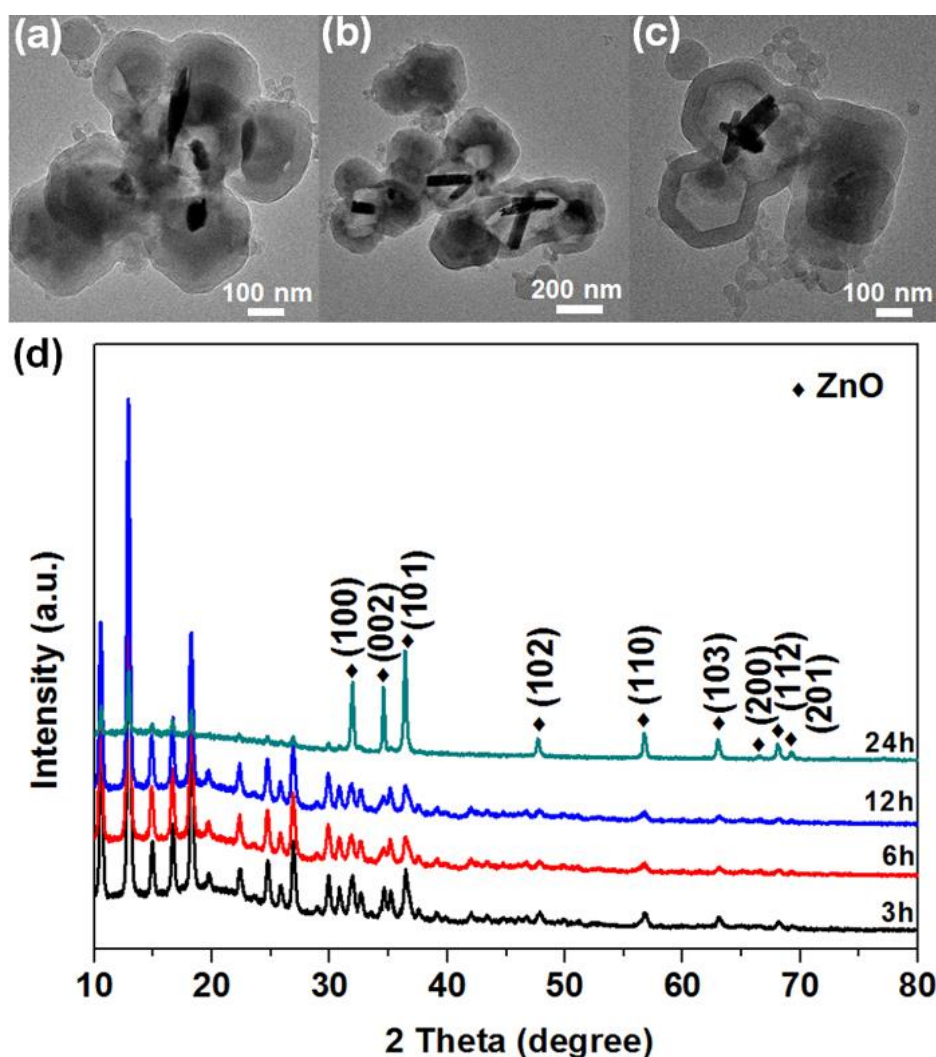


**Figure 5.5.** TEM images of ZP-3h(a), ZP-6h (b), ZP-12h (c) and XRD patterns of ZP-3h, ZP-6h, ZP-12h and ZP-24h.

Morphology evolution of ZIF-8@polymer after hydrothermal treatment at 100°C for 3h, 6h and 12h is displayed in the TEM images of **Figure 5.5a-5.5c**. After 3h, the image **Figure 5.5a** shows the presence of a number of dark nanoparticles formed in the polymer shell. At 6 h in **Figure 5.5b**, the evidence of nanoribbon formation with up to 250 nm in length and 50 nm in width is apparent in the sample. As hydrothermal temperature continues to 12h in **Figure S4c**, the nanoribbons are present with different sizes and extents and the hollow void is also generated. By 24h in **Figure 5.5c**, the dark

nanoparticles have disappeared with well-defined nanoribbons remaining. The complex XRD pattern at different hydrothermal treatment times in **Figure 5.5d** highlights transformation of the crystal phase of these samples. The 3h, 6h, 12h profiles have noticeably peaks of ZIF-8, which may be attributed to the lack of nanoribbon formation until hydrothermal treatment for 12h. The 24h profile displays additional peaks compared to the 60 °C profile with new peaks appearing at about 32°, 34.5°, 35.5°, 48°, 57°, 63°, 67°, 68° and 69°, demonstrating the formation of new crystal phases with this nanoparticles. Those new generated peaks can be attributed to wurtzite ZnO (JCPDS 36-1451).

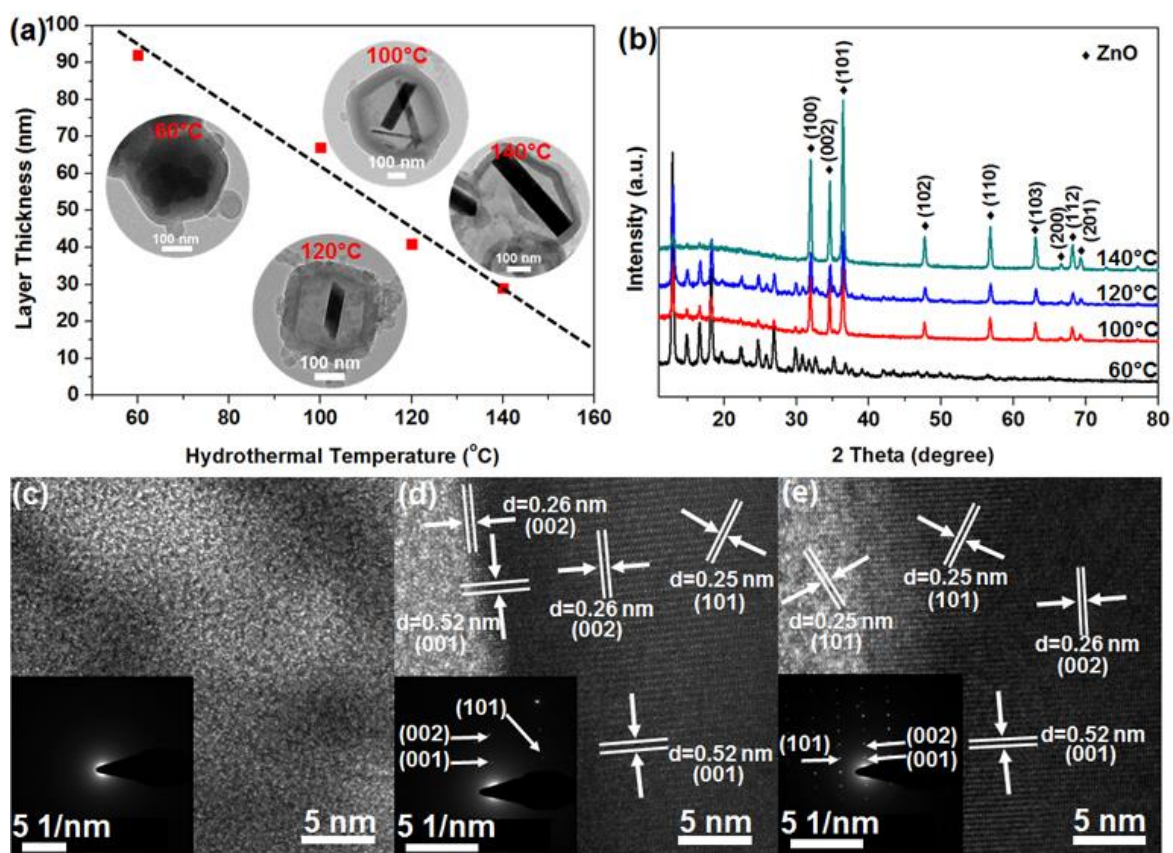


**Figure 5.6.** (a) The relationship between the hydrothermal temperature and the layer thickness (inset: TEM images of ZP-60 (1), ZP-100 (2), ZP-120 (3), ZP-140 (4)) (b) their corresponding XRD patterns. HRTEM image of ZP-60(c), ZP-100(d) and ZP-140(e) (inset: their corresponding SAED patterns).

In order to deeply investigate the transformation from core-shell structure to yolk-shell structure, the effect of hydrothermal temperature and the layer thickness are also examined. TEM images of ZIF-8@polymer with different hydrothermal temperature 60°C, 80°C, 120°C, 140°C are illustrated in **Figure 5.6a** and **Figure 5.7**. With increasing the hydrothermal temperature from 60° to 140 °, the shell thickness shows a linear decrease from 93 nm to 28 nm. Hydrothermal treatment at 60° invokes partial transformation of ZIF-8 to needle-like nanoparticles, but some core-shell structured particles are still present. At 100 °C and 120 °C evidence of nanoribbon formation with short length and thin thickness is apparent. As hydrothermal temperature elevated to 140 °C, well-defined and long nanoribbons are present and ZIF-8 particles have essentially disappeared.

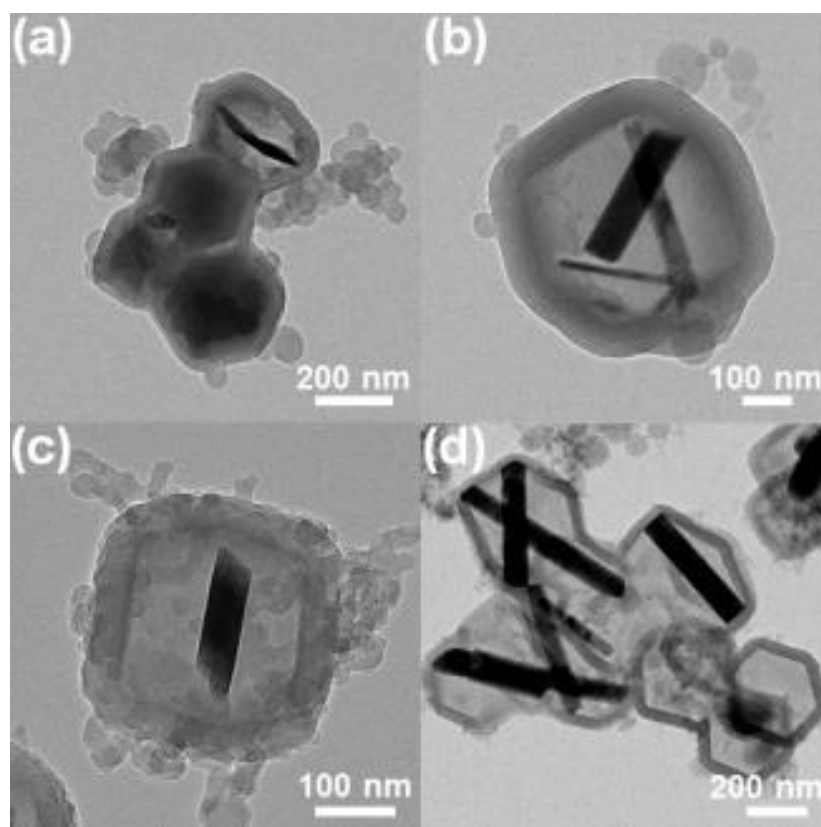


**Figure 5.7.** TEM images of ZP-60 (a), ZP-100 (b), ZP-120 (c), ZP-140 (d).

The crystal structure and composition of the nanoribbons and particles observed in **Figure 5.6** are investigated by XRD. The complex XRD pattern at different hydrothermal temperatures highlights the formation of nanoribbon of these samples. XRD patterns of ZP-60 (**Figure 5.6b**) presented that the peaks of ZIF-8 were still existed in ZP-60 and the peaks of ZnO are hardly observed probably due to the amorphous nature at this temperature. This is also confirmed from the TEM images of ZP-60 in **Figure 5.6c**. The 100 °C and 120 °C profiles display additional peaks compared to the 60 °C profile with new peaks formation of wurtzite ZnO (JCPDS 36-1451). In addition, it is still obvious that the XRD patterns of ZIF-8 are present during hydrothermal treatment at 100 °C and 120 °C. Yu et al. reported the transformation temperature from ZIF-8 to wurtzite ZnO nanocrystals was above 400 °C.<sup>29</sup> This also highlighted the nanoconfinement effect of polymer coating on the surface of ZIF-8 which can accelerate the transformation process. After hydrothermal treatment at 140 °C, the peaks of ZIF-8 have totally disappeared, indicating that the complete transformation from ZIF-8 to ZnO nanoribbon. The synthesized ZP-140 has the strongest XRD peaks, suggesting its high degree of crystallinity and large crystallite size. As expected, with increasing hydrothermal temperature, the XRD peaks exhibit increased intensity, indicating enhanced degree of crystallinity and promoted growth of crystallite size.

HRTEM and SAED (**Figure 5.6c-5.6e**) of ZP-60, ZP-100 and ZP-140 for different temperatures provide further details on crystal growth during preparation of these nanoparticles. ZP-60 nanoparticles formed during hydrothermal treatment at 60 °C provided no d-spacing lattice in HRTEM and no diffraction pattern (**Figure 5.6c**), indicating these nanoparticles are amorphous. HRTEM result of nanoribbon structures as shown in the 100 °C profile (**Figure 5.6d**) indicates that the calculated lattice spacing are 0.52 nm, 0.26 nm and 0.25 nm, which can be ascribed to (001), (002) and (101) crystal planes of ZnO. It seems that the growth of ZnO nanoparticles is along [001] direction. The inset SAED patterns in **Figure 5.6d** also confirm the appearance of those crystal planes which also agree well with XRD patterns in **Figure 5.6b**. Further increasing the hydrothermal temperature to 140 °C also induces the same growth of

[001] direction, as shown in **Figure 5.6e**. It is also very interesting to observe that the lattice spacing at the edge in this nanoribbon is 0.25 nm, which is corresponded with the (101) crystal plane. During 140 °C hydrothermal treatment, the ribbon was getting longer along [001], so the growth direction was [001].

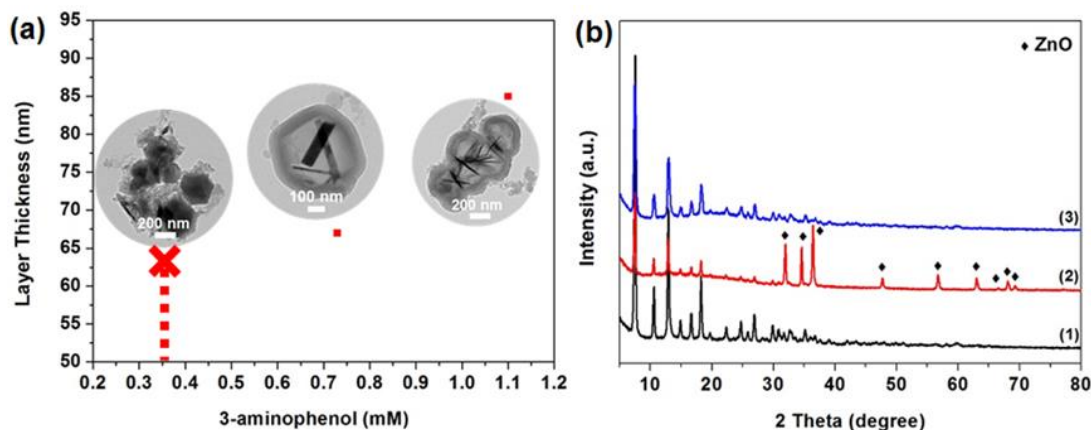
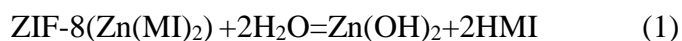


**Figure 5.8.** (a) The relationship between the polymer amount and the layer thickness (inset: TEM images of ZP-1, ZP-100, ZP-2) (b) their corresponding XRD patterns.

To investigate the effect of shell thickness for the synthesis of yolk-shell structured ZnO@polymer, different amount of 3-aminophenol and formaldehyde are introduced during the synthesis of ZIF-8@polymer. **Figure 5.8a** shows the relationship between the polymer amount and the layer thickness with the TEM image of ZP-1, ZP-100 and ZP-2. As revealed in **Figure 5.8a**, after increasing the polymer layer thickness to about 85 nm, needle-like nanoparticles are formed and confined in the hollow polymer shell. This is probably because that the relatively thick polymer restricts the heat transfer from the outside of shell to the inside core, further impeding the formation of nanoribbon. However, when the amount of 3-aminophenol is decreased to 0.37 mM, it is found that yolk-shell structured ZnO@polymer and ZnO nanoribbons are not generated probably because not enough polymer are formed to coat on the surface of ZIF-8. These findings are also confirmed from XRD patterns in **Figure 5.8b**, illustrating that the existence of ZIF-8.

The sequence of TEM images, HRTEM images, SAED patterns and XRD patterns related to the formation and growth of nanoribbon with different hydrothermal reaction time and temperature have provided insights into final formation of yolk-shell structure. ZIF-8 nanoparticles with sodalite topology were consisted with tetrahedral Zn ions bridged by imidazolate.<sup>30</sup> As shown from **Figure 5.5**, hydrothermal treatment for 3h, 6 h and 12 h results in the shrinkage and dissolution of the ZIF-8 core and the partially transformation from polyhedron structure to small nanoparticles, revealing that prolonging temperature breaks the Zn-N coordination bonds, then starts to dissolve Zn-imidazole compound and further induced amorphous nanoparticles formation. It is very clear that the void between the core and shell started to form asymmetrically, also indicating the region of the edge of ZIF-8 is less dense or easier decomposed than the centre. This is obvious from the produced dark and amorphous nanoparticles detected from TEM image (in **Figure 5.5**). Until hydrothermal treatment for 24 h (**Figure 5.1c**), well-defined nanoribbons are generated.

TEM images in **Figure 5.6** and **Figure 5.7** depict the impact of hydrothermal temperature for inside ZnO nanoribbons on their morphology. Hydrothermal treatment at lower temperature such as 60 °C induces the conversion from polyhedron-structured ZIF-8 nanoparticles into needle-like structure. When increasing the hydrothermal temperature to above 100 °C, the polymer shell thickness decreased, resulting in fast heat transfer from the outside solution to the inner core and the total dissolve of ZIF-8 at 140 °C. The conversion from Zn-N coordination bonds to Zn-O covalent bond is completed under relatively high temperatures such as 140 °C. Formation of zinc oxide can be described by the following chemical reactions during hydrothermal treatment:



Therefore, ZnO nanoribbon generation is observed to occur via the dissolution of ZIF-8 and formation of the intermediate needle-like nanoparticles.

In addition, the wurtzite ZnO nanoribbon formation stages can be explained as follows. Based on the XRD, HRTEM and SAED patterns at 60 °C, the amorphous needle-like nanoparticle and partially dissolve of ZIF-8 were observed at lower temperatures. When

ZIF-8@polymer were treated at 100 °C, the ZnO nanoribbon with (001), (002) and (101) crystal planes were present. ZP-140 has a more clearly defined crystal structure than ZP-100.

After thermal treatment of ZP-100 in flowing nitrogen at 700 °C, yolk-shell structured ZC with decreased shell thickness about 45nm are achieved (as shown in **Figure 5.9a** and **5.9b**). The nanoribbons in the core are destroyed into small nanoparticles. The HAADF image and elemental mapping results (**Figure 5.9c**) are acquired to identify the distribution of nitrogen, carbon, oxygen and zinc. As shown in **Figure 5.9c**, similar elemental distribution is also reached compared with that of ZP-100, indicating that elemental zinc is confined in the hollow carbon shell. XRD measurement is performed to investigate the phase structure of ZC (**Figure 5.9d**). Wurtzite ZnO (JCPDS 36-1451) is the only phase present in ZC. The peaks around 25° probably can be attributed to amorphous carbon. The N<sub>2</sub> adsorption–desorption isotherm and the corresponding pore size distribution of ZC nanoparticles according to Barrett-Joyner-Halenda (BJH) model are shown in **Figure 5.9e**. The ZC nanoparticles exhibit BET surface area about 621 m<sup>2</sup> g<sup>-1</sup> and pore volume about 1.0 cm<sup>3</sup> g<sup>-1</sup>. The pore sizes mainly centered at 4.3 nm (see inset in **Figure 5.9e**), indicating the existence of mesopores. The XPS pattern (**Figure 5.10a**) displays four typical peaks for C 1s, N 1s, O 1s and Zn 2p on the survey spectrum with their elemental content of 86.5%, 6.4%, 6.5% and 0.6%, respectively, indicating zinc elements are confined in the hollow carbon shell. The XPS high resolution narrow scan (**Figure 5.10b**) shows four overlapping N1s peaks corresponding to quaternary nitrogen (401.2 eV), pyrrolic nitrogen (399.6 eV), pyridinic nitrogen (398.2 eV) and N-Oxide (402.8 eV) with the relative concentration of about 25.2%, 33.4%, 28.5% and 12.9%. To confirm the yolk-shell structure of the ZC, HAADF-STEM tomography was applied. The volume rendering of the obtained 3D reconstruction of ZC is shown in **Figure 5.9f**, **5.9g** and **5.9h**. In order to investigate ZnO nanoparticles are moveable or attached to the shell, **Figure 5.11** illustrates that the TEM image of ZC nanoparticles with tilted to -30° and +30° and it is observed that the ZnO core materials are also connected to the shell.

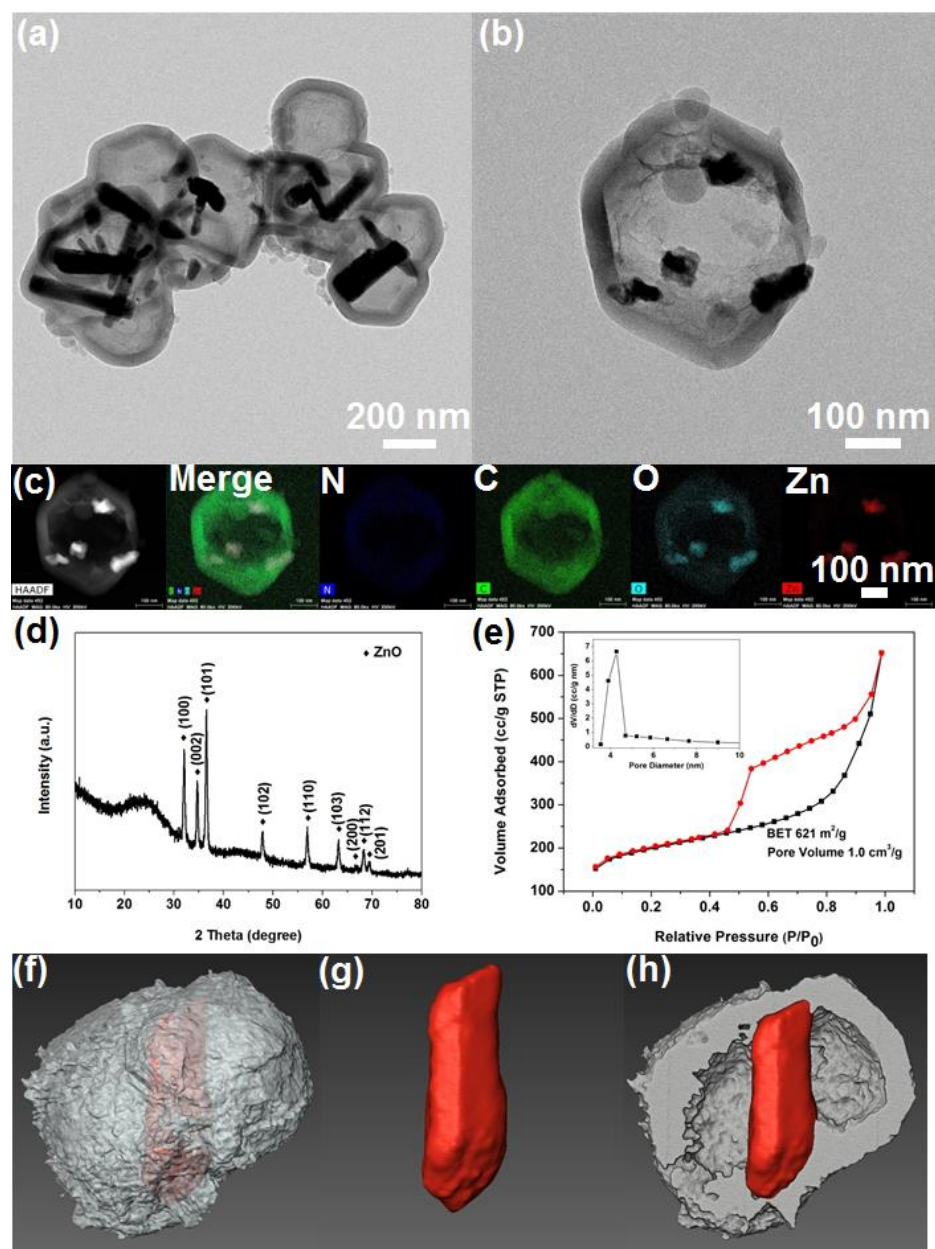


**Figure 5.9.** TEM (a)(b), STEM and EDS mapping(c), XRD pattern (d) and N<sub>2</sub> adsorption–desorption isotherm (e) of ZC, (f)(g)(h) 3D representation of the ZC reconstruction.

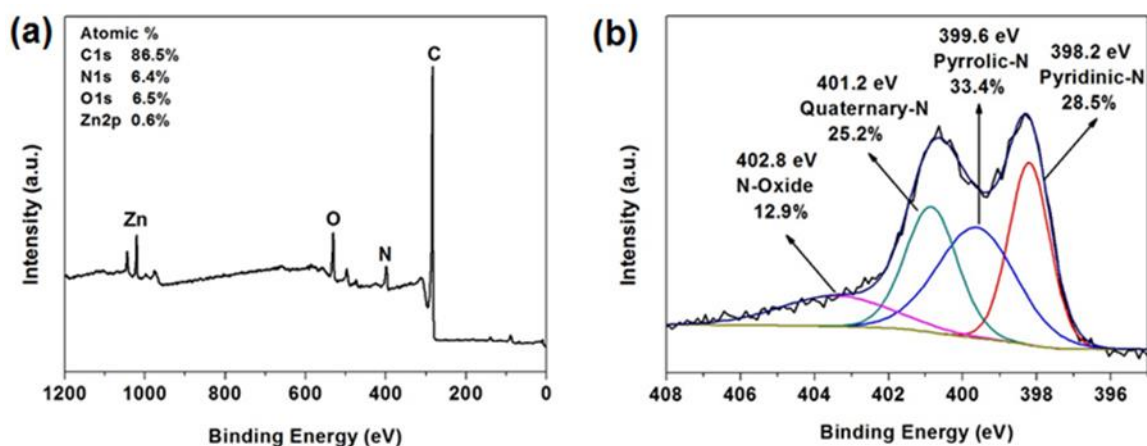


Figure 5.10. XPS survey spectrum (a) and high resolution N1s spectrum (b) of ZC.

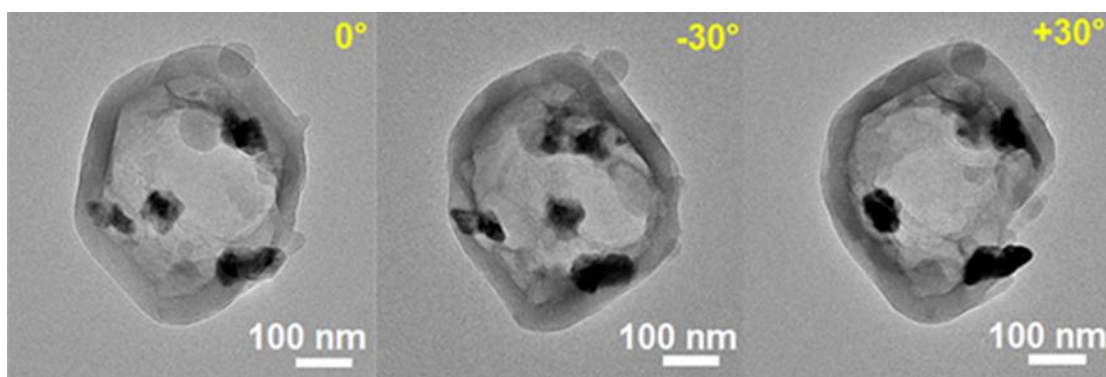
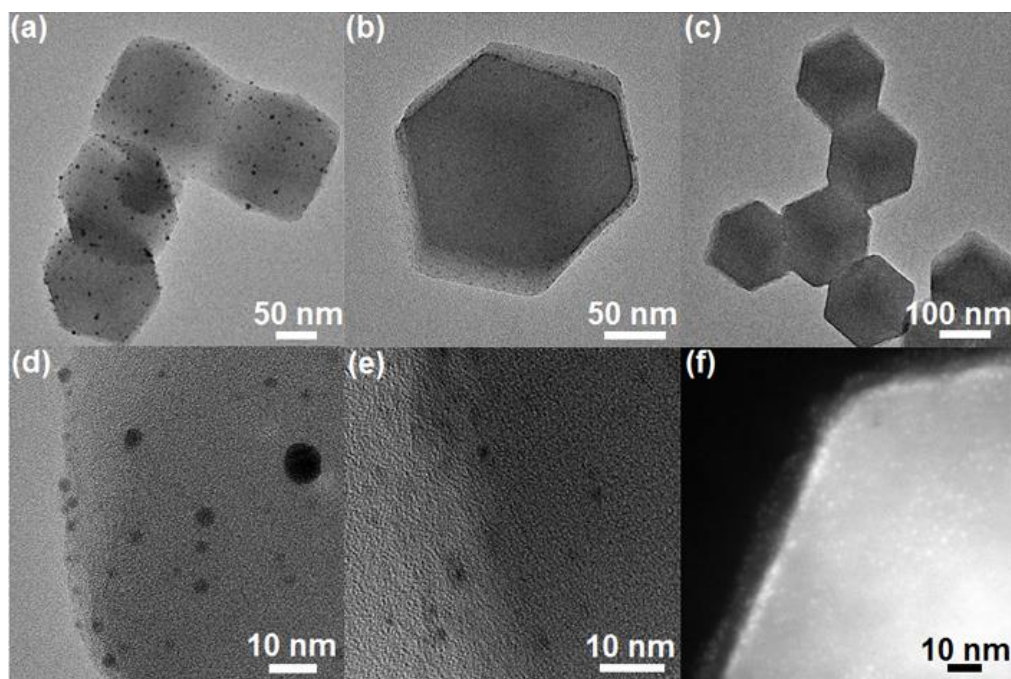


Figure 5.11. TEM images of ZC with the sample holder tilted to  $-30^\circ$ ,  $0^\circ$ ,  $+30^\circ$  by rotation around the axis of the holder.

We further demonstrate that metal nanoparticles can be confined in the interior of yolk-shell structured ZnO@carbon to generate metal-encapsulated ZnO@carbon structures. The synthesis strategy of these nanoparticles is also schematically depicted in **Scheme 5.1b**. The similar polymer coating method, hydrothermal treatment and the following carbonization process with yolk-shell structured ZnO@carbon are also applied during the synthesis of metal-encapsulated ZnO@carbon. Because the noble nanoparticles were obtained through wet-chemical reduction process with the presence of  $\text{NaBH}_4$ , this synthetic route can be easily applied to most noble metal species such as Au, Pt and Pd. The TEM images in **Figure 5.12a-5.12f** show highly-dispersed metal nanoparticles (Au, Pt and Pd) have been successfully loaded on the surface of ZIF-8 nanoparticles. The

mean particle size of Au, Pt and Pd was estimated to be 3.6 nm, 2.4 nm and 2.5 nm, respectively. After coating polymer on the surface of metal-ZIF-8 and the following hydrothermal treatment, noble metal nanoparticles have been successfully incorporated in the shell of yolk-shell structured ZnO@polymer, as shown in **Figure 5.13a, 5.13e and 5.13i**. The polymer layer thickness of Au-ZIF-8@polymer, Pt-ZIF-8@polymer and Pd-ZIF-8@polymer are 63 nm, 47nm and 48nm, respectively. To determine the elemental dispersion in metal-loaded ZnO@polymer, HAADF image and element mapping has been used to reveal that nitrogen atoms are homogeneously distributed in the polymer framework and metal nanoparticles are also uniformly situated inside of polymer shell and on the surface of ZnO nanoribbons. It is also very interesting to find out that after hydrothermal treatment, the mean size of Pt nanoparticles remain to be 2.5 nm the same as the Pt particle size of Pt-ZIF-8, although the mean particle size of Au and Pd increased to 5.5 nm and 12 nm, respectively. This is probably attributed to the faster nucleation rate of Au and Pd than Pt during the hydrothermal treatment.



**Figure 5.12.** TEM images of Au-ZIF-8 (a)(d), Pt-ZIF-8 (b)(e), Pd-ZIF-8 (c). HAADF image (f) of Pd-ZIF-8.

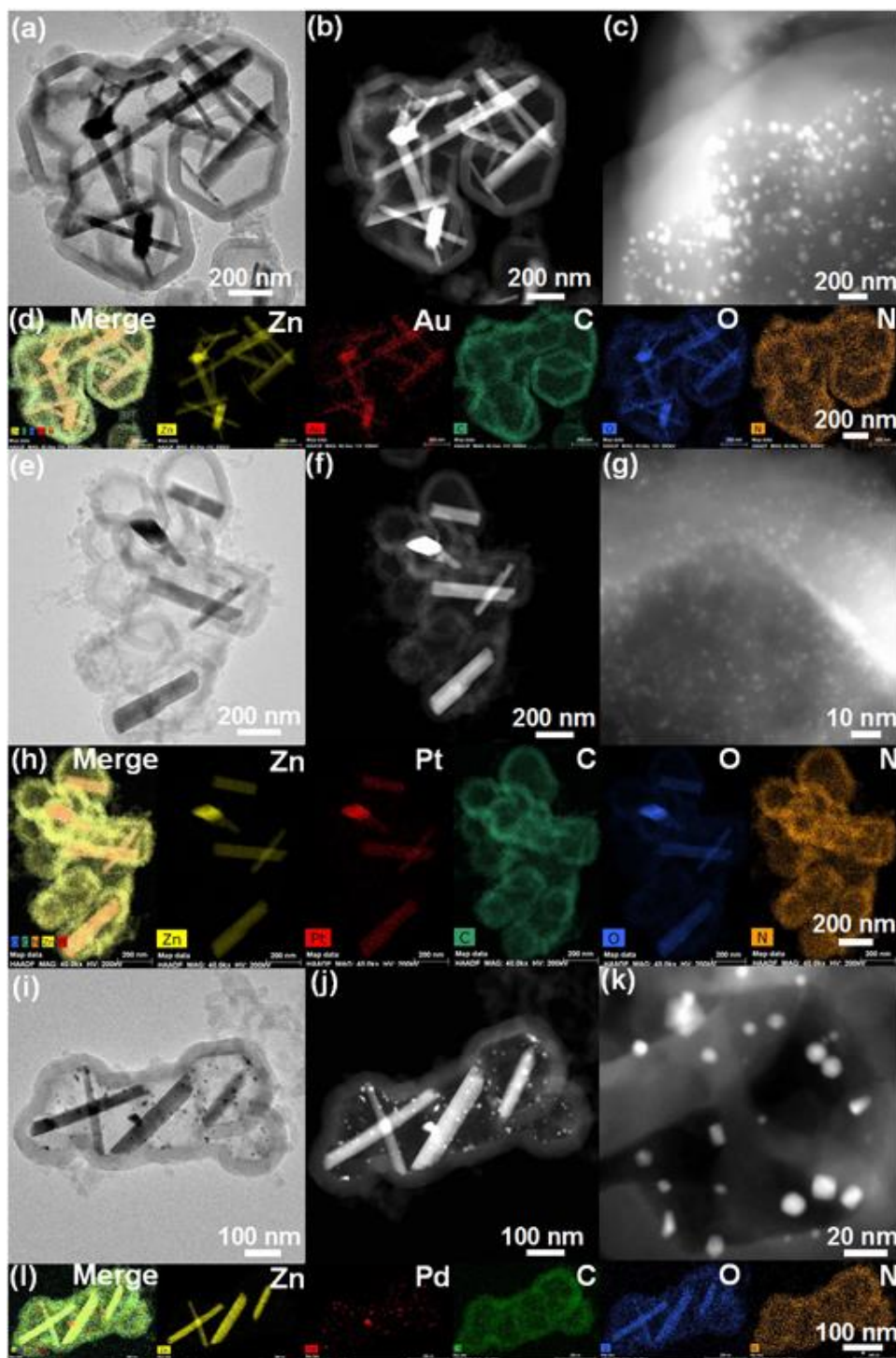


**Figure 5.13.** TEM images (a),(e),(i); HAADF images (b)(c), (f)(g), (j)(k) and element mapping images (d),(h),(l) of Au-ZnO@polymer, Pt-ZnO@polymer, and Pd-ZnO@polymer.

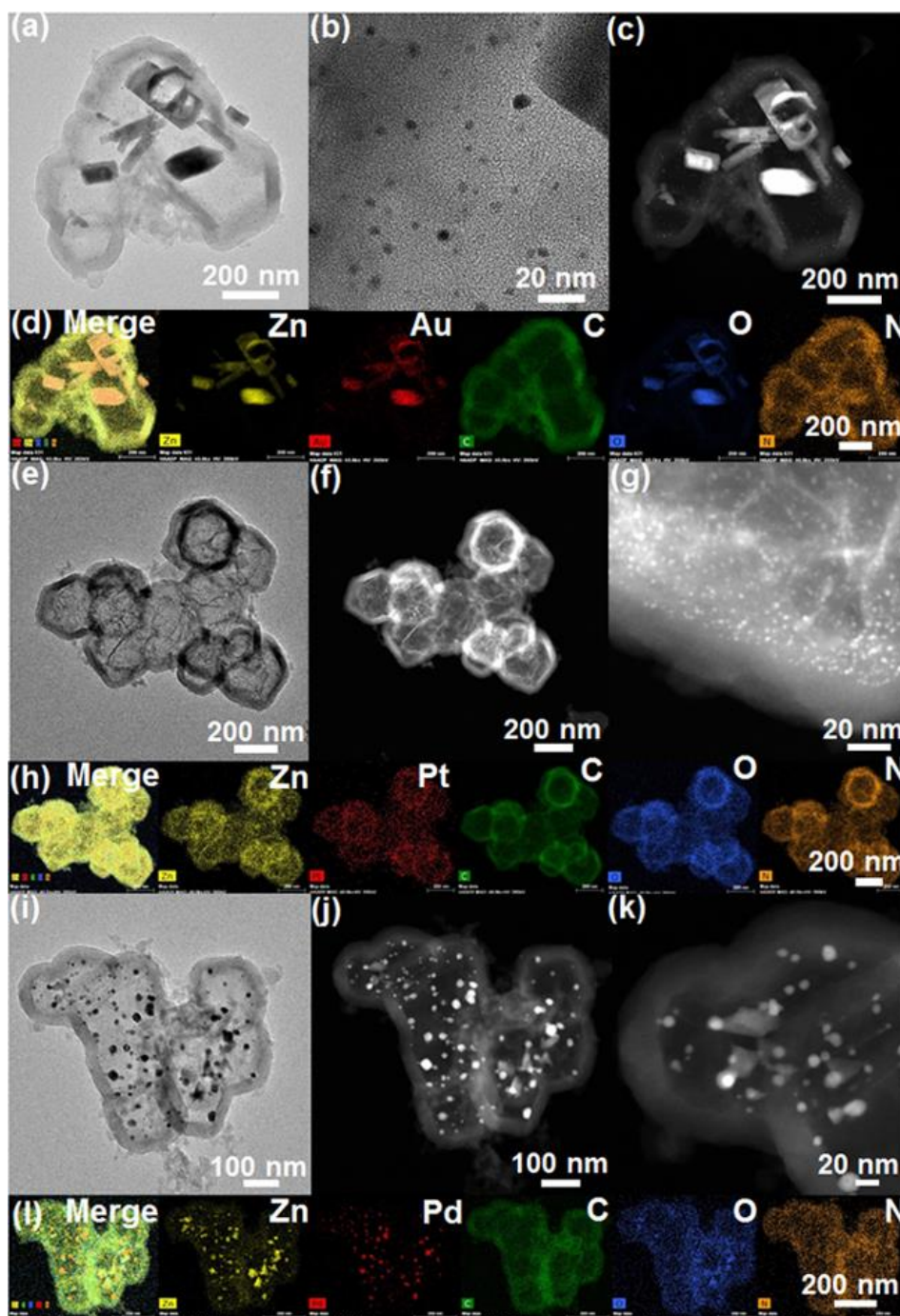


**Figure 5.14.** TEM images (a) (b), HAADF images(c), element mapping images (d) of Au-encapsulated ZnO@carbon; TEM images (e), HAADF images (f) (g), element mapping images (h) of Pt-encapsulated ZnO@carbon; TEM images (i), HAADF images (g)(k), element mapping images (l) of Pd-encapsulated ZnO@carbon.

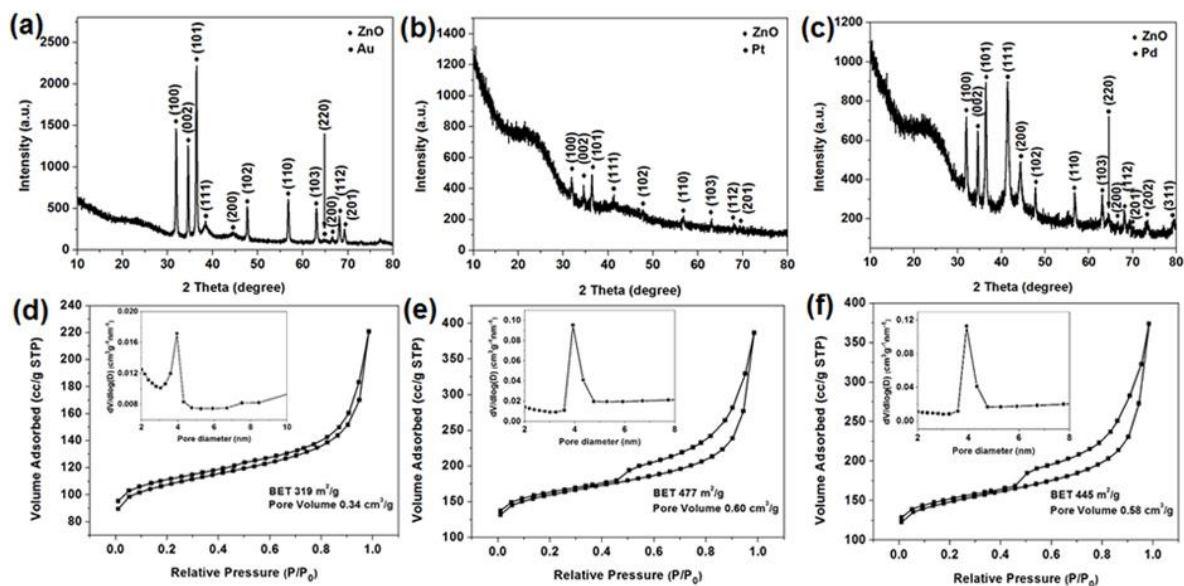


**Figure 5.15.** XRD patterns (a) (b) (c) and  $N_2$  adsorption–desorption isotherm and the corresponding pore size distribution curve (inset) (d) (e) (f) of Au-encapsulated ZnO@carbon, Pt-encapsulated ZnO@carbon and Pd-encapsulated ZnO@carbon.

The as-prepared metal-loaded ZIF-8@polymer were carbonized in  $N_2$  atmosphere to achieve metal-encapsulated ZnO@carbon. TEM images **Figure 5.14a** and **5.14b** indicate the Au metal nanoparticles are homogeneously distributed within the hollow carbon shell and the inside ZnO nanoparticles. It is observed that nanoribbon structure has been damaged into small nanoparticles, which is resulted from the reduction of ZnO to amorphous Zn metal by carbon at  $700^\circ\text{C}$ .<sup>31</sup> The mean Au particle size is estimated to be 4.6 nm, which is larger than that of Au-ZnO@polymer. To investigate elemental dispersion in Au-encapsulated ZnO@carbon, HAADF imaging and element mapping (**Figure 5.14c** and **Figure 5.14d**) has been used to reveal that nitrogen atoms are uniformly distributed in the carbon framework, zinc and oxygen atoms are located on ZnO nanoribbons, and metal nanoparticles are also uniformly situated inside of carbon shell and on the surface of ZnO nanoribbons. The formation of Au metal nanoparticles is also further confirmed by the XRD patterns (**Figure 5.15a**), which exhibited distinct reflections at  $2\theta$  of  $38.6^\circ$ ,  $44.5^\circ$  and  $64.8^\circ$  attributed to the (111), (200) and (220) peaks of face-centered cubic (FCC) Au nanoparticles. Based on the (111) Au peak, the

Scherrer equation estimated the Au<sup>0</sup> crystallite size to be 4.2 nm, which is consistent with the results from TEM images. The XRD pattern of Au-encapsulated ZnO@carbon also shows well-defined crystalline structure of ZnO, indicating ZnO crystall structures are well maintained during the carbonization process. The N<sub>2</sub> adsorption–desorption isotherm and the corresponding pore size distribution of ZC nanoparticles according to Barrett-Joyner-Halenda (BJH) model are shown in **Figure 5.15d**. The Au-encapsulated ZnO@carbon nanoparticles exhibit BET surface area about 319 m<sup>2</sup> g<sup>-1</sup> and pore volume about 0.34 cm<sup>3</sup> g<sup>-1</sup>. The pore sizes mainly centered at 3.9 nm (see inset in **Figure 5.15d**), indicating the existence of mesopores.

Interestingly, when replacing Au nanoparticles to Pt nanoparticles, the inside nanoribbon structure disappeared with the appearance of needle-like structure, as shown in **Figure 5.14e**. Based on HAADF images in **Figure 5.14f** and **5.14g**, the mean Pt nanoparticle size is about 2.6 nm, which is the same as the Pt nanoparticle size of Pt-ZIF-8 and Pt-ZnO@polymer. HAADF imaging and element mapping (**Figure 5.14f** and **Figure 5.14h**) is used to investigate the element distribution of Pt-encapsulated ZnO@carbon. It is found that elemental carbon, nitrogen, zinc, oxygen and platinum are uniformly distributed within the carbon framework. This highly dispersion of elemental zinc is probably due to that the highly monodispersed Pt nanoparticles catalyze the transformation of well-defined ZnO crystallines to amorphous zinc metal during carbonization process. It is also confirmed from XRD patterns (**Figure 5.15b**) of Au-encapsulated ZnO@carbon showing that the intensities of ZnO peaks have been significantly decreased, indicating the poor crystalline structures of ZnO nanoparticles. The peak at 41.3° can be ascribed to the (111) peak of face-centered cubic (FCC) Pt nanoparticles. The Scherrer equation is used to estimate the Pt<sup>0</sup> crystallite size to be 2.3 nm according to (111) Pt peak, which is consistent with the results from TEM images. The shells of Pt-encapsulated ZnO@carbon are mesoporous as evidence by the type IV shape of adsorption and desorption isotherms having H3 hysteresis loop (**Figure 5.15e**). Based on the aforementioned adsorption isotherm, the BET surface area and the pore volume obtained are 477 m<sup>2</sup> g<sup>-1</sup> and 0.60 cm<sup>3</sup> g<sup>-1</sup>, respectively.

Amazingly, after incorporation Pd metal nanoparticles in the yolk-shell structured ZnO@carbon, small cubic clusters with mean particle size about 15 nm are present and nanoribbon structures are absent in the hollow carbon structures with shell thickness about 40 nm (**Figure 5.14i**). Nitrogen atoms are uniformly dispersed in the carbon structure, zinc, oxygen and palladium atoms are situated on cubic clusters, as shown from HAADF-STEM element mapping (**Figure 5.14j, 5.14k and 5.14l**). XRD patterns in **Figure 5.15c** shows the decreased ZnO intensities, revealing the catalytic conversion from nanoribbon structure to cubic clusters. The sharp and enhanced peaks at  $41.5^\circ$ ,  $44.3^\circ$  and  $64.6^\circ$  can be attributed to the (111), (200) and (220) peak of face-centered cubic (FCC) Pd nanoparticles. The Scherrer equation is used to estimate the Pd<sup>0</sup> crystallite size to be 12 nm according to (111) Pd peak, which agrees well with the results from TEM images. It is observed that the mean particle size of Pd nanoparticles is larger than that of Au and Pt nanoparticles, indicating Pd nanoparticles own faster nucleation rate than that of Au and Pt nanoparticles during the carbonization process. The N<sub>2</sub> sorption isotherm shows a mixture of I and IV type with a steep H<sub>3</sub> hysteresis loop, revealing a hierarchical porous structure with combined microporous, and mesoporous structure (**Figure 5.15f**). The Pd-encapsulated ZnO@carbon has a BET surface area ( $445 \text{ m}^2 \text{ g}^{-1}$  and) with large pore volume ( $0.58 \text{ cm}^3 \text{ g}^{-1}$ ).

In order to evaluate catalytic performance of the as-prepared metal-encapsulated ZnO@carbon nanoparticles, the selective hydrogenation of phenylacetylene to phenylethylene was performed at  $30^\circ \text{C}$  under 1 bar of H<sub>2</sub> over a period of 80 mins. As shown in **Figure 5.16a**, Au-encapsulated ZnO@carbon nanoparticles (TON value 164) proved to be inferior catalysts for the hydrogenation of phenylacetylene. The catalytic activity of Pd-encapsulated ZnO@carbon nanoparticles demonstrate better activity (turn over number 761) than Pt-encapsulated ZnO@carbon nanoparticles (turn over number 725) with similar selectivity (99%). In addition, compared with the Pd-encapsulated ZnO@carbon nanoparticles, Pd/ZnO nanoparticles (TON value 320) and Pd/C nanoparticles (TON value 433) showed relatively lower hydrogenation efficiency (with same Pd loading) and selectivity in the hydrogenation of phenylacetylene. Based on literatures, several factors including nanoparticle composition, size and the nature of the

support materials are of importance for catalysts performances. The high activity and selectivity are ascribed to the size of metal nanoparticles and their interface between metal nanoparticles and support materials, resulting preferential adsorption of the substrates for the reduction of alkynes to alkene. In our system, the distinguished phenylacetylene conversion and phenylethylene selectivity probably ascribes to the novel nanoreactor benefiting desorption of the phenylethylene.

In order to evaluate the reusability of Pd-encapsulated ZnO@carbon and Pt-encapsulated ZnO@carbon, five consecutive cycles were carried out and the reaction time in each cycle was fixed at 80 min. As shown in **Figure 5.16b**, both conversion activity and selectivity of Pd-encapsulated ZnO@carbon and Pt-encapsulated ZnO@carbon in 5 cycles are maintained, with a selectivity of about 99% at a phenylacetylene conversion of around 95.5% and 85.5%, respectively. These results indicate the good stability of the Pd-encapsulated ZnO@carbon and Pt-encapsulated ZnO@carbon catalyst, which is expected to a promising candidate for the selective hydrogenation of phenylacetylene. This reveals that there are no obvious variations in the size, shape and yolk-shell nanostructures and the carbon shells effectively encapsulate the active noble metal cores and prevent leaching or severe particle agglomerations.

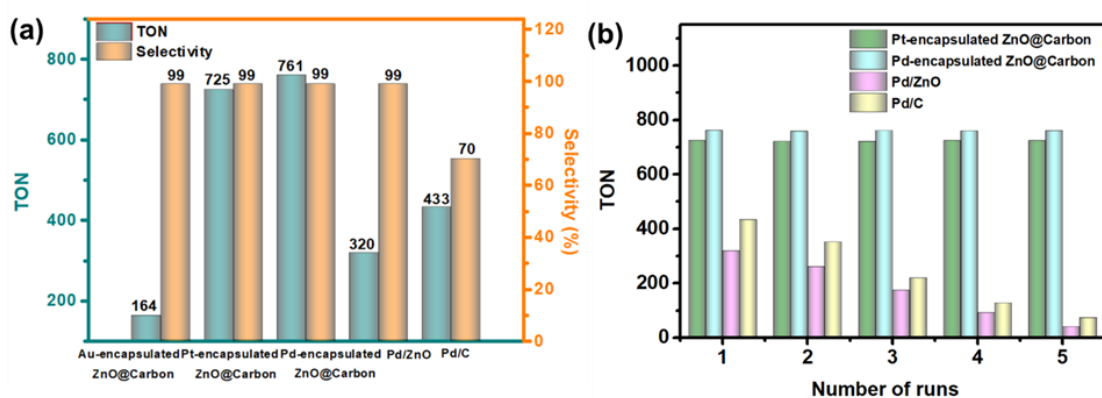


**Figure 5.16.** (a) TONs and selectivity to phenylacetylene hydrogenation (b) recycling tests catalysed by metal-encapsulated ZnO@carbon nanoparticles. (Standard conditions: 30 °C; 60 min; 20 mg of catalyst; 1 bar H<sub>2</sub>; 2.9 mmol of substrate; 25 mL ethanol as solvent. TON = mol phenylacetylene consumed divided by total mol metal.

**Table 5.1.** Physical properties of FC.

Sample	BET surface area (m <sup>2</sup> /g) <sup>a</sup>	Pore volume (cm <sup>3</sup> /g) <sup>b</sup>	Pore size (nm) <sup>a</sup>	Layer thickness(nm) <sup>c</sup>	Metal average crystalline size <sup>d</sup> (nm)	Metal nanoparticle size <sup>c</sup> (nm)
Au-ZIF-8	-	-	-	-	-	3.6
Pt-ZIF-8	-	-	-	-	-	2.4
Pd-ZIF-8	-	-	-	-	-	2.5
Au-ZnO@polymer	-	-	-	63	-	5.5
Pt-ZnO@polymer	-	-	-	47	-	2.5
Pd-ZnO@polymer	-	-	-	48	-	12
Au-encapsulated ZnO@carbon	319	0.34	3.9	52	4.2	4.6
Pt-encapsulated ZnO@carbon	477	0.60	3.9	26	2.3	2.6
Pd-encapsulated ZnO@carbon	445	0.58	3.9	40	12	15

<sup>a</sup> Specific surface area and pore size were calculated by BET modelling. <sup>b</sup> Specific pore volume was measured by single point adsorption at P/P<sub>0</sub>~0.99. <sup>c</sup> Mean layer thickness and metal nanoparticle size were estimated by TEM analysis. <sup>d</sup> Calculated using the Scherrer equation for the metal (111) peak in the XRD profiles

#### 5.4. Conclusion

In summary, we demonstrated the facile synthesis of YSNs with controllable chemical compositions, spatial locations of active components, and tuneable shell layers. Novel yolk-shell structured ZnO@polymer nanoparticles were prepared through coating polymer and the following hydrothermal treatment. Yolk-shell structured ZnO@carbon can be generated through the carbonization process of ZnO@polymer nanoparticles. ZnO nanoribbon evolution is observed to occur via the dissolution of ZIF-8 and formation of the intermediate needle-like nanoparticles. At relative high temperature, the ZnO nanoribbon with (001), (002) and (101) crystal planes were present. The dominate ZnO growth followed the direction of [001] plane. Various noble metal (Pt, Au and Pd) nanoparticles are loaded on the inner shell of ZnO@carbon nanoparticles through carbonization of hydrothermally-treated metal-ZIF-8@polymer. During the carbonization process, it is found that the metal nucleation rate follows the sequence

Pd>Au>Pt and the conversion rate of ZnO nanoribbon shows the opposite trend. A remarkable higher activity of CO oxidation for Au-encapsulated ZnO@carbon is observed than Pd-and Pt-encapsulated ZnO@carbon most likely attributed to the dominate interface effects between the metal nanoparticles and ZnO supports. Furthermore, the yolk-shell structures can immobilize the Au nanoparticles and prevent possible migration and sintering, leading to superior catalytic stability. This nanoconfinement effect presented in this paper may open up new prospects for the applications of multiple functionalized YSNs as efficient nanoreactors for various applications

### 5.5 References

1. X. W. Lou, L. A. Archer and Z. Yang, *Adv. Mater.*, 2008, **20**, 3987-4019.
2. J. Liu, N. P. Wickramaratne, S. Z. Qiao and M. Jaroniec, *Nat. Mater.*, 2015, **14**, 763-774.
3. J. Liu, S. Z. Qiao, J. S. Chen, X. W. Lou, X. Xing and G. Q. Lu, *Chem. Commun.*, 2011, **47**, 12578-12591.
4. J. Liu, H. Q. Yang, F. Kleitz, Z. G. Chen, T. Yang, E. Strounina, G. Q. Lu and S. Z. Qiao, *Adv. Funct. Mater.*, 2012, **22**, 591-599.
5. Z. Teng, X. Su, Y. Zheng, J. Zhang, Y. Liu, S. Wang, J. Wu, G. Chen, J. Wang, D. Zhao and G. Lu, *J. Am. Chem. Soc.*, 2015, **137**, 7935-7944.
6. J. Liu, T. Yang, D.-W. Wang, G. Q. Lu, D. Zhao and S. Z. Qiao, *Nat. Commun.*, 2013, **4**, 2798.
7. H. Tian, M. Saunders, A. Dodd, K. O'Donnell, M. Jaroniec, S. Liu and J. Liu, *J. Mater. Chem. A*, 2016, **4**, 3721-3727.
8. J. Zhang, H. Hu, Z. Li and X. W. Lou, *Angew. Chem. Int. Ed.*, 2016, **55**, 3982-3986.
9. J. Liu, S. Z. Qiao, S. Budi Hartono and G. Q. Lu, *Angew. Chem. Int. Ed.*, 2010, **49**, 4981-4985.
10. Y. Chen, H. Chen, L. Guo, Q. He, F. Chen, J. Zhou, J. Feng and J. Shi, *ACS Nano*, 2010, **4**, 529-539.

11. S. J. Ding, J. S. Chen, G. G. Qi, X. N. Duan, Z. Y. Wang, E. P. Giannelis, L. A. Archer and X. W. Lou, *J. Am. Chem. Soc.*, 2011, **133**, 21-23.
12. B. Liu and H. C. Zeng, *Small*, 2005, **1**, 566-571.
13. E. C. Cho, P. H. C. Camargo and Y. N. Xia, *Adv. Mater.*, 2010, **22**, 744-748.
14. Y. D. Yin, R. M. Rioux, C. K. Erdonmez, S. Hughes, G. A. Somorjai and A. P. Alivisatos, *Science*, 2004, **304**, 711-714.
15. R. Banerjee, A. Phan, B. Wang, C. Knobler, H. Furukawa, M. O'Keeffe and O. M. Yaghi, *Science*, 2008, **319**, 939-943.
16. R. R. Salunkhe, Y. V. Kaneti, J. Kim, J. H. Kim and Y. Yamauchi, *Acc. Chem. Res.*, 2016, **49**, 2796-2806.
17. Y. V. Kaneti, J. Tang, R. R. Salunkhe, X. Jiang, A. Yu, K. C. W. Wu and Y. Yamauchi, *Adv. Mater.*, 2016, DOI: 10.1002/adma.201604898, 1604898-1604938.
18. J. Yang, F. Zhang, X. Wang, D. He, G. Wu, Q. Yang, X. Hong, Y. Wu and Y. Li, *Angew. Chem. Int. Ed.*, 2016, **55**, 12854-12858.
19. J. Tang, R. R. Salunkhe, J. Liu, N. L. Torad, M. Imura, S. Furukawa and Y. Yamauchi, *J. Am. Chem. Soc.*, 2015, **137**, 1572-1580.
20. M. Zhao, K. Yuan, Y. Wang, G. Li, J. Guo, L. Gu, W. Hu, H. Zhao and Z. Tang, *Nature*, 2016, **539**, 76-80.
21. P. Yin, T. Yao, Y. Wu, L. Zheng, Y. Lin, W. Liu, H. Ju, J. Zhu, X. Hong, Z. Deng, G. Zhou, S. Wei and Y. Li, *Angew. Chem. Int. Ed.*, 2016, **55**, 10800-10805.
22. C.-H. Kuo, Y. Tang, L.-Y. Chou, B. T. Sneed, C. N. Brodsky, Z. Zhao and C.-K. Tsung, *J. Am. Chem. Soc.*, 2012, **134**, 14345-14348.
23. F. Zhang, Y. Wei, X. Wu, H. Jiang, W. Wang and H. Li, *J. Am. Chem. Soc.*, 2014, **136**, 13963-13966.
24. J. Yang, F. Zhang, H. Lu, X. Hong, H. Jiang, Y. Wu and Y. Li, *Angew. Chem. Int. Ed.*, 2015, **54**, 10889-10893.
25. G. Lu, S. Li, Z. Guo, O. K. Farha, B. G. Hauser, X. Qi, Y. Wang, X. Wang, S. Han, X. Liu, J. S. DuChene, H. Zhang, Q. Zhang, X. Chen, J. Ma, S. C. J. Loo, W. D. Wei, Y. Yang, J. T. Hupp and F. Huo, *Nat. Chem.*, 2012, **4**, 310-316.

26. H. Hu, B. Guan, B. Xia and X. W. Lou, *J. Am. Chem. Soc.*, 2015, **137**, 5590-5595.
27. J. Liu, S. Z. Qiao, H. Liu, J. Chen, A. Orpe, D. Zhao and G. Q. M. Lu, *Angew. Chem. Int. Ed.*, 2011, **50**, 5947-5951.
28. W. Zhang, Y. Liu, G. Lu, Y. Wang, S. Li, C. Cui, J. Wu, Z. Xu, D. Tian, W. Huang, J. S. DuCheneu, W. D. Wei, H. Chen, Y. Yang and F. Huo, *Adv. Mater.*, 2015, **27**, 2923-2929.
29. S. Liu, J. Wang and J. Yu, *RSC Adv.*, 2016, **6**, 59998-60006.
30. K. S. Park, Z. Ni, A. P. Côté, J. Y. Choi, R. Huang, F. J. Uribe-Romo, H. K. Chae, M. O’Keeffe and O. M. Yaghi, *Proc. Natl. Acad. Sci. U. S. A.*, 2006, **103**, 10186-10191.
31. H. Yang, S. J. Bradley, A. Chan, G. I. N. Waterhouse, T. Nann, P. E. Kruger and S. G. Telfer, *J. Am. Chem. Soc.*, 2016, **138**, 11872-11881.
32. I. X. Green, W. Tang, M. Neurock and J. T. Yates, *Science*, 2011, **333**, 736-739.

*Every reasonable effort has been made to acknowledge the owners of copyright material. I would be pleased to hear from any copyright owner who has been omitted or incorrectly acknowledged.*

---

# Chapter 6. Metal–organic-framework-derived formation of Co-N-doped carbon materials for efficient oxygen reduction reaction

## 6.1. Introduction

Electrocatalysis for oxygen reduction reaction (ORR) have drawn enormous attention in the field of energy conversion.<sup>1,2</sup> It is well-recognized that Pt-related catalysts are the best active catalysts towards oxygen reduction reaction,<sup>3,4</sup> but high costs and low abundance of Pt still restrict its widespread application. In addition, there are still some problems that need to be solved such as intermediate poisoning, poor stability and fuel crossover in the electrochemical system. To overcome these problems, recent intensive research has focused toward to fabricate alternative nonprecious (Pt) electrocatalysts.<sup>5,6</sup> Among them, Co/N doped porous carbon (Co-N-carbon) electrochemical catalysts prepared from the calcination of nitrogen and cobalt containing raw materials such as aniline,<sup>7</sup> melamine,<sup>8</sup> pyrrole,<sup>9</sup> and metal-organic frameworks<sup>10-12</sup> are very promising candidates. Therefore, it is imperative to explore a simple approach to prepare Co-N-carbon nanoparticles with large specific surface area and excellent electrical conductivity in a facile and effective method to synergistically enhance ORR catalytic activity.

Until now, phenolic resin polymer spheres, carbon spheres and silica spheres have been synthesized through the simple Stöber method.<sup>13-15</sup> It is greatly desirable to use polymer coating technique to prepare core@polymer and core@carbon structures. Until now,

core-shell Au@carbon, Fe<sub>3</sub>O<sub>4</sub>@carbon, mesoporous silica nanoparticles@carbon, NaYF<sub>4</sub>@carbon, and PEI-SiO<sub>2</sub>@carbon have been successfully synthesized.<sup>16</sup> Recently, Yang et al. reported a simple method for the generation of hollow carbon capsules with monometallic and bimetallic nanoparticles through polymer coating strategy and the following carbonization process.<sup>17</sup> Therefore, it is still challenging to provide a facile approach to synthesize the composites of Co, N-doped carbon nanoparticles as effective electrochemical catalysts with relatively low costs starting from the Stöber method.

Herein, the preparation of cobalt nanoparticles@polymer yolk-shell structure under mild solvent hydrothermal conditions through phase transformation from ZIF-67@polymer core-shell framework was reported. Coating resin polymer on the surface of ZIF-67 creates a “nanoreactor” to complete the phase transformation. After pyrolysis in nitrogen atmosphere, Co-N-doped carbon materials are achieved. This unique synthetic strategy empowered the rational design of cobalt and nitrogen doped carbon nanoparticles with large surface area, high graphitization degree and nitrogen doping beneficial to the superior ORR performance.

## 6.2. Experimental section

### 6.2.1. Materials

The chemicals used in this project were provided as follows: formaldehyde (37%), ammonia solution (25%), ethanol (95-100%), cobalt nitrate hexahydrate (Co(NO<sub>3</sub>)<sub>2</sub>·6H<sub>2</sub>O), 3-aminophenol (99%), 2-methylimidazole and methanol (99%) were commercial and used as received. Reagent grade ethanol and ultrapure water were utilized for sample washings and solution preparations.

### 6.2.2. Synthesis of ZIF-67

Typically, 30 mL of methanol solution involving Co(NO<sub>3</sub>)<sub>2</sub>·6H<sub>2</sub>O (0.87 g) was firstly prepared. 2-methylimidazole (1.97g) was dissolved in 20 mL of methanol and this

mixture was poured into  $\text{Co}(\text{NO}_3)_2$  solution. The mixed solution was kept stirring at room temperature for 24 h. The remaining white products were collected through centrifuging and washing with methanol a few times, and finally dried at 80 °C overnight.

### **6.2.3. Synthesis of Co nanoparticles@polymer (CP)**

Firstly, an aqueous solution containing CTAB (0.1 g), water (20 mL) and ethanol (8 mL) was prepared. Then, 0.2 mL aqueous solution of ammonia was added and kept stirring for 0.5 h, followed by the addition of 0.1 g ZIF-67. After this mixture remained stirring for 0.5 h, 0.08 g 3-aminophenol was added into that solution. Followed by stirring for extra 30 min, 0.112 mL formaldehyde were added. Subsequently, the mixture continued stirring for 24 h at room temperature and afterwards hydrothermal treated for 24 h at 100 °C in a Teflon-lined autoclave. The remaining products were collected through centrifuging and washing and dried at 80 °C for 24 h.

### **6.2.4. Synthesis of Co-N-C nanoparticles**

The ZIF-67@polymers were calcined in  $\text{N}_2$  atmosphere in a tube furnace with a ramping rate of 1 °C  $\text{min}^{-1}$  up to 350 °C, remain for 2 h, and resuming ramping rate at 1 °C  $\text{min}^{-1}$  up to various temperatures (700, 800, and 900 °C) and dwell for 4 h. The final samples were represented as Co-N-C-X (X denotes calcination temperature of 700, 800, and 900 °C, respectively).

### **6.2.5. Synthesis of ZIF-67@polymer before hydrothermal reaction**

0.1 g CTAB was dissolved in an aqueous solution containing 20 mL water and 8 mL ethanol. Then, 0.2 mL ammonia solution was added and stirred at room temperature for 0.5 h, followed by addition of 0.1 g ZIF-67. This suspension was kept stirring for 0.5 h at room temperature and subsequently hydrothermally treated for 24 h at 100 °C in a

Teflon-lined autoclave. The remaining products were collected through centrifuging and washing with ethanol and dried at 80 °C for 24 h.

### 6.2.6 Oxygen reduction reaction (ORR) performance test

Catalyst inks were prepared by ultrasonically dispersing catalyst (4.0 mg) in a solution containing 0.5 mL of ethanol isopropanol (1:1 vol) and 16  $\mu\text{L}$  of 5 wt.% Nafion solution (Alfa Aesar). The dispersion was sonicated for 1 h. Then, 5  $\mu\text{L}$  of the ink was dropped onto a rotating disk electrode (RDE, 5 mm diameter, 0.196  $\text{cm}^2$  geometric surface areas). Cyclic voltammetry (CV) data were recorded on an electrochemical workstation (Electrochemical Workstation ZENNIUM, USA) equipped with a three-electrode cell system. For the use of the counter electrode and the reference electrode a Pt wire and an Ag/AgCl electrode were chosen, respectively. For the use of electrolyte, 0.1 M KOH was prepared. CV spectra were recorded at a scan rate of 50  $\text{mV s}^{-1}$  at room temperature. RDE measurements with a scan rate of 10  $\text{mV s}^{-1}$  and various rotating rates of 400, 625, 900, 1225, 1600 and 2025 rpm were conducted at room temperature. Through the calculation of Koutecky-Levich (K-L) equation, the electron transfer number ( $n$ ) per oxygen molecule in an ORR process was obtained:

$$J^{-1} = J_k^{-1} + (B\omega^{1/2})^{-1}$$

$$B = 0.2nF(D_0)^{2/3}v^{-1/6}C_0$$

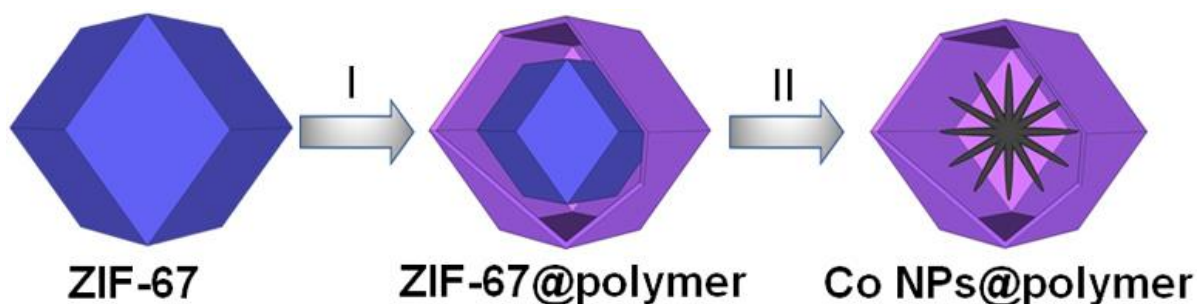
$$J_k = nFkC_0$$

where  $J$  is the measured current density during ORR,  $J_k$  is the kinetic current density,  $\omega$  is the electrode rotating angular velocity (rpm),  $B$  is the slope of K-L plots,  $n$  represents the electron transfer number per oxygen molecule,  $F$  is the Faraday constant ( $F = 96485 \text{ C mol}^{-1}$ ),  $D_0$  is the diffusion coefficient of  $\text{O}_2$  in 0.1 M KOH ( $1.9 \times 10^{-5} \text{ cm}^2 \text{ s}^{-1}$ ),  $v$  is the kinetic viscosity ( $0.01 \text{ cm}^2 \text{ s}^{-1}$ ),  $C_0$  is the bulk concentration of  $\text{O}_2$  ( $1.2 \times 10^{-3} \text{ mol L}^{-1}$ ).

### 6.2.7 Materials Characterization

The sample structure was characterized through a transmission electron microscope (TEM, FEI Titan G2 80-200) with High Angle Annular Dark Field Scanning Transmission Electron Microscopy (HAADF-STEM) imaging and elemental distribution map which was operated at 200 kV. The element maps were achieved by energy dispersive X-ray spectroscopy with Super-X detector on the TEM equipment using a probe size about 1 nm and a probe current of approximately 0.4 nA. X-ray diffractometer (Bruker D8 Advance) was used to perform Powder X-ray powder diffraction (XRD) analysis with Cu K $\alpha$  radiation at 40 kV and 30 mA. Micromeritics TriStar II Surface Area and Porosity Analyzer was utilized to obtain the BET specific surface area and single-point pore volume from nitrogen adsorption isotherms measured at -196 °C. Before the measurement of nitrogen adsorption, the samples were degassed at 250 °C for 10 h. A Kratos Axis Ultra DLD spectrometer with a monochromatic AlK $\alpha$  (1486.6 eV) irradiation source which was operated at 150 W was used for X-ray photoelectron spectroscopy (XPS) acquisitions. The vacuum pressure of the analysis chamber of the spectrometer was maintained a  $5 \times 10^{-11}$  Torr or lower. Samples were mounted for analysis by suspending a small amount of the powder sample in isopropanol, then drop casting the resultant mixture onto a 5mm x 10mm silicon wafer. The samples were allowed to gently dry under a heat lamp before being introduced into the ultra-high vacuum analytical chamber of the XPS instrument.

### 6.3. Results and discussion



**Scheme 6.1.** Fabrication of yolk-shell structured Co nanoparticles@polymer (CP): I) uniform coating of polymer onto the surface of ZIF-67; II) hydrothermal treatment of ZIF-67@polymer.

The synthesis strategy of yolk-shell structured Co nanoparticles@polymer (CP) is schematically illustrated in **Scheme 6.1**. Well-ordered ZIF-67 nanoparticles are prepared and polymer layer is coated on the surface of these hard templates through extended Stöber method. Followed by hydrothermal treatment of ZIF-67@polymer core-shell structures, yolk-shell structured Co nanoparticles@polymer (ZP) nanoparticles are achieved. Carbonization of these yolk-shell structured CP in nitrogen atmosphere can generate Co-N-C samples.

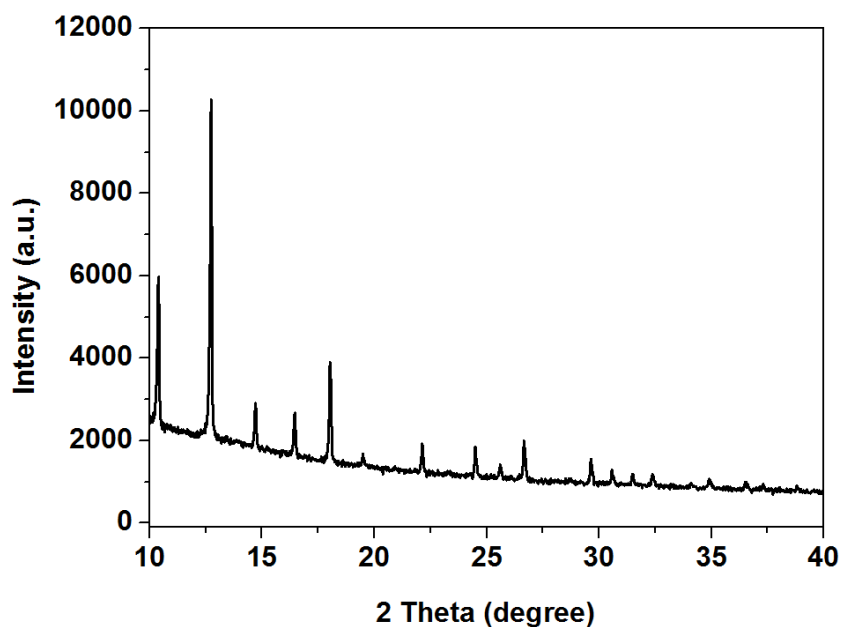


**Figure 6.1.** XRD pattern of ZIF-67.

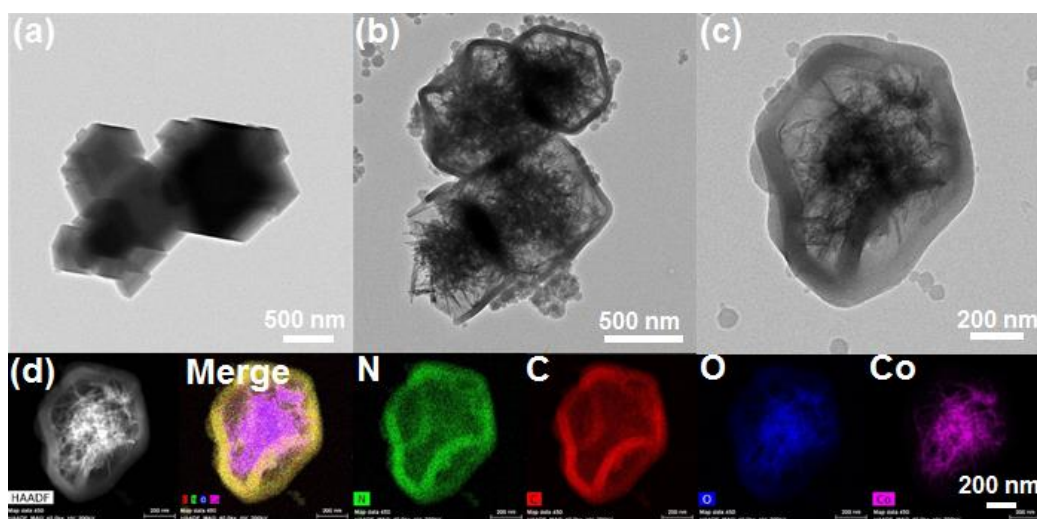


**Figure 6.2.** TEM images of ZIF-67 (a), ZIF-67@polymer after hydrothermal treatment (b) (c), STEM and EDS mapping (d).

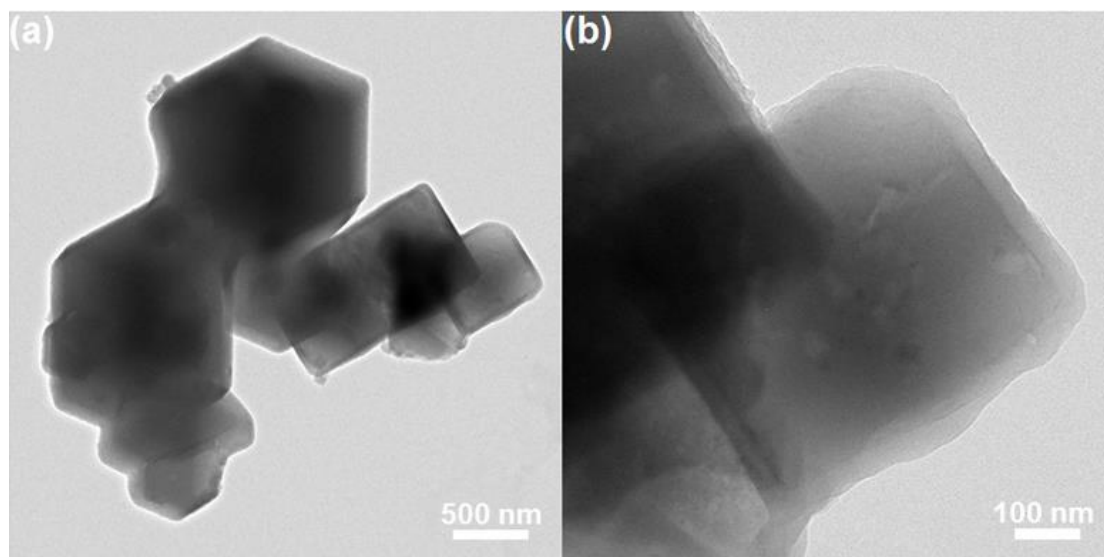
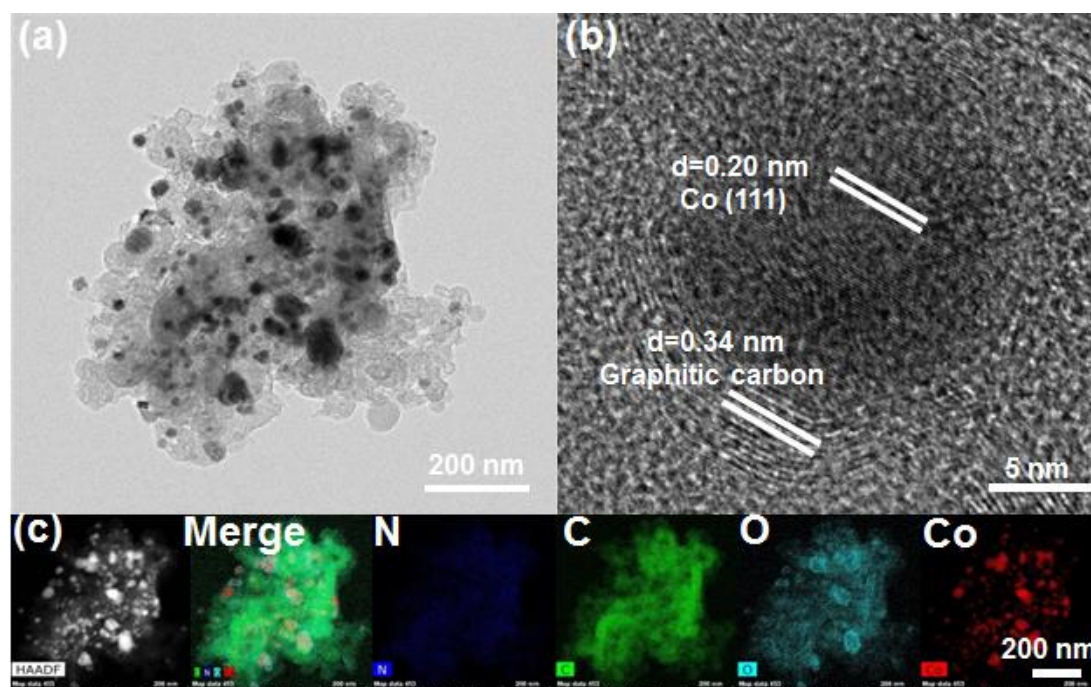
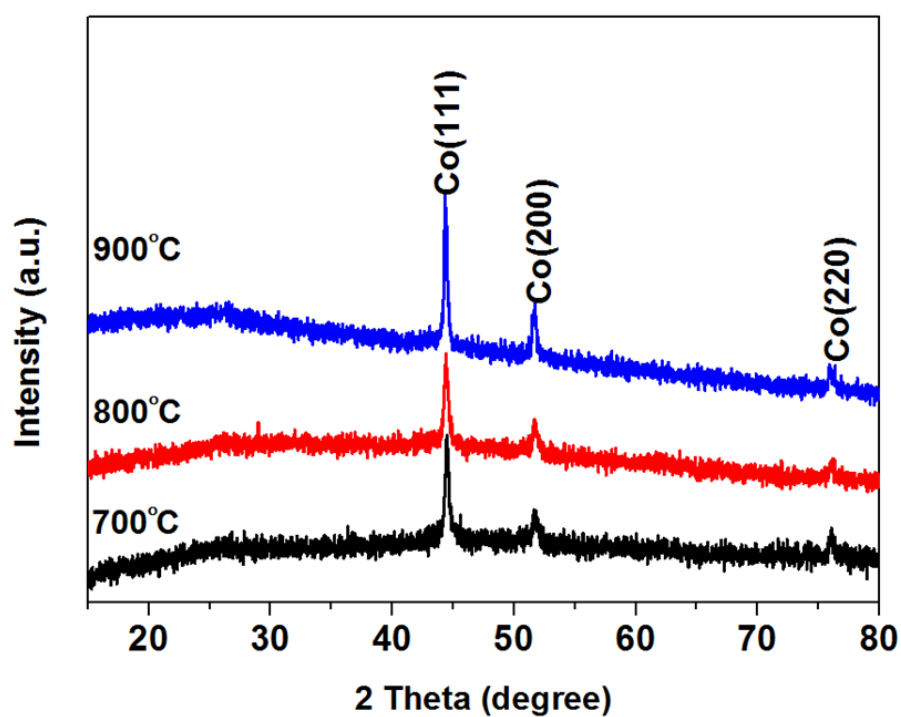


Figure 6.3. TEM images of ZIF-67@polymer before hydrothermal reaction.

The structures formed at different procedures are characterized by XRD, TEM and HAADF imaging and element mapping. The XRD results of ZIF-67 nanoparticles (**Figure 6.1**) is in agreement well with previous literatures<sup>18</sup> and a polyhedral shape with a smooth surface is presented in TEM image of ZIF-67 particles (**Figure 6.2a**). After generation of ZIF-67@polymer core-shell structures (**Figure 6.3**) and subsequent hydrothermal treatment for 24 hour, yolk-shell structured materials with shell thickness about 81 nm (**Figure 6.2b** and **Figure 6.2c**) are achieved. Noticeably, it is also very interesting to find the inside needle-like Co nanoparticles are generated in the hollow polymer shell. The HAADF imaging and elemental mapping results (**Figure 6.2d**) are obtained to investigate the distribution of nitrogen, carbon, oxygen and cobalt in this hollow structure. Elemental carbon and nitrogen are homogenously distributed in the carbon shell, but cobalt and most oxygen atoms are only present in the core materials, confirming elemental cobalt were confined in the hollow carbon shell.



**Figure 6.4.** TEM image (a), HRTEM image (b) and HAADF image and mapping images (c) of Co-N-C-700.



**Figure 6.5.** XRD patterns of the prepared catalysts.

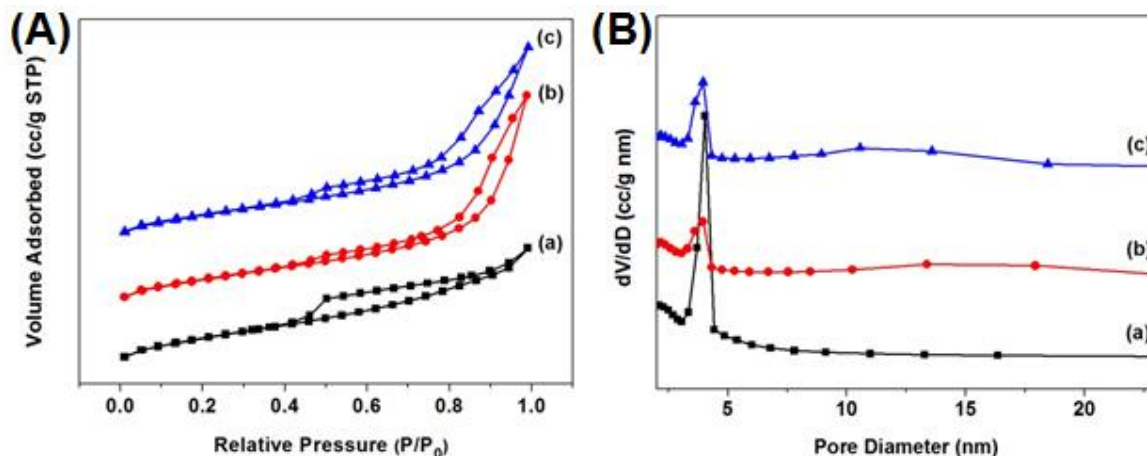


**Figure 6.6.** (A)  $N_2$  adsorption isotherms and (B) pore size distributions of (a) Co-N-C-700 (b) Co-N-C-800 and (c) Co-N-C-900.

After thermal treatment of CP in flowing nitrogen at 700 °C, a stacked carbon structure with the deposition of cobalt-related nanoparticles can be observed (as shown in **Figure 6.4a**). As shown in HRTEM image in Figure 2b, cobalt nanoparticles were enclosed among porous carbon layers. It is determined that interlayer distance is 0.34 nm, which is related to graphitic carbon with (002) plane.<sup>19</sup> As displayed in **Figure 6.4b**, the d-spacing is about 0.20 nm, ascribed to (111) lattice plane of cobalt metal with cubic phase. This is also confirmed from XRD patterns (**Figure 6.5**) that the peak around 25° probably can be attributed to graphitic carbon and other peaks at about 44.3°, 51.6° and 76.1° can be ascribed to cubic cobalt metal (JCPDS No.15-0806). The HAADF image and the elemental mapping results (**Figure 6.4c**) are acquired to explore the elemental distribution of nitrogen, carbon, oxygen and cobalt. As shown in **Figure 6.4c**, nitrogen and oxygen atoms are uniformly dispersed in the graphitic carbon structure and cobalt nanoparticles are wrapped with elemental oxygen. The  $N_2$  adsorption–desorption isotherm and the corresponding pore size distribution of Co-N-C-700 nanoparticles according to Barrett-Joyner-Halenda (BJH) model are shown in **Figure 6.6a**. The Co-N-C-700 nanoparticles exhibit BET surface area about 514 m<sup>2</sup> g<sup>-1</sup> and pore volume about 0.57 cm<sup>3</sup> g<sup>-1</sup>. The pore sizes mainly centered at 3.9 nm (**Figure 6.6b**), indicating the existence of mesopores. XPS measurement is conducted to explore chemical

composition and the nitrogen species in Co-N-C nanoparticles. XPS pattern of Co-N-C-700 catalysts exhibit four typical peaks for C 1s, N 1s, O 1s and Co 2p on the survey spectrum with the corresponding content of each element of 84.3%, 3.1%, 9.0% and 3.6%, respectively (**Figure 6.7a**). After deconvolution as presented in **Figure 6.7b**, six peaks at 779.4, 779.9, 788.2, 786.1, 794.5, 795.0 and 803.7 eV are displayed in high resolution spectra Co 2p. Among them, the peaks at 779.4 and 779.9 eV are corresponded to Co 2p<sub>3/2</sub> of Co<sup>2+</sup> species and the peak at 794.5 and 795.0 eV can be assigned to the Co 2p<sub>1/2</sub> of Co<sup>3+</sup> species in Co-N-C samples.<sup>20</sup> The satellite peaks at 788.2 and 803.7 eV can be referred to the shakeup excitation of Co<sup>2+</sup> species in Co-N-C nanoparticles.<sup>21</sup> The existence of Co<sup>2+</sup> and Co<sup>3+</sup> may derive from the surface oxidation of the Co metal deposits exposing to air. Furthermore, Co<sub>2</sub>O<sub>3</sub> and CoO are absent in the XRD spectra of Co-N-C-700 as shown earlier in Figure S3a. The inability of XRD to detect Co<sub>2</sub>O<sub>3</sub> and CoO is likely to be resulted from the resolution of the technique providing information mainly on the bulk particle and not the surface.<sup>22</sup> The symmetric C1s peak for the Co-N-C-700 (**Figure 6.7c**) was centered at approximately 284.5 eV, which could be ascribed to sp<sup>2</sup> graphitic carbon. The XPS high resolution N 1s scan (**Figure 6.7d**) displays four overlapping N 1s peaks corresponding to pyrrolic nitrogen (400.0 eV), pyridinic nitrogen (398.2 eV), N-oxide (403.4 eV) and quaternary nitrogen (400.9 eV) with the relative concentration of each of about 27.0%, 29.6%, 27.6% and 15.8%, respectively (Figure 3d).<sup>23</sup> Generally, while pyrrolic nitrogen and pyridinic nitrogen can be considered as coordination locations due to their unique lone-pair electrons, quaternary nitrogen and pyridinic nitrogen play a vital role in the enhancement of oxygen reduction reaction.<sup>24, 25</sup> Considering the XRD, TEM and XPS results together, it appears the cobalt nanoparticles containing cobalt metal crystallites with an oxidized shell and/or smaller (or amorphous) cobalt-oxide deposits appear on the surface of graphitic carbons.

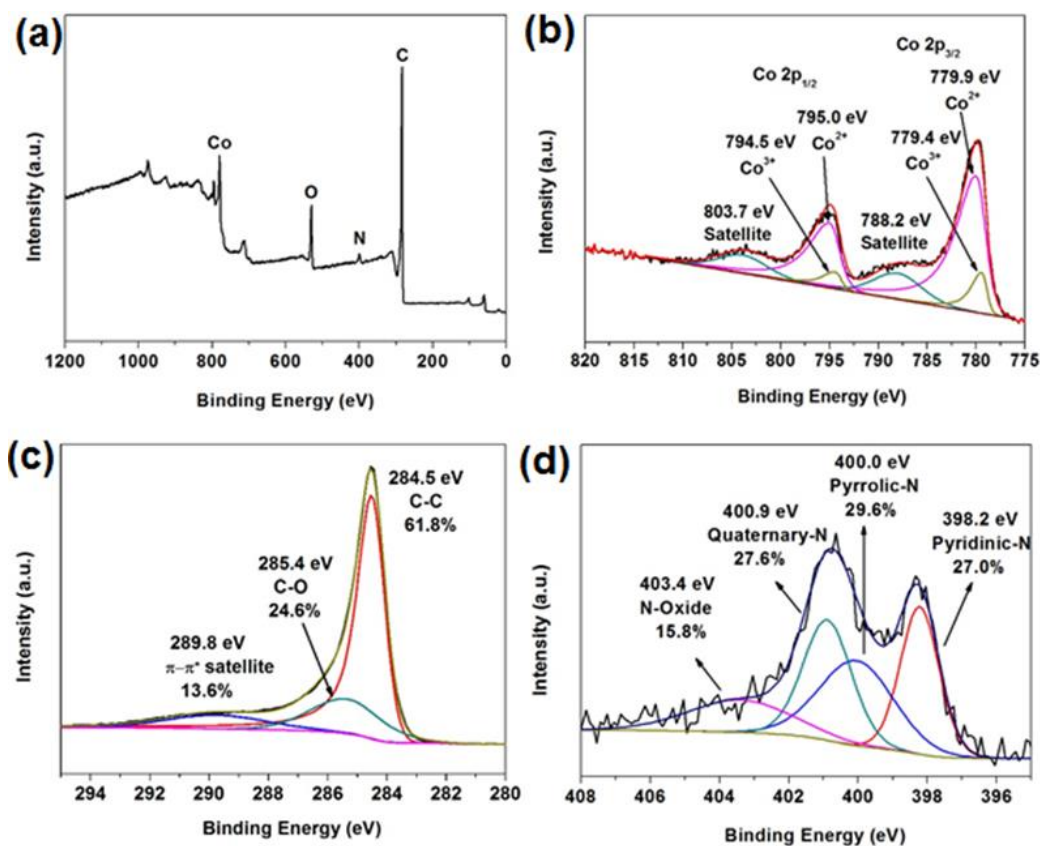


**Figure 6.7.** Full-scan XPS spectra(a), high resolution spectra Co 2p (b), C 1s (c), N 1s (d) of Co-N-C-700.

**Table 6.1.** Structural properties of the prepared nanoparticles.

Sample	BET surface area (m <sup>2</sup> /g) <sup>a</sup>	Pore volume (cm <sup>3</sup> /g) <sup>b</sup>	Pore size (nm) <sup>a</sup>
Co-N-C-700	514	0.57	3.9
Co-N-C-800	498	0.90	3.9
Co-N-C-900	472	0.83	3.9

<sup>a</sup> Specific surface area and pore size were calculated by BET method. <sup>b</sup> Specific pore volume was measured by single point adsorption at P/P<sub>0</sub>~0.99.

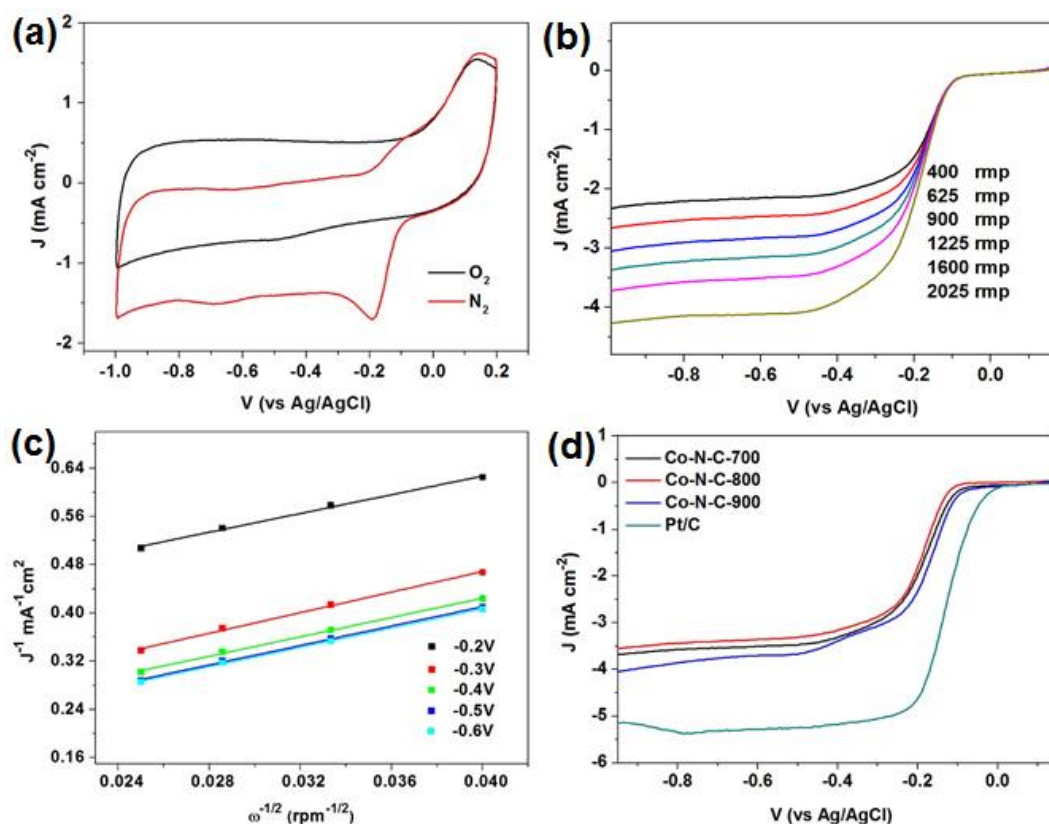


**Figure 6.8.** Electrochemical characterizations of Co-N-C catalysts for ORR. (a) CV curves in  $N_2$ -saturated and  $O_2$ -saturated 0.1 M KOH solution. (b) RDE polarization curves in  $O_2$ -saturated 0.1 M KOH solution with a sweep rate of  $10 \text{ mV s}^{-1}$ . (c) K–L plots. (d) LSV curves for Co-N-C-700, Co-N-C-800, Co-N-C-900, and Pt/C nanoparticles.

Because of large surface area and unique pore structure of Co-N-C nanoparticles, it is anticipated to be advantageous for fast mass transfer processes and easy access to active sites. Cyclic voltammetry (CV) was firstly utilized to evaluate electrocatalytic performance of Co-N-C-700 nanoparticles in saturated 0.1 M KOH solution with nitrogen and oxygen gas purging, separately. **Figure 6.8a** presented no redox peaks can be detected for Co-N-C-700 in the  $N_2$ -saturated condition between -1.0 and 0.2 V. Nevertheless, when it is tested in  $O_2$ -saturated electrolyte, a reduction peak was displayed at -0.19 V, indicating a superior ORR electrocatalytic behavior. Rotating disk electrode (RDE) measurements with rotating speeds in the range between 400 and 2500

rpm were conducted to study the reaction kinetics, revealing a direct 4-electron transfer pathway (**Figure 6.8b** and **6.8c**). Synthetic parameters for Co-N-C electrocatalysts such as calcination temperature play a vital role in the ORR test. The electrocatalytic behavior of Co-N-C samples synthesized at different calcination temperatures are also compared and the results have been shown in **Figure 6.8d**. The Co-N-C-900 presented superior ORR activity among the prepared samples from 700 to 900°C. This agrees well with the highest degree of graphitization among the three samples, which is proved from the XRD patterns (Figure S3) that the highest intensity of Co-N-C-900 presents at 26°, which can be attributed to the (002) plane of the graphitic carbon. The value of  $E_{1/2}$  and  $B$  of Co-N-C-900 ( $-0.17$  V and  $5.2$  mA cm $^{-2}$ ) were better than that of Co-N-C-800 ( $-0.19$  V and  $3.6$  mA cm $^{-2}$ ) and Co-N-C-700 ( $-0.17$  V and  $3.7$  mA cm $^{-2}$ ). The Tafel slope of Co-N-C-900 ( $77$  mV decade $^{-1}$ ) at low over potential was superior to Co-N-C-800 ( $65$  mV decade $^{-1}$ ) and Co-N-C-700 ( $71$  mV decade $^{-1}$ ) (**Figure 6.9**).

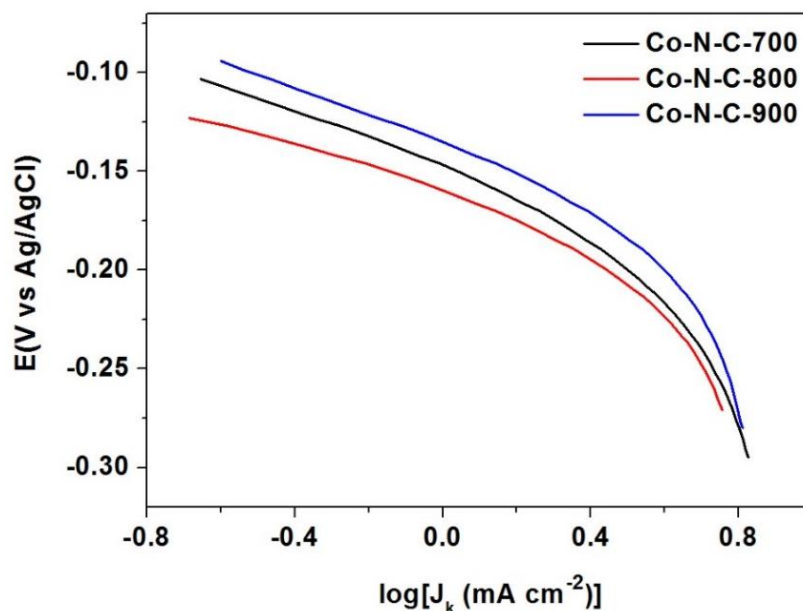


**Figure 6.9.** Tafel plots derived from LSV curves at 1600 rpm for the above catalysts.

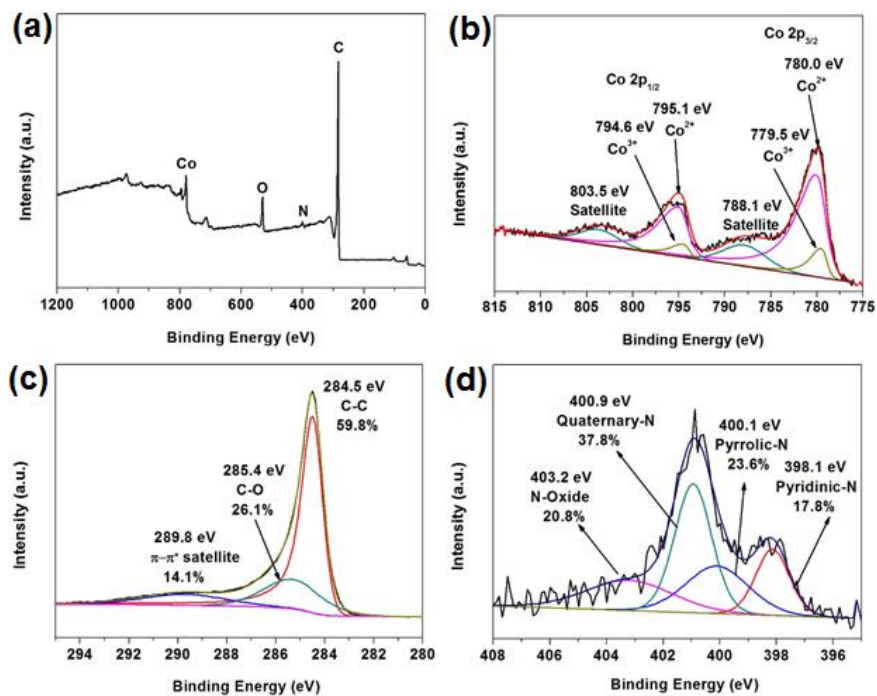


**Figure 6.10.** Full-scan XPS spectra (a), high resolution spectra Co 2p (b), C 1s (c), N 1s (d) of Co-N-C-800.

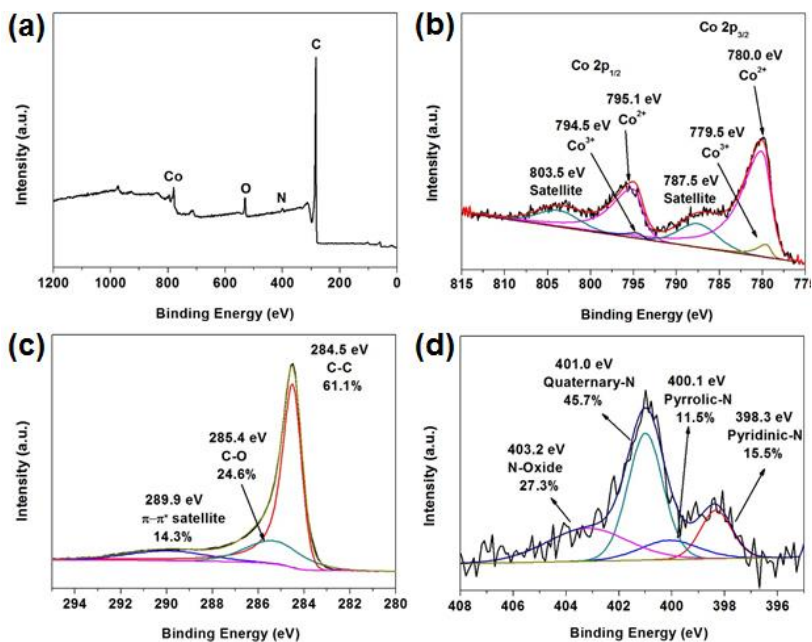


**Figure 6.11.** Full-scan XPS spectra (a), high resolution spectra Co 2p (b), C 1s (c), N 1s (d) of Co-N-C-900.

As shown above in **Figure 6.8d**, while the calcination temperature increased to 800°C, a decreased ORR behavior was observed for Co-N-C-800, although an improved degree of graphitization than Co-N-C-700. Wu et al. reported that the decreased surface area can induce the declined ORR activity.<sup>26</sup> Indeed, the BET surface area of Co-N-C-800 is 498 m<sup>2</sup>/g (**Figure 6.6** and **Table 6.1**), lower than that of Co-N-C-700. XPS results (**Figure 6.10**, **Figure 6.11** and **Table 6.2**) illustrate a decrease nitrogen and cobalt content of Co-N-C nanoparticles with increased calcination temperature, which seems to be the dominate factor of the vital factor of the reduction of ORR behavior of Co-N-C-800. In addition, **Figure 6.12** shows the content difference of nitrogen species including nitrogen-oxide, quaternary nitrogen atoms, pyrrolic nitrogen, and pyridinic nitrogen acquired from the high resolution of spectra N 1s and atomic percentage from the full survey (**Figure 6.7**, **6.10**, **6.11**, **Table 6.2** and **Table 6.3**). It is observed that the content of pyridinic N and pyrrolic N decreased with elevating temperatures, which is responsible for ORR activity.<sup>27, 28</sup> In addition, higher percentages of quaternary N and N-oxide were detected when the samples were treated at high temperatures, indicating that more pyrrolic and pyridinic nitrogen are transformed into quaternary nitrogen with the increase of temperatures. Therefore, the best calcination condition among the prepared Co-N-C samples is 900°C, which indicates a combination effect of graphitic character, surface area and the content of nitrogen (especially pyridinic N and pyrrolic N) and cobalt.

**Table 6.2.** The chemical compositions of the prepared catalysts obtained by XPS characterization.

Sample	C (at.%)	N (at.%)	O (at.%)	Co (at.%)
Co-N-C-700	84.3	3.1	9.0	3.6
Co-N-C-800	88.8	1.8	7.2	2.2
Co-N-C-900	92.5	1.7	4.3	1.5

**Table 6.3.** The atomic percentage of pyridinic nitrogen, pyrrolic nitrogen, graphitic nitrogen and nitrogen oxide of the above catalysts obtained by their corresponding high resolution XPS spectra N 1s.

Sample	Pyridinic N (at.%)	Pyrrolic N (at.%)	Quaternary N (at.%)	N-Oxide (at.%)
Co-N-C-700	27.0	29.6	27.6	15.8
Co-N-C-800	17.8	23.6	37.8	20.8
Co-N-C-900	15.5	11.5	45.7	27.3

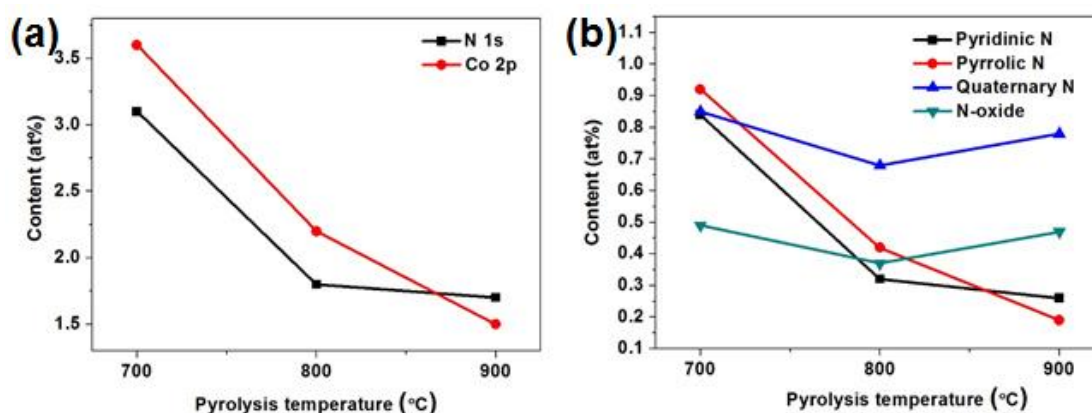


**Figure 6.12.** (a) The contents of cobalt and nitrogen (b) The contents of quaternary nitrogen, pyrrolic nitrogen, pyridinic nitrogen, and nitrogen-oxide in above catalysts.

#### 6.4. Conclusion

In summary, we have established a simple method to generate a new family of cobalt/N/C porous nanocomposite by pyrolysis of yolk-shell structured Co nanoparticles@polymer. Novel yolk-shell structured Co nanoparticles@polymer were prepared through coating polymer on the surface of ZIF-67 and the following hydrothermal treatment. Co-N-C-900 presents the best electroactivity among prepared samples due to the compromise of the factors such as surface area, graphitic degree and the content of nitrogen and cobalt. The design and fabrication of efficient metal/N/C catalysts at low cost for energy conversion applications can be inspired by this work.

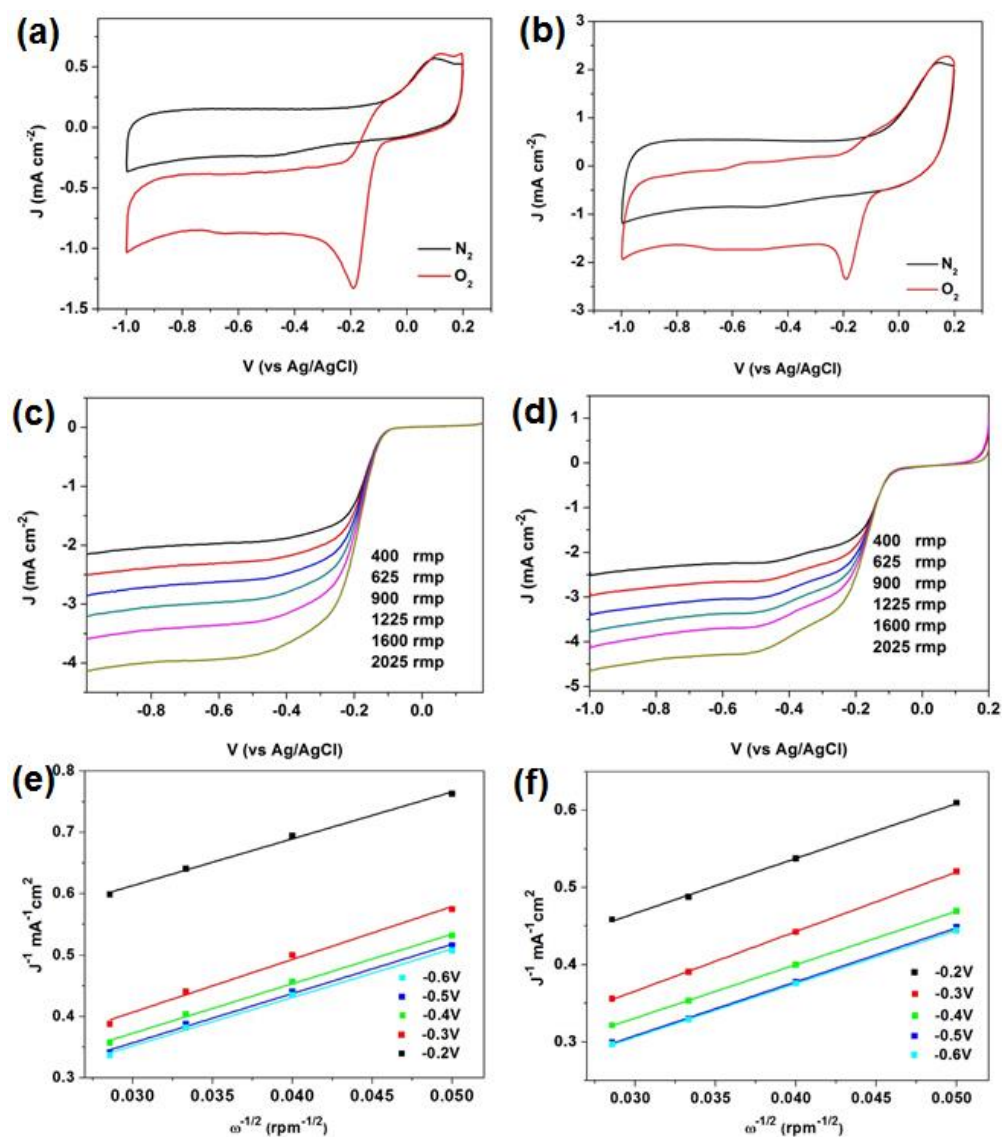


**Figure 6.13.** CV curves of Co-N-C-800 (a) and Co-N-C-900 (b) in  $\text{N}_2$ -saturated and  $\text{O}_2$ -saturated 0.1 M KOH solution. (b) RDE polarization curves of Co-N-C-800 (c) and Co-N-C-900 (d) in  $\text{O}_2$ -saturated 0.1 M KOH solution with a sweep rate of  $10 \text{ mV s}^{-1}$ . K–L plots of Co-N-C-800 (e) and Co-N-C-900 (f).

### 6.5 References

1. B. C. H. Steele and A. Heinzl, *Nature*, 2001, **414**, 345-352.
2. M. Armand and J. M. Tarascon, *Nature*, 2008, **451**, 652-657.
3. C. Cui, L. Gan, M. Heggen, S. Rudi and P. Strasser, *Nat Mater*, 2013, **12**, 765-771.

4. C. Chen, Y. Kang, Z. Huo, Z. Zhu, W. Huang, H. L. Xin, J. D. Snyder, D. Li, J. A. Herron, M. Mavrikakis, M. Chi, K. L. More, Y. Li, N. M. Markovic, G. A. Somorjai, P. Yang and V. R. Stamenkovic, *Science*, 2014, **343**, 1339-1343.
5. Y. Nie, L. Li and Z. Wei, *Chem. Soc. Rev.*, 2015, **44**, 2168-2201.
6. M. Shao, Q. Chang, J.-P. Dodelet and R. Chenitz, *Chem. Rev.*, 2016, **116**, 3594-3657.
7. G. Wu, K. L. More, C. M. Johnston and P. Zelenay, *Science*, 2011, **332**, 443-447.
8. J. Liu, X. Sun, P. Song, Y. Zhang, W. Xing and W. Xu, *Adv. Mater.*, 2013, **25**, 6879-6883.
9. R. Bashyam and P. Zelenay, *Nature*, 2006, **443**, 63-66.
10. D. Zhao, J.-L. Shui, L. R. Grabstanowicz, C. Chen, S. M. Commet, T. Xu, J. Lu and D.-J. Liu, *Adv. Mater.*, 2014, **26**, 1093-1097.
11. Y.-Z. Chen, C. Wang, Z.-Y. Wu, Y. Xiong, Q. Xu, S.-H. Yu and H.-L. Jiang, *Adv. Mater.*, 2015, **27**, 5010-5016.
12. L. Shang, H. Yu, X. Huang, T. Bian, R. Shi, Y. Zhao, G. I. N. Waterhouse, L.-Z. Wu, C.-H. Tung and T. Zhang, *Adv. Mater.*, 2016, **28**, 1668-1674.
13. W. Stöber, A. Fink and E. Bohn, *J. Colloid Interface Sci.*, 1968, **26**, 62-69.
14. J. Liu, S. Z. Qiao, H. Liu, J. Chen, A. Orpe, D. Zhao and G. Q. Lu, *Angew. Chem. Int. Ed.*, 2011, **50**, 5947-5951.
15. A.-H. Lu, G.-P. Hao and Q. Sun, *Angew. Chem. Int. Ed.*, 2011, **50**, 9023-9025.
16. B. Guan, X. Wang, Y. Xiao, Y. Liu and Q. Huo, *Nanoscale*, 2013, **5**, 2469-2475.
17. H. Yang, S. J. Bradley, A. Chan, G. I. N. Waterhouse, T. Nann, P. E. Kruger and S. G. Telfer, *J. Am. Chem. Soc.*, 2016, **138**, 11872-11881.
18. H. Hu, B. Guan, B. Xia and X. W. Lou, *J. Am. Chem. Soc.*, 2015, **137**, 5590-5595.
19. C. Zhu, Y. Wen, P. A. van Aken, J. Maier and Y. Yu, *Adv. Funct. Mater.*, 2015, **25**, 2335-2342.
20. H. L. Fei, J. C. Dong, M. J. Arellano-Jimenez, G. L. Ye, N. D. Kim, E. L. G. Samuel, Z. W. Peng, Z. Zhu, F. Qin, J. M. Bao, M. J. Yacaman, P. M. Ajayan, D. L. Chen and J. M. Tour, *Nat Commun*, 2015, **6**, 8668-8674.
21. X. Zou and Y. Zhang, *Chem. Soc. Rev.*, 2015, **44**, 5148-5180.

22. H. Tian, X. L. Zhang, J. Scott, C. Ng and R. Amal, *J. Mater. Chem. A*, 2014, **2**, 6432-6438.
23. T. Yang, J. Liu, R. Zhou, Z. Chen, H. Xu, S. Z. Qiao and M. J. Monteiro, *J. Mater. Chem. A*, 2014, **2**, 18139-18146.
24. Z.-Y. Wu, X.-X. Xu, B.-C. Hu, H.-W. Liang, Y. Lin, L.-F. Chen and S.-H. Yu, *Angew. Chem. Int. Ed.*, 2015, **54**, 8179-8183.
25. L. Lin, Q. Zhu and A.-W. Xu, *J. Am. Chem. Soc.*, 2014, **136**, 11027-11033.
26. G. Wu, C. M. Johnston, N. H. Mack, K. Artyushkova, M. Ferrandon, M. Nelson, J. S. Lezama-Pacheco, S. D. Conradson, K. L. More, D. J. Myers and P. Zelenay, *J. Mater. Chem.*, 2011, **21**, 11392-11405.
27. M. Xiao, J. Zhu, L. Feng, C. Liu and W. Xing, *Adv. Mater.*, 2015, **27**, 2521-2527.
28. Y. Zhu, B. Zhang, X. Liu, D.-W. Wang and D. S. Su, *Angew. Chem. Int. Ed.*, 2014, **53**, 10673-10677.

*Every reasonable effort has been made to acknowledge the owners of copyright material. I would be pleased to hear from any copyright owner who has been omitted or incorrectly acknowledge*

# Chapter 7 Conclusions and recommendations

## 7.1 Conclusions

The overall aim of this thesis was to develop carbon nanocomposites with desired morphologies, compositions and porosities. Carbon nanocomposites with different morphologies such as raspberry-like, core-shell and yolk-shell structures have been successfully synthesized through the state-of-art Stöber method. Additionally, in order to enhance the electrochemical behavior of carbon composites, doping atoms such as nitrogen and sulphur in the carbon structure and graphitization of carbon framework have been effectively introduced. Moreover, metal nanoparticles have also been incorporated into the yolk-shell structured carbon capsules. This series of carbon nanocomposites have presented potential applications in the research area of energy storage and conversion such as supercapacitors and lithium ion batteries.

The first major contribution of this thesis is to develop polymer-silica nanospheres via the extended Stöber method and the following carbonization process resulted in the formation of N, S dual-doped carbon-silica spheres. Silica nanoparticles can be easily controlled to grow on the surface of carbon cores and the core-shell structured carbon-silica spheres can also be obtained. Moreover, hetero-atoms such as nitrogen and sulphur can be incorporated into the carbon composites through the introduction of nitrogen precursor (3-aminophenol) and sulphur precursor (TESPTS) during the self-assembly process. In addition, the particle size of carbon-silica spheres and hollow silica spheres can be tuned through controlling the molar ratio of TESPTS/PR. Our method is considered to be easily-manipulated for adjusting the surface functionality, roughness and porous structures. Therefore, the prepared carbon-silica composites have shown the great potentials in multi-purpose applications such as catalyst supports, drug delivery carriers and hard templates,

which have been confirmed by their excellent behavior when used as adsorbents for CO<sub>2</sub> capture (67 cm<sup>3</sup>/g at 0 ± 1 °C and 1.0 bar) and as supercapacitor electrode with high specific capacitance in basic media (221 F/g, 6 M KOH).

The second major contribution in this thesis is to develop Fe<sub>3</sub>O<sub>4</sub>-carbon composites with core-shell, yolk-shell and hollow microboxes through polymer coating of Fe<sub>3</sub>O<sub>4</sub> microboxes followed by carbonization at different temperatures. Fe<sub>3</sub>O<sub>4</sub>-carbon composites with core-shell structure can be achieved at lower calcination temperature (500 °C), while the yolk-shell and hollow Fe<sub>3</sub>O<sub>4</sub>-carbon composites can be obtained at higher temperature (700 °C and 900 °C, respectively) when the polymer thickness reaches 23 nm. In addition, highly reversible capacity of 857 mAh g<sup>-1</sup> at the current density of 0.1 A g<sup>-1</sup> after 100 cycles can be delivered when core-shell structured FC-23-500 nanoparticles were used as anode materials for lithium ion batteries. At the current density of 5 A g<sup>-1</sup>, a superior high-rate capability and achieved the reversible capacity of 384 mAh g<sup>-1</sup> can be acquired. However, the yolk-shell structured (FC-23-700) and hollow Fe<sub>3</sub>O<sub>4</sub>-carbon composites (FC-23-900) showed an inferior cycle performance and rate capability because of an inadequate protective carbon shell and Fe<sub>3</sub>O<sub>4</sub> leaching out of the carbon shells. This rational design and fabrication of core-shell Fe<sub>3</sub>O<sub>4</sub>-carbon particles with tunable structures, multi-chemical composition and improved functionalities opens up new prospects of designing various anode materials with high performances.

Thirdly, yolk-shell structured ZnO@polymer nanoparticles were prepared through controllable coating on the surface of ZIF-8 by using extended Stöber method. The following carbonization process resulted in the formation of yolk-shell structured ZnO@carbon nanoparticles. Through the investigation of the formation of ZnO nanoribbon, the dissolution of ZIF-8 and the generation of needle-like nanoparticles inside of the shell are observed. In addition, various noble metal (Pt, Au and Pd) nanoparticles were incorporated on the inner shell of ZnO@carbon nanoparticles through carbonization of hydrothermally-treated metal-ZIF-8@polymer. It is interesting to find that the metal nucleation rate followed the sequence Pd>Au>Pt and the conversion rate of ZnO nanoribbon shows the opposite trend. When evaluated for CO oxidation reaction, Au-

encapsulated ZnO@carbon nanoparticles showed better catalytic performance than Pd- and Pt-encapsulated ZnO@carbon most likely due to the dominate interface effects between the metal nanoparticles and ZnO supports and possible lower rate of migration and sintering. Therefore, this nanoconfinement effect paves the way for the fabrication of novel yolk-shell structured nanoparticles with multiple functionalities as efficient nanoreactors for various applications.

In the last part of the thesis, a new series of cobalt carbon nanocomposites was prepared via carbonization of yolk-shell structured Co nanoparticles@polymer. The generation of yolk-shell structured Co nanoparticles@polymer can be simply prepared through hydrothermal treatment of ZIF-67@polymer. Cobalt carbon nanocomposites calcined at 900 °C (Co-N-C-900) showed better ORR electro-activity than that calcined at 700 °C (Co-N-C-700) and 800 °C (Co-N-C-800). This is attributed to the compromise of the factors such as surface area, graphitic degree and the content of nitrogen and cobalt. This work can inspire further research on the design and fabrication ORR catalysts with high efficiency and low cost to substitute the noble Pt-based catalysts for energy conversion applications.

## 7.2 Recommendations

Although this thesis shows great advances in the development of carbon nanocomposites with well-designed morphologies, controllable morphologies, manipulated porosities and adjustable functionalities, there are still many challenges for carbon nanocomposites with desired structural and compositional complexity in the research area of energy storage and conversion. Based on the finding from this research, some recommendations for future researches are suggested to further explore carbon nanocomposites and presented as follows.

Further studies are required toward controlling the uniformity and size of nanoparticles and the thickness of shells because the uniform size distribution and shape of nanoparticles are necessary for enhancing catalytic performances. For example, Yu et al. investigated

the effect of light scattering effect in the range of 260-800 nm and found the nanoparticles with 450 nm showed the light-scattering effect.<sup>1</sup> This resulted in its highest photovoltaic conversion efficiency when used for dye-sensitized solar cells due to its size-uniformity and long-range ordering. Uniformity is also of great importance especially when uptake and release kinetics should be considered. For example, well-ordered MOF crystals can significantly improve separation efficiency of hydrocarbons.<sup>2</sup>

To enhance thermal and chemical stability, great electronic conductivity and field emission behavior, carbon nanocomposites with graphitic structure should be synthesized and designed. For example, during materials synthesis, metal precursors such as Fe, Ni and Co can be introduced to improve the graphitization degree.<sup>3</sup> So in the next step of my research, Co/CoO@graphitic carbon hollow capsules derived from MOFs have been successfully synthesized and will be evaluated as anode materials for lithium ion batteries.

In addition, because micro, meso-porous carbon nanocomposites could afford high surface area to enhance reaction rate and macro-porous carbon nanocomposites could facilitate mass transfer and diffusion of reactants and products in the reaction, hierarchical porous structures with micropores, mesopores and macropores and pore size distribution with high uniformity and desired range need to be better investigated. Additionally, it should also be worthy of consideration to construct special structures such as Janus structure with two completely different functionalities on each side such as hydrophilic/hydrophobic and positively/negatively charged.

To reach the requirement for large-scale production of carbon nanocomposites, future researches need to be focused on design and synthesis cheap and environmental-friendly carbon nanocomposites with relatively high chemical performances. At present, we can prepare the carbon nanoparticles in the range of milligrams and grams, but for practical applications tons of carbon nanocomposites should be required. To address this problem, it is vital to find alternative cheap precursors for production of carbon nanocomposites, which needs us to understand the synthetic mechanisms deeply. Environmental problems always arouse the public attention in the development of new materials, so low-toxic

reagents should be considered during the preparation. Considering the above mentioned problems, bio-related materials may be considered as excellent candidates because of their abundance in earth and easy acquire. A further development of the computationally assisted design and fabrication such as density functional theory (DFT) calculation of carbon nanocomposites is needed for structural estimation and reduction of the amount of prepared samples.

With regard to materials application, the prepared carbon nanocomposites have showed great performances in energy-related applications, but the relationship between the physicochemical properties including pore size (hierarchical porous structure), graphitization degree, doping effect, composition and morphology and the performances should be deeply discussed to better understand the role of different factors to achieve high-rate devices. In addition, carbon nanocomposites should also be further probably investigated in the area of drug delivery, gas separation, absorption and storage or supports for bio-molecular immobilization in the field of bioscience.

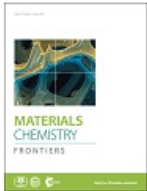
### 7.3 References

1. I. G. Yu, Y. J. Kim, H. J. Kim, C. Lee and W. I. Lee, *J. Mater. Chem.*, 2011, **21**, 532-538.
2. E. D. Bloch, W. L. Queen, R. Krishna, C. M. Brown, J. R. Long, *Science*, 2012, **335**, 1606–1610.
3. T. Y. Yang, J. Liu, R. F. Zhou, Z. G. Chen, H. Y. Xu, S. Z. Qiao and M. J. Monteiro, *J. Mater. Chem. A*, 2014, **2**, 18139-18146

*Every reasonable effort has been made to acknowledge the owners of copyright material. I would be pleased to hear from any copyright owner who has been omitted or incorrectly acknowledge*

# Appendix I

## Permission of Reproduction from the Copyright Owner



**Title:** Fabrication of core-shell, yolk-shell and hollow Fe<sub>3</sub>O<sub>4</sub>@carbon microboxes for high-performance lithium-ion batteries

**Author:** Hao Tian, Hao Liu, Tianyu Yang, Jean-Pierre Veder, Guoxiu Wang, Ming Hu, Shaobin Wang, Mietek Jaroniec, Jian Liu

**Publication:** Materials Chemistry Frontiers

**Publisher:** Royal Society of Chemistry

**Date:** Mar 6, 2017

Copyright © 2017, Royal Society of Chemistry

Logged in as:  
Hao Tian  
Account #:  
3001011847

LOGOUT

This reuse request is free of charge. Please review guidelines related to author permissions here:  
<http://www.rsc.org/AboutUs/Copyright/Permissionrequests.asp>

BACK

CLOSE WINDOW

Copyright © 2017 Copyright Clearance Center, Inc. All Rights Reserved. [Privacy statement](#). [Terms and Conditions](#).  
Comments? We would like to hear from you. E-mail us at [customercare@copyright.com](mailto:customercare@copyright.com)